EMERGING NANOMATERIALS FOR ENERGY CONVERSION AND STORAGE APPLICATIONS

EDITED BY: Guohua Jia, Hongbo Li and Zongyou Yin
PUBLISHED IN: Frontiers in Chemistry

frontiers Research Topics

ISSN 1664-8714
ISBN 978-2-88966-888-5
DOI 10.3389/978-2-88966-888-5

About Frontiers

Frontiers is more than just an open-access publisher of scholarly articles: it is a pioneering approach to the world of academia, radically improving the way scholarly research is managed. The grand vision of Frontiers is a world where all people have an equal opportunity to seek, share and generate knowledge. Frontiers provides immediate and permanent online open access to all its publications, but this alone is not enough to realize our grand goals.

Frontiers Journal Series

The Frontiers Journal Series is a multi-tier and interdisciplinary set of open-access, online journals, promising a paradigm shift from the current review, selection and dissemination processes in academic publishing. All Frontiers journals are driven by researchers for researchers; therefore, they constitute a service to the scholarly community. At the same time, the Frontiers Journal Series operates on a revolutionary invention, the tiered publishing system, initially addressing specific communities of scholars, and gradually climbing up to broader public understanding, thus serving the interests of the lay society, too.

Dedication to Quality

Each Frontiers article is a landmark of the highest quality, thanks to genuinely collaborative interactions between authors and review editors, who include some of the world's best academicians. Research must be certified by peers before entering a stream of knowledge that may eventually reach the public - and shape society; therefore, Frontiers only applies the most rigorous and unbiased reviews.
Frontiers revolutionizes research publishing by freely delivering the most outstanding research, evaluated with no bias from both the academic and social point of view. By applying the most advanced information technologies, Frontiers is catapulting scholarly publishing into a new generation.

What are Frontiers Research Topics?

Frontiers Research Topics are very popular trademarks of the Frontiers Journals Series: they are collections of at least ten articles, all centered on a particular subject. With their unique mix of varied contributions from Original Research to Review Articles, Frontiers Research Topics unify the most influential researchers, the latest key findings and historical advances in a hot research area! Find out more on how to host your own Frontiers Research Topic or contribute to one as an author by contacting the Frontiers Editorial Office: frontiersin.org/about/contact

EMERGING NANOMATERIALS FOR ENERGY CONVERSION AND STORAGE APPLICATIONS

Topic Editors:
Guohua Jia, Curtin University, Australia
Hongbo Li, Beijing Institute of Technology, China
Zongyou Yin, Australian National University, Australia

Citation: Jia, G., Li, H., Yin, Z., eds. (2021). Emerging Nanomaterials for Energy Conversion and Storage Applications. Lausanne: Frontiers Media SA.
doi: 10.3389/978-2-88966-888-5

Table of Contents

frontiers in Chemistry

ORIGINAL RESEARCH
published: 08 April 2020
doi: 10.3389/fchem.2020.00222

Mechanism of Remediation of Cadmium-Contaminated Soil With Low-Energy Plant Snapdragon

Yang Zhi[1]*, *Qixing Zhou*[2], *Xue Leng*[1] and *Chunlei Zhao*[3]

[1] School of Pharmaceutical Engineering, Shenyang Pharmaceutical University, Shenyang, China, [2] Key Laboratory of Pollution Processes and Environmental Criteria (Ministry of Education)/Tianjin Key Laboratory of Environmental Remediation and Pollution Control, College of Environmental Science and Engineering, Nankai University, Tianjin, China, [3] School of Traditional Chinese Medicine, Shenyang Pharmaceutical University, Shenyang, China

In the process of remediation of contaminated soil, we should give full play to the role of low-energy plants and fully display the concept of modern energy-saving and environmental protection. Phytoremediation is an effective method to remediate cadmium-contaminated soil, and root exudates play an important part in this process. Here, the response of snapdragon in a pot-culture experiment under two concentrations of Cd (1.0 and 2.5 mg/kg) was evaluated. Snapdragon is a medicinal plant with low energy consumption, which has low requirements on environmental factors and strong resistance. The results showed that both Cd concentrations interfere with the uptake of B, P, Cu, Mn, Mo, and Zn by the soil. The results also showed that plant type and Cd stress can significantly change the concentrations and species of root exudates. The metabolic changes of root exudates revealed the active defense mechanism of plants to Cd stress: up-regulating of amino acids to sequester/exclude Cd, regulation of citric acid on chelation/complexation, and precipitation of cadmium ions. The application of snapdragon can effectively reduce energy consumption and gradually improve the utilization rate of vegetation, which promotes the degradation of cadmium pollutants in soil.

Keywords: snapdragon, low-energy plant, cadmium pollution, mineral nutrients, root exudates

OPEN ACCESS

Edited by:
Zongyou Yin,
Australian National University, Australia

Reviewed by:
Hongtao Fan,
Liaoning Shihua University, China
Yun Wang,
Northeastern University, China

***Correspondence:**
Yang Zhi
zhiyang0412@163.com

Specialty section:
This article was submitted to Inorganic Chemistry, a section of the journal Frontiers in Chemistry

Received: *10 February 2020*
Accepted: *09 March 2020*
Published: *08 April 2020*

Citation:
Zhi Y, Zhou Q, Leng X and Zhao C (2020) Mechanism of Remediation of Cadmium-Contaminated Soil With Low-Energy Plant Snapdragon. Front. Chem. 8:222. doi: 10.3389/fchem.2020.00222

INTRODUCTION

Low-energy-consuming plants can effectively photosynthesize to a certain extent, which has an impact on the surrounding vegetation, and can help all kinds of vegetation absorb more nutrients, so as to achieve the unity of economic and social benefits. Planting snapdragon does not need to use chemical fertilizers and pesticides; it needs to match the environment and can achieve minimum consumption. Snapdragon, a perennial herbaceous plant, is highly valued in traditional Chinese medicine. It provides treatments for clearing away heat, detoxicating, cooling blood, and relieving swelling. The application of snapdragon can accelerate the speed of photosynthesis and respiration of vegetation, and to some extent, it can effectively alleviate the environmental pressure of the city.

With the continuous development of social economy, industrial and agricultural activities, such as the application of fertilizers, lime, manure, sewage sludge, and compost, result in loss of energy and soil contamination by heavy metals (Zhou et al., 2016). In China, Cd has posed a serious threat to the safety of crops and food production; one-fifth of the farmland, at least 2×10^5 km^2 of farmland, has been polluted by Cd to varying degrees (Fan et al., 2013). Cadmium (Cd) is a potentially harmful heavy metal that can be toxic to plants even at very low concentrations (0.5

μg Cd g^{-1} soil). In recent years, the content of heavy metals in medicinal plants has attracted worldwide attention, because these elements usually enter the food chain through plants and gradually pass to the final consumers, resulting in a large number of health problems. Accumulation of cadmium in soils can lead to soil degradation and decreased yields of medicinal plants, with long-term risks to ecosystems and human health (Chary et al., 2008). It is important to focus on medicinal plants, especially the monitoring of Chinese medicinal materials from areas that may be polluted by heavy metals to prevent heavy metals from exceeding standards and ensure the safety of medication.

Conventional techniques to remediate heavy metal(loid)s from contaminated soils are based on physical, chemical, and biological methods, which may be used in combination with one another to remediate contaminated sites. Despite high efficiency, majority of these techniques are costly, have high energy consumption, and are environmentally destructive (Khalid et al., 2017). In order to reduce the toxicity of cadmium in medicinal plants, we screened the common medicinal plants and found that snapdragon was a low cadmium accumulation plant. Further, we would like to understand the restoration mechanism of snapdragon. Among them, root exudates, which are closely related to the roots of plants, is preferred because it can affect the growth and metal uptake of plants in an environmentally friendly way (Zhou et al., 2016; Li et al., 2018). Root exudates are mainly photosynthetic products transferred from the root and released to the rhizosphere (Walker et al., 2003) Plant roots can release a variety of compounds including carbohydrates, organic acids, amino acids, fatty acids, sterols, and vitamins (Carvalhais et al., 2011; Lu et al., 2017). These compounds play an important role in plant stress resistance and external removal of pollutants. A large amount of evidence shows that plants chelate or complex toxic metals (such as Al, Cd, Zn, Fe, and Cu) by up-regulating certain organic acids (including amino acids), thus hindering their transfer to aboveground plant tissues. It is well-known that about 30–40% of the photosynthate carbon will be transferred to the rhizosphere in the form of root exudates, including organic acids, amino acids, sugars, proteins, phenolic compounds, and CO_2. In the soil–plant system, the interaction between organic acids and metals is of great significance for the dissolution/combination of metals in the insoluble mineral phases in soils.

Therefore, the specific objectives of this research were to (1) investigate the uptake, translocation, and accumulations of Cd in low-energy plant snapdragon tissues; (2) explore the response of root exudates (organic acids, amino acids) of snapdragon to cadmium toxicity; and (3) test the influence of Cd on the accumulation of mineral nutrient (Ca, Cu, Fe, Mg, Mn, Mo, P, and Zn) in different tissues of snapdragon.

MATERIALS AND METHODS

Experimental Site and Soil Characterization

The pot-culture experiment was carried out in a greenhouse at the Shenyang Pharmaceutical University. The temperature in greenhouse was maintained at 27°C during the day and 21°C at night. Soil samples were collected from the surface soil of meadow burozem topsoil (0–20 cm) in a field at the Shenyang Experimental Ecology Station (41° 31′ N and 123° 41′ E), Chinese Academy of Sciences, which is located at the south of Shenyang City, Liaoning Province, China, where the mean temperature was about 6–10°C. The frost-free period lasts 127–164 days per year. According to the routine analysis methods of pesticides and soil, the basic physical and chemical properties of the tested soil were analyzed (Lu, 1999). Chemical analysis showed that soil organic matter content was 2.62%, pH value was 6.87, cation exchange capacity (CEC) was 0.473 mol kg^{-1}, and Cd background concentration was 0.15 mg kg^{-1}.

Experimental Design

The soil sample was mixed with an appropriate concentration of $CdCl_2 \cdot 2.5\ H_2O$, ground and passed through a 4-mm mesh, and then 2.5 kg of soil was filled in each plastic basin ($\Phi = 20$ cm, $H = 15$ cm). There were three treatments: CK (control, no Cd) and two Cd treatments: T_1 (1.0 mg Cd kg^{-1} soil) and T_2 (2.5 mg Cd kg^{-1} soil). Two levels (1.0 and 2.5 mg Cd kg^{-1} soil) indicate low to moderate pollution according to the single pollution index evaluation method and the soil grading scale for heavy metal contamination (Zhou and Song, 2004; Chai et al., 2006; Liu et al., 2010). Accurately weigh 500 g of the corresponding soil and put it into a 300-mesh nylon rhizosphere bag. The diameter of the rhizosphere bag was about 15 cm. One rhizosphere bag is placed in each plastic flowerpot, and the soil in the bag is used as the rhizosphere soil of the plant. The soil is watered and then covered with tarpaulin to keep it perfectly balanced for up to 8 weeks, a long enough time to allow a natural balance of the various adsorption mechanisms in the soil. These pots are arranged in a completely random square design. Each treatment was repeated three times to minimize experimental errors.

Snapdragon seeds used in the experiment came from a seed company in Shenyang, China. The seeds were sterilized with 2% (V/V) hydrogen peroxide for 10 min and then washed with distilled water for several times. Subsequently, the seeds are transferred to paper towels to germinate. Place the rolled paper towel with the seeds in a box with distilled water on the bottom and leave it in the dark for 3 days, then expose it to light for 1 day. After germination in the greenhouse, 6 seeds were sown in each pot. The pots did not use fertilizers. During the experiment, water loss was replenished to maintain 75% of the soil's water holding capacity, and a dish was placed under each pot to collect potential leachate.

Cd and Nutrient Elements Analysis

At harvest time, snapdragon plants are thoroughly washed three times with tap water and then three times with deionized water. These plants are divided into roots and shoots. The samples were dried at 105°C for 5 min and oven-dried for 3 days at 70°C, then the rhizosphere soil was collected by shaking root method and put into the rhizosphere bag. Soil samples were dried, ground with a mortar and pestle, and passed through a 0.149-mm sieve (Wei and Zhou, 2004). Plant sample (0.50 g) and a soil sample (0.50 g) were digested with 12 ml of solution containing 87%

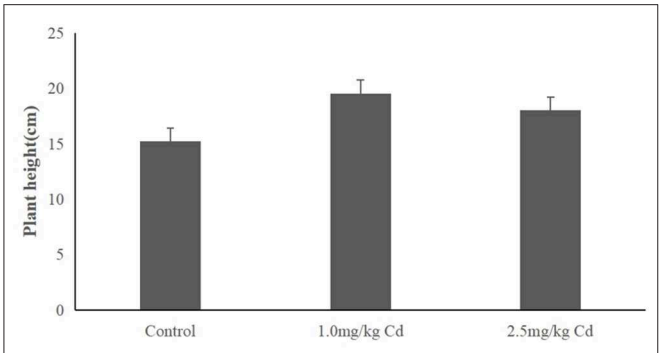

FIGURE 1 | The height of snapdragons in the pot-culture experiment.

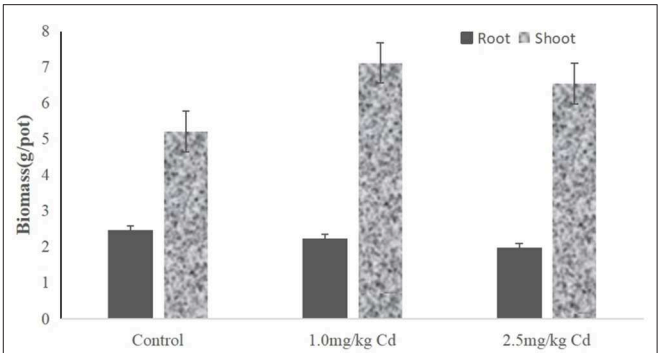

FIGURE 2 | The biomass of different tissues from snapdragons treated with Cd at 0, 1.0, and 2.5 mg/kg.

concentrated HNO_3 and 13% concentrated $HClO_4$ (V/V) (Wei et al., 2005). The concentration of Cd, Ca, Cu, Fe, Mg, Mn, Mo, P, and Zn was analyzed using ICP-AES (Spectro arcos, Germany). The recoveries for all the elements were between 92 and 99%.

Root Exudates Collection and Analysis

Weigh about 2 g of rhizosphere soil and put it into a 10-ml centrifuge tube. On the basis of the previous study, 4 ml of solution containing 0.1% H_3PO_4 was added to the solution of each component of root exudate to inhibit microbial activity. The tube was shaken on a rotary shaker at 200 rpm in the dark to achieve apparent equilibrium desorption. All microorganisms were then removed by centrifugation at 5,000 rpm for 5 min followed immediately by centrifugation with a syringe filter (0.45 μm). The organic acids in the soil was extracted and analyzed using a reported method (Sun et al., 2010). The soil samples (0.25 g) were digested with 6 mol/L HCl 20 ml at 105°C for 12 h in a 100-ml hydrolysis bottle. The amino acids in the soil were extracted and analyzed (Hou et al., 2006).

Statistical Analysis

Data were analyzed by Excel 2018 and SPSS 18.0. All values are expressed as mean ± standard deviation ($n = 3$). When $P < 0.05$, the treatment effect was statistically significant. Data were analyzed by one-way ANOVA and Tukey multiple range test. All results are expressed as dry weight.

RESULTS AND DISCUSSION

Impact of Cd on Snapdragon Growth

The plant height of snapdragon in different Cd treatments was depicted in **Figure 1**. Snapdragon plants exhibited significant increase in plant height compared to the control after 60 days of exposure to 1.0 and 2.5 mg/kg of Cd. The result indicated that the snapdragon plants had tolerance to Cd toxicity.

Root biomass decreased by 9.8 and 11.3% at 1.0 and 2.5 mg/kg Cd treatment, respectively (**Figure 2**), but only at 2.5 mg/kg was Cd treatment significant ($P < 0.05$). Compared with the root system, the effect of Cd on the aboveground biomass (including stem and leaf) was not significant. The shoot biomass of the snapdragon plants under 1.0 mg/kg Cd also increased significantly ($P < 0.05$) compared with control and Cd at 2.5 mg/kg. A large number of studies have shown that cadmium has a certain dose effect on plant growth; that is, low concentration of cadmium has a stimulating effect on plant growth (Jia et al., 2013; Zhou et al., 2013; Janota et al., 2015; Guo et al., 2018). Similar results have been reported in asparagus bean (Zhu et al., 2007), paddy rice (Yu et al., 2006), Chinese cabbage (Liu et al., 2010), tomato (Zhu et al., 2006), and soybean (Zhi et al., 2014). Two possible reasons can be suggested. One possible reason is that metal ions can act as activators of enzymes in cytokinin metabolism and promote plant growth (Shentu et al., 2008). Another possible reason is that low concentrations of cadmium hyperpolarize the plasma membrane at the root surface, increasing the transmembrane potential as a source of energy for cation absorption (Kennedy and Gonsalves, 1987). Therefore, it is difficult for farmers to find cadmium pollution in snapdragon, which will increase the harm of cadmium pollution products in snapdragon to human health.

Cd Accumulation and Distribution

We observed that Cd concentration in plants (root and shoot) treated with 1.0 and 2.5 mg/kg was significantly higher than that of control (**Figure 3**). The results showed that Cd content in plants increased with the increase of Cd concentration in soil. Cd was absorbed by plants and transported from roots to shoots within 60 days. There was no significant ($P > 0.05$) difference in distribution of Cd in the tissue of the plant under two treatments. Cadmium was mainly in roots (55.3–58.6%) and then in shoots (41.4–44.7%). Therefore, most of the Cd absorbed by the plant is reused in the root chamber, and the rest of the Cd is transported to the upper tissue. Cd is transported to the upper tissue. This is consistent with previous reports showing that the Cd is located primarily at the root. Jarvis et al. (1976) reported that more than 70% of supplied Cd was incorporated in roots of *Zea mays* and other plants (Jarvis et al., 1976).

The accumulation of cadmium in plants is closely related to the physiological processes of plant absorption, transportation, and detoxification. It is generally accepted that the uptake of heavy metals in soil is either passive, that is, a large amount of water enters the roots, or active transport through the plasma

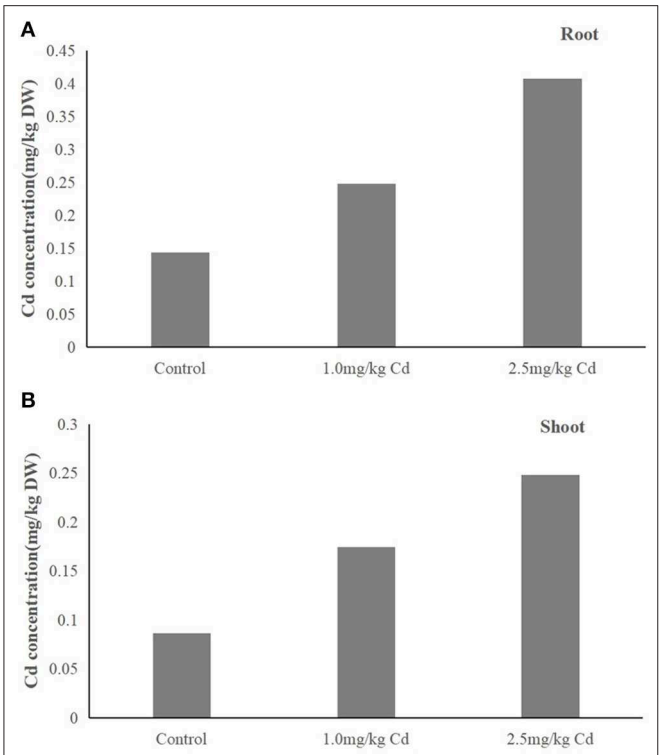

FIGURE 3 | (A,B) Distribution of Cd in the tissues of snapdragons under two Cd treatments.

TABLE 1 | Enrichment Factor (EF) and Translocation Factor (TF) in snapdragons under different cadmium concentrations.

	TF	EF
Control	0.60	
1.0 mg/kg Cd	0.71	0.17
2.5 mg/kg Cd	0.81	0.10

membrane of root epidermal cells (Yoon et al., 2006). The distribution of Cd in the aboveground and underground parts of plants is affected by the absorption, transportation, chelation, and compartmentalization of Cd (Wei et al., 2012).

EF and TF

Enrichment factors (EF) (Chen et al., 2004; Zhi et al., 2014) were calculated using the following formula to assess the ability of plants to accumulate heavy metals:

$$\mathrm{EF} = \frac{C_{shoot}}{C_{soil}}$$

where C_{shoot} is the average Cd concentration (DW) of the plant and C_{soil} is the total concentration of Cd in the corresponding soil. The EF values in plants were found to be lower than 0.20 under the two Cd treatments (**Table 1**).

In addition, translocation factor (TF) is the ratio of metal concentrations in the shoot to those in the root (Bose and Bhattacharyya, 2008). By calculating transfer factors (Baker and Whiting, 2002; Zhi et al., 2014), we assessed the potential for Cd transfer from root to shoot as follows:

$$\mathrm{TF} = \frac{C_{shoot}}{C_{root}}$$

where C_{shoot} is the average Cd concentration (DW) of the plant and C_{root} is the average Cd concentration (DW) of the root of each corresponding plant. There was an upward tendency that all the TF values were lower than 1.0 (**Table 1**). It is worth noting that with the increase of Cd concentration, the TF value tends to increase, while the EF value decreases (**Table 1**).

The results showed that the uptake capacity of Cd in soil was low, but the transport capacity of root to shoot was relatively high. In snapdragon, when the Cd concentration in soil increased slightly, the Cd concentration in shoot increased correspondingly. It is considered that the excessive migration of Cd from soil to plants can make up for the deficiency of Cd migration from roots to shoots, which can easily lead to the risk of Cd pollution in snapdragon. Therefore, pollution-safe varieties are varieties that grow in contaminated soil and have concentrations of certain pollutants in their edible parts that are low enough to be safe to eat, which is a cost-effective way to reduce cadmium accumulation in crops (Liu et al., 2005; Yu et al., 2006). Based on previous investigations (Baker and Whiting, 2002; Zhi et al., 2015), four criteria were applied to screen for medicinal plants with low cadmium accumulation: (1) the edible fraction should have a Cd concentration <0.3 mg/kg DW according to Green Standards of Medicinal Plants and Preparations for Foreign Trade and Economy (WM/T2-2004); (2) EF < 1.0; (3) TF < 1.0; and (4) Cd tolerance as measured by shoot biomass and height when grown in contaminated soil. The results showed that snapdragons were a low Cd accumulator when the concentration of Cd was <1 and 2.5 mg/kg. In addition, the EF and TF of these plants were lower than 1.0.

Mineral Nutrients

Cadmium is a non-essential element (Liñero et al., 2015), which can actively enter plant cells through the absorption mechanism and absorb essential elements such as Zn, Ca, and Fe (Lu et al., 2009). As shown in **Table 2**, there were significant differences in nutrient elements among the different Cd treatments. The concentrations of B, P, Fe, Ca, Cu, and Mg in different tissues of snapdragon decreased. Except for Cu in root ($p = 0.071$) and Mg in shoot ($p = 0.114$), the others decreased significantly ($p \leq 0.05$). In addition, Cd reduced the uptake of Mn by roots, but had little effect on shoots. Several studies have shown that excessive Cd can reduce the absorption of minerals. The addition of high concentrations of Cd to the soil reduced the uptake of Mg by roots and the accumulation of Mg in brown rice (Khaliq et al., 2019). Carvalho et al. also found that the avoidance of leaf B accumulation reduced the response of tomato to Cd toxicity. The degree of Cd toxicity was enhanced by both the excess in leaves and Mn deficiency in roots (Carvalho et al., 2019). Cd is believed to have a common entry route with Fe and Mn (Ishimaru et al., 2012; Sasaki et al., 2012)).

TABLE 2 | Effects of Cd on mineral nutrient accumulation in snapdragon tissues (mg/kg, DW).

	Zn	B	P	Fe	Mn	Ca	Cu	Mo	Mg
Root									
Control	386^{a}	85^{a}	211^{a}	510^{a}	168^{a}	622^{a}	25^{a}	119^{a}	6,593^{a}
1.0 mg/kg	355^{ab}	59^{ab}	190^{b}	263^{ab}	134^{ab}	621^{a}	12^{a}	110^{b}	5,197^{b}
2.5 mg/kg	560^{b}	47^{b}	152^{b}	211^{b}	115^{b}	617^{b}	11^{a}	112^{b}	3,341^{c}
p-value	0.021	0.03	0.009	0.041	0.004	0	0.071	0.001	0.033
Shoot									
Control	17^{a}	58^{a}	145^{a}	28^{a}	32^{a}	379^{a}	11^{a}	39^{a}	1,341^{a}
1.0 mg/kg	13^{ab}	36^{b}	129^{b}	16^{b}	20^{ab}	314^{ab}	7^{b}	27^{b}	689^{a}
2.5 mg/kg	28^{b}	35^{b}	118^{b}	12^{b}	28^{b}	192^{b}	5^{b}	28^{b}	341^{a}
p-value	0.047	0.029	0.001	0.031	0.017	0.033	0.049	0.015	0.114

Different letters stand for statistical differences at $p \leq 0.05$.

The interaction between Cd and Zn was antagonistic at low concentration of Cd, but synergistic at high concentration of Cd. Under the treatment of 2.5 mg/kg Cd, the absorption and accumulation of Zn in roots and shoots increased. Under the treatment of 2.5 mg/kg Cd, the uptake and accumulation of Zn in roots and shoots increased. Lasat et al. (2000) discovered the Zn transporter gene *ZNT1*, which can promote the transport of Cd in plants. The long-distance transport mechanism of Cd in plants may be the same as that of Zn (Liu et al., 2003). The content of Fe in different parts of snapdragon was significantly negatively correlated with the concentration of Cd, which was consistent with previous studies (Sasaki et al., 2012; Khaliq et al., 2019). An Fe-Cd correlation was found in the roots and shoots of snapdragon, as both Fe and Cd are transported by same transporters (*OsNRAMP1*) (Curie et al., 2000). It is clear that addition of high concentrations of Cd inhibited Fe accumulation in the snapdragon. Therefore, the accumulation of Fe in snapdragon was inhibited by adding high concentration of Cd.

The decrease of Ca concentration in various tissues is due to the fact that Cd and Ca share a common transport system. Studies have shown that a large number of Cd in plants do not enter the symplast, but remain in the cell wall. Beyersmann and Hechtenberg proved that Cd could interfere with the activation of some signal transduction pathways based on the binding characteristics of Cd to some calcium binding sites in animal cells. This leads to a decrease in the amount of Ca accumulated by plants (Beyersmann and Hechtenberg, 1997).

Metabolomics Analysis of Amino Acids Extracted From Root

The research results listed in **Figure 4** indicate that there were 16 amino acids to be detected in root exudates. They are Alanine (Ala), Arginine (Arg), Cysteine (Cys), Glutamic acid (Glu), Glycine (Gly), Histidine (His), Isoline (Ile), Leucine (Leu), Lysine (Lys), Methionine (Met), Phenylalanine (Phe), Proline (Pro), Serine (Ser), Threonine (Thr), Tyrosine (Tyr), and Valine (Val). They were significantly up-regulated in response to Cd. Increased amino acid secretion may be an active defense response in snapdragon. When plants are under stress, root exudates can change the form of insoluble nutrients in soil to facilitate plant absorption and regulate rhizosphere microbial activity, which is one of the mechanisms of plants coping with stress. Amino acid is an important component of soil organic nitrogen and an important source of nutrients for microorganisms in soil. Amino acids are consumed by microorganisms to synthesize growth regulators, which regulate and stimulate plant growth. The metabolic products of microorganisms will affect the secretion of amino acids. Up-regulated amino acids can provide multiple binding sites for Cd, which hinders Cd transport from the root cell membrane. Therefore, on the one hand, the amino acids secreted by the root of snapdragon under cadmium stress may form a stable chelate complex with cadmium ion and reduce its activity. On the other hand, it may indirectly participate in the process of plant resistance to cadmium toxicity by affecting the species, quantity, and physiological activity of rhizosphere microorganisms. This mechanism needs further discussion and demonstration.

Previous studies have shown that amino acids play an important role in the process of chelating Cd^{2+}. Tang (1998) observed that amino acid could reduce the toxicity of metal ions. Up-regulated amino acids may also reflect an attempt by snapdragon to quarantine cadmium in the stem. Amino acids may also be secreted in xylem sap and bound to Cd^{2+} in transpiration. Amino acids in root exudates not only can bind metals but also can act as signal molecules and have antioxidant defense function. These results suggest that amino acids may detoxify cadmium by binding to cadmium ions.

Detoxification of Organic Acids Secreted by Roots Under Cadmium Stress

Organic acids can decrease the pH value of rhizosphere soil, activate insoluble minerals in soil, and improve the bioavailability of heavy metals. In this study, snapdragon root exudates were collected, and the organic acids were identified by HPLC (**Figure 5**). Tartaric acid, citric acid, succinic acid, malic acid, and oxalic acid were found in snapdragon root exudates. Surprisingly, patterns of succinic acid were not changed by Cd, which indicates that succinic acid did not respond to Cd stress. In contrast, tartaric acid, citric acid, malic acid, and oxalic acid were up-regulated by Cd. The excretion of citric acid was the largest,

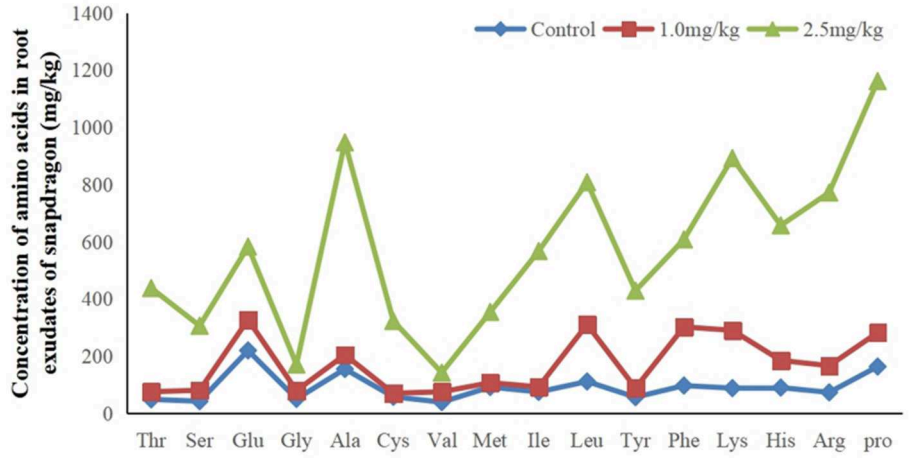

FIGURE 4 | Sixteen up-regulated amino acids in root exudates in response to exposure at 1.0 and 2.5 mg/kg Cd.

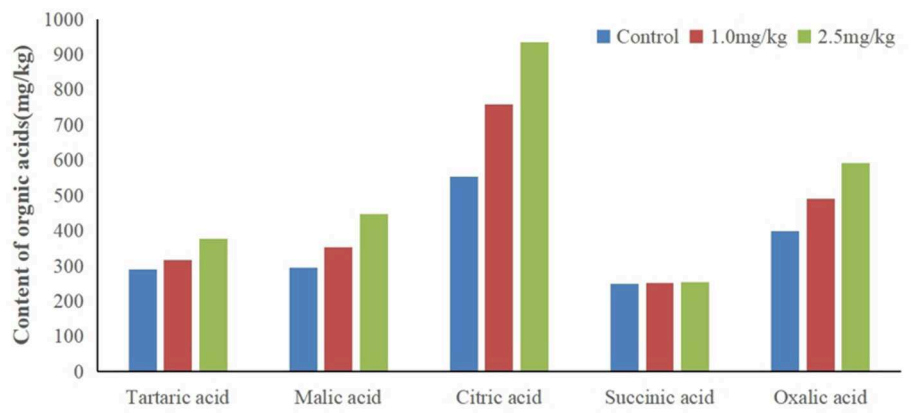

FIGURE 5 | Contents of different organic acids in root exudates of snapdragons under cadmium stress.

and the percentage of citric acid in organic acid increased with the increase of cadmium stress concentration, and exceeded 40% under two cadmium stress concentration. The citric acid content in the root exudate of snapdragon treated with 1.0 and 2.5 mg/kg Cd was 1.1 times and 1.4 times higher than that of the control, respectively. It is known that organic acids have strong binding capacity with heavy metals. Hoffland et al. considered that the abundance of citric acid in rhizosphere can be one factor contributing to the poor efficiency of P amendment practices (Hoffland et al., 1992). These organic acid radical ions can form metal cation–organic acid complexes with metal ions such as iron through complexation/chelation, which can promote the release of phosphorus in insoluble phosphorus compounds and alleviate the shortage of available phosphorus in soil. Previous studies have shown that citric acid can improve the solubility of ferrous iron, but it is reluctant to provide iron to Caco-2 epithelial cells, resulting in iron malabsorption (Salovaara et al., 2003). The action of citric acid may occur through its carboxyl and hydroxyl groups, which prevent the polymerization of iron hydroxides by forming soluble complexes with iron (Ballot et al., 1987). Therefore, the detoxification mechanism of snapdragon on cadmium stress is to release organic acids to combine with cadmium ion or to change the existing form of cadmium ion in order to reduce the toxicity of cadmium on plant roots. Other reports showed that organic acids, especially those taking part in the tricarboxylic acid cycle, could facilitate mineral nutrient uptake and sequester toxic metals. Zinc plays an important role in photosynthesis, respiration, active oxygen metabolism, and interaction between phosphorus and zinc in plants. Under zinc deficiency stress, the transportation and utilization of zinc in plants can be affected by increasing the concentration of organic acids, which can act as an important ligand binding to zinc in plants and participate in the transportation, distribution, and detoxification of zinc in plants (Rehman et al., 2012). Citric acid has shown to aid in the absorption of zinc by snapdragons. The up-regulation of citric acid may be an active process to increase

the solubility, absorption, and transport of Cd in snapdragon. Because citric acid can form a stable extracellular complex with Cd, it can reduce the transfer of Cd from roots to shoots.

We found that the pH went from 6.57 (1.0 mg/kg Cd) to 6.27 (2.5 mg/kg Cd). The root exudates decreased the pH value of rhizosphere soil by 0.3–0.6 pH units. The decrease of pH value resulted in the higher concentration of soluble Cd^{2+} than that of the control. The results showed that citric acid had a strong capacity to dissolve Cd by decreasing the pH of the system. The roots of some plants, such as wheat and buckwheat, excrete organic acids (e.g., oxalic, malic, and citric) that bind Cd^{2+} and prevent it from entering the roots (Dong et al., 2007). Up-regulation of amino acids and citric acid may be a strategy for plants to inhibit Cd absorption and remove Cd toxicity.

CONCLUSIONS

The application of snapdragon can effectively reduce energy consumption and gradually improve the utilization rate of vegetation, which reflects the concept of energy saving and environmental protection to a certain extent and meets the actual needs of low-carbon life. The results showed that both Cd concentrations interfere with the uptake of B, P, Cu, Mn, Mo, and Zn by the soil. Root exudates can affect the absorption of heavy metals by changing the physical and chemical properties of rhizosphere soil. Because the nutrient source of rhizosphere microorganisms comes from root exudates, the changes of amino acids, carboxylic acids, and carbohydrate metabolites may affect the activity and community of rhizosphere microorganisms. The results showed that Cd changed the content of amino acids and organic acids in root exudates and thus changed the feedback relationship between plants and rhizosphere microorganisms. These findings are of great significance for understanding the chemical behavior of heavy metals at the root/soil interface and reducing the toxicity of heavy metals to medicinal plants.

DATA AVAILABILITY STATEMENT

All datasets generated for this study are included in the article/supplementary material.

AUTHOR CONTRIBUTIONS

YZ conceived and set up the experiment, analyzed the results, and wrote the manuscript. QZ conducted the experiment, analyzed the results, and helped YZ write the manuscript. XL and CZ analyzed the results and helped YZ write the manuscript. All authors reviewed the manuscript.

FUNDING

This work was financially supported by the National Natural Science Foundation of China (No. 31600415).

REFERENCES

Baker, A. J. M., and Whiting, S. N. (2002). In search of the holy grail—a further step in understanding metal hyperaccumulation? *New Phytol.* 155, 1–7. doi: 10.1046/j.1469-8137.2002.00449_1.x

Ballot, D., Baynes, R. D., Bothwell, T. H., Gillooly, M., MacFarlane, B. J., MacPhail, A. P., et al. (1987). The effects of fruit juices and fruits on the absorption of iron from a rice meal. *Br. J. Nutr.* 57, 331–343. doi: 10.1079/BJN19870041

Beyersmann, D., and Hechtenberg, S. (1997). Cadmium, gene regulation, and cellular signaling in mammalian cells. *Toxicol. Appl. Pharm.* 14, 247–261. doi: 10.1006/taap.1997.8125

Bose, S., and Bhattacharyya, A. K. (2008). Heavy metal accumulation in wheat plant grown in soil amended with industrial sludge. *Chemosphere* 70, 1264–1272. doi: 10.1016/j.chemosphere.2007.07.062

Carvalhais, L. C., Dennis, P. G., Fedoseyenko, D., Hajirezaei, M. R., Borriss, R., and Wirén, N. V. (2011). Root exudation of sugars, amino acids, and organic acids by maize as afected by nitrogen, phosphorus, potassium, and iron defciency. *J. Plant Nutr. Soil Sci.* 174, 3–11. doi: 10.1002/jpln.201000085

Carvalho, M. E. A., Piotto, F. A., Franco, M. R., Rossi, M. L., Martinelli, A. P., Cuypers, A., et al. (2019). Relationship between Mg, B and Mn status and tomato tolerance against Cd toxicity. *J. Environ. Manag.* 240, 84–92. doi: 10.1016/j.jenvman.2019.03.026

Chai, S. W., Wen, Y. M., Zhang, Y. L., and Zhao, J. F. (2006). Evaluation on the pollution of agricultural soil heavy metal in Guangzhou City. *Res. Environ. Sci.* 19, 138–142 (in Chinese with English abstract). doi: 10.13198/j.res.2006.04.140.chaishw.027

Chary, N., Kamala, C., and Raj, D. (2008). Assessing risk of heavy metals from consuming food grown on sewage irrigated soils and food chain transfer. *Ecotox. Environ. Safe* 69, 513–524. doi: 10.1016/j.ecoenv.2007.04.013

Chen, Y., Shen, Z., and Li, X. (2004). The use of vetiver grass (Vetiveria zizanioides) in the phytoremediation of soils contaminated with heavy metals. *Appl. Geochem.* 19, 1553–1565. doi: 10.1016/j.apgeochem.2004.02.003

Curie, C., Alonso, J. M., Le Jean, M., Ecker, J. R., and Briat, J. F. (2000). Involvement of NRAMP1 from *Arabidopsis thaliana* in iron transport. *Biochem. J.* 347, 749–755. doi: 10.1042/bj3470749

Dong, J., Mao, W. H., Zhang, G. P., Wu, F. B., and Cai, Y. (2007). Root excretion and plant tolerance to cadmium toxicity – a review. *Plant Soil Environ.* 53, 193–200. doi: 10.17221/2205-PSE

Fan, T., Ye, W. L., Chen, H. Y., Lu, H. J., Zhang, Y. H., Li, D. X., et al. (2013). Review on contamination and remediation technology of heavy metal in agricultural soil. *Ecol. Environ. Sci.* 22, 1727–1736 (in Chinese). doi: 10.16258/j.cnki.1674-5906.2013.10.016

Guo, J. J., Tan, X., Fu, H. L., Chen, J. X., Lin, X. X., Ma, Y., et al. (2018). Selection for Cd pollution-safe cultivars of Chinese Kale (*Brassica alboglabra* L. H. Bailey) and biochemical mechanisms of the cultivar-dependent Cd accumulation involving in Cd subcellular distribution. *J. Agric. Food Chem.* 66, 1923–1934. doi: 10.1021/acs.jafc.7b05123

Hoffland, E., Boogaard, R. V. E., Nelemans, J., and Findenegg, G. (1992). Biosynthesis and root exudation of citric and malic acid in phosphate-starved rape plants. *New Phytol.* 122, 675–680. doi: 10.1111/j.1469-8137.1992.tb00096.x

Hou, S. M., Sun, J., He, H. B., Zhang, X. D., and Wang, Y. H. (2006). Simultaneous determination of amino acids in soil by reversed phase high performance liquid chromatography by using 6-aminoquinoly-N-hydroxysuccinmiidyl carbamate as a precolumn derivatization reagent. *Chinese J. Anal. Chem.* 34, 1395–1400.

Ishimaru, Y., Takahashi, R., Bashir, K., Shimo, H., Senoura, T., Sugimoto, K., et al. (2012). Characterizing the role of rice NRAMP5 in manganese iron and cadmium transport. *Sci. Rep.* 2:286. doi: 10.1038/srep00286

Janota, A., Szopinski, M., Naprzał, M., Sitko, K., and Małkowski, E. (2015). "New data on hormesis mechanism in maize seedlings treated with Cd and Pb," in *7th Conference of Polish Society for Experimental Plant Biology* (Gdansk).

Jarvis, S. C., Jones, H. P., and Hopper, M. J. (1976). Cadmium uptake from solution by plants and its transport from roots to shoots. *Plant Soil*. 44, 179–191. doi: 10.1007/BF00016965

Jia, L., He, X., Chen, W., Liu, Z., Huang, Y., and Yu, S. (2013). Hormesis phenomena under cd stress in a hyperaccumulator–*Lonicera japonica* thunb. *Ecotoxicology* 22, 476–485. doi: 10.1007/s10646-013-1041-5

Kennedy, C. D., and Gonsalves, F. A. N. (1987). The action of divalent zinc, cadmium, mercury, copper and lead on the trans-root potential and H+ efflux of excised roots. *J. Exp. Bot*. 38, 800–817. doi: 10.1093/jxb/38.5.800

Khalid, S., Shahid, M., Niazi, N. K., Murtaza, B., Bibi, I., and Dumat, C. (2017). A comparison of technologies for remediation of heavy metal contaminated soils. *J. Geochem. Explor*. 182, 247–268. doi: 10.1016/j.gexplo.2016.11.021

Khaliq, M. A., James, B., Chen, Y. H., Saqib, H. S. A., Li, H. H., Jayasuriya, P., et al. (2019). Uptake, translocation, and accumulation of Cd and its interaction with mineral nutrients (Fe, Zn, Ni, Ca, Mg) in upland *rice. Chemosphere* 215, 916–924. doi: 10.1016/j.chemosphere.2018.10.077

Lasat, M. M., Pence, N. S., Garvin, D. F., Ebbs, S. D., and Kochian, L. V. (2000). Molecular physiology of zinc transport in the hyperaccumulator *Thlaspi caerulescens*. *J. Exp. Bot*. 51, 71–79. doi: 10.1093/jxb/51.342.71

Li, Q., Sun, Y., Guo, H. J., Sang, F., Ma, H. Y., Peng, H., et al. (2018). Quality control of the traditional Chinese medicine Ruyi jinhuang powder based on high-throughput sequencing and real-time PCR. *Sci. Rep.* 8:8261. doi: 10.1038/s41598-018-26520-3

Liñero, O., Cidad, M., Carrero, J. A., Nguyen, C., and Diego, A. D. (2015). Accumulation and translocation of essential and nonessential elements by tomato plants (Solanum lycopersicum) cultivated in open-air plots under organic or conventional farming techniques. *J. Agric. Food Chem*. 63, 9461–9470. doi: 10.1021/acs.jafc.5b03878

Liu, J.,Zhu, Q., Zhang, Z., Xu, J., Yang, J., and Ming, H. W. (2005). Variations in cadmium accumulation among rice cultivars and types and the selection of cultivars for reducing cadmium in the diet. *J. Sci. Food Agric*. 85, 147–153. doi: 10.1002/jsfa.1973

Liu, J. G., Li, K. Q., Xu, J. K., Zhang, Z. J., Ma, T. B., Lu, X. L., et al. (2003). Lead toxicity, uptake, and translocation in different rice cultivars. *Plant Sci*. 165, 793–802. doi: 10.1016/S0168-9452(03)00273-5

Liu, W. T., Zhou, Q. X., Zhang, Y. L., and Wei, S. H. (2010). Lead accumulation in different Chinese cabbage cultivars and screening for pollution-safe cultivars. *J. Environ. Manag*. 91, 781–788. doi: 10.1016/j.jenvman.2009.10.009

Lu, H. N., Sun, J. T., and Zhu, L. Z. (2017). The role of artificial root exudate components in facilitating the degradation of pyrene in soil. *Sci. Rep*. 7, 1–10. doi: 10.1038/s41598-017-07413-3

Lu, L. L., Tian, S. K., Yang, X. E., Li, T. Q., and He, Z. L. (2009). Cadmium uptake and xylem loading are active processes in the hyperaccumulator *Sedum alfredii*. *J. Plant Physiol*. 166, 579–587. doi: 10.1016/j.jplph.2008.09.001

Lu, R. K. (1999). *Analytical Methods of Agricultural Chemistry in Soil*. Beijing: China Agricultural Science and Technology Press (in Chinese).

Rehman, H. U., Aziz, T., Farooq, M., Wakeel, A., and Rengel, Z. (2012). Zinc nutrition in rice production systems: a review. *Plant and Soil*. 361, 203–226. doi: 10.1007/s11104-012-1346-9

Salovaara, S., Sandberg, A. S., and Andlid, T. (2003). Combined impact of pH and organic acids on iron uptake by Caco-2 cells. *J. Agric. Food Chem*. 51, 7820–7824. doi: 10.1021/jf030177n

Sasaki, A.,Yamaji,N., Yokosho, K., and Ma J, F. (2012). Nramp5 is a major transporter responsible for manganese and cadmium uptake in rice. *Plant Cell*. 24, 2155–2167. doi: 10.1105/tpc.112.096925

Shentu, J. L., He, Z. L., Yang, X. E., and Li, T. Q. (2008). Accumulation properties of cadmium in a selected vegetable-rotation system of southeastern China. *J. Agric. Food Chem*. 56, 6382–6388. doi: 10.1021/jf800882q

Sun, B. L., Huang, J. L., He, X. W., Li, Y. H., and Tong, C. F. (2010). Determination of organic acids in soil by high performance liquid chromatography. *Chinese J. Anal. Lab*. 29, 51–54 (in Chinese). doi: 10.13595/j.cnki.issn1000-0720.2010.0367

Tang, M. (1998). Progress in study on *VA*-mycorrhizal *Fungi* in enhancing plant resistance to salines-alkali and heavy metals. *Soils* 30, 251–254 (in chinese).

Walker, T. S., Bais, H. P., Grotewold, E., and Vivanco, J. M. (2003). Root exudation and rhizosphere biology. *Plant Physiol*. 32, 44–51. doi: 10.1104/pp.102.019661

Wei, J. L., Lai, H. Y., and Chen, Z. S. (2012). Chelator effects on bioconcentration and translocation of cadmium by hyperaccumulators, tagetes patula, and impatiens walleriana. *Ecotoxicol. Environ. Saf*. 84, 173–178. doi: 10.1016/j.ecoenv.2012.07.004

Wei, S.H., Zhou, Q. X., Wang, X. (2005). Identification of weed plants excluding the absorption of heavy metals. *Environ. Int*. 31, 829–834.

Wei, S. H., and Zhou, Q. X. (2004). Identification of weed species with hyperaccumulative characteristics of heavy metals. *Prog. Nat. Sci*. 14, 495–503. doi: 10.1080/10020070412331343851

Yoon, J., Cao, X., Zhou, Q., and Ma, L. Q. (2006). Accumulation of pb, cu, and zn in native plants growing on a contaminated florida site. *Sci. Total Environ*. 368, 456–464. doi: 10.1016/j.scitotenv.2006.01.016

Yu, H., Wang, J. L., Fang, W., Yuan, J. G., and Yang, Z. Y. (2006). Cadmium accumulation in different rice cultivars and screening for pollution-safe cultivars of rice. *Sci. Total Environ*. 370, 302–309. doi: 10.1016/j.scitotenv.2006.06.013

Zhi, Y., He, K., Sun, T., and Zhou, Q. X. (2015). Assessment of potential cadmium excluder cultivars at different concentrations of Cd in soils. *J. Environ. Sci*. 15, 108–114. doi: 10.1016/j.jes.2015.01.031

Zhi, Y., Sun, T., and Zhou, Q. X. (2014). Assessment of lead tolerance in 23 Chinese soybean cultivars and the effect of lead on their mineral ion complement. *Environ. Sci. Pollut. Res*. 21, 12909–12921. doi: 10.1007/s11356-014-3181-4

Zhou, Q., Liu, Z. D., Liu,Y., Jiang, J., and Xu, R. K. (2016). Relative abundance of chemical forms of Cu(II) and Cd(II) on soybean roots as influenced by pH, cations and organic acids. *Sci. Rep. doi: 10.1038/srep36373*

Zhou, Q. X., and Song, Y. F. (2004). *Remediation of Contaminated Soils.* Beijing: Principles and Methods, Science Press (in Chinese).

Zhou, Y., Xue, M., Yang, Z., Gong, Y., Yuan, J., Zhou, C., et al. (2013). High cadmium pollution risk on vegetable amaranth and a selection for pollution-safe cultivars to lower the risk. *Front. Environ. Sci. Eng*. 7, 219–230. doi: 10.1007/s11783-012-0469-9

Zhu, F., Fang, W., and Yang, Z. Y. (2006). Variations of Cd absorption and accumulation of 36 Lycopersicon esculentum varieties. *Acta Ecol Sinica* 26, 196–206.

Zhu, Y., Yu, H., Wang, J. L., Fang, W., Yuan, J. G., and Yang, Z. Y. (2007). Heavy metal accumulations of 24 asparagus bean cultivars grown in soil contaminated with Cd alone and with multiple metals (Cd, Pb, and Zn). *J. Agric. Food Chem*. 55, 1045–1052. doi: 10.1021/jf062971p

Conflict of Interest: The authors declare that the research was conducted in the absence of any commercial or financial relationships that could be construed as a potential conflict of interest.

frontiers in Chemistry

ORIGINAL RESEARCH
published: 17 April 2020
doi: 10.3389/fchem.2020.00266

Highly Efficient Near-Infrared Light-Emitting Diodes Based on Chloride Treated CdTe/CdSe Type-II Quantum Dots

Huwei Feng, Jiaojiao Song, Bin Song, Qingli Lin, Huaibin Shen, Lin Song Li, Hongzhe Wang* and Zuliang Du*

Key Lab for Special Functional Materials, Ministry of Education, National and Local Joint Engineering Research Center for High-Efficiency Display and Lighting Technology, School of Materials Science and Engineering, Collaborative Innovation Center of Nano Functional Materials and Applications, Henan University, Kaifeng, China

Quantum dot light-emitting diodes (QLEDs) have been considered as the most promising candidate of light sources for the new generation display and solid-state lighting applications. Especially, the performance of visible QLEDs based on II-VI quantum dots (QDs) has satisfied the requirements of the above applications. However, the optoelectronic properties of the corresponding near-infrared (NIR) QLEDs still lag far behind the visible ones. Here, we demonstrated the highly efficient NIR QLEDs based on chloride treated CdTe/CdSe type-II QDs. The maximum radiant emittance and peak external quantum efficiency (EQE) increased by 24.5 and 26.3%, up to 66 mW/cm^2 and 7.2% for the corresponding devices based on the chloride treated CdTe/CdSe QDs with the PL peak located at 788 nm, respectively, compared with those of devices before chloride treatment. Remarkably, the EQE of $>$ 5% can be sustained at the current density of 0.3–250 mA/cm^2 after the chloride treatment. Compared with NIR LEDs based on transition metal complex, the efficiency roll-off has been suppressed to some extent for chloride treated CdTe/CdSe based NIR QLEDs. Based on the optimized conditions, the peak EQE of 7.4, 5.0, and 1.8% can be obtained for other devices based on chloride treated CdTe/CdSe with PL peak of 744, 852, and 910 nm, respectively. This improved performance can be mainly attributed to the chloride surface ligand that not only increases the carrier mobility and reduces the carrier accumulation, but also increases the probability of electron-hole radiative efficiency within QD layers.

Keywords: near-infrared, chloride, CdTe/CdSe, QD, electroluminescence

OPEN ACCESS

Edited by:
Zongyou Yin,
Australian National University, Australia

Reviewed by:
Xuyong Yang,
Shanghai University, China
Xiaoyong Huang,
Taiyuan University of Technology, China

****Correspondence:***
Qingli Lin
qingli1112@126.com
Hongzhe Wang
whz@henu.edu.cn

Specialty section:
This article was submitted to Nanoscience, a section of the journal Frontiers in Chemistry

Received: *05 February 2020*
Accepted: *18 March 2020*
Published: *17 April 2020*

Citation:
Feng H, Song J, Song B, Lin Q, Shen H, Li LS, Wang H and Du Z (2020) Highly Efficient Near-Infrared Light-Emitting Diodes Based on Chloride Treated CdTe/CdSe Type-II Quantum Dots. Front. Chem. 8:266. doi: 10.3389/fchem.2020.00266

INTRODUCTION

Near-infrared (NIR) light-emitting diodes (LEDs) have a rapid development in last decades, because their foreseeable great potential for applications in bio-imaging and clinical diagnosis, night-vision equipments, fiber-optic communications, and computing (Graham et al., 2011; Sun et al., 2012; Dai et al., 2017; Panfil et al., 2018; Song E. et al., 2019). Recently, the peak external quantum efficiency (EQE) of NIR light sources based on transition metal complex (such as osmium, iridium, and platinum), organic LEDs (OLEDs) and perovskite LEDs (PeLEDs) has been up to $>$ 9%, 10% (at 721 nm), and even more than 20% (20.7% at 803 nm, and 21.6% at 800 nm),

respectively (Graham et al., 2011; Cao et al., 2018; Kim et al., 2018; Xu et al., 2019). However, for NIR LEDs based on transition metal complex, high costs, relatively scarce resources and the roll-off of efficiency at high brightness remain huge challenges for their large-scale and long-term applications (Wang et al., 2015); organic dyes and semiconductor polymers frequently suffer from the low photoluminescence (PL) quantum yield (QY) in the NIR regime (Gong et al., 2016); perovskite semiconductors often sustain severe trap-mediated non-radiative losses, which have been identified as a major efficiency-limiting factor for LEDs (Xu et al., 2019), moreover, the highly unstable property still hinders their industrialization.

As an alternative material, II-VI semiconductor quantum dots (QDs) demonstrate unique superiorities as NIR emitters, due to high PL QY, easily tunable size-dependent emissions, low-cost solution processability and scalable production of high-quality QDs (Kwak et al., 2012; Shirasaki et al., 2012; Chen et al., 2013; Qin et al., 2013; Zhang et al., 2019). Recent advances in visible LEDs based on II-VI QDs (especially type I structure) have already satisfied the requirements for display and solid-state lighting (Dai et al., 2014; Yang et al., 2015; Zhang et al., 2017; Li et al., 2019; Shen et al., 2019; Song J. et al., 2019). In particular, very recently, the novel strategy that optimizes shell materials to get a better energy level matching with the highest occupied molecular orbital (HOMO) of the hole transport layers facilitates their industrialization (Yang et al., 2015; Li et al., 2019; Shen et al., 2019). However, simple tuning the size of high-quality type-I QDs could not modulate their emission wavelengths to deep-red or near-infrared regions, which restricted their application in NIR fields. Whereas, CdTe/CdSe type-II QDs can be extended into the NIR region easily, along with high PL QY and good stability, due to the higher energies of valence and conduction bands of the core than those of the shell (Kim et al., 2003; Shea-Rohwer et al., 2013), which make them kind of the most promising NIR materials.

Usually, during the synthesis process of QDs, long-chain alkyl ligands are often used to passivate the surface dangling bonds of QDs and facilitate their dispersion in organic solvents with reduced aggregation (Shen et al., 2015). But these long aliphatic ligands act as barriers for charge carrier injection or extraction and lower potential performance of QDs in many optoelectronic devices (Zanella et al., 2013; Page et al., 2014). To solve this issue, on one hand, short-chain thiol ligands [such as 1-octanthiol, tris(mercaptomethyl) and 2-ethylhexane-1-thiol] are used to replace the long-chain ligands by the solution-phase ligand exchange method to improve carrier mobility, which has been demonstrated in the high-performance visible QLEDs (Shen et al., 2015; Li et al., 2016; Song J. et al., 2019). On the other hand, embedding QDs in a high-mobility hybrid perovskite matrix has been demonstrated to be effective by Gong et al. (2016). They achieved a record electroluminescence power conversion efficiency of 4.9% of NIR LEDs (Gong et al., 2016). Recently, the method of the QD surface passivation by inorganic chloride ion has been paid more attention. In 2015, Page et al. reported that Cl passivation on CdTe QDs led to almost total suppression of surface trapping of photogenerated charge carriers and an increase of PL QY from ca. 5% to up to 97.2 ± 2.5% (Page et al., 2014). Recently, Li et al. demonstrated the high brightness QLEDs with low efficiency roll-off by using thionyl chloride ($SOCl_2$) to replace the organic ligands capped on the QD surface, in which the chlorination improved the conductivity of QD films and further facilitated the charge carrier injection and mitigated the carrier accumulation (Li et al., 2018). The above results suggest that chloride ion as the ligand not only effectively passivates the dangling bonds on QD surface, but also improves the carrier mobility and suppress the efficiency roll-off. Therefore, the chloride treated QDs as the emissive layers would be expected to enhance the performance of NIR QLEDs.

For this purpose, herein, we demonstrated the highly efficient NIR LEDs based on chloride treated CdTe/CdSe type-II QDs through the all solution-processable procedure. By employing CdTe/CdSe QDs with PL peak at 788 nm as the emitting layer, the maximum radiant emittance and EQE increased from 53 mW/cm^2 and 5.7% to 66 mW/cm^2 and 7.2%, respectively, after the chloride treatment. Specially, the EQE of > 5% can be sustained in the range of 0.3–250 mA/cm^2. Compared to NIR LEDs based on transition metal complex, the efficiency roll-off has been suppressed to a certain extent for chloride treated CdTe/CdSe based NIR QLEDs. Based on the optimized conditions, the maximum EQE of 7.4, 5.0, and 1.8% can also be achieved for other NIR QLEDs based on chloride treated CdTe/CdSe QDs with PL peaks positioned at 744, 852, and 910 nm, respectively. These results may offer new ideas for the further development of NIR QLEDs and facilitate their applications in NIR fields.

MATERIALS AND METHODS

Materials

All reagents were used as received without further experimental purification. Cadmium oxide (CdO, 99.998%), cadmium chloride ($CdCl_2$, 99.99%), tellurium powder (Te, 99.8%), tri-n-octylphosphine oxide (TOPO, 90%), oleic acid (OA, 90%), 1-octadecene (ODE, 90%), tri-n-octylphosphine (TOP, 90%), selenium (Se, 99.99%, powder), zinc acetate (99.99%), dimethyl sulfoxide (DMSO, 99.7%), tetradecylphosphoric acid (TDPA, 97%), tributylphosphine (TBP, 90%), tetramethylammoniumhydroxide (TMAH, 97%), and chlorobenzene (99%) were purchased from Aldrich. *n*-Octane (>99%) and isopropanol (99.8%) were purchased from Acros Organics. Hexane (analytical grade), acetone (analytical grade), and methanol (analytical grade) were obtained from Beijing Chemical Reagent Co., Ltd. China.

Synthesis of Near-Infrared CdTe/CdSe QDs

CdTe/CdSe core/shell QDs were prepared according to the modification of previously reported procedures of our group (Shen et al., 2010, 2013). Details of synthesis are provided in the **Supplementary Material**.

Ligand Exchange

0.30 g (1.64 mmol) $CdCl_2$ and 0.033 g (0.12 mmol) TDPA were dissolved in 5.0 mL oleylamine and degassed at 120°C for 30 min, then, cooled down to 60°C under N_2 flow for further reaction.

Five milliliters toluene solution of CdTe/CdSe QDs (15 mg/mL) was degassed at 60°C for 30 min followed by quickly injection into $CdCl_2$ stock solution and reacting for 15 min. The as-prepared chloride CdTe/CdSe QDs were purified and dissolved in octane with a concentration of 10 mg/mL.

Device Fabrication

ZnO nanoparticles were synthesized according to a previous report (Qian et al., 2010). Typically, a stoichiometric amount of TMAH in ethanol (0.5 M) were dropwise added into 0.1 M zinc acetate in DMSO, and stirred for 1 h under ambient atmosphere, and the reaction product of ZnO was then washed and redispersed in ethanol to form a clear solution with a concentration of 30 mg/mL.

QLEDs were fabricated based on the glass substrates with prepatterned ITO, with a sheet resistance of $\sim$15 Ω sq^{-1}. The substrates were ultrasonically cleaned with different solvents of deionized water, acetone and isopropanol, each for 15 min. Then the substrates were dried under nitrogen flow and followed by 15 min of UV-Ozone treatment to obtain clean and active surfaces. PEDOT:PSS [Poly(3,4-ethylenedioxythiophene)/poly(styrenesulfonate), AI 4083] was filtrated and spin-coated onto the glass/ITO substrates with spin speed of 5,000 rpm and baked at 150°C for 15 min in air to form a smooth hole injection layer (HIL). These substrates were then immediately transferred into a glove box filled with N_2 for the further preparation. TFB (poly[9,9-dioctylfluorene-co-N-[4-(3-methylpropyl)]-diphenylamine]) with a concentration of 8 mg/mL (in chlorobenzene) was spin-casted at 3,000 rpm for 30 s, and then baked at 150°C for 30 min to form the hole transport layer (HTL). QDs (10 mg/mL, in octane) and ZnO (30 mg/mL, in ethanol) were sequentially spin-coated onto the layer of TFB at the same spin-speed of 3,000 rpm, followed by a 30 min annealing process at 60°C for each layer. QDs and ZnO were used as the emissive layer and the electron transport layer (ETL), respectively. Finally, these samples were moved into a high-vacuum deposition chamber that located in the glove box to evaporate the 100 nm thick Al cathode. An active device area of 4 mm^2 was eventually formed with the assistance of an *in situ* shadow mask under a back ground pressure of $\sim 3 \times 10^{-7}$ torr.

Measurements and Characterization

Room temperature UV-vis absorption were tested by using an UV-vis spectrometer of PerkinElmer Lambda 950. The PL spectra, absolute QY data, and the time-resolved fluorescence spectra of the QDs were recorded by a JY HORIBA FluoroLog-3 fluorescence spectrometer accompanied with an integrating sphere. The optical density (OD) values of the QD samples were set in the range of 0.02–0.05 for UV-vis and PL characterization. Dropcast QD films were deposited on glass substrates for the phase and the crystallographic structure analysis, which was characterized by an X-ray diffractometer (XRD) of Bruker D8-ADVANCE. Transmission electron microscopy (TEM) studies were performed using a JEOL JEM-2100 with an accelerating voltage of 200 kV. X-Ray photoelectron spectroscopy (XPS) was obtained with a monochromatic Al Kα source, 15 kV/8 mA using a Kratos Axis-Ultra spectrometer.

The current density-voltage-radiance characteristics for the QLEDs were measured using a Keithley 2400 source meter and a picoammeter (Keithley 6485) with a calibrated Newport silicon diode under ambient conditions. The electroluminescence spectra were powered by a Keithley 2400 source meter and were recorded by an Ocean Optics USB2000 spectrometer. The EQE is calculated according to the published reference (Forrest et al., 2003), as presented Equation (2).

RESULTS AND DISCUSSION

High-quality CdTe/CdSe type-II QDs were synthesized according to previously reported method. QDs with different emission wavelength could be obtained by coating different thickness of CdSe shells onto the CdTe cores. **Supplementary Figures 1A–D** shows the absorbance and PL spectra of as-prepared type-II CdTe/CdSe QDs with PL peaks at 744, 788, 852, and 910 nm, accompanied by the PL QYs of ∼73, ∼69, ∼66, and 65%, respectively. According to the TEM images (**Supplementary Figures 1E–H**), the average sizes are estimated to be ∼4.6, ∼6.7, ∼7.6, and ∼9.7 nm, respectively. HRTEM images (insets of **Supplementary Figures 1E–H**) show the clear lattice fringes throughout the whole QDs, indicating the high crystallinity nature of such type-II CdTe/CdSe QDs. In order to further explore the evolution of crystal structures of CdTe/CdSe core/shell QDs, their phase and crystallographic properties were investigated by XRD (**Supplementary Figure 2**). As can be seen from the XRD patterns, the diffraction peak positions of the QDs with PL peak located at 744 nm are in good agreement with the structure of bulk cubic CdTe. With the continuous growth of CdSe shell, a small diffraction peak shift to the reference peaks of cubic CdSe could be observed, which was accompanied by a redshift of PL emission.

Taking the CdTe/CdSe QDs with PL peak at 788 nm as an example, we adopted chloride ions to modify the QD surface, aimed to improve the electroluminescence performance of NIR QLEDs. In **Figures 1A,B**, TEM images show no obvious change in the size and morphology before and after chloride treatment. **Figure 1C** shows the UV-vis absorption and PL spectra of untreated and chloride treated CdTe/CdSe QDs. After chloride treatment, the absorbance spectra exhibit no obvious change, indicating that there is little net effect on the band gap (Li et al., 2016). While, the PL peak has a blue shift of ∼3 nm, and full width at half maximum (FWHM) of PL narrowed to 46 nm. Moreover, the PL QY of chloride treated CdTe/CdSe still sustained 60%, which indicates that chloride modification on the QD surface have no obviously negative influence on the PL properties. Correspondingly, the PL QYs of ∼65, ∼59, and ∼57% is for the chloride treated QDs with PL peak of 744, 852, and 910 nm, respectively. This result is also supported by the PL decay dynamics of CdTe/CdSe QDs before and after chloride treatment in **Figure 1D**. The PL decay of CdTe/CdSe QDs could be well fitted into a tri-exponential decay function, including the fast PL decay (τ_1) from the recombination of band-edge exciton states, moderate PL decay (τ_2) resulted from the shallow trap-assisted exciton recombination, and long PL decay

(τ_3) related to deep trap-assisted exciton recombination. The average PL lifetime of CdTe/CdSe QDs just reduced from 58.4 to 54.7 ns. As shown in **Supplementary Table 1**, for chloride treated CdTe/CdSe QDs, the fraction of long PL lifetime (τ_2 and τ_3) caused by the surface traps showed no dramatical decrease compared to untreated CdTe/CdSe QDs. This result suggests that few of new surface traps were introduced into QDs during the process of chloride treatment. XPS were used to confirm the existence of chloride ions on the surface of the treated CdTe/CdSe QDs. As shown in **Figure 1E**, upon chloride treatment, a Cl 2p doublet peak appears in the spectrum, which is absent for the untreated samples.

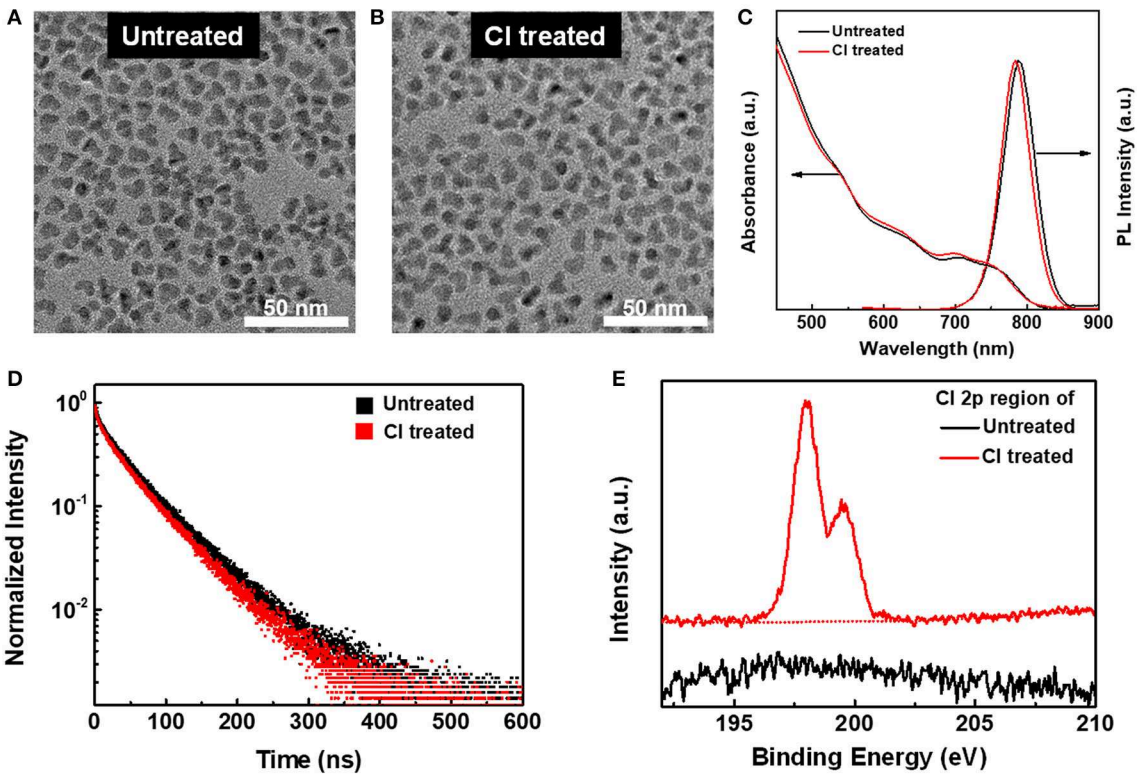

FIGURE 1 | (A,B) TEM images of CdTe/CdSe QDs with PL peak at 788 nm **(A)** before and **(B)** after chloride treatment. **(C)** UV-visible absorption and PL spectra of CdTe/CdSe (λ_{ex} = 430 nm) before and after chloride treatment. **(D)** PL decay dynamics of CdTe/CdSe QDs before and after chloride treatment. **(E)** Cl 2p XPS of CdTe/CdSe QDs before chloride treatment and after chloride treatment.

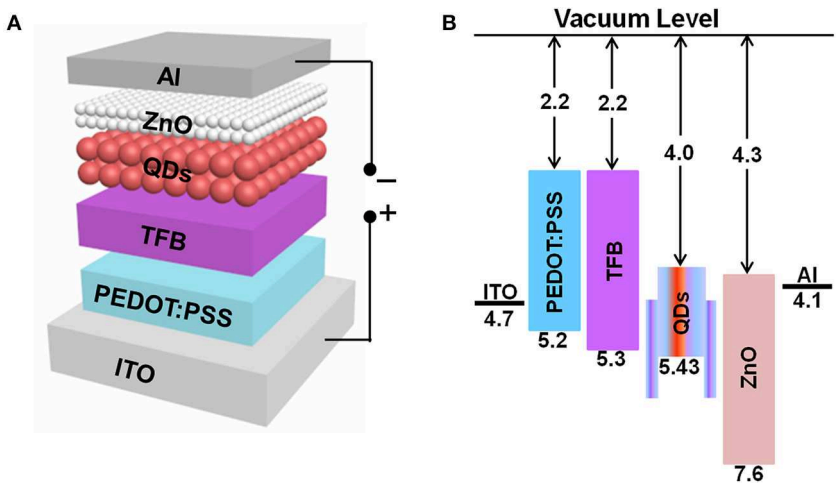

FIGURE 2 | (A) The schematic representation of all-solution-processed NIR QLEDs. **(B)** Energy band diagram of QLEDs. The energy values of type-II QDs are cited from Lo et al. (2011).

To evaluate the performance of QLEDs based on chloride treated and untreated CdTe/CdSe QD emitters, multilayered solution-processable device architecture shown in **Figure 2A** were employed, details for device fabrication were described in the previous section. Based the energy band diagram shown in **Figure 2B**, TFB is chosen as the HTL due to its relatively low HOMO level of 5.4 eV and high hole mobility of 1.0×10^{-2} cm^2 V^{-1} s^{-1}, which can facilitate the hole injection and transport (Choulis et al., 2005). With an electron affinity of ∼4.3 eV and an ionization potential of ∼7.6 eV (Qian et al., 2011), ZnO was chosen as ETL, consequently facilitates both the electron injection from the cathode and impedes the hole transport to the cathode. Such a structure was designed to increase the probability of hole-electron recombination within the QD layer.

Figure 3 characterizes the optical-electronic performance of NIR QLEDs based on chloride treated and untreated CdTe/CdSe type-II QDs. In **Figure 3A**, both of devices exhibit a low turn-on voltage (at which the optical signals can be completely responded by the picoammeter (Keithley 6485) with a calibrated Newport silicon diode) of ∼1.5 V. After chloride treatment, the device exhibits much lower leakage current at the voltage of < 2.0 V and a slightly higher current density and radiant emittance at a given voltage than that of the device based on untreated CdTe/CdSe QDs. For example, the maximum radiant emittance of 53 mW/cm^2 was obtained at the voltage of 6.3 V for the device based on untreated CdTe/CdSe QDs. While, for the device based on chloride treated QDs, the same value of radiant emittance could be achieved just at the voltage of 5.1 V, and the maximum radiant emittance increased by ∼24.5%, up to 66 mW/cm^2. Simultaneously, the NIR QLEDs based on untreated CdTe/CdSe QDs exhibit the maximum EQE of 5.7% at the current density of 37.5 mA/cm^2, as shown in **Figure 3B**. Moreover, this efficiency increases to 7.1% at 37.5 mA/cm^2, as well, the maximum EQE is 7.2% for the devices based on chloride treated QDs, which is more than 26.3% higher than that of untreated CdTe/CdSe QDs. Remarkably, EQE of > 5% can be maintained in the range of 0.3–250 mA/cm^2, which indicates that the efficiency roll-off has been suppressed to some extent, compared to that of device based on transition metal complex. This improved performance can be attributed to the chloride treatment that not only increases the carrier mobility and reduces the carrier accumulation, but also increases the probability of electron-hole radiative efficiency within QD layers.

Figure 3C shows the PL spectra of chloride treated CdTe/CdSe QDs with PL at 788 nm in solution and electroluminescence (EL) spectra of corresponding devices. Compared to the PL spectra, the EL spectra have a red shift of ∼8 nm, which is attributed to the combination

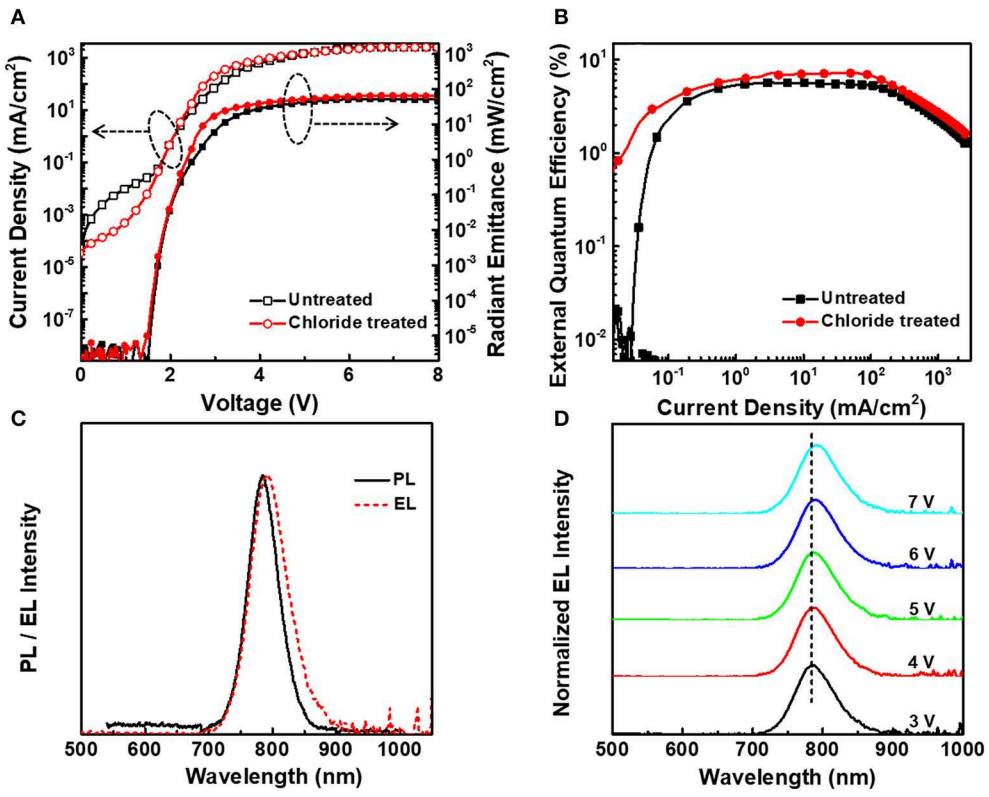

FIGURE 3 | (A) Characteristics of current density-voltage-radiant emittance of CdTe/CdSe with PL peak at 788 nm based NIR QLEDs before and after chloride treatment. **(B)** Dependence of EQE on the current density of the corresponding devices. **(C)** PL spectrum of CdTe/CdSe QD solution and the corresponding EL spectrum of the device. **(D)** The evolution of EL spectra of NIR QLEDs with increasing driving voltage.

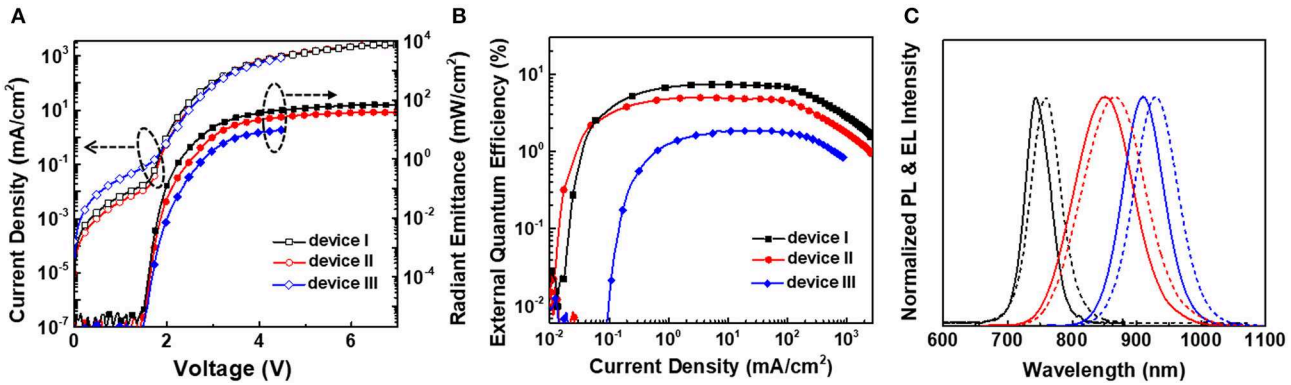

FIGURE 4 | (A) Characteristics of current density-voltage-radiant emittance of NIR LEDs based on chloride treated CdTe/CdSe QDs with PL peak of 744, 852, and 910 nm. **(B)** Dependence of external quantum efficiency on the current density of the corresponding devices. **(C)** Normalized PL spectra (solid lines) and EL spectra (dashed lines) of these QLEDs with different emission wavelengths. Herein, device I, II, and III is corresponding to the chloride treated QDs with PL peak of 744 (black), 852 (red), and 910 nm (blue), respectively.

TABLE 1 | Summary of performance parameters of NIR QLEDs based on chloride treated CdTe/CdSe with different emission wavelength.

Device	λ_{EL} (nm)	FWHM (nm)	V_T (V)	max. radiant emittance (mW/cm^2)	max. EQE (%)
Device I	758	55	1.5	69.6	7.4
Device II	867	113	1.5	39.1	5.0
Device III	929	80	1.5	9.8	1.8

Herein, device I, II, and III is corresponding to the chloride treated QDs with PL peak of 744 (black), 852 (red), and 910 nm (blue), respectively.

of interdot interactions within the closely packed QD solids, and the strong electric field that acts to decrease the energy of exciton recombination through the Stark effect (Bae et al., 2013; Mashford et al., 2013). The FWHM of EL spectra increases by ∼12 nm, but the parasitical emission cannot be observed, which suggests the excitons have been well-confined in the QD layers. As the voltage increases, the EL peak red shifts ∼7 nm owing to the quantum-confined Stark effect (QCSE), but without obviously broadened FWHM.

Based on the optimized conditions, chloride treated CdTe/CdSe QDs with PL peaks at 744, 852, and 910 nm have been used to fabricate QLEDs respectively according to the structure shown in **Figure 2A**, and the relevant electrical characteristics are provided in **Figure 4**. The maximum radiant emittance of 69.6, 39.1, and 9.8 mW/cm^2, and the peak EQE of 7.4, 5.0, and 1.8% can be obtained for the devices based on chloride treated CdTe/CdSe QD with PL peak at 744, 852, and 910 nm, respectively. The turn-on voltage is ∼1.5 V for all these devices. **Figure 4C** exhibits the EL spectra of these devices. It can be seen that the EL spectra show a red-shift of 14–19 nm, and are slightly broadened by ∼10 nm. The corresponding performance parameters of these devices are summarized in **Table 1**.

CONCLUSION

In summary, we have demonstrated highly efficient NIR QLEDs based on chloride treated CdTe/CdSe type-II QDs. After chloride treatment, the maximum radiant emittance and peak EQE increase by 24.5 and 26.3%, up to 66 mW/cm^2 and 7.2%, respectively, for the devices based CdTe/CdSe with PL peak at 788 nm. Particularly, EQE of > 5% can be maintained at the current density of 0.3–250 mA/cm^2, which indicates the suppressed efficiency roll-off as compared with that of transition metal complex-based NIR LEDs. This improved performance is mainly ascribed to the chloride surface ligand, which increases the carrier mobility and reduces the carrier accumulation, and increases the probability of electron-hole radiative efficiency within QD layers. Correspondingly, the maximum EQE of 7.4, 5.0, and 1.8% can be achieved for the devices based on chloride treated CdTe/CdSe QDs with PL peaks of 744, 852, and 910 nm, respectively. These results offer the possibility of chloride treated type-II CdTe/CdSe QDs for the applications in the NIR LEDs.

DATA AVAILABILITY STATEMENT

All datasets generated for this study are included in the article/**Supplementary Material**.

AUTHOR CONTRIBUTIONS

HF and BS synthesized materials and characterized the QDs. JS and QL fabricated devices and collected the performance data of QLEDs. QL and HW wrote the manuscript. HS provided the idea. HW, HS, LL, and ZD helped to modify the manuscript.

ACKNOWLEDGMENTS

The authors gratefully acknowledge the financial support from the National Natural Science Foundation of China

(Grant Nos. 51802079, 61922028, 61874039, and 21671058), Key Project of National Natural Science Foundation of China (Grant No. U1604261), and the Innovation Research Team of Science and Technology in Henan Province (20IRTSTHN020).

SUPPLEMENTARY MATERIAL

The Supplementary Material for this article can be found online at: https://www.frontiersin.org/articles/10.3389/fchem.2020.00266/full#supplementary-material

REFERENCES

Bae, W. K., Park, Y.-S., Lim, J., Lee, D., Padilha, L. A., McDaniel, H., et al. (2013). Controlling the influence of Auger recombination on the performance of quantum-dot light-emitting diodes. *Nat. Commun.* 4:2661. doi: 10.1038/ncomms3661

Cao, Y., Wang, N., Tian, H., Guo, J., Wei, Y., Chen, H., et al. (2018). Perovskite light-emitting diodes based on spontaneously formed submicrometre-scale structures. *Nature* 562, 249–253. doi: 10.1038/s41586-018-0576-2

Chen, O., Zhao, J., Chauhan, V. P., Cui, J., Wong, C., Harris, D. K., et al. (2013). Compact high-quality CdSe-CdS core-shell nanocrystals with narrow emission linewidths and suppressed blinking. *Nat. Mater.* 12, 445–451. doi: 10.1038/nmat3539

Choulis, S. A., Choong, V.-E., Mathai, M. K., and So, F. (2005). The effect of interfacial layer on the performance of organic light-emitting diodes. *Appl. Phys. Lett.* 87:113503. doi: 10.1063/1.2042635

Dai, X., Deng, Y., Peng, X., and Jin, Y. (2017). Quantum-dot light-emitting diodes for large-area displays: towards the dawn of commercialization. *Adv. Mater.* 29:1607022. doi: 10.1002/adma.201607022

Dai, X., Zhang, Z., Jin, Y., Niu, Y., Cao, H., Liang, X., et al. (2014). Solution-processed, high-performance light-emitting diodes based on quantum dots. *Nature* 515, 96–99. doi: 10.1038/nature13829

Forrest, S. R., Bradley, D. D. C., and Thompson, M. E. (2003). Measuring the efficiency of organic light-emitting devices. *Adv. Mater.* 15, 1043–1048. doi: 10.1002/adma.200302151

Gong, X., Yang, Z., Walters, G., Comin, R., Ning, Z., Beauregard, E., et al. (2016). Highly efficient quantum dot near-infrared light-emitting diodes. *Nat. Photonics* 10, 253–257. doi: 10.1038/nphoton.2016.11

Graham, K. R., Yang, Y., Sommer, J. R., Shelton, A. H., Schanze, K. S., Xue, J., et al. (2011). Extended conjugation platinum(II) porphyrins for use in near-infrared emitting organic light emitting diodes. *Chem. Mater.* 23, 5305–5312. doi: 10.1021/cm202242x

Kim, D.-H., D'Aléo, A., Chen, X.-K., Sandanayaka, A. D. S., Yao, D., Zhao, L., et al. (2018). High-efficiency electroluminescence and amplified spontaneous emission from a thermally activated delayed fluorescent near-infrared emitter. *Nat. Photonics* 12, 98–104. doi: 10.1038/s41566-017-0087-y

Kim, S., Fisher, B., Eisler, H.-J., and Bawendi, M. (2003). Type-II quantum dots: CdTe/CdSe (core/shell) and CdSe/ZnTe (core/shell) heterostructures. *J. Am. Chem. Soc.* 125, 11466–11467. doi: 10.1021/ja0361749

Kwak, J., Bae, W. K., Lee, D., Park, I., Lim, J., Park, M., et al. (2012). Bright and efficient full-color colloidal quantum dot light-emitting diodes using an inverted device structure. *Nano Lett.* 12, 2362–2366. doi: 10.1021/nl3003254

Li, X., Lin, Q., Song, J., Shen, H., Zhang, H., Li, L. S., et al. (2019). Quantum-dot light-emitting diodes for outdoor displays with high stability at high brightness. *Adv. Opt. Mater.* 8:1901145. doi: 10.1002/adom.201901145

Li, X., Zhao, Y.-B., Fan, F., Levina, L., Liu, M., Quintero-Bermudez, R., et al. (2018). Bright colloidal quantum dot light-emitting diodes enabled by efficient chlorination. *Nat. Photonics* 12, 159–164. doi: 10.1038/s41566-018-0105-8

Li, Z., Hu, Y., Shen, H., Lin, Q., Wang, L., Wang, H., et al. (2016). Efficient and long-life green light-emitting diodes comprising tridentate thiol capped quantum dots. *Laser Photon. Rev.* 11:1600227. doi: 10.1002/lpor.201600227

Lo, S. S., Mirkovic, T., Chuang, C.-H., Burda, C., and Scholes, G. D. (2011). Emergent properties resulting from type-II band alignment in semiconductor nanoheterostructures. *Adv. Mater.* 23, 180–197. doi: 10.1002/adma.201002290

Mashford, B. S., Stevenson, M., Popovic, Z., Hamilton, C., Zhou, Z., Breen, C., et al. (2013). High-efficiency quantum-dot light-emitting devices with enhanced charge injection. *Nat. Photonics* 7, 407–412. doi: 10.1038/nphoton.2013.70

Page, R. C., Espinobarro-Velazquez, D., Leontiadou, M. A., Smith, C., Lewis, E. A., et al. (2014). Near-unity quantum yields from chloride treated CdTe colloidal quantum dots. *Small* 11, 1548–1554. doi: 10.1002/smll.201402264

Panfil, Y. E., Oded, M., and Banin, U. (2018). Colloidal quantum nanostructures: emerging materials for display applications. *Angew. Chem. Int. Ed.* 57, 4274–4295. doi: 10.1002/anie.201708510

Qian, L., Zheng, Y., Choudhury, K. R., Bera, D., So, F., Xue, J., et al. (2010). Electroluminescence from light-emitting polymer/ZnO nanoparticle heterojunctions at sub-bandgap voltages. *Nano Today* 5, 384–389. doi: 10.1016/j.nantod.2010.08.010

Qian, L., Zheng, Y., Xue, J., and Holloway, P. H. (2011). Stable and efficient quantum-dot light-emitting diodes based on solution-processed multilayer structures. *Nat. Photonics* 5, 543–548. doi: 10.1038/nphoton.2011.171

Qin, H., Niu, Y., Meng, R., Lin, X., Lai, R., Fang, W., et al. (2013). Single-dot spectroscopy of zinc-blende CdSe/CdS core/shell nanocrystals: nonblinking and correlation with ensemble measurements. *J. Am. Chem. Soc.* 136, 179–187. doi: 10.1021/ja4078528

Shea-Rohwer, L. E., Martin, J. E., Cai, X., and Kelley, D. F. (2013). Red-emitting quantum dots for solid-state lighting. *ECS J. Solid State Sci. Technol.* 2, R3112–R3118. doi: 10.1149/2.015302jss

Shen, H., Cao, W., Shewmon, N. T., Yang, C., Li, L. S., and Xue, J. (2015). High-efficiency, low turn-on voltage blue-violet quantum-dot-based light-emitting diodes. *Nano Lett.* 15, 1211–1216. doi: 10.1021/nl504328f

Shen, H., Gao, Q., Zhang, Y., Lin, Y., Lin, Q., Li, Z., et al. (2019). Visible quantum dot light-emitting diodes with simultaneous high brightness and efficiency. *Nat. Photonics* 13, 192–197. doi: 10.1038/s41566-019-0364-z

Shen, H., Wang, H., Chen, X., Niu, J. Z., Xu, W., Li, X. M., et al. (2010). Size- and shape-controlled synthesis of CdTe and PbTe nanocrystals using tellurium dioxide as the tellurium precursor. *Chem. Mater.* 22, 4756–4761. doi: 10.1021/cm1013009

Shen, H., Zheng, Y., Wang, H., Xu, W., Qian, L., Yang, Y., et al. (2013). Highly efficient near-infrared light-emitting diodes by using type-II CdTe/CdSe core/shell quantum dots as a phosphor. *Nanotechnology* 24:475603. doi: 10.1088/0957-4484/24/47/475603

Shirasaki, Y., Supran, G. J., Bawendi, M. G., and Bulović, V. (2012). Emergence of colloidal quantum-dot light-emitting technologies. *Nat. Photonics* 7, 13–23. doi: 10.1038/nphoton.2012.328

Song, E., Jiang, X., Zhou, Y., Lin, Z., Ye, S., Xia, Z., et al. (2019). Heavy Mn^{2+} doped $MgAl_2O_4$ phosphor for high-efficient near-infrared light-emitting diode and the night-vision application. *Adv. Opt. Mater.* 7:1901105. doi: 10.1002/adom.201901105

Song, J., Wang, O., Shen, H., Lin, Q., Li, Z., Wang, L., et al. (2019). Over 30% external quantum efficiency light-Emitting diodes by engineering quantum dot-assisted energy level match for hole transport layer. *Adv. Funct. Mater.* 29:1808377. doi: 10.1002/adfm.201808377

Sun, L., Choi, J. J., Stachnik, D., Bartnik, A. C., Hyun, B.-R., Malliaras, G. G., et al. (2012). Bright infrared quantum-dot light-emitting diodes through inter-dot spacing control. *Nat. Nanotechnol.* 7, 369–373. doi: 10.1038/nnano.2012.63

Wang, S., Yan, X., Cheng, Z., Zhang, H., Liu, Y., and Wang, Y. (2015). Highly efficient near-infrared delayed fluorescence organic light emitting diodes using a phenanthrene-based charge-transfer compound. *Angew. Chem. Int. Ed.* 54, 13068–13072. doi: 10.1002/anie.201506687

Xu, W., Hu, Q., Bai, S., Bao, C., Miao, Y., Yuan, Z., et al. (2019). Rational molecular passivation for high-performance perovskite light-emitting diodes. *Nat. Photonics* 13, 418–424. doi: 10.1038/s41566-019-0390-x

Yang, Y., Zheng, Y., Cao, W., Titov, A., Hyvonen, J., Manders, J. R., et al. (2015). High-efficiency light-emitting devices based on quantum dots with tailored nanostructures. *Nat. Photonics* 9, 259–266. doi: 10.1038/nphoton.2015.36

Zanella, M., Maserati, L., Pernia Leal, M., Prato, M., Lavieville, R., Povia, M., et al. (2013). Atomic ligand passivation of colloidal nanocrystal films via their reaction with propyltrichlorosilane. *Chem. Mater*. 25, 1423–1429. doi: 10.1021/cm303022w

Zhang, H., Chen, S., and Sun, X. W. (2017). Efficient red/green/blue tandem quantum-dot light-emitting diodes with external quantum efficiency exceeding 21%. *ACS Nano* 12, 697–704. doi: 10.1021/acsnano.7b07867

Zhang, H., Hu, N., Zeng, Z., Lin, Q., Zhang, F., Tang, A., et al. (2019). High-efficiency green InP quantum dot-based electroluminescent device comprising thick-shell quantum dots. *Adv. Opt. Mater*. 7:1801602. doi: 10.1002/adom.201801602

Conflict of Interest: The authors declare that the research was conducted in the absence of any commercial or financial relationships that could be construed as a potential conflict of interest.

frontiers in Chemistry

ORIGINAL RESEARCH
published: 23 April 2020
doi: 10.3389/fchem.2020.00265

Improved Efficiency of All-Inorganic Quantum-Dot Light-Emitting Diodes via Interface Engineering

Qiulei Xu, Xinyu Li, Qingli Lin, Huaibin Shen, Hongzhe Wang* and Zuliang Du*

Key Lab for Special Functional Materials, Ministry of Education, National and Local Joint Engineering Research Center for High-Efficiency Display and Lighting Technology, Collaborative Innovation Center of Nano Functional Materials and Applications, School of Materials Science and Engineering, Henan University, Kaifeng, China

As the charge transport layer of quantum dot (QD) light-emitting diodes (QLEDs), metal oxides are expected to be more stable compared with organic materials. However, the efficiency of metal oxide-based all-inorganic QLEDs is still far behind that of organic–inorganic hybrid ones. The main reason is the strong interaction between metal oxide and QDs leading to the emission quenching of QDs. Here, we demonstrated nickel oxide (NiO_x)-based all-inorganic QLEDs with a maximum current efficiency of 20.4 cd A^{-1} and external quantum efficiency (EQE) of 5.5%, which is among the most efficient all-inorganic QLEDs. The high efficiency is mainly attributed to the aluminum oxide (Al_2O_3) deposited at the NiO_x/QDs interface to suppress the strong quenching effect of NiO_x on the QD emission, together with the molybdenum oxide (MoO_x) that reduced the leakage current and facilitated hole injection, more than 300% enhancement was achieved compared with the pristine NiO_x-based QLEDs. Our study confirmed the effect of decorating the NiO_x/QDs interface on the performance enhancement of the all-inorganic QLEDs.

Keywords: NiO_x, all-inorganic, quantum dots, light-emitting devices, high efficiency

OPEN ACCESS

Edited by:
Hongbo Li,
Beijing Institute of Technology, China

Reviewed by:
Jialong Zhao,
Jilin Normal University, China
Aiwei Tang,
Beijing Jiaotong University, China

****Correspondence:***
Qingli Lin
qingli1112@126.com
Hongzhe Wang
whz@henu.edu.cn

Specialty section:
This article was submitted to Nanoscience, a section of the journal Frontiers in Chemistry

Received: *04 February 2020*
Accepted: *18 March 2020*
Published: *23 April 2020*

Citation:
Xu Q, Li X, Lin Q, Shen H, Wang H and Du Z (2020) Improved Efficiency of All-Inorganic Quantum-Dot Light-Emitting Diodes via Interface Engineering. Front. Chem. 8:265. doi: 10.3389/fchem.2020.00265

INTRODUCTION

Quantum dots (QDs) have many advantages including high color purity, high photoluminescence (PL) quantum yield (QY), and high stability, which make them promising luminescent materials for light-emitting diodes (LEDs) (Anikeeva et al., 2009; Bae et al., 2013; Shirasaki et al., 2013; Shen et al., 2015; Chen et al., 2018; Cao et al., 2019; Zhang et al., 2019). Recently, the performance of QD LEDs (QLEDs) has been improved greatly, the external quantum efficiencies (EQEs) for tricolor QLEDs have all surpassed 20%, with peak EQEs of 30.4% for red, 22.9% for green, and 19.8% for blue QLEDs, respectively (Wang et al., 2017; Shen et al., 2019; Song et al., 2019). At present, highly efficient QLEDs are mainly based on hybrid organic–inorganic structure, in which poly(3,4-ethylenedioxythiophene) polystyrene sulfonate (PEDOT:PSS) is widely used as the hole injection layer (HIL); poly[N,N'-bis(4-butylphenyl)-N,N'-bis(phenyl)benzidine] (Poly-TPD), poly{9,9-dioctylfluorene-co-N-[4-(3-methylpropyl)]diphenylamine} (TFB), or poly(N-vinyl carbazole) (PVK) are adopted as the hole transport layer (HTL); and zinc oxide (ZnO) nanoparticles (NPs) are used as the electron transport layer (ETL) (Qian et al., 2011; Dai et al., 2014; Zhang et al., 2019). As we know, organic materials are sensitive to moisture and may degrade under high operating currents, which affect the stability of devices, and consequently, the strict encapsulation technology is indispensable. To solve this problem, it is necessary to seek more stable hole transport materials that can endure a high carrier density at high luminance.

Many inorganic metal oxides [nickel oxide (NiO_x), tungsten oxide (WO_x), molybdenum oxide (MoO_x), vanadium oxide (VO_x), etc.] have been applied as HIL in optical electronic devices to improve the device stability (Murase and Yang, 2012; Huu Tuan et al., 2014; Yang et al., 2014; Zhang et al., 2017), and NiO_x is a promising hole transport material among them due to its nature of intrinsic p-type semiconductor with a wide bandgap and high transparency. Moreover, NiO_x possesses relatively proper band energy for efficient hole injection and electron blocking to confine the excitons in the QD emitting layer [∼5.2 eV for the valance band maximum (VBM) and ∼1.6 eV for the conductive band minimum (CBM)]. Nevertheless, NiO_x-based all-inorganic QLEDs with ZnO as ETL exhibited poor efficiency (Mashford et al., 2010), which is mainly attributed to two reasons. First, the higher electron mobility [$\sim 10^{-2}$ cm^2 $(V{\cdot}s)^{-1}$] of ZnO NPs and small energy barrier of the conductive band at the QDs/ZnO interface lead to imbalanced carrier transport due to easier electron injection. Second, the excitons formed near the NiO_x layer are subject to the surface of NiO_x, and a large number of free carriers and defects/traps on the surface of adjacent NiO_x HTL leads to the quenching of QD emission (Caruge et al., 2006, 2008; Wu and Yeow, 2010). It is reported that many dipolar surface species of NiOOH are present on the solution-processed NiO_x films and induce a strong localized electric field, which facilitates radiationless decay channels with a charge-transfer/charging and/or energy transfer processes and leads to a severe decrease of device efficiency (Ratcliff et al., 2011; Liu et al., 2015).

To address this issue, a modification of the NiO_x/QD interface is needed. Several kinds of buffer layer have been inserted to suppress the exciton quenching induced by NiO_x. By introducing ultrathin aluminum oxide (Al_2O_3) layer at the NiO_x/QD layer interface (Zhang et al., 2016; Ji et al., 2017, 2018), Ji et al. fabricated highly efficient green all-inorganic QLEDs, in which over 800% enhancement for the current efficiency/EQE of up to 34.1 $cd{\cdot}A^{-1}$/8.1% was achieved when the Al_2O_3 layer was obtained by atomic layer deposition (ALD), and this represented the highest EQE for all-inorganic QLEDs reported ever. With ultrathin lithium fluoride (LiF) being inserted at the NiO_x/QD interface and ultrathin Al_2O_3 being inserted between the QDs and ZnO layer (Yang et al., 2018), Yang et al. reported highly efficient all-inorganic QLEDs with a maximum EQE of 6.52% and a long device life time of 16,120 h at 100 $cd{\cdot}m^{-2}$. Li et al. reported all-inorganic QLEDs of the highest maximum brightness of 40,000 $cd{\cdot}m^{-2}$ by sputtering ultrathin MgO at the NiMgO/QD interface; however, the maximum EQE is only 1.5% (Jiang et al., 2019). These results indicate the importance of decoration of the NiO_x/QD interface on suppressing the QD emission quenching and improving the performance of the all-inorganic QLED efficiency. Among them, the Al_2O_3 buffer layer obtained by ALD technology has more advantages since the film thickness can be precisely controlled at atomic level by alternating the exposure cycle of trimethylaluminum [$Al(CH_3)_3$] and H_2O, and the as-prepared films possess good uniformity over large substrates and excellent conformality on three-dimensional surface topologies. Furthermore, the hydroxyl (-OH) in the NiOOH species can be consumed during the exposure to $Al(CH_3)_3$ deposition cycles. Nevertheless, the maximum EQE for all-inorganic QLEDs with Al_2O_3 buffer layer is still very low, which is likely due to imbalanced carrier transport in devices resulting from the inefficient hole injection from indium tin oxide (ITO) to the NiO_x layer and the relatively higher energy barrier between the NiO_x layer and QD layer. To solve this problem, more researches are still needed to optimize the structure of NiO_x-based all-inorganic QLEDs and improve the device efficiency.

Here, we demonstrated highly efficient all-inorganic QLEDs with an optimized structure of ITO/solution-processed MoO_x ($sMoO_x$)/NiO_x/Al_2O_3/QDs/ZnO/Al through all solution-process method except for Al_2O_3 layer and the electrodes. The ultrathin Al_2O_3 inserted at the NiO_x/QDs interface was to suppress the strong quenching effect of NiO_x on the emission of QD. And the $sMoO_x$ introduced before the NiO_x layer was aimed to reduce leakage current and facilitate the hole injection from anode to the emitting layer and minimize the hole-blocking effect of Al_2O_3 layer. Our resultant all-inorganic QLEDs reached a high current efficiency of 20.4 cd A^{-1} and a maximum EQE of 5.5%, more than 300% enhancement was achieved compared with the pristine NiO_x-based QLEDs.

MATERIALS AND METHODS

Preparation of Green Quantum Dots and Metal Oxide Solution

Cadmium selenide (CdSe)/zinc sulfide (ZnS) QDs were synthesized according to the method reported in the literature (Li et al., 2019). The QDs in octane solution exhibited a green emission with the PL peak at 525 nm (**Supplementary Figure 1**). The NiO_x precursor was prepared by a modified method (Mashford et al., 2010); the mixture of nickel acetate tetrahydrate [$Ni(OAc)_2{\cdot}4H_2O$; purchased from Aldrich] and equimolar quantity of monoethanolamine (MEA; purchased from Aldrich) in ethanol was heated at 60°C for 2 h and stirred overnight. 0.1 M MoO_x solutions were synthesized by a thermal decomposition method using ammonium heptamolybdate [$(NH_4)_6Mo_7O_{24}{\cdot}4H_2O$] as a precursor (Murase and Yang, 2012; Vu et al., 2016). The ZnO NPs were prepared by slowly mixing 0.1 M zinc acetate in dimethyl sulfoxide (DMSO) and 0.3 M tetramethylammonium hydroxide (TMAH) in ethanol together for 1 h, and the ZnO particles were precipitated by adding hexane/ethanol to the solution.

Fabrication of Quantum Dot Light-Emitting Diode Devices

The all-inorganic QLED structure consists of ITO/MoO_x/NiO_x/Al_2O_3 (x cycles)/QDs/ZnO/Al. The NiO_x, QDs, and ZnO are used as HTL, emission layer, and ETL, respectively. Before fabricating the devices, the ITO substrates were ultrasonically cleaned in detergent, DI water, acetone, and isopropyl alcohol for 15 min successively followed by an *ex situ* UV ozone treatment in air for 15 min. This as-prepared MoO_x precursor solution was spin-coated onto the UV ozone-treated ITO substrates at 4,000 rpm and then baked at 120°C for 10 min to get the MoO_x film. Then, the NiO_x precursor was spin-coated at 2,000 rpm and annealed at 275°C for 30 min in air to obtain

a highly conductive layer. The Al_2O_3 layer was deposited by alternating exposures of $Al(CH_3)_3$ and H_2O with the same substrate and maintaining the temperature at 200°C, and the thickness is approximately 0.1 nm for each ALD cycle. Al_2O_3 layers with different thicknesses were deposited on the NiO_x films for device A (zero cycle), B (one cycle), C (two cycles), and D (three cycles), respectively. Note that no MoO_x layers were inserted for devices A to C, and device A is a control device without the Al_2O_3 interlayer. The QD octane solution (18 $mg{\cdot}ml^{-1}$) was then spin-coated on the NiO_x/Al_2O_3 layer at 2,000 rpm in N_2-filled glove box. After that, ZnO ethanol solution (30 $mg{\cdot}ml^{-1}$) was spin-coated at 2,000 rpm and annealed at 60°C for 30 min to remove the residual solvent. Finally, the Al cathode was thermal evaporated in the vacuum chamber at pressure below 4×10^{-6} Torr. The Al cathode lines with a width of 2.0 mm were deposited orthogonally to the 2 mm ITO anode lines to form a 4 mm^2 active area.

Measurements and Characterization

Current density–voltage–luminance (J–V–L) characteristics of QLEDs were tested using a Keithley 2400 source meter and a picoammeter (Keithley 6485) with a calibrated Newport silicon diode under ambient conditions. The luminance was calibrated using a Minolta luminance meter (CS-100). The electroluminescence spectra were obtained with an Ocean Optics spectrometer (USB2000, relative irradiance mode) and a Keithley 2400 source meter. The room temperature PL spectrum of the QDs in octane was collected by the Ocean Optics Maya 2000-Pro spectrometer under an excitation wavelength of 365 nm. Time-resolved PL (TRPL) measurements were carried out with Edinburgh Instruments FL920 spectrometer, utilizing a 400-nm excitation light source. X-ray photoelectron spectroscopy (XPS) was obtained using a Kratos Axis-Ultra spectrometer with a monochromatic Al Kα source, 15 kV/8 mA. The atomic force microscopy (AFM) images were recorded in the tapping mode by Bruker Multimode-8. The UV photoelectron spectroscopy (UPS; Thermo Scientific ESCALAB 250 XI) measurement was performed using a He I discharge lamp (hv = 21.22 eV) under high vacuum (2.5×10^{-8} mbar) and the UPS spectra of MoO_x and NiO_x was meaured (**Supplementary Figure 4**).

RESULTS AND DISCUSSION

The composition of the solution-processed NiO_x films was studied by XPS analysis. **Figure 1A** shows the XPS spectrum for Ni $2p_{3/2}$ state possessing three peaks. The first peak centered at a binding energy of 854.2 eV corresponds to Ni^{2+} in the standard Ni-O octahedral bonding configuration in cubic rock salt NiO_x. The adjacent peak shoulder located at 855.9 eV was ascribed to Ni^{2+} vacancy-induced Ni^{3+} ion and NiOOH (Sasi and Gopchandran, 2007; Manders et al., 2013). The broad peak centered at 861.0 eV has been ascribed to a shake-up process in the NiO structure. **Figure 1B** shows the XPS spectrum for the O 1s state, the peak centered at 529.5 eV confirms the Ni-O octahedral bonding in NiO_x. The peak at 531.2 eV is indicative of nickel hydroxides and oxyhydroxides, including defective NiO_x with hydroxyl groups adsorbed on the surface (Han et al., 2006; Ratcliff et al., 2011).

The morphology evolution of each layer within the QLEDs was assessed by atomic force microscopy (AFM; **Figure 2**). The root-mean-square (RMS) roughness of pure ITO (**Supplementary Figure 2**) is 2.38 nm, and the value decreased to 1.23 nm after the spin-coating of NiO_x, which suggested that the ITO substrate was smoothed. The following ultrathin Al_2O_3 deposition (second cycle) had little effect on the roughness of the NiO_x film. Then, the RMS roughness for substrate increased slightly as the layer number increased, which showed 1.51 nm for QD layer and 2.12 nm for ZnO layer, respectively.

Since Al_2O_3 is an insulating material, it is very important to control its thickness precisely *via* the ALD process. To get the optical thickness of Al_2O_3, we first fabricated all-inorganic QLEDs consisting of a structure of ITO/NiO_x/Al_2O_3 (n cycle)/QDs/ZnO/Al. Different deposition cycles of Al_2O_3 (0C, 1C, 2C, 3C) were applied at the NiO_x/QD interface, and the corresponding photoelectrical properties of devices were characterized and shown in **Figure 3**. Al_2O_3 showed

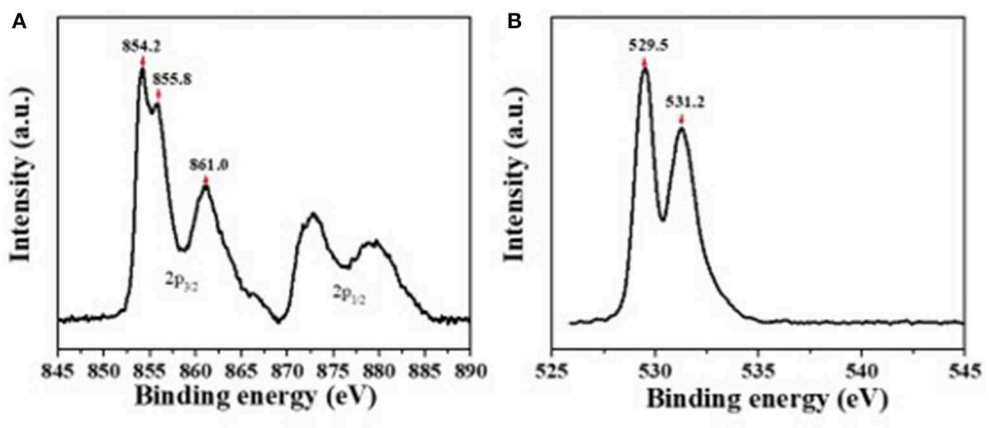

FIGURE 1 | The X-ray photoelectron spectroscopy (XPS) spectra for Ni 2p **(A)** and O1s **(B)**.

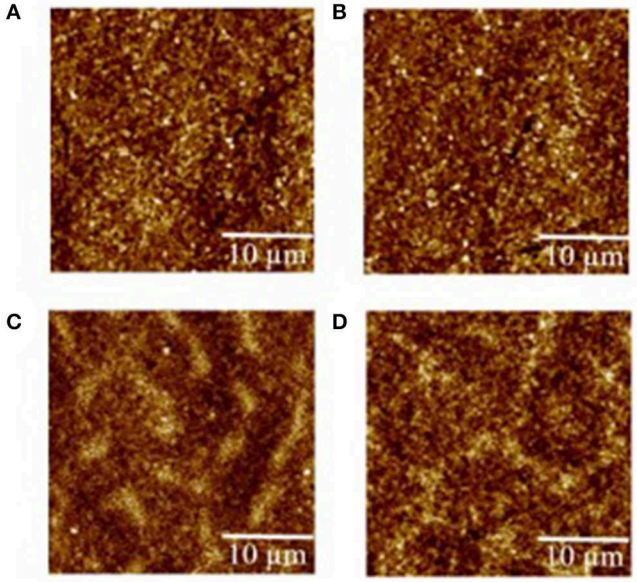

FIGURE 2 | Atomic force microscopy (AFM) images of **(A)** indium tin oxide (ITO)/nickel oxide (NiO_x), **(B)** ITO/NiO_x/aluminum oxide (Al_2O_3) (two cycles), **(C)** ITO/NiO_x/Al_2O_3 (two cycles)/quantum dots (QDs), and **(D)** ITO/NiO_x/Al_2O_3 (two cycles)/QDs/zinc oxide (ZnO). The corresponding root-mean-square (RMS) values of the samples are 1.23, 1.24, 1.51, 2.12 nm, respectively.

a remarkable influence on the performance of all-inorganic QLEDs. The current density decreased evidently with the increasing thickness of Al_2O_3 at a given voltage. For example, the current density for devices with even one cycle (0.1 nm) of Al_2O_3 deposition dropped to 1.4 mA·cm^{-2} at 5 V, which is four times lower than that of the QLEDs without the Al_2O_3 layer. The reduced current density is probably due to the insulated Al_2O_3 layer, which limits the hole injection from NiO_x, and this can be confirmed by the lower hole density in hole-only devices consisting of ITO/NiO_x/Al_2O_3/QDs/MoO_3/Al than that without the ultrathin Al_2O_3 layer (**Supplementary Figure 3**). The turn-on voltage slightly increased from 4.1 V (0 C) to 4.4 V (3 C) with the increasing thickness of Al_2O_3 layer. Despite the lower current density and higher turn-on voltage, the QLEDs with Al_2O_3 passivated layer exhibited more than 600% enhancement in luminance and more than 200% improvement in current efficiency and EQE (see **Supplementary Table 1** in supporting information), which suggested that the emission quenching induced by NiO_x played a more critical role in deterring the performance of NiO_x-based all-inorganic QLEDs. Particularly, devices with two cycles of Al_2O_3 deposition showed the highest current efficiency/maximum EQE of 12.8 cd A^{-1}/3.5% at 5.5 V, respectively.

To study the effect of ultrathin Al_2O_3 layer on the improvement of QLEDs performance, five samples were prepared, namely, F1: Glass/QDs, F2: ITO/NiO_x/QDs, F3: ITO/NiO_x/Al_2O_3 (1C)/QDs, F4: ITO/NiO_x/Al_2O_3 (2C)/QDs/ZnO, and F5: ITO/NiO_x/Al_2O_3 (3C)/QDs/ZnO, to measure their steady-state and time-resolved PL spectroscopy (as shown in **Figure 4**). The exciton lifetimes for different film

TABLE 1 | Summary of the PL peak and the decay lifetime for different samples.

Sample	PL Peak (nm)	Lifetime (ns)
QD in octane	525	
F1: Glass/QDs	528	7.3
F2: ITO/NiO_x/QDs	532	5.2
F3: ITO/NiO_x/Al_2O_3 (1C)/QDs	528	5.8
F4: ITO/NiO_x/Al_2O_3 (2C)/QDs	528	6.0
F5: ITO/NiO_x/Al_2O_3 (3C)/QDs	528	6.0

Al_2O_3, aluminum oxide; ITO, indium tin oxide; NiO_x, nickel oxide; PL, photoluminescence; QD, quantum dot.

samples were summarized in **Table 1**. It can be seen that the emission of QD film on glass substrate was peaked at 528 nm with an exciton lifetime of 7.3 ns, while that on NiO_x substrate red-shifted to 532 nm and the corresponding emission intensity and exciton lifetime decreased remarkably due to the interaction between QDs and NiO_x. For samples from F3 to F5, the PL peak blue-shifted to the original location of QD film (528 nm) with Al_2O_3 insertion, and the emission intensity and lifetime also showed an obvious increase, which confirmed the positive effect on passivating the surface of the NiO_x layer and suppressing the emission quenching induced by NiO_x through the introduction of the Al_2O_3 layer, and such results were consistent with the previously reported findings.

It is reported that the $sMoO_x$ film showed a higher work function of 5.6 eV, better transparency, and smoother surface morphology, providing the QLEDs with good Ohmic contact and small charge transfer resistance (He et al., 2013; Vu et al., 2016). The device structure was further optimized by using $sMoO_x$ as HIL to expect an even better device performance. Three kinds of QLEDs were fabricated with structures of ITO/NiO_x/QDs/ZnO ITO/Al, ITO/$sMoO_x$/NiO_x/QDs/ZnO, and ITO/$sMoO_x$/NiO_x/Al_2O_3 (two cycles)/QDs/ZnO/Al for device I, device II, and device III, respectively. The related optoelectronic characteristic curves were shown in **Figure 5**, and the corresponding performance parameters were summarized in **Table 2**. Remarkably, device II with $sMoO_x$ layer showed a maximum current efficiency of 15.9 cd A^{-1} and an EQE of 4.3%, which was more than two times higher of that of device I (7.5 cd A^{-}1/1.7%), and this suggested that the $sMoO_x$ was comparable to the ultrathin Al_2O_3 in improving the efficiency of NiO_x-based QLEDs. The device performance improvement for device II can be ascribed to the $sMoO_x$ modified layer, which reduced the leakage current and led to a more balanced carrier injection in emitting layer. For device III possessing $sMoO_x$ layer as well as two cycles of Al_2O_3 layer, the maximum luminance was further improved to 9,140 cd m^{-2} at 9.7 V, which was about 1.8 times of that of device II (4,930 cd m^{-2} at 8.5 V). The maximum current efficiency and EQE for device III were 20.4 cd A^{-1} and 5.5%, respectively, which were about 1.2 times of that of device II. The relatively higher increase in luminance reconfirmed the importance of the Al_2O_3 layer in maintaining the high emitting efficiency of the QD layer. The maximum efficiency for device III was obtained at higher-voltage regime, which meant that charge transport became more balanced at higher driving voltage

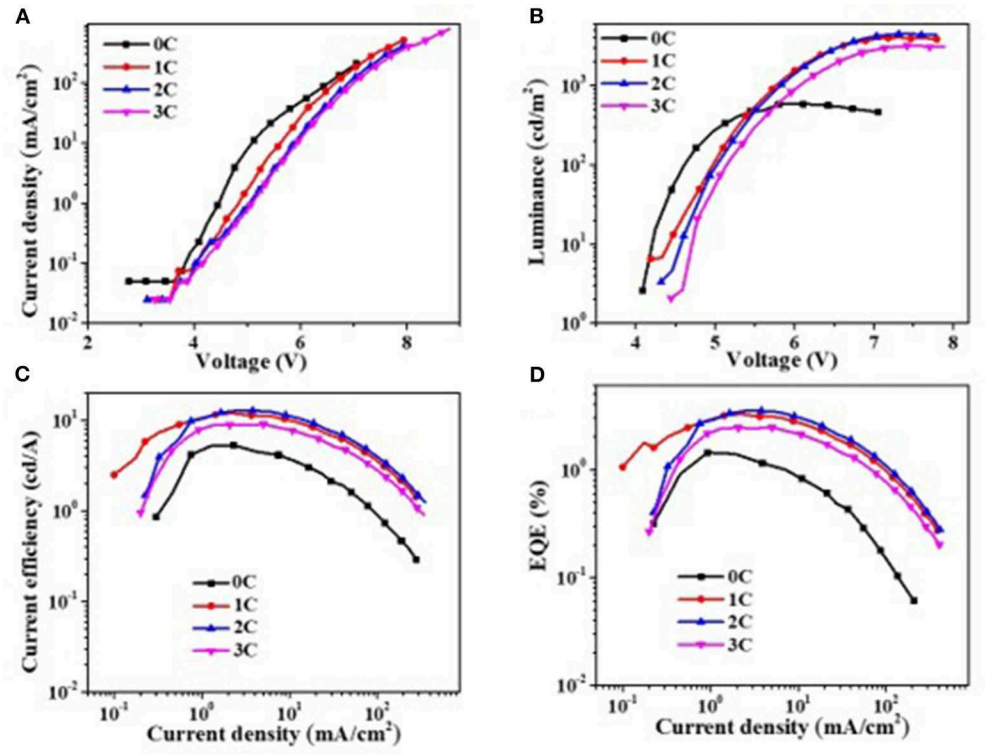

FIGURE 3 | Photoelectric properties of quantum dot light-emitting diodes (QLEDs). **(A)** Voltage vs. current density (V–J), **(B)** voltage vs. luminance (V–L), **(C)** current density–luminous efficiency, and **(D)** current density–external quantum efficiency. 0 C means 0 cycle deposition of aluminum oxide (Al_2O_3), each cycle is about 0.1 nm.

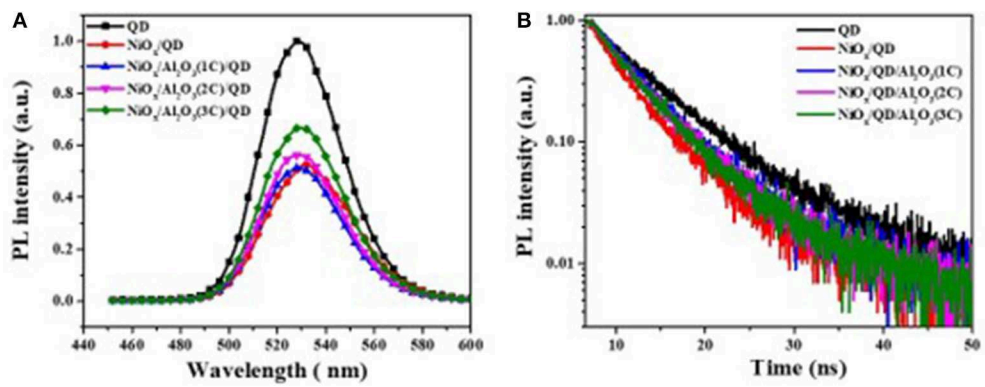

FIGURE 4 | (A) Steady-state and **(B)** time-resolved photoluminescence (PL) spectra of samples with and without the aluminum oxide (Al_2O_3) layer.

TABLE 2 | Summary of the electrical properties of the QLEDs.

Device	λ_{max} (nm)	V_T (V)	L_{max} (cd/m^2)	EQE_{max} (%)	η_{Amax} (cd/A)	η_{Pmax} (lm/W)
I	532	3.9	3,786 (7.6 V)	1.7 (5.3 V)	7.5 (5.3 V)	4.5 (5.3 V)
II	534	4.3	4,930 (8.5 V)	4.3 (5.2 V)	15.9 (5.2 V)	9.6 (5.2 V)
III	534	4.7	9,140 (9.0 V)	5.5 (6.2 V)	20.4 (6.2 V)	10.7 (5.8 V)

EQE, external quantum efficiency; QLED, quantum dot light-emitting diode.

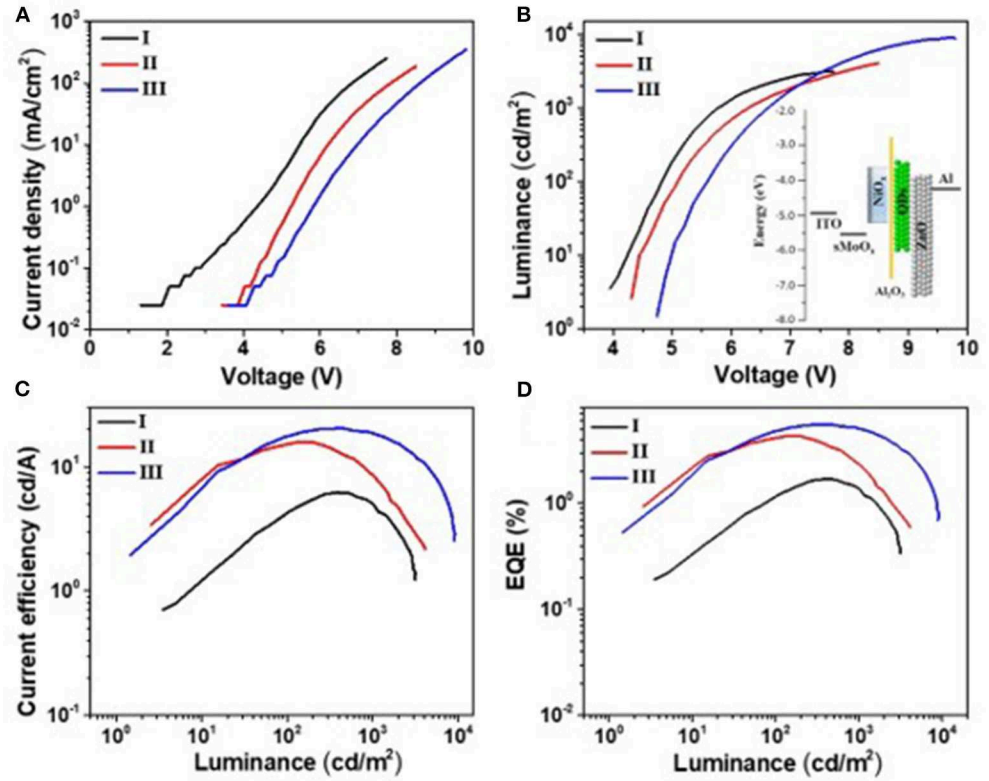

FIGURE 5 | Photoelectric properties of devices I, II, and III. **(A)** Voltage vs. current density (*V–J*), **(B)** voltage vs. luminance (*V–L*), **(C)** luminance–current efficiency, and **(D)** luminance–external quantum efficiency. The inset in **(B)** is the energy level diagrams of quantum dot light-emitting diode (QLED) III.

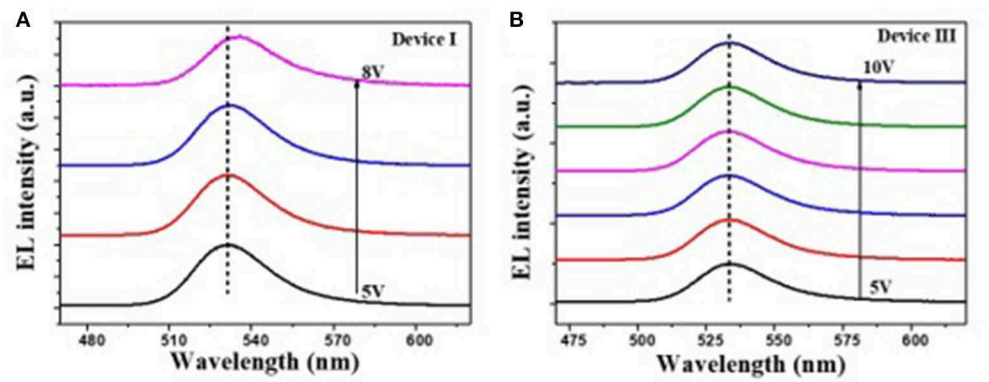

FIGURE 6 | Electroluminescence (EL) spectra of devices I **(A)** and III **(B)** under different voltages.

and better tolerance to higher operating voltage for device III than the other two. It is also confirmed from the EL spectra under increasing driving voltage of devices I and III (**Figure 6**). The EL peak for device I without Al_2O_3 layer exhibited a red shift of 4 nm as the voltage increased to 8 V, while that for device III kept its profile from 5 to 10 V. Despite the slightly higher turn-on voltage, the insertion of $sMoO_x$ layer combining Al_2O_3 layer in NiO_x-based all-organic QLEDs improved not only the device efficiency but also the performance stability. A comparison of the performance of all-inorganic QLEDs between our work and others in literature was summarized (see **Supplementary Table 2**).

CONCLUSION

All-inorganic QLEDs with high efficiency were fabricated using solution-processed NiO_x as the HTL and ZnO as the ETL, and ultrathin Al_2O_3 was deposited at the NiO_x/QDs interface by the

ALD process to reduce the strong quenching effect of NiO_x on the QD emission. The corresponding all-inorganic QLEDs exhibited a maximum current efficiency of 19.8 cd A^{-1} and EQE of 4.5%, which is 260% enhancement compared with the QLEDs without Al_2O_3 insertion, making them among the highest efficient inorganic QLEDs. This result suggests that the Al_2O_3 passivating layer is critical to device efficiency improvement by suppressing QDs emission quenching induced by NiO_x. Despite great device improvement, the maximum EQE for NiO_x all-inorganic QLEDs is still below 10%, which is probably due to the relatively lower hole mobility of NiO_x and higher energy barrier for hole transfer from NiO_x to the QD layer, resulting in an imbalanced charge injection in devices. The energy level regulating as well as improving electrical performance of NiO_x are vital strategies to fabricate high-performance all-inorganic QLEDs.

DATA AVAILABILITY STATEMENT

All datasets generated for this study are included in the article/**Supplementary Material**.

AUTHOR CONTRIBUTIONS

All authors listed have made a substantial, direct and intellectual contribution to the work, and approved it for publication.

FUNDING

The authors gratefully acknowledge the financial support from the National Natural Science Foundation of China (Grant Nos. 51802079, 61922028, 61874039, and 21671058), the Key Project of National Natural Science Foundation of China (Grant No. U1604261), and the Innovation Research Team of Science and Technology in Henan Province (20IRTSTHN020).

SUPPLEMENTARY MATERIAL

The Supplementary Material for this article can be found online at: https://www.frontiersin.org/articles/10.3389/fchem.2020.00265/full#supplementary-material

REFERENCES

Anikeeva, P. O., Halpert, J. E., Bawendi, M. G., and Bulovic, V. (2009). Quantum dot light-emitting devices with electroluminescence tunable over the entire visible spectrum. *Nano Lett.* 9, 2532–2536. doi: 10.1021/nl9002969

Bae, W. K., Brovelli, S., and Klimov, V. I. (2013). Spectroscopic insights into the performance of quantum dot light-emitting diodes. *Mrs Bull.* 38, 721–730. doi: 10.1557/mrs.2013.182

Cao, M., Xu, Y., Li, P., Zhong, Q., Yang, D., and Zhang, Q. (2019). Recent advances and perspectives on light emitting diodes fabricated from halide metal perovskite nanocrystals. *J. Mater. Chem. C* 7, 14412–14440. doi: 10.1039/C9TC03978C

Caruge, J.-M., Halpert, J. E., Bulovic, V., and Bawendi, M. G. (2006). NiO as an inorganic hole-transporting layer in quantum-dot light-emitting devices. *Nano Lett.* 6, 2991–2994. doi: 10.1021/nl0623208

Caruge, J. M., Halpert, J. E., Wood, V., Bulovic, V., and Bawendi, M. G. (2008). Colloidal quantum-dot light-emitting diodes with metal-oxide charge transport layers. *Nat. Photonics* 2, 247–250. doi: 10.1038/nphoton.2008.34

Chen, F., Guan, Z., and Tang, A. (2018). Nanostructure and device architecture engineering for high-performance quantum-dot light-emitting diodes. *J. Mater. Chem. C* 6, 10958–10981. doi: 10.1039/C8TC04028A

Dai, X., Zhang, Z., Jin, Y., Niu, Y., Cao, H., Liang, X., et al. (2014). Solution-processed, high-performance light-emitting diodes based on quantum dots. *Nature* 515, 96–99. doi: 10.1038/nature13829

Han, S. Y., Lee, D. H., Chang, Y. J., Ryu, S. O., Lee, T. J., and Chang, C. H. (2006). The growth mechanism of nickel oxide thin films by room-temperature chemical bath deposition. *J. Electrochem. S* 153, C382–C386. doi: 10.1149/1.2186767

He, S., Li, S., Wang, F., Wang, A. Y., Lin, J., Tan, Z., et al. (2013). Efficient quantum dot light-emitting diodes with solution-processable MoO as the anode buffer layer. *Nanotechnology* 24:175201. doi: 10.1088/0957-4484/24/17/175201

Huu Tuan, N., Jeong, H., Park, J.-Y., Ahn, Y. H., and Lee, S. (2014). Charge transport in light emitting devices based on colloidal quantum dots and a solution-processed nickel oxide layer. *ACS Appl. Mater. Interfaces* 6, 7286–7291. doi: 10.1021/am500593a

Ji, W., Liu, S., Zhang, H., Wang, R., Xie, W., and Zhang, H. (2017). Ultrasonic spray processed, highly efficient all-inorganic quantum-dot light-emitting diodes. *ACS Photonics* 4, 1271–1278. doi: 10.1021/acsphotonics.7b00216

Ji, W., Shen, H., Zhang, H., Kang, Z., and Zhang, H. (2018). Over 800% efficiency enhancement of all-inorganic quantum-dot light emitting diodes with an ultrathin alumina passivating layer. *Nanoscale* 10, 11103–11109. doi: 10.1039/c8nr01460d

Jiang, Y., Jiang, L., Yeung, F. S. Y., Xu, P., Chen, S., Kwok, H.-S., et al. (2019). All-inorganic quantum-dot light-emitting diodes with reduced exciton quenching by a MgO decorated inorganic hole transport layer. *ACS Appl. Mater. Interfaces* 11, 11119–11124. doi: 10.1021/acsami.9b01742

Li, X., Lin, Q., Song, J., Shen, H., Zhang, H., Li, L. S., et al. (2019). *Quantum-dot light-emitting diodes for outdoor displays with high stability at high brightness. Adv. Opt. Mater.* 8:1901145. doi: 10.1002/adom.201901145

Liu, S., Ho, S., Chen, Y., and So, F. (2015). Passivation of metal oxide surfaces for high-performance organic and hybrid optoelectronic devices. *Chem. Mater.* 27, 2532–2539. doi: 10.1021/acs.chemmater.5b00129

Manders, J. R., Tsang, S.-W., Hartel, M. J., Lai, T.-H., Chen, S., Amb, C. M., et al. (2013). Solution-processed nickel oxide hole transport layers in high efficiency polymer photovoltaic cells. *Adv. Funct. Mater.* 23, 2993–3001. doi: 10.1002/adfm.201202269

Mashford, B. S., Nguyen, T.-L., Wilson, G. J., and Mulvaney, P. (2010). All-inorganic quantum-dot light-emitting devices formed via low-cost, wet-chemical processing. *J. Mater. Chem.* 20, 167–172. doi: 10.1039/B905256A

Murase, S., and Yang, Y. (2012). Solution processed MoO3 interfacial layer for organic photovoltaics prepared by a facile synthesis method. *Adv. Mater.* 24, 2459–2462. doi: 10.1002/adma.201104771

Qian, L., Zheng, Y., Xue, J., and Holloway, P. H. (2011). Stable and efficient quantum-dot light-emitting diodes based on solution-processed multilayer structures. *Nat. Photonics* 5, 543–548. doi: 10.1038/nphoton.2011.171

Ratcliff, E. L., Meyer, J., Steirer, K. X., Garcia, A., Berry, J. J., Ginley, D. S., et al. (2011). Evidence for near-surface NiOOH species in solution-processed NiOx selective interlayer materials: impact on energetics and the performance of polymer bulk heterojunction photovoltaics. *Chem. Mater.* 23, 4988–5000. doi: 10.1021/cm202296p

Sasi, B., and Gopchandran, K. G. (2007). Nanostructured mesoporous nickel oxide thin films. *Nanotechnology* 18:115613. doi: 10.1088/0957-4484/18/11/115613

Shen, H., Cao, W., Shewmon, N. T., Yang, C., Li, L. S., and Xue, J. (2015). High-efficiency, low turn-on voltage blue-violet quantum-dot-based light-emitting diodes. *Nano Lett.* 15, 1211–1216. doi: 10.1021/nl504328f

Shen, H., Gao, Q., Zhang, Y., Lin, Y., Lin, Q., Li, Z., et al. (2019). Visible quantum dot light-emitting diodes with simultaneous high brightness and efficiency. *Nat. Photonics* 13, 192–197. doi: 10.1038/s41566-019-0364-z

Shirasaki, Y., Supran, G. J., Bawendi, M. G., and Bulovic, V. (2013). Emergence of colloidal quantum-dot light-emitting technologies. *Nat. Photonics* 7, 13–23. doi: 10.1038/nphoton.2012.328

Song, J., Wang, O., Shen, H., Lin, Q., Li, Z., Wang, L., et al. (2019). Over 30% external quantum efficiency light-emitting diodes by engineering quantum dot-assisted energy level match for hole transport layer. *Adv. Funct. Mater.* 29:1808377. doi: 10.1002/adfm.201808377

Vu, H.-T., Su, Y.-K., Chiang, R.-K., Huang, C.-Y., Chen, C.-J., and Yu, H.-C. (2016). Solution-processable MoOx for efficient light-emitting diodes based on giant quantum dots. *IEEE Photon. Technol. Lett.* 28, 2156–2159. doi: 10.1109/LPT.2016.2578643

Wang, L., Lin, J., Hu, Y., Guo, X., Lv, Y., Tang, Z., et al. (2017). Blue quantum dot light-emitting diodes with high electroluminescent efficiency. *ACS Appl. Mater. Interfaces* 9, 38755–38760. doi: 10.1021/acsami.7b10785

Wu, X., and Yeow, E. K. L. (2010). Charge-transfer processes in single CdSe/ZnS quantum dots with p-type NiO nanoparticles. *Chem. Commun.* 46, 4390–4392. doi: 10.1039/c0cc00271b

Yang, X., Ma, Y., Mutlugun, E., Zhao, Y., Leck, K. S., Tan, S. T., et al. (2014). WO3, TPD. *ACS Appl. Mater. Interfaces* 6, 495–499. doi: 10.1021/am404540z

Yang, X., Zhang, Z.-H., Ding, T., Wang, N., Chen, G., Dang, C., et al. (2018). High-efficiency all-inorganic full-colour quantum dot light-emitting diodes. *Nano Energy* 46, 229–233. doi: 10.1016/j.nanoen.2018.02.002

Zhang, H., Hu, N., Zeng, Z. P., Lin, Q., l., Zhang, F., Tang, A., et al. (2019). High-efficiency green InP quantum dot-based electroluminescent device comprising thick-shell quantum dots. *Adv. Opt. Mater.* 7:9. doi: 10.1002/adom.201801602

Zhang, H., Sui, N., Chi, X., Wang, Y., Liu, Q., Zhang, H., et al. (2016). Ultrastable quantum-dot light-emitting diodes by suppression of leakage current and exciton quenching processes. *ACS Appl. Mater. Interfaces* 8, 31385–31391. doi: 10.1021/acsami.6b09246

Zhang, H., Wang, S., Sun, X., and Chen, S. (2017). Solution-processed vanadium oxide as an efficient hole injection layer for quantum-dot light-emitting diodes. *J. Mater. Chem. C* 5, 817–823. doi: 10.1039/C6TC04050K

Conflict of Interest: The authors declare that the research was conducted in the absence of any commercial or financial relationships that could be construed as a potential conflict of interest.

frontiers in Chemistry

ORIGINAL RESEARCH
published: 24 July 2020
doi: 10.3389/fchem.2020.00573

Clean the Ni-Rich Cathode Material Surface With Boric Acid to Improve Its Storage Performance

Yuefeng Su[1,2], Gang Chen[1,2], Lai Chen[1,2], Linwei Li[1], Cong Li[1], Rui Ding[1], Jiahui Liu[1], Zhao Lv[3], Yun Lu[1,2], Liying Bao[1], Guoqiang Tan[1,2], Shi Chen[1] and Feng Wu[1,2]*

[1] Beijing Key Laboratory of Environmental Science and Engineering, School of Materials Science and Engineering, Beijing Institute of Technology, Beijing, China, [2] Beijing Institute of Technology Chongqing Innovation Center, Chongqing, China, [3] School of Materials Science and Engineering, Beijing Institute of Technology, Beijing, China

The existence of residual lithium compounds (RLCs) on the surface of layered Ni-rich materials will deteriorate the electrochemical properties and cause safety problem. This work presents an effective surface washing method to remove the RLCs from $LiNi_{0.90}Co_{0.06}Mn_{0.04}O_2$ material surface, *via* ethyl alcohol solution that contains low concentration of boric acid. It is a low-cost process because the filter liquor can be recycled. The optimal parameters including washing time, boric acid concentration, and solid–liquid ratio were systematically studied. It has been determined by powder pH and Fourier transform infrared spectra results that the amount of RLCs was reduced effectively, and the storage performance was significantly enhanced for the washed samples. The 150th capacity retentions after storing had increased from 68.39% of pristine material to 85.46–94.84% of the washed materials. The performance enhancements should be ascribed to the surface washing process, which removed not only the RLCs, but also the loose primary particles effectively.

Keywords: Ni-rich materials, surface washing, boric acid, residual lithium compounds, storage performance

OPEN ACCESS

Edited by:
Guohua Jia,
Curtin University, Australia

Reviewed by:
Dawei Su,
University of Technology Sydney, Australia
Liqiang Xu,
Shandong University, China

***Correspondence:**
Lai Chen
chenlai144@sina.com

Specialty section:
This article was submitted to Inorganic Chemistry, a section of the journal Frontiers in Chemistry

Received: *09 April 2020*
Accepted: *03 June 2020*
Published: *24 July 2020*

Citation:
Su Y, Chen G, Chen L, Li L, Li C, Ding R, Liu J, Lv Z, Lu Y, Bao L, Tan G, Chen S and Wu F (2020) Clean the Ni-Rich Cathode Material Surface With Boric Acid to Improve Its Storage Performance. Front. Chem. 8:573. doi: 10.3389/fchem.2020.00573

INTRODUCTION

Nowadays, lithium-ion batteries (LIBs) have been considered as the most feasible equipment to utilize the electrical energy. However, it is still urgent to develop high-energy density LIBs to satisfy the ever-growing demands of electric vehicles (He et al., 2018; Su et al., 2018a; Kong et al., 2019; Liang et al., 2019). The cathode materials have been considered as the focus and weak link of high-energy LIBs; thus, the high-capacity layered Ni-rich $LiNi_xCo_yMn_{1-x-y}O_2$ ($0.5 < x < 1, 0 < y < 0.5$) materials emerged and had been studied widely as one of the most promising cathode materials in recent years (Lin et al., 2014; Wu et al., 2018, 2019; Qiu et al., 2019).

However, although increased nickel content in Ni-rich cathode materials enables them to deliver higher capacity, more residual lithium compounds (RLCs) will be formed on their surface. The RLC mainly contains Li_2O, Li_2O_2, LiOH, $LiHCO_3$, and Li_2CO_3 (Liu et al., 2004; Kim et al., 2006; Bichon et al., 2019; Xu S. et al., 2019; Zhang et al., 2019), which origins from the vestigial of lithium salts and spontaneous reduction reaction of Ni^{3+} during the synthesis and storage process (Junhyeok et al., 2018). In detail, excess 5 mol% lithium salts are usually applied to compensate the evaporation loss during high-temperature calcination process (Liang et al., 2017). The obvious side effect, however, is that in the event of an inadequate calcination process, it will bring excessive lithium salts (e.g., LiOH and Li_2CO_3), and the undecomposed lithium compound intermediates (like Li_2O and Li_2O_2) that

linger on the surface of Ni-rich cathode materials. Especially, with higher nickel content (especially >60%), the calcination temperature needs to be lower and thus more likely leading to the formation of RLC (Junhyeok et al., 2018; Park J. -H. et al., 2018). On the other side, the surface active lattice lithium and oxygen species of Ni-rich cathode materials would react with the H_2O and CO_2 in the air during storage under the influence of reduction of sensitive Ni^{3+}, forming the undesirable RLC and surface NiO rock-salt layer (Huang et al., 2019).

This undesired RLC has many adverse effects on the Ni-rich materials. First, RLC would absorb the trace water in the air and increase the powder alkalinity, which will further gel the slurry during electrode fabrication process, corrode the current collector, and worsen the consistency of electrode and the corresponding batteries (He et al., 2018; Junhyeok et al., 2018; Bichon et al., 2019). Second, this insulating RLC would also react with the electrolyte and produce gas such as CO_2, thus deteriorating the electrochemical performances and causing safety problem (Hatsukade et al., 2018). Third, Grenier et al. (2017) had proved that the existence of Li_2CO_3 layer on the surface of Ni-rich materials will induce a "two-phase" behavior during the initial charge process, which severely hinders the exploration of the intrinsic reaction mechanism of Ni-rich materials. Last but not least, the formation of RLC during the storage consumes the lithium inventory, which will cause deteriorative electrochemical performance.

The most common way to reduce the RLC is water washing (Kimijima et al., 2016; Li et al., 2018). Unfortunately, although this treatment can remove the RLC on the surface of materials, it cannot prevent the treated materials from keeping reacting with water and carbon dioxide in the air. More seriously, the water washing process will worsen the thermal stability of the Ni-rich materials at some extent and make the washed materials be more sensitive to the air (Xiong et al., 2013). As a result, some improved strategies have emerged; for instance, Xu et al. (2017) used protonated polyaniline (PANI) in *N*-methyl pyrrolidone solvent to wash the $LiNi_{0.8}Co_{0.1}Mn_{0.1}O_2$ material. The H^+ in the solvent reacted with the RLC, whereas the remained conductive PANI formed a protective layer on $LiNi_{0.8}Co_{0.1}Mn_{0.1}O_2$ surface after washing. Liu et al. (2018) adopted the pure ethanol solvent instead of water to wash the $LiNi_{0.8}Co_{0.15}Al_{0.05}O_2$ materials. These results show that washing method is indeed an effective way to reduce the amount of RLC, whereas the ethanol solvent can further enhance the material resistance to the humidity in the air.

Here we propose a universal surface washing method *via* ethanol solvent with appropriate amount of boric acid (BA) for Ni-rich $LiNi_{0.90}Co_{0.06}Mn_{0.04}O_2$ cathode material. Boron element has been widely used to modify the Ni-rich cathode materials (Hu et al., 2017; Lv et al., 2017; Chen et al., 2018; Park K. -J. et al., 2018), whereas BA can react with RLC easily without bringing harmful effects because it is a weak acid. Besides, the ethanol solvent also could remove the RLC. The schematic diagram for the washing process is shown in **Figure 1**. During this process, the filtrate can be recycled and used to wash the cathode materials again, which lowers the cost. The key parameters of this washing method, including washing time, concentration of BA, and solid–liquid ratio of $LiNi_{0.90}Co_{0.06}Mn_{0.04}O_2$ material to ethyl alcohol solution, had been investigated systematically in this work. The testing results show that benefiting from the washing process, the pH values of treated materials were reduced effectively. Accordingly, their electrochemical performances, especially the short-time storage performances, had been significantly enhanced. Overall, our work provides a promising strategy for treating the RLC on Ni-rich material surface with lower cost and simple steps.

EXPERIMENTAL SECTION

The Preparations of Pristine and Washed Materials

The $LiNi_{0.90}Co_{0.06}Mn_{0.04}O_2$ was prepared *via* a coprecipitation method with solid-state reaction method according to our previous report (Su et al., 2018a), and the details are exhibited

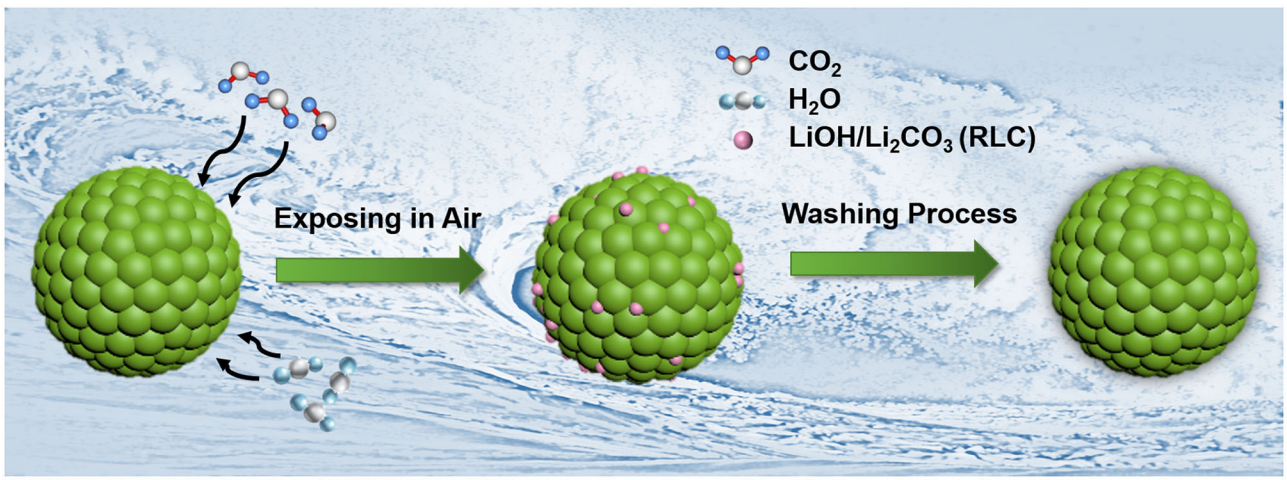

FIGURE 1 | The schematic diagrams for the washing process of $LiNi_{0.90}Co_{0.06}Mn_{0.04}O_2$ materials.

TABLE 1 | Summary of the treat parameters and Li/Ni/Co/Mn molar ratios calculated from ICP-OES of all the samples.

Sample no.	Solid–liquid ratio (g:mL)	Washing time (min)	Concentration of BA (g/L)	Li/Ni/Co/Mn calculated from ICP
BA-0	0	0	0	100.5:90.1:5.9:4.0
BA-1	1:1	5	0.25	100.3:89.9:6.0:4.1
BA-2	1:1	10	0.5	100.1:90.0:6.1:4.0
BA-3	1:1	20	1	99.9:89.8:6.1:4.1
BA-4	1:5	5	1	100.0:90.1:6.0:3.9
BA-5	1:5	10	0.5	100.0:90.0:6.0:4.0
BA-6	1:5	20	0.25	100.0:90.0:5.9:4.1
BA-7	1:10	5	0.25	100.3:89.9:6.0:4.1
BA-8	1:10	10	1	99.8:90.2:5.8:4.0
BA-9	1:10	20	0.5	100.1:90.1:6.0:3.9

in the **Supporting Information**. The pristine sample was labeled as "BA-0" and used for further modifying experiments. To prepare the washed materials, some amount of BA was dissolved in pure ethyl alcohol to form a clear washing liquid first. Then 1 g of the freshly prepared powders was dispersed in the ethanol solvent and stirred for several minutes. After the washing stage, the powders were filtered, and the filtrate was collected for reusing. The parameters of washing process, labeled as washing time, concentration of BA, and solid–liquid ratio of $LiNi_{0.90}Co_{0.06}Mn_{0.04}O_2$ material to ethyl alcohol solution, are summarized in **Table 1**, and their corresponding samples were labeled as BA-1 to BA-9. After the filtration, the powders were stored in the air randomly. Before fabricating the cathode electrodes, all the powders, including BA-0, were dried up at 80°C for 1 h and then sintered at 400°C for 2 h under oxygen atmosphere to remove all possible ethyl alcohol remained on the NCM particle surface and rule out the influences of reheat process.

Characterizations of the Materials

The compositions, morphologies, and crystalline structures of all samples were detected by inductively coupled plasma optical emission spectrometry (ICP-OES; Agilent ICPOES730, USA), powder X-ray diffraction (XRD; Rigaku UltimaIV-185 instrument, Japan), X-ray photoelectron spectroscopy (XPS; ULVAC-PHI, Inc., Japan), field-emission scanning electron microscopy (SEM; FEI Quanta 250 instrument, USA), and high-resolution transmission electron microscopy (HR-TEM; JEOL JEM-2100 instrument, Japan). The pH values were confirmed by a Mettler Toledo FE20 pH meter (Mettler Toledo, Switzerland), while the existence of RLC was proven by Fourier transform infrared spectra (FT-IR; Nicolet IS10, USA).

Electrochemical Measurements

All the samples were assembled into CR2025 coin-type half cells, which consist of lithium metal anode and a commercial Celgard 2500 separator. The manufacturing details of cathode electrode and cells were kept the same with our previous work (Su et al., 2019). The electrochemical cycling tests (2.75–4.3 V, vs. Li^+/Li) and the potentiostatic intermittent titration technique (PITT) experiments of cells were operated on the CT2001A Land Instruments (Wuhan, China) at room temperature. Electrochemical impedance spectroscopy (EIS) and measurements were operated at CHI660E electrochemical workstation (Shanghai, China).

RESULTS AND DISCUSSION

The compositions of all the samples were tested by ICP-OES, and the results are listed in **Table 1**. The similar molar ratio values, as we expected, reveal that the faintly acid BA had not damaged the samples as the transition metal elements were not leached out after washing. Note that the lithium contents of the washed materials are decreased with the increasing washing time and BA concentration. The cause of reduced amount of lithium needs further confirmation, which may originate from the reduction of RLC or the dissolution of lattice lithium from H^+/Li^+ ion exchange.

To further ascertain the influences of washing process to Ni-rich materials, the morphologies of all the washed samples were observed by SEM images as exhibited in **Figure 2**, whereas that of BA-0 is shown in **Figure S1**. The secondary particles exhibit similar morphology, but the magnified inserts indicate that there are slightly differences in primary particles. Not only that the primary particles size of the washed materials seems larger, but also their surface becomes clearer than those of pristine material. The larger particle size may result from the introduction of boron element (Chen et al., 2018), whereas the cleaner surface may ascribe to falling off of RLC (Xu S. et al., 2019).

The surface changes in morphology are generally accompanied by the changes in lattice structure. The XRD patterns exhibited in **Figure 3** reveal that all samples belong to a hexagonal α-$NaFeO_2$ structure with an $R\bar{3}m$ space group (Xie et al., 2019; Su et al., 2020). The clear splitting between (006)/(102) peaks and (018)/(110) peaks of all samples proves that the materials have a well-ordered layered structure, whereas the BA or ethyl alcohol has not deteriorated the bulk structure of Ni-rich materials. Another comforting phenomenon is that all XRD patterns show no extra impurity peaks, indicating that the contents of impurity phases such as RLC or the possible H_3BO_3-based materials are absent or very low (Xu G. -L. et al., 2019). The ratios of $I_{(003)}/I_{(104)}$ of all samples were also calculated, and the results are listed in **Table S1**. Although the ratio values of some samples are reduced, all the calculated values are still higher than 1.2, meaning the low cation mixing degree (Zhang et al., 2018; Weigel et al., 2019). The changed $I_{(003)}/I_{(104)}$ values of the washed samples indicate the washing process may affect the lattice structure. To further investigate the detailed structure changes after washing, the (003) peaks of all samples are magnified as shown in **Figure 3** and **Table S1**. Comparing with the peak position of the BA-0 sample, the (003) peaks of all washed materials shift to a lower angle in varying degrees, which manifests larger interplanar spacings (Wang et al., 2016).

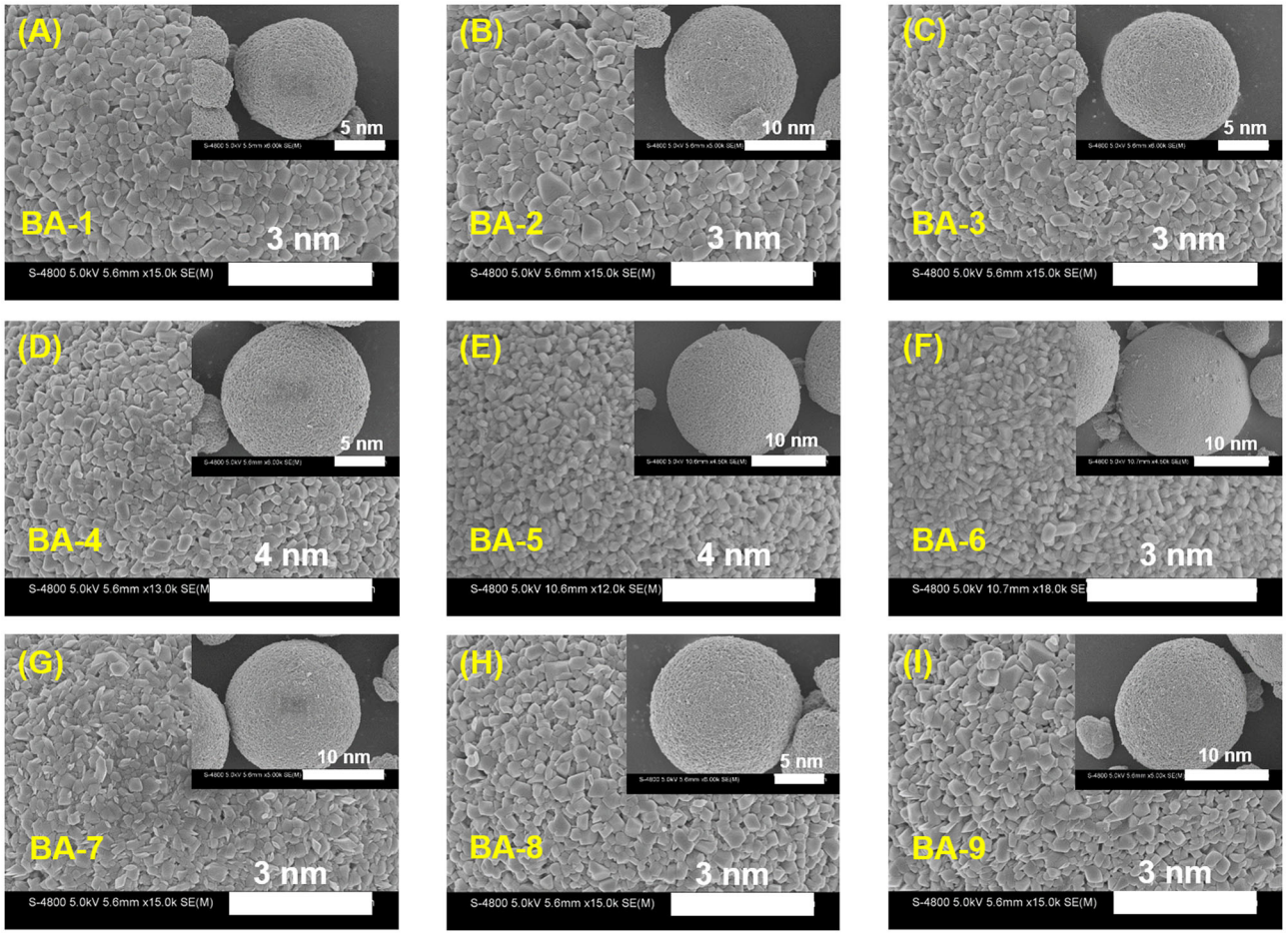

FIGURE 2 | The magnifying SEM images of **(A–I)** BA-1 to BA-9. The inserts are SEM images of their corresponding particles.

The larger interplanar spacing may result from the dissolution of lattice lithium during the washing process, which consists with the ICP-OES results.

The pH measurements were adopted to check if the RLC had been removed from the samples surface. The pH value curves are presented in **Figure 4A**. All the pH curves in **Figure 4A** exhibit an increasing tendency followed by stable values. The increase in pH value at the first 30 s may ascribe to the dissolution of alkaline LiOH (Xiong et al., 2013), and the final pH value of BA-0 is much higher than all those of the treated materials. Because the pH value could reflect the total amount of RLC on the surface of materials as mentioned previously, therefore it is indubitable that the washing process we proposed could reduce the amount of RLC effectively.

To further confirm the content of the RLC on the samples surface, the FT-IR test was applied, and the results in **Figure 4B** give more evidence of the surface changes. The peak at 3,200–3,650 cm^{-1} belongs to the O-H stretching vibration from LiOH, whereas the other two bands at 870 and 1,450 cm^{-1}, respectively, originated from the C=O and O=C=O vibration in Li_2CO_3 (Xiong et al., 2013). All the FT-IR patterns demonstrate stronger signal of LiOH than that of Li_2CO_3, which means there are more LiOH on the surface of samples before storage. Meanwhile, compared with the BA-0, the washed materials show significantly decreased peak intensities of LiOH, indicating an effective removal of RLC *via* our washing process.

The washing process may influence the valence states of elements and microstructures of Ni-rich materials. Therefore, the XPS measurements and HR-TEM analysis were applied to the BA-0 and BA-7 samples to verify the washing effects and structural changes, and the results are shown in **Figure S2**. **Figures S2A–D** exhibits the XPS spectra of BA-0 and BA-7, proving the similar binding energies of two samples and the same valence states of Co and Mn. It should be noted that the binding energies of Ni $2p_{3/2}$ in **Figure S2B** are different, which originated from the different content ratios of Ni^{2+}/Ni^{3+} in these samples. The Ni^{2+}/Ni^{3+} ratio value decreases from 0.52 to 0.33 after washing process, and the reduction of Ni^{2+} implies that there might be structural variations in Ni-rich materials, which could be confirmed by the HR-TEM tests. As can be seen from **Figures S2E,F**, the surface of BA-0 could be divided into two regions, as circled in rock-salt phase E1 and layered phase E2,

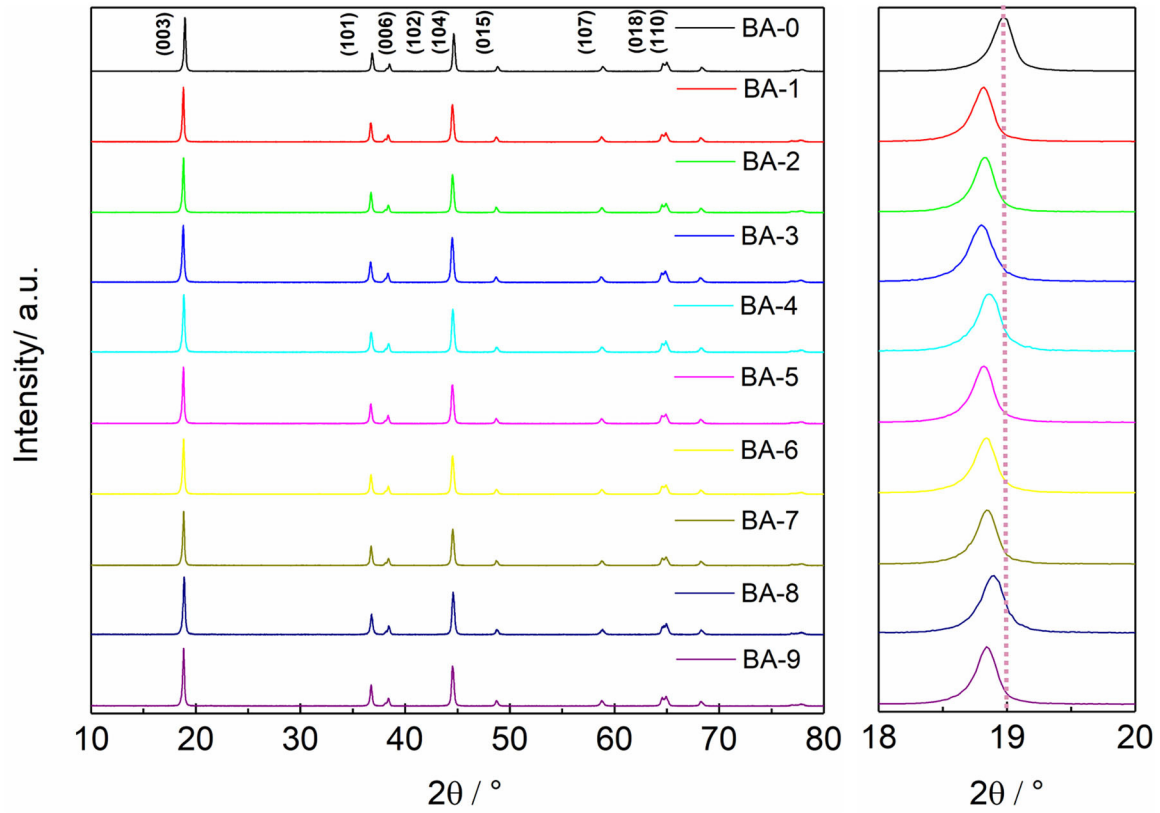

FIGURE 3 | The whole and detailed XRD patterns of all samples.

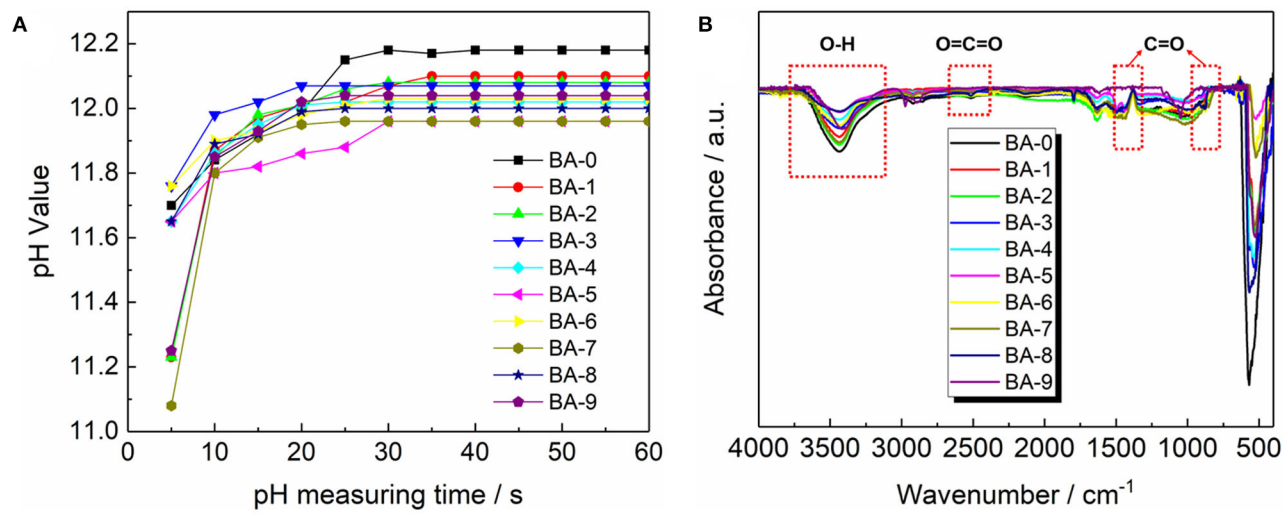

FIGURE 4 | (A) Plot of pH vs. the pH measuring time and **(B)** the FT-IR spectra of all the samples.

whereas le that of BA-7 is keeping the same layered phase (as circled in F1 and F2) from surface to bulk. The disappearance of rock-salt phase, which is also known as NiO in Ni-rich materials, explains the reduction of Ni^{2+} in **Figure S2B**. However, the $I_{(003)}/I_{(104)}$ values in **Table S1** also exhibit that some of the modified materials suffer more severe cation mixing than BA-0, conflicting with the conclusions in **Figure S2**. Therefore, we put forward a hypothesis that weak acid such as BA has uneven

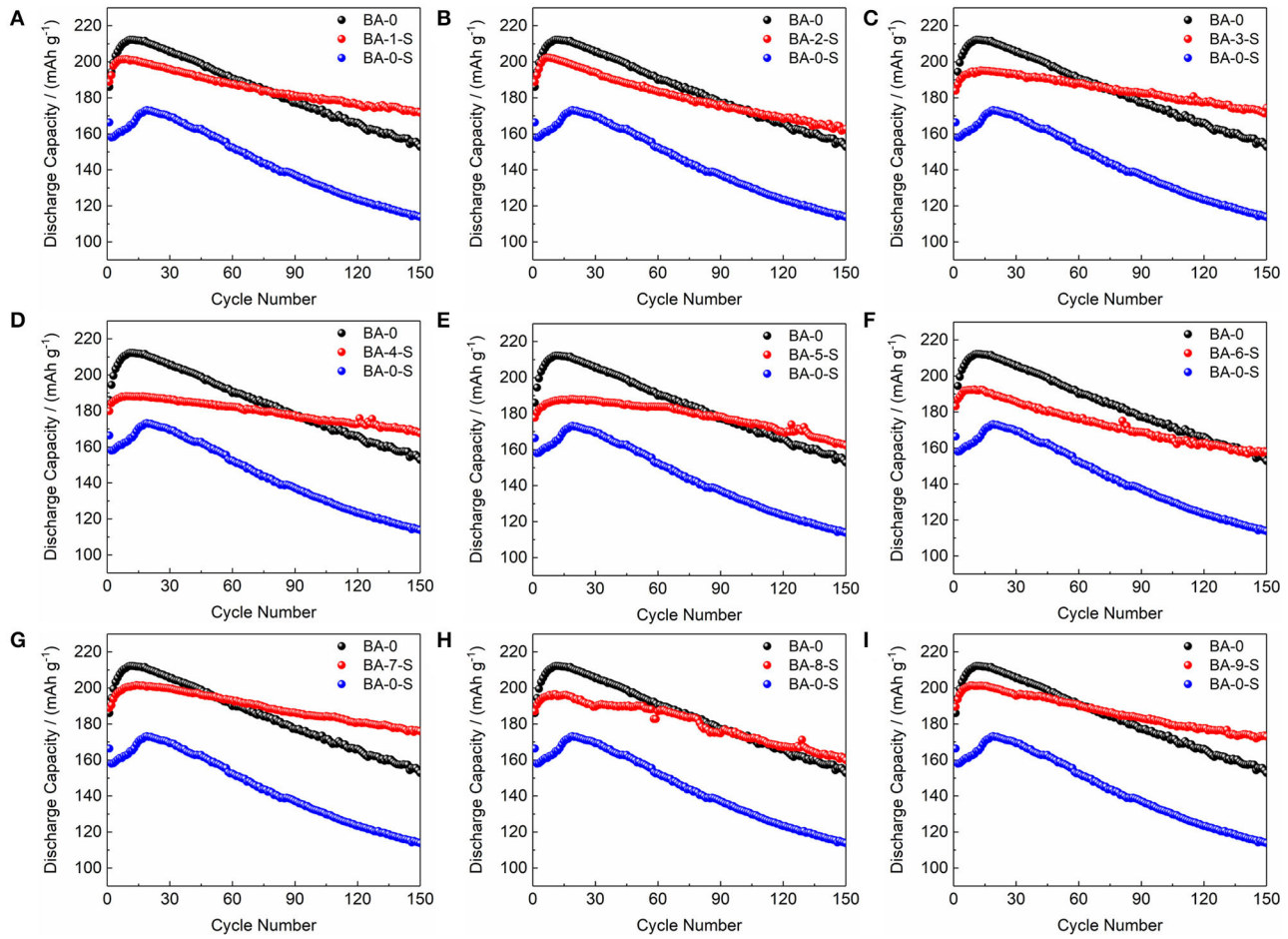

FIGURE 5 | The comparisons of cycling performance of **(A–I)** BA-1-S to BA-9-S with BA-0 and BA-0-S at 0.2 C rate.

leaching effect on the Ni-rich materials based on the results mentioned previously, which will be explored in the future.

There are several literatures pointing out that the materials will be more sensitive to the air/water after water washing (Xiong et al., 2013; Junhyeok et al., 2018). Hence, we also checked the storage performances of all the washed samples here. All of them were stored in the air for 15 days, and the relative humidity curve during store stage is shown in **Figure S3**. We renamed the samples after storage as BA-1-S–BA-9-S to distinguish the samples before from after storage. The TEM measurement was carried out first. As displayed in **Figures S4A,B**, the amount of impurity phase on the BA-0-S is much higher than BA-0, indicating that the RLC would easily form on the particles surface during storage. The TEM image of BA-7-S, one of the stored washed materials, is also placed in **Figure S4C**. There is only a little of amorphous impurities (which was marked by red circle) on the particle surface, suggesting the sensitivity of the treated samples to humid air had not been improved.

The electrochemical performances of stored materials, BA-1-S–BA-9-S, were tested as shown in **Figure 5**, **Figure S5**, and **Table 2** (1 C = 200 mA/g). BA-1 and BA-0-S were also exhibited for comparisons. **Figures S5A,C, Figure 5** point out that the BA-0 and BA-0-S have similar rapid drop tendency during cycling with a ∼40 mAh/g difference, indicating an abrupt electrochemical performance degradation of Ni-rich material after storage. The first cycle voltage profiles of BA-0 and BA-0-S at 0.2 C rate are exhibited in **Figure S5B**, in which the BA-0-S owns a huge IR drop at discharge stage and a long constant voltage platform during charging. The huge IR drop comes from drastic parasitic reactions. Moreover, the charge capacity of all washed samples at constant voltage stage is shorter than BA-0-S as demonstrated on the bottom of **Figure S5B**, implying that the side reactions between RLC and electrolyte were suppressed after washing (Zhang et al., 2019). **Figure 5** exhibits the detailed comparisons of stored treated materials with BA-0 and BA-S at 0.2 C cycling, which splits from **Figure S5A**. Even though the initial discharge capacities of all stored treated materials are lower than that of BA-0, their discharge capacity values are much larger than that of BA-0-S, indicating enhanced storage performances. The 150th capacity retentions after storing had increased from 68.39% of pristine material to 85.46–94.84% of the washed materials.

The side reactions between RLC and electrolyte will form a cathode–electrolyte interphase (CEI) film and influence the electrochemical kinetics (Grenier et al., 2017). The EIS analysis of all stored samples was applied after the 1st and 150th cycles to estimate the electrochemical kinetics changes, and the fresh BA-0 was also tested as a comparison. As the Nyquist plots shown in **Figure 6**, all curves consist of two semicircles and a line. The first semicircle at high frequency corresponds to the resistance of CEI film (R_{int}), whereas the secondary one at intermediate frequency presents the charge transfer resistance (R_{ct}) (Su et al., 2018a). All the samples exhibit different electrochemical kinetics even only after the first cycle (**Figure 6A**). BA-0-S owns the highest R_{int} and R_{ct} values among all samples, whereas the BA-0 owns the small R_{int} value but the second largest R_{ct} value. Because BA-0-S inherited from BA-0, it is easy to speculate that the large R_{int} values resulted from the RLC on the surface, which is formed during the storage. Benefiting from the reduced RLC amount, the washed samples exhibit better surface charge transfer, according to their smaller R_{ct} values than those of BA-0 and BA-0-S, no matter in 1st or 150th cycle. The low R_{ct} value of cathode material is in favor of its electrochemical performances (Su et al., 2018b), which is in accord with the better electrochemical performances of washed samples shown in **Figure 5** and **Table 2**.

Not only the EIS, but also the PITT test, was performed to calculate the Li^+ diffusion coefficient for analyzing the

TABLE 2 | Summary of the electrochemical performances of all the samples.

Sample no.	Initial discharge capacity at 0.2 C	150th capacity retention at 0.2 C	Initial discharge capacity at 1 C	150th capacity retention at 1 C
BA-0	190	80.42%	188.9	71.36%
BA-0-S	166.4	68.39%	167.3	59.83%
BA-1-S	188.9	90.95%	180.4	84.87%
BA-2-S	188.8	86.18%	183.1	83.67%
BA-3-S	184	94.84%	175.9	85.79%
BA-4-S	179.9	93.16%	184.3	86.00%
BA-5-S	177.7	91.33%	170.7	90.22%
BA-6-S	183.2	86.14%	183.3	79.71%
BA-7-S	188.8	93.22%	183.6	88.73%
BA-8-S	187.1	85.46%	177.6	85.25%
BA-9-S	189.6	91.24%	179.5	83.73%

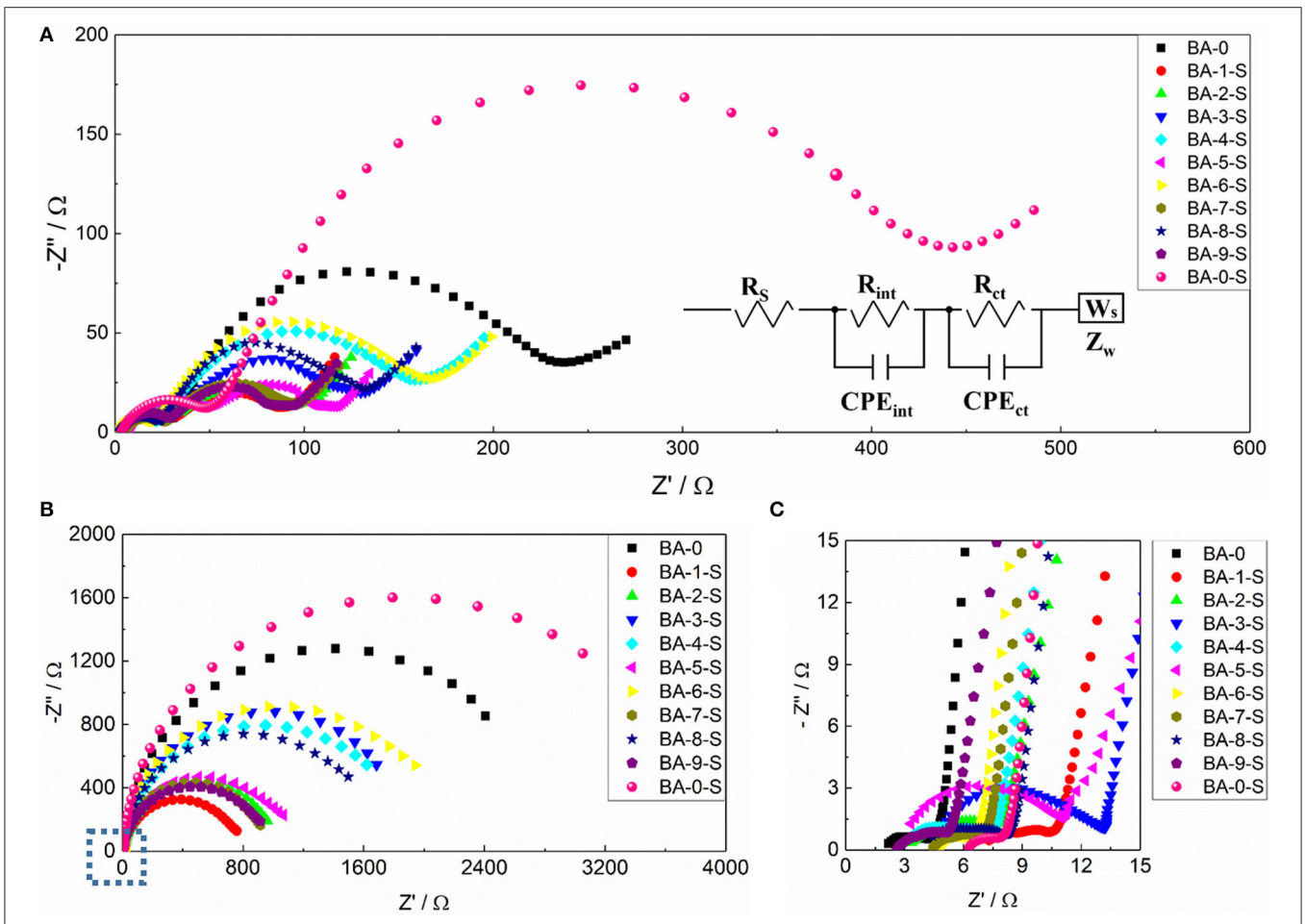

FIGURE 6 | Nyquist plots of all samples after **(A)** 1st and **(B)** 100th cycles at 1 C/1 C rate and **(C)** the magnified area of marked area in **(B)**. The insert in **(A)** is the equivalent circuit model of all samples.

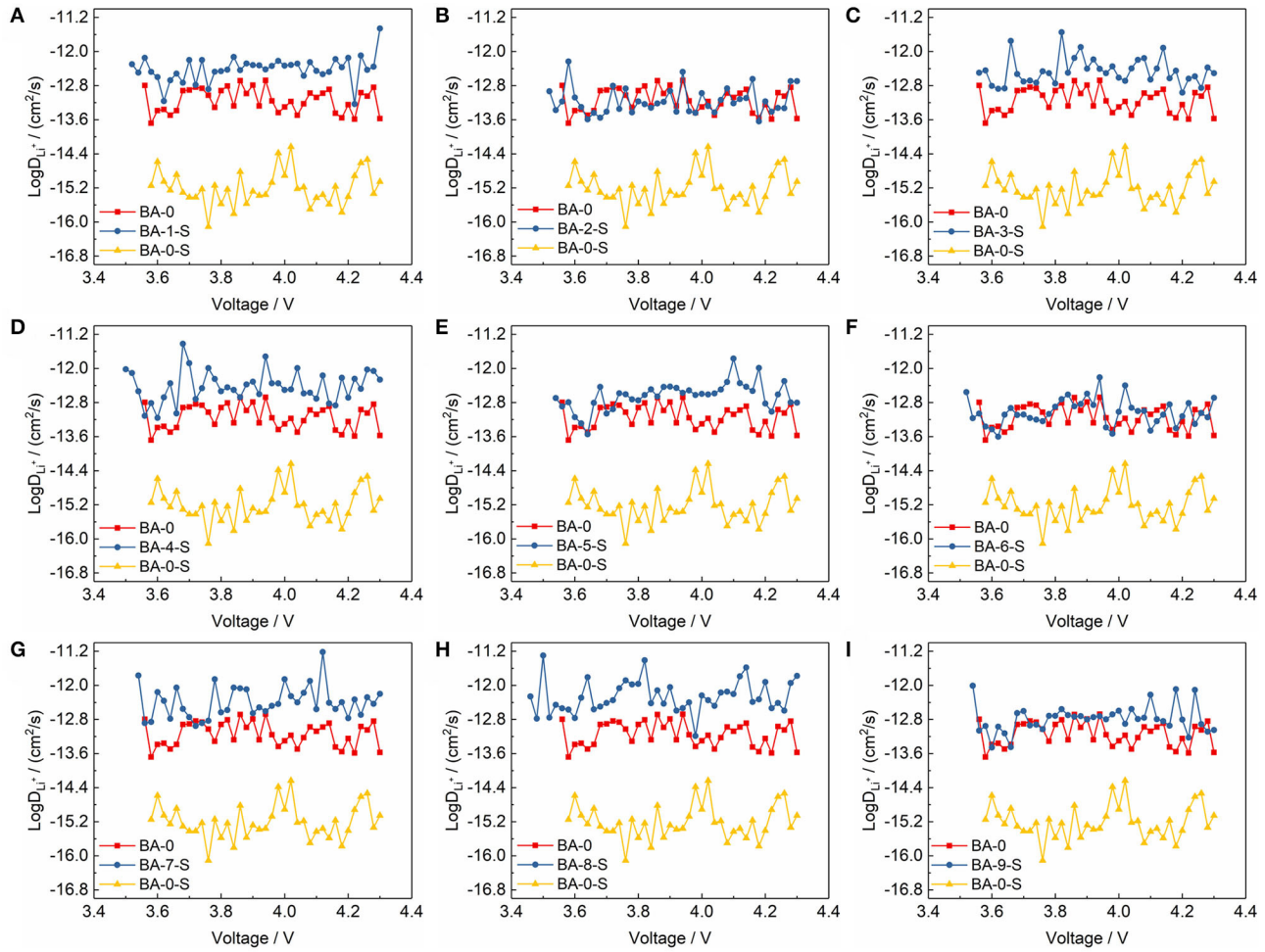

FIGURE 7 | The comparisons of Li^+ diffusion coefficients of **(A–I)** BA-1-S to BA-9-S with BA-0 and BA-0-S.

electrochemical kinetics of electrodes. The details of PITT test curves are shown in **Figure S6**, and the calculated Li^+ diffusion coefficients are shown in **Figure 7**. We present three Li^+ diffusion coefficient curves in **Figures 7A–I**, including one of stored washed materials, BA-0 and BA-0-S. The Li^+ diffusion coefficient of BA-0-S is much smaller than BA-0 and all washed materials, which may ascribe to the block effect of RLC on the material surface. Meanwhile, the Li^+ diffusion coefficient curves of BA-0 and all stored treated materials are similar, illustrating that the washing process will enhance the resistance of Ni-rich material to the air, suppressing the formation of RLC (Su et al., 2018a).

In conclusion, the positive effects of surface washing method *via* ethanol solvent with a little BA for Ni-rich $LiNi_{0.90}Co_{0.06}Mn_{0.04}O_2$ material have been proved, whereas the influences of washing parameters on the storage materials should also be evaluated. The analysis results of orthogonal factor level table, which were based on the capacity retention of stored materials at 0.2 C rate, are listed in **Table 3**. The ranking numbers of electrochemical result of all samples were defined from 1 to 9, and the material with higher capacity retention owns a lower number value. The I_L,II_L, and III_L values could be used to estimate the effects of levels A, B, and C on the corresponding factors. The K_1, K_2, and K_3 values reflect the average rate of change, which equal to the values of $I_L/3$, $II_L/3$, and $III_L/3$, respectively, in this work. R is the max–min values of corresponding K columns, reflecting the extent of effect of factors. According to the calculated estimates of the horizontal effects, we can figure out that the smaller solid–liquid ratio, shorter washing time, and higher concentration of BA would be better for the washing process. The optimal parameters are as follows: the solid–liquid ratio is 1 g/mL, the concentration of BA is 1 g/L, and the washing time is 5 min. Because the final pH values of all washed samples are still higher than 11.5, we can easily draw a conclusion that there are still lots of RLC on the surface of treated samples. The superfluous RLC means the whole washing process is incomplete, reflecting that more BA is needed in this treatment. With lower solid–liquid ratio and higher concentration of BA, the removal of RLC and undesired NiO phase would be more complete, which is a benefit for the electrochemical performances of Ni-rich materials. It is also

TABLE 3 | Orthogonal factor level table of washed samples based on the electrochemical performance of stored materials at 0.2 C rate.

Sample no.	Factors			Electrochemical results
	Solid–liquid ratio (g/mL)	Washing time (min)	Concentration of BA (g/L)	
	Level			
	A	B	C	No.
BA-1	1	5	0.25	6
BA-2	1	10	0.5	7
BA-3	1	20	1	1
BA-4	5	5	1	3
BA-5	5	10	0.5	4
BA-6	5	20	0.25	8
BA-7	10	5	0.25	2
BA-8	10	10	1	9
BA-9	10	20	0.5	5
I_L	14	11	16	$T = 45$
II_L	15	20	16	
III_L	16	14	13	
K_1	4.67	3.67	5.33	
K_2	5	6.67	5.33	
K_3	5.33	4.67	4.33	
R	0.66	3	1	
Better level	A_1	B_1	C_3	

worth noting that when prolonging the washing time, the positive effect was also achieved. With the largest *R* value in washing time column, it could be explained by the following reasons. When the washing time is short, the reaction products between BA and RLC would adhere on the surface of Ni-rich materials and transform into a thin layer of $LiBO_2$ after calcination (Hu et al., 2017). The fast ionic conductor $LiBO_2$ could not only improve the migration of Li^+, but also protect the cathode material from the electrolyte erosion. Meanwhile, when the washing time become longer, the washing process would be thorough. The RLC and the reactants between BA and RLC, even some nanoparticles (Xu S. et al., 2019), would fell off from the surface of the secondary particles. Without the side reactions between RLC and small primary particles with electrolyte, the cycling stability of materials should be enhanced.

CONCLUSION

We proposed a low-cost surface washing method *via* ethanol solvent that contains low concentration of BA for $LiNi_{0.90}Co_{0.06}Mn_{0.04}O_2$ material. It has been determined that this treatment has the positive effects on removing the RLCs from the surface of Ni-rich cathode material. The fluid washing process could not only remove the RLC effectively, but also suppress the formation of RLC during the storage, leading to the superior storage electrochemical performances. The 150th capacity retentions after 15-day storing had increased from 68.39% of pristine material to 85.46–94.84% of treated materials. Besides, the effects of washing parameters such as solid–liquid ratio, washing time, and the concentration of BA to materials were also systematically studied. According to the orthogonal analysis, the suitable washing process needs smaller solid–liquid ratio, shorter washing time, and higher concentration of BA. This work provides a promising surface washing strategy for Ni-rich materials, which shows a great prospect in the industrial application.

DATA AVAILABILITY STATEMENT

The original contributions presented in the study are included in the article/**Supplementary Material**, further inquiries can be directed to the corresponding author/s.

AUTHOR CONTRIBUTIONS

YS, GC, and LC designed the experiment, characterized the samples, and wrote the manuscript. LL, CL, RD, and JL helped to the material synthesis. ZL contributed to the TEM test and corresponding analysis. YL, LB, GT, SC, and FW contributed to the data analysis and manuscript revision. All authors reviewed and approved the final submitted version of manuscript.

FUNDING

This work was supported by National Key R&D Program of China (2016YFB0100301), National Natural Science Foundation of China (21875022, 51802020, and U1664255), Science and Technology Innovation Foundation of Beijing Institute of Technology Chongqing Innovation Center (2020CX5100006), and Young Elite Scientists Sponsorship Program by CAST (2018QNRC001). LC acknowledges the support from the Beijing Institute of Technology Research Fund Program for Young Scholars and GT acknowledges the support from the Beijing Institute of Technology (BIT) Teli Young Fellow Program (No. 3090011181903).

SUPPLEMENTARY MATERIAL

The Supplementary Material for this article can be found online at: https://www.frontiersin.org/articles/10.3389/fchem.2020.00573/full#supplementary-material

REFERENCES

Bichon, M., Sotta, D., Dupré, N., De Vito, E., Boulineau, A., Porcher, W., et al. (2019). Study of immersion of $LiNi_{0.5}Mn_{0.3}Co_{0.2}O_2$ material in water for aqueous processing of positive electrode for Li-ion batteries. *ACS Appl. Mater. Interfaces* 11, 18331–18341. doi: 10.1021/acsami.9b00999

Chen, T., Li, X., Wang, H., Yan, X., Wang, L., Deng, B., et al. (2018). The effect of gradient boracic polyanion-doping on structure, morphology,

and cycling performance of Ni-rich $LiNi_{0.8}Co_{0.15}Al_{0.05}O_2$ cathode material. *J. Power Sources* 374, 1–11. doi: 10.1016/j.jpowsour.2017.11.020

Grenier, A., Liu, H., Wiaderek, K. M., Lebens-Higgins, Z. W., Borkiewicz, O. J., Piper, L. F. J., et al. (2017). Reaction heterogeneity in $LiNi_{0.8}Co_{0.15}Al_{0.05}O_2$ induced by surface layer. *Chem. Mater.* 29, 7345–7352. doi: 10.1021/acs.chemmater.7b02236

Hatsukade, T., Schiele, A., Hartmann, P., Brezesinski, T., and Janek, J. (2018). Origin of carbon dioxide evolved during cycling of nickel-rich layered NCM cathodes. *ACS Appl. Mater. Interfaces* 10, 38892–38899. doi: 10.1021/acsami.8b13158

He, T., Lu, Y., Su, Y., Bao, L., Tan, J., Chen, L., et al. (2018). Sufficient utilization of zirconium ions to improve the structure and surface properties of nickel-rich cathode materials for lithium-ion batteries. *ChemSusChem* 11, 1639–1648. doi: 10.1002/cssc.201702451

Hu, W., Zhang, C., Jiang, H., Zheng, M., Wu, Q.-H., and Dong, Q. (2017). Improving the electrochemistry performance of layer $LiNi_{0.5}Mn_{0.3}Co_{0.2}O_2$ material at 4.5V cutoff potential using lithium metaborate. *Electrochim. Acta* 243, 105–111. doi: 10.1016/j.electacta.2017.05.075

Huang, B., Liu, D., Qian, K., Zhang, L., Zhou, K., Liu, Y., et al. (2019). A simple method for the complete performance recovery of degraded Ni-rich $LiNi_{0.70}Co_{0.15}Mn_{0.15}O_2$ cathode via surface reconstruction. *ACS Appl. Mater. Interfaces* 11, 14076–14084. doi: 10.1021/acsami.8b22529

Junhyeok, K., Hyomyung, L., Hyungyeon, C., Moonsu, Y., Minjoon, P., and Jaephil, C. (2018). Prospect and reality of Ni-rich cathode for commercialization. *Adv. Energy Mater.* 8:1702028. doi: 10.1002/aenm.201702028

Kim, J., Hong, Y. S., Ryu, K. S., Kim, M. G., and Cho, J. (2006). Washing effect of a $LiNi_{0.83}Co_{0.15}Al_{0.02}O_2$ cathode in water. *Electrochem. Solid State Lett.* 9, A19–A23. doi: 10.1149/1.2135427

Kimijima, T., Zettsu, N., Yubuta, K., Hirata, K., Kami, K., and Teshima, K. (2016). Molybdate flux growth of idiomorphic $Li(Ni_{1/3}Co_{1/3}Mn_{1/3})O_2$ single crystals and characterization of their capabilities as cathode materials for lithium-ion batteries. *J. Mater. Chem. A* 4, 7289–7296. doi: 10.1039/C6TA01593J

Kong, D., Hu, J., Chen, Z., Song, K., Li, C., Weng, M., et al. (2019). Ti-gradient doping to stabilize layered surface structure for high performance high-Ni oxide cathode of Li-ion battery. *Adv. Energy Mater.* 9:1901756. doi: 10.1002/aenm.201901756

Li, H., Li, J., Ma, X., and Dahn, J. R. (2018). Synthesis of single crystal $LiNi_{0.6}Mn_{0.2}Co_{0.2}O_2$ with enhanced electrochemical performance for lithium ion batteries. *J. Electrochem. Soc.* 165, A1038–A1045. doi: 10.1149/2.0951805jes

Liang, M., Song, D., Zhang, H., Shi, X., Wang, Q., and Zhang, L. (2017). Improved performances of $LiNi_{0.8}Co_{0.15}Al_{0.05}O_2$ material employing $NaAlO_2$ as a new aluminum source. *ACS Appl. Mater. Interfaces* 9, 38567–38574. doi: 10.1021/acsami.7b12306

Liang, M., Sun, Y., Song, D., Shi, X., Han, Y., Zhang, H., et al. (2019). Superior electrochemical performance of quasi-concentration-gradient $LiNi_{0.8}Co_{0.15}Al_{0.05}O_2$ cathode material synthesized with multi-shell precursor and new aluminum source. *Electrochim. Acta* 300, 426–436. doi: 10.1016/j.electacta.2019.01.125

Lin, F., Nordlund, D., Markus, I. M., Weng, T.-C., Xin, H. L., and Doeff, M. M. (2014). Profiling the nanoscale gradient in stoichiometric layered cathode particles for lithium-ion batteries. *Energy Environ. Sci.* 7, 3077–3085. doi: 10.1039/C4EE01400F

Liu, H. S., Zhang, Z. R., Gong, Z. L., and Yang, Y. (2004). Origin of deterioration for $LiNiO_2$ cathode material during storage in air. *Electrochem. Solid State Lett.* 7, A190–A193. doi: 10.1149/1.1738471

Liu, W., Qin, M., Xu, L., Yi, S., Deng, J., and Huang, Z. (2018). Washing effect on properties of $LiNi_{0.8}Co_{0.15}Al_{0.05}O_2$ cathode material by ethanol solvent. *Trans. Nonferrous Met. Soc. China* 28, 1626–1631. doi: 10.1016/S1003-6326(18)64805-8

Lv, D., Wang, L., Hu, P., Sun, Z., Chen, Z., Zhang, Q., et al. (2017). Li_2O-B_2O_3-Li_2SO_4 modified $LiNi_1/3Co_1/3Mn_1/3O_2$ cathode material for enhanced electrochemical performance. *Electrochim. Acta* 247, 803–811. doi: 10.1016/j.electacta.2017.07.068

Park, J. -H., Choi, B., Kang, Y.-S., Park, S. Y., Yun, D. J., Park, I., et al. (2018). Effect of residual lithium rearrangement on Ni-rich layered oxide cathodes for lithium-ion batteries. *Energy Technol.* 6, 1361–1369. doi: 10.1002/ente.201700950

Park, K. -J., Jung, H.-G., Kuo, L.-Y., Kaghazchi, P., Yoon, C. S., and Sun, Y.-K. (2018). Improved cycling stability of $Li[Ni_{0.90}Co_{0.05}Mn_{0.05}]O_2$ through microstructure modification by boron doping for Li-ion batteries. *Adv. Energy Mater.* 8:1801202. doi: 10.1002/aenm.201801202

Qiu, L., Xiang, W., Tian, W., Xu, C.-L., Li, Y.-C., Wu, Z.-G., et al. (2019). Polyanion and cation co-doping stabilized Ni-rich Ni–Co–Al material as cathode with enhanced electrochemical performance for Li-ion battery. *Nano Energy* 63:103818. doi: 10.1016/j.nanoen.2019.06.014

Su, Y., Chen, G., Chen, L., Li, W., Zhang, Q., Yang, Z., et al. (2018a). Exposing the {010} planes by oriented self-assembly with nanosheets to improve the electrochemical performances of Ni-rich Li[Ni0.8Co0.1Mn0.1]O2 microspheres. *ACS Appl. Mater. Interfaces* 10, 6407–6414. doi: 10.1021/acsami.7b18933

Su, Y., Chen, G., Chen, L., Lu, Y., Zhang, Q., Lv, Z., et al. (2019). High-rate structure-gradient Ni-rich cathode material for lithium-ion batteries. *ACS Appl. Mater. Interfaces* 11, 36697–36704. doi: 10.1021/acsami.9b12113

Su, Y., Yang, Y., Chen, L., Lu, Y., Bao, L., Chen, G., et al. (2018b). Improving the cycling stability of Ni-rich cathode materials by fabricating surface rock salt phase. *Electrochim. Acta* 292, 217–226. doi: 10.1016/j.electacta.2018.09.158

Su, Y., Zhang, Q., Chen, L., Bao, L., Lu, Y., Shi, Q., et al. (2020). Improved stability of layered and porous nickel-rich cathode materials by relieving the accumulation of inner stress. *ChemSusChem* 13, 426–433. doi: 10.1002/cssc.201902385

Wang, D., Wang, Z., Li, X., Guo, H., Xu, Y., Fan, Y., et al. (2016). Effect of surface fluorine substitution on high voltage electrochemical performances of layered $LiNi_{0.5}Co_{0.2}Mn_{0.3}O_2$ cathode materials. *Appl. Surf. Sci* 371, 172–179. doi: 10.1016/j.apsusc.2016.02.224

Weigel, T., Schipper, F., Erickson, E. M., Susai, F. A., Markovsky, B., and Aurbach, D. (2019). Structural and electrochemical aspects of $LiNi_{0.8}Co_{0.1}Mn_{0.1}O_2$ cathode materials doped by various cations. *ACS Energy Lett.* 4, 508–516. doi: 10.1021/acsenergylett.8b02302

Wu, F., Li, Q., Bao, L., Zheng, Y., Lu, Y., Su, Y., et al. (2018). Role of $LaNiO_3$ in suppressing voltage decay of layered lithium-rich cathode materials. *Electrochim. Acta* 260, 986–993. doi: 10.1016/j.electacta.2017.12.034

Wu, F., Li, Q., Chen, L., Lu, Y., Su, Y., Bao, L., et al. (2019). Use of Ce to reinforce the interface of Ni-rich $LiNi_{0.8}Co_{0.1}Mn_{0.1}O_2$ cathode materials for lithium-ion batteries under high operating voltage. *ChemSusChem* 12, 935–943. doi: 10.1002/cssc.201802304

Xie, Q., Li, W., Dolocan, A., and Manthiram, A. (2019). Insights into boron-based polyanion-tuned high-nickel cathodes for high-energy-density lithium-ion batteries. *Chem. Mat.* 31, 8886–8897. doi: 10.1021/acs.chemmater.9b02916

Xiong, X., Wang, Z., Yue, P., Guo, H., Wu, F., Wang, J., et al. (2013). Washing effects on electrochemical performance and storage characteristics of $LiNi_{0.8}Co_{0.1}Mn_{0.1}O_2$ as cathode material for lithium-ion batteries. *J. Power Sources* 222, 318–325. doi: 10.1016/j.jpowsour.2012.08.029

Xu, G. -L., Liu, Q., Lau, K. K. S., Liu, Y., Liu, X., Gao, H., et al. (2019). Building ultraconformal protective layers on both secondary and primary particles of layered lithium transition metal oxide cathodes. *Nat. Energy* 4, 484–494. doi: 10.1038/s41560-019-0387-1

Xu, S., Du, C., Xu, X., Han, G., Zuo, P., Cheng, X., et al. (2017). A mild surface washing method using protonated polyaniline for Ni-rich $LiNi_{0.8}Co_{0.1}Mn_{0.1}O_2$ material of lithium ion batteries. *Electrochim. Acta* 248, 534–540. doi: 10.1016/j.electacta.2017.07.169

Xu, S., Wang, X., Zhang, W., Xu, K., Zhou, X., Zhang, Y., et al. (2019). The effects of washing on $LiNi_{0.83}Co_{0.13}Mn_{0.04}O_2$ cathode materials. *Solid State Ionics* 334, 105–110. doi: 10.1016/j.ssi.2019.01.037

Zhang, Q., Su, Y., Chen, L., Lu, Y., Bao, L., He, T., et al. (2018). Pre-oxidizing the precursors of Nickel-rich cathode materials to regulate their Li^+/Ni^{2+} cation ordering towards cyclability improvements. *J. Power Sources* 396, 734–741. doi: 10.1016/j.jpowsour.2018.06.091

Zhang, S. S., Fan, X., and Wang, C. (2019). Enhanced electrochemical performance of Ni-rich layered cathode materials by using $LiPF_6$ as a cathode additive. *ChemElectroChem* 6, 1536–1541. doi: 10.1002/celc.201801858

Conflict of Interest: The authors declare that the research was conducted in the absence of any commercial or financial relationships that could be construed as a potential conflict of interest.

frontiers in Chemistry

MINI REVIEW
published: 28 July 2020
doi: 10.3389/fchem.2020.00592

Stabilizing Organic–Inorganic Lead Halide Perovskite Solar Cells With Efficiency Beyond 20%

*Ching Lin**

Science & Technology Policy Research and Information Center, National Applied Research Laboratories, Taipei, Taiwan

The power conversion efficiency (PCE) of organic–inorganic lead halide perovskite solar cells (PSCs) has exceeded 25%, approaching the best record of their silicon counterpart. However, lifetime issues still stand between PSCs and the goal of mass commercialization. For instance, most photoactive perovskites are hydrophilic, and moisture can quickly turn some of their constituents to compounds yielding trap states. Some perovskites are not thermally stable in the temperature window of solar cell operation and will transform into photo-inactive non-perovskites. If a perovskite is of an inadequate quality, e.g., vacancies, surface area, or grain boundaries per unit volume are high, there exist more defect sites, acting as migration pathways for perovskite ions under photo-bias, and the migration changes the perovskite's composition. An unstable perovskite/charge transport material (CTM) interface allows cross-contamination between molecules from both sides of the interface. Even without external stress, perovskite ions in an operating PSC undergo redox processes, which create defect states or initiate chemical chain reactions to accelerate PSC degradation. This mini-review discussed recent progress in solving issues, including the above, to stabilize PSCs with competitive PCE beyond 20%. The remarkable longevity of 15 PSCs under accelerated aging tests was probed in depth from three viewpoints: (1) perovskite compositions and dopants, (2) perovskite additives, and (3) CTMs. This mini-review, within which crucial perovskite-stabilizing methods were systematically analyzed, can be used as a quick-start guide when dealing with PSCs' stability in the future.

Keywords: perovskite solar cells, stability, passivation, efficiency, defects, dopants, oriented crystal growth, charge transport materials

OPEN ACCESS

Edited by:
Hongbo Li,
Beijing Institute of Technology, China

Reviewed by:
Wuqiang Wu,
Sun Yat-sen University, China
Hongjie Zhang,
Changchun University of Science and Technology, China

***Correspondence:**
Ching Lin
clin@narlabs.org.tw

Specialty section:
This article was submitted to Inorganic Chemistry, a section of the journal Frontiers in Chemistry

Received: *30 April 2020*
Accepted: *08 June 2020*
Published: *28 July 2020*

Citation:
Lin C (2020) Stabilizing Organic–Inorganic Lead Halide Perovskite Solar Cells With Efficiency Beyond 20%. Front. Chem. 8:592. doi: 10.3389/fchem.2020.00592

INTRODUCTION

The power conversion efficiency (PCE) of organic–inorganic lead halide perovskite solar cells (PSCs) has exceeded 25%, approaching 26.7% of crystalline silicon solar cells (National Renewable Energy Laboratory, 2020). However, stability issues still keep PSCs from mass commercialization. A marketable solar cell requires a warranty of 20–25 years. One is considered to match this requirement if retaining ≥90% of initial PCE after an accelerated aging test (AAT) of a 1,000-h continuous operation under 100 mW cm^{-2} AM 1.5 G illumination (denoted as 90%@1,000 h here; Grancini et al., 2017). This mini-review briefed recent efforts on stabilizing PSCs to have PCEs beyond 20% and lifetimes that prove they are qualified or nearly qualified by 90%@1,000 h tests.

Organic–inorganic lead halide perovskite is obtained by reacting halides of lead and organic ammonium with dopants. Because the chemical bonds, including ionic bonds, hydrogen bonds, and van der Waals interactions, between the constituents are relatively weak, a perovskite can decompose under moisture, thermal, or light stress. The perovskite structure may undergo irreversible hydrolyzation when exposed to moisture (Song et al., 2016), and the hydrolyzation can be accelerated by heat (Han et al., 2015). Some perovskites even transform into photo-inactive non-perovskites in the temperature window of solar cell operation without moisture exposure (Li et al., 2016). Defect sites within a perovskite act as charge recombination centers and migration pathways for perovskite ions under photo-bias; the migration changes the perovskite's composition (Gao et al., 2020b). More degradation mechanisms are discussed in the corresponding sections.

Table 1 outlines device structures, champion PCEs, and AAT results and conditions of 15 highlighted PSCs (the abbreviations and chemical structures of the materials can be found in the **Supplementary Material**). They are ranked by lifetimes and named accordingly, while the ones surviving high-temperature AATs are prioritized. Although the PCE of D0 is far below 20%, its survival under 10,000-h AAT without any PCE loss makes it worth discussing. It should be noticed that AATs in these references are not standardized for commercial uses and alter from one another. An AAT temperature of ∼60°C is close to that of a solar cell operating under the sun, whereas using a 25°C AAT may overestimate a PSC's performance. The column "lifetime" records residual percentages of the initial PCEs after the hours of AATs (for example, 95%@1,000 h represents 95% remained after 1,000-h aging). The AATs were all performed at the maximum power point (MPP tracking) except that for D10, which was exposed to continuous light under an open-circuit condition (open-circuit light-soaking). The MPP tracking ages a PSC more severely than the open-circuit light-soaking does. For example, D11 retained 92% of initial PCE after 1,500-h open-circuit light-soaking, but the PCE dropped to 91% of initial value only after 500-h MPP tracking. D0∼D14's short-circuit photocurrent (J_{SC}), open-circuit voltage (V_{OC}), and fill factors (FFs) can be found in **Supplementary Table 1**. Considering the Shockley–Queisser (SQ) limit (theoretical PCE limit; see Park and Segawa, 2018) and using FFs of well-developed solar cells as references (Green et al., 2019), there are still ∼20% for improvements in these aspects. Inefficient light harvest or incomplete carrier collection lowers a PSC's J_{SC}, whereas electrical losses, such as carrier recombination and parasitic resistance, reduce V_{OC} or FFs (Jena et al., 2019). Although many reported PSCs with PCEs less than 20% had longer lifetimes, the insufficient PCEs kept them even farther from the goal of mass commercialization. Their PSC-stabilizing mechanisms may not be as effective when applied to a PSC with higher PCE. Scaling up the PSC area can worsen the problems further. Therefore, only D0 among them was discussed here as a representative example.

As summarized from the references, a PSC can be stabilized via (1) modifying perovskite composition by dopants, (2) applying perovskite additives, or (3) adjusting charge transport materials (CTMs). These three subjects are discussed in the following. D0∼D14 are organized in **Figure 1** according

TABLE 1 | Information about the highlighted 15 PSCs.

Name	Anode/ETL/PVK/HTL/cathode	PCE (%)	Lifetime	Condition	Temp.	References
D0	FTT/$ZrO_2^{\dagger}$/$(AVA)_2PbI_4$/$MAPbI_3$/C/G	11.9	>100%@10,000 h	Air, UV filtered, encap.	55	Grancini et al., 2017
D1	FTT/(Cs,FA,MA)Pb(I,Br)$_3^{\ddagger}$/CuSCN/rGO/Au	20.4	95%@1,000 h	N_2, unencap.	60	Arora et al., 2017
D2	FTT/SN, $(FAI)_{0.9}Cs_{0.1}(PbI_2)_{1.05}$/S/A	20.9	98.1%@1,000 h	Ar, unencap.	60	Bi et al., 2018
D3	ITO/SnO_2/$FA_xMA_{1-x}Pb_{1+y}I_3^{\ddagger}$/Pb/Cl-GO/PTAA/Au	21.1	90%@1,000 h	Encap.	60	Wang Y. et al., 2019
D4	FTT/LiTFSI/$(FAPbI_3)_{0.95}(MAPbBr_3)_{0.05}$/HTAB-PVK/P3HT/Au	23.3	95%@1,370 h	RH30% air, encap.	25	Jung et al., 2019
D5	ITO/$^{S}C_{60}$/SnO_x/PCBM/$FA_{0.83}MA_{0.17}Pb_{1.1}Br_{0.50}I_{2.80}$/PDCBT/Ta-$WO_x$/Au	21.2	95%@1,000 h	N_2, unencap.	RT	Hou et al., 2017
D6	FTT/(Cs,FA,MA)$PbI_3^{\ddagger}$/$(FEAI)_2PbI_4$/S/A/MgF_2	22.2	90%@1,000 h	RH40–60% air, unencap.	RT	Liu et al., 2019
D7	ITO/SnO_2/$Rb_{0.09}Cs_{0.05}[(FA_{0.85}MA_{0.15})Pb(I_{0.85}Br_{0.15})_3]$/S/A	20.9	80%@1,000 h	Air, encap.	20	Ma et al., 2020
D8	FTT/SnO_2/$(Cs_{0.17}FA_{0.83})Pb(I_{0.82}Br_{0.15}Cl_{0.03})_3$/S/A	20.5	80%@1,000 h	Ar, unencap.	RT	Gao et al., 2020a
D9	FTT/(Cs,FA,MA)Pb(I,Br)$_3^{\ddagger}$/S/A	22.0	>100%@600 h	N_2, unencap.	25	Seo et al., 2018
D10	ITO/SnO_2/(FA,MA)Pb(I,Cl)$_3^{\ddagger}$,^{2D}ThMA/Spiro/MoO_3/Au	21.5	94%@576 h	N_2, unencap., open-circuit light-soaking	N/A	Zhou et al., 2019
D11	ITO/SnO_2/Eu, (Cs,FA,MA)Pb(I,Br,Cl)$_3^{\ddagger}$/PTAA,Spiro/Au	21.9	91%@500 h	N/A	N/A	Wang L. et al., 2019
D12	FTT/$(FAPbI_3)_{0.95}(MAPbBr_3)_{0.05}$/DM/Au	23.2	92.6%@310 h	RH25% air, encap.	25	Jeon et al., 2018
D13*	Cu/BCP/C_{60}/$Cs_{0.05}FA_{0.81}MA_{0.14}PbI_{2.55}Br_{0.45}$/PTAA/ITO	21.1	96.8%@1,200 h	RH60% air, encap.	65	Yang et al., 2019
D14*	Cu/BCP/C_{60}/$Cs_{0.05}(FA_{0.92}MA_{0.08})_{0.95}Pb(I_{0.92}Br_{0.08})_3$/PTAA/ITO	23.0	>100%@1,000 h	N_2, UV filtered, encap.	40	Zheng et al., 2020

**The only two p–i–ndevices discussed here; $^{\dagger}ZrO_2$spacer; ‡the perovskite composition detail was not specified in the reference.*

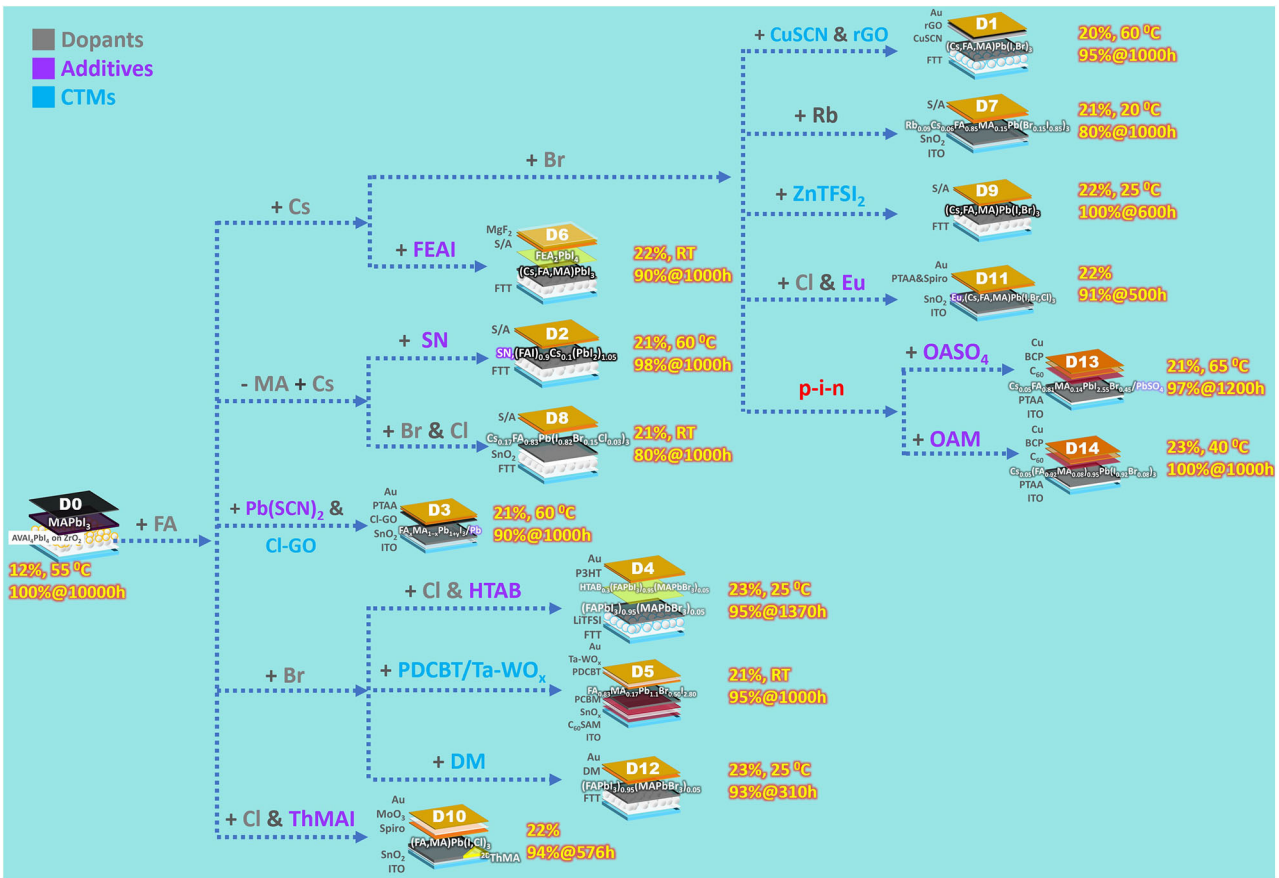

FIGURE 1 | PSC-stabilizing flowchart according to key components applied to a PSC.

to dopants, additives, or CTMs applied to a PSC. The term dopant used here is defined as perovskite impurities altering a photoactive perovskite's intrinsic properties, while additives do not influence the photoactive perovskites' chemical composition *per se*, whose functions are discussed in the corresponding section.

PEROVSKITE COMPOSITIONS AND DOPANTS

A perovskite's decomposition normally starts at the surface. If the surface area per unit volume can be reduced, even $MAPbI_3$, a perovskite considered very vulnerable, can have longevity. Grancini et al. (2017) reported a $MAPbI_3$ PSC (D0) surviving a 10,000-h, 55°C AAT with zero loss in PCE. Slowly dried onto a mesoporous TiO_2 ETM, the $MAPbI_3$ film was formed bottom-up by a thin oriented phase within the mesoporous TiO_2 and a tetragonal phase on top of it (the additive stimulating this process is discussed in the section of Perovskite Additives). The longevity of the $MAPbI_3$ PSC is probably due solely to this ordered crystal rearrangement, which lowers the surface area per unit volume. Although the PCE of D0 stayed above the initial value throughout the AAT, it kept changing in the first 4,000 h. This phenomenon can be attributed to light- or field-induced ion migration, interfacial charge accumulation, etc., which is the evidence of $MAPbI_3$'s instability.

The perovskite used in the first effective PSC was $MAPbI_3$ (Kojima et al., 2009). Since then, the approach of incorporating dopants or totally replacing MA^+ has been found to stabilize perovskites (**Figure 1**). The general formula of perovskite can be expressed as ABX_3, wherein A is a cation (e.g., organic ammonium or other dopants), B is Pb^{2+}, and X is a halogen anion. The Goldschmidt tolerance factor, determined by radii of A, B, and X, is an empirical index used to predict perovskites' structural stability (Li et al., 2016). An ideal photoactive perovskite has a cubic structure, within which BX_6^{4-} forms a sub-lattice octahedral framework, while A^+ ions occupy cube corners (Jena et al., 2019). Larger A^+ ions usually result in a higher tolerance factor. For example, photoactive cubic (α)-phase $FAPbI_3$ (effective ionic radius of FA^+ is 2.53 Å; see Hoefler et al., 2017), having a large tolerance factor, is unstable at RT, and tends to convert to a photo-inactive non-perovskite hexagonal phase. When alloying $FAPbI_3$ with small-tolerance-factor $CsPbI_3$ (effective ionic radius of Cs^+ is 1.88 Å), the cubic phase can be stabilized. Furthermore, Cs^+ has strong interaction with

the BX_6^{4-} framework, which greatly improves the photostability (Chen et al., 2019). Incorporating small and oxidation-stable rubidium cation (effective ionic radius of Rb^+ is 1.72 Å) stabilizes a perovskite in a similar manner.

On the other hand, incorporating X^- other than I^-, namely, Cl^- and Br^-, influences not merely the tolerance factor but the crystal growth, morphology, and hence the charge recombination. For example, the inclusion of MACl in perovskite precursor solution stabilizes $FAPbI_3$'s cubic phase (Kim et al., 2019). Cl^- in this perovskite film were verified to be all evaporated after the following annealing (perovskite films for PSC use are annealed to enhance crystal growth), suggesting that Cl^- from precursor solutions may not exist in every annealed perovskite film (e.g., D4, D8, D10, and D11). The effects of dopants on PSCs' stability can be observed from D7 to D8, since their device structures are simpler, compared to the others in **Table 1**, without additives or fancy CTMs. The perovskites used in D7 and D8 are $Rb_{0.09}Cs_{0.05}[(FA_{0.85}MA_{0.15})Pb(I_{0.85}Br_{0.15})_3]$ and $(Cs_{0.17}FA_{0.83})Pb(I_{0.82}Br_{0.15}Cl_{0.03})_3$, respectively. Both coupling with the unstable HTM of spiro-OMeTAD (the instability is discussed in the corresponding section), D7 and D8 nonetheless retained >80% of initial PCEs after 1,000-h AATs. In addition, $(Cs,FA)PbI_3$ is very thermally stable. The PSC with the device structure of FTT/$(FAI)_{0.9}Cs_{0.1}(PbI_2)_{1.05}$/S/A (the control compared to D2) retained 88.4% of its initial PCE after 1,000-h 60°C AATs.

PEROVSKITE ADDITIVES

The additives' summarized perovskite-stabilizing mechanisms are (i) crystallization promotion, (ii) surface passivation, and (iii) ion regeneration. A crystallization-promoting additive promotes a photoactive perovskite's crystal growth. A surface-passivating additive provokes the formation of a moisture barrier or passivates defects on a photoactive perovskite's surface. Both the crystallization-promoting and surface-passivating additives may induce a two-dimensional (2D) perovskite; these kinds of additives were defined according to the 2D perovskite's function of crystallization-promoting or surface-passivating. An ion-regenerating additive regenerates perovskite ions consumed after PSC operation. An additive may stabilize a perovskite via more than one mechanism.

Crystallization Promotion

The first example of a crystallization-promoting molecule is AVAI, a 2D perovskite layer induced by which plays a foundation layer for photoactive 3D perovskite to grow orderly. The D0 device was made by infiltrating a perovskite precursor solution including 3 vol% AVAI through carbon cathode into a ZrO_2 spacer layer on a nanoporous TiO_2 ETM. After drying at 50°C, the precursor molecules self-assembled as a 2D/3D perovskite bilayer rather than mixed 2D/3D perovskites. A thin AVA_2PbI_4 2D perovskite layer, with AVA's carboxylic acid group bonding the oxides, covered the ETM, and the 3D layer mentioned in the previous section grew on the 2D layer. The interface between the 2D and 3D perovskites oriented in a preferential growth direction of the 3D phase. Since the 2D layer substantially stayed close to the ETM, the AVAI additive contributed mainly to allow growing the stable, oriented 3D phase.

The second example is SN (see D2). An SN molecule provides three functional groups, –NH on the tetrazole moiety, thione (C=S), and ammonium. When filming a perovskite precursor solution containing SN molecules, they promote perovskite crystal growth via surface interactions, rather than incorporating into the perovskite structure. The surface interactions, including hydrogen-bonding the donor groups ($-NH_3^+$, –NH) to the perovskite surface and coordinating thione to Pb^{2+}, direct assembly pathways, suppress the formation of unwanted impurities such as PbI_2, and stabilize the grown structure of α-phase $FAPbI_3$. The D2 device retained 98.1% of initial PCE after 1,000-h 60°C AAT, within which SN molecules provided further improvement to the lifetime of already thermally stable $(FAI)_{0.9}Cs_{0.1}(PbI_2)_{1.05}$ PSCs, which retained aforementioned 88.4% of initial PCE.

The third example is ThMAI (see D10). A 2D/3D hybrid perovskite was formed by coating an organic ammonium halide solution containing ThMAI on top of a PbI_2 film with subsequent annealing. In the 2D/3D hybrid perovskite film, ThMA cations' π-stacking thiophene rings self-assembled organic sheets, which spaced the 2D and 3D perovskites. ThMAI induced perovskite crystal growth perpendicular to the PSC substrate with highly oriented, enlarged crystal grains. The unencapsulated D10 device retained 94% of initial PCE after a 576-h continuous light illumination in N_2 under open-circuit condition.

The fourth example is oleylamine (OAM; see D14). Filming a perovskite precursor solution including <0.3 mol% of OAM makes the filmed perovskite have OAMs assembled on grain surfaces. During perovskite growth, the OAM assemblies act like scaffolds restricting grains' tilt and enable the grains to grow perpendicularly to the substrate. In the meantime, OAMs are expelled to the enlarging grains' surfaces and passivate them. The oriented grains show anisotropic electronic properties, and the perovskite with OAM has lower trap-state density than that without OAM. The encapsulated D14 device survived 1,000-h 40°C AAT in N_2 without any PCE decrease.

The fifth example is HTAB (see D4). HTAB, whose crystallization-promoted object is different from those of the others discussed above, directs HTM assembly. Contrary to AVAI, inducing a 2D perovskite layer close to the bottom ETM, HTAB induces an ultrathin wide-bandgap halide (WBH) layer in the topmost part of the original perovskite. P3HT was used as the HTM in D4. The WBH layer improves the self-assembling ability of P3HT while filming a P3HT solution onto the WBH layer. The part about P3HT is elucidated in the section of Charge Transport Materials.

Surface Passivation

The aforementioned AVAI (D0), SN (D2), HTAB (D4), and ThMAI (D10) play a dual role in crystallization-promoting and surface-passivating. For D0, since the AVA_2PbI_4 2D layer stays close to the TiO_2 ETM, it may protect the photoactive 3D perovskite from TiO_2, whose photocatalytic nature is the reason why it is chosen as an ETM in the first place. For D2, SN's

ammonium group mitigates the "A" cation vacancies, and the thione group passivates coordinatively unsaturated Pb^{2+} on the crystal surface. For D4, the WBH layer improves the perovskite's resistivity to moisture by hydrophobic long carbon chains of HTA^+. For D10, the bulky organic sheets probably suppress the perovskite's ions from migration.

The fifth example of perovskite-passivating molecules is FEAI (see D6). FEAI is a phenylethylammonium iodide (PEAI; see Lee et al., 2018) having its phenyl moiety perfluorinated. They both induced the formation of a 2D perovskite phase, i.e., $(FEAI)_2PbI_4$ phase by FEAI and $(PEAI)_2PbI_4$ phase by PEAI. Since the FEAI solution was coated upon a formed 3D perovskite layer and PEAI was coated as part of a perovskite precursor solution, $(FEAI)_2PbI_4$ crystals appeared uniformly within an 8-nm range on top of the corresponding 3D perovskite layer, while $(PEAI)_2PbI_4$ existed allover grain boundaries within its corresponding one. The unencapsulated D6 device with $(FEAI)_2PbI_4$ retained 90% of initial PCE after 1,000-h room-temperature AAT at MPP in RH40∼60% air, while the encapsulated PSC with $(PEAI)_2PbI_4$, aged in a less harsh condition of open-circuit light-soaking, lost >20% of initial PCE after 500-h AAT. The $(FEAI)_2PbI_4$ and $(PEAI)_2PbI_4$ layers both protect 3D perovskites from moisture and inhibit ion migration, but the $(FEAI)_2PbI_4$ layer's better performance suggests ultra-hydrophobic fluorinated molecules' superiority. The $(FEAI)_2PbI_4$ 2D layer also mitigates charge collection losses between the incompatible hydrophilic perovskite and the hydrophobic HTM.

The sixth example is alkyl ammonium sulfate. A 3–4-nm wide-band-gap $PbSO_4$ layer capping a perovskite's surface is induced by coating dilute octylammonium sulfate ($OASO_4$ in **Figure 1**) solution onto a pristine perovskite film (see D13). A perovskite wrapped with a thicker one of this $PbSO_4$ layer is even waterproof underwater. The encapsulated D13 device had enhanced V_{OC} and FFs, was hysteresis-free, and retained 96.8% of initial PCE after 1,200-h 65°C AAT in RH60% air.

Ion Regeneration

During PSC operation, Pb^{2+} are reduced to Pb^0, acting primary deep defect states, whereas I^0 are oxidized from I^- and become carrier recombination centers. I^0 further initiate chemical chain reactions to accelerate PSC degradation. Filming a perovskite precursor solution containing europium acetylacetonate [$Eu(acac)_3$] creates Eu^{3+} ions in the filmed perovskite. When Eu^{3+} encounter Pb^0, Eu^{3+} oxidize Pb^0 and turn into Eu^{2+} themselves, which can reduce I^0. The Eu^{3+}/Eu^{2+} pairs can transfer electrons from Pb^0 to I^0 defects in a cyclic manner and regenerate Pb^{2+} and I^- during PSC operation. The device with the Eu^{3+}/Eu^{2+} pairs retained 91% of initial PCE after 500-h AAT (see D11).

CHARGE TRANSPORT MATERIALS

Organic–inorganic lead halide perovskite's photoactivity was found when adopted as a solid-state dye for dye-sensitized solar cells (DSSC). The majority of PSC researchers have stuck with solid-state DSSC's n–i–p structure (Cappel et al., 2012), i.e., using FTO/c-TiO_2/mp-TiO_2 as the bottom anode–ETM combination and spiro-OMeTAD/Au as the capping HTM–cathode combination. In such a case, in order to avoid a leakage current, the spiro-OMeTAD layer should be thick enough (>100 nm) to conformally cover the perovskite layer. The conductivity of spiro-OMeTAD is not high enough to transport injected holes through the thick HTM, and dopants, i.e., bis(trifluoromethane)sulfonamide lithium (LiTFSI), 4-*tert*-butylpyridine (tBP), and cobalt(III) complexes, are included into the HTM to facilitate the hole transport. Incorporating dopants reduces glass transition temperature (T_g) of spiro-OMeTAD to that below a solar cell's average operational temperature (∼60°C). This causes PSC constituents (e.g., perovskite ions, HTM dopants, and electrode molecules) to migrate across the perovskite/HTM interface and deteriorates the PSC. Moreover, the ionic HTM dopants' hygroscopic nature brings degradation pathways to a PSC.

Increasing doped HTM's T_g eases this problem. When using DM as HTM (D12), which has higher T_g (∼90°C) than that of spiro-OMeTAD (∼50°C) as doped, the stability was improved but not satisfying (92.1%@310 h). In another study (D9), $ZnTFSI_2$ was used to replace LiTFSI. $ZnTFSI_2$, bulkier than LiTFSI, reduces doped spiro-OMeTAD's T_g less severely. The D9 device surprisingly had zero PCE loss after AAT at 25°C (>100%@600 h for D9 and 80%@600 h for PSC with LiTFSI). However, at a more realistic operational temperature of 50°C, the D9 device lost 20% of initial PCE after 100-h AAT. Using hygroscopic-ion-free HTM dopants is a better choice in this regard. Conductive tantalum-doped tungsten oxide (Ta-WO_x), as a hygroscopic-ion-free dopant, enables the HTM of PDCBT to provide sufficient hole transport (D5). In addition, the deeper highest occupied molecular orbital (HOMO) level of PDCBT (−5.3 eV) than that of spiro-OMeTAD (−5.0 eV) inhibits reaction between the HTM and I^0 from the perovskite when photo-biased. The unencapsulated D5 device retained 95% of initial PCE after 1,000-h room-temperature AAT in N_2.

Eliminating dopants is an obvious solution if the HTM has sufficient hole mobility. P3HT's acceptable energy level and hole mobility as high as 0.1 $cm^2\ V^{-1}\ s^{-1}$ without any dopants make it a superior HTM candidate. However, the high mobility can be achieved only when P3HT molecules assemble orderly. HTA^+ ions in the aforementioned WBH layer (D4) offer n-hexyl moieties to interdigitate with P3HT molecules' n-hexyl moieties and enable them to orderly assemble fibril structures. The encapsulated D4 device retained 95% of initial PCE after 1,370-h 25°C AAT in RH30% air. Another solution is inserting a spacer between perovskite and HTM to inhibit constituent cross-contamination. Yet, a spacer interferes in hole transport. A Pb-rich layer was induced onto the perovskite film of D3 by coating $Pb(SCN)_2$ solution, ensuring stable bonding between the film and the spacer, i.e., Pb–O and Pb–Cl between the film and the spacer of chlorinated graphene oxide, and hence sufficient hole transport. Despite coupling with doped PTAA, whose T_g is lower than that of doped spiro-OMeTAD, the encapsulated D3 device retained 90% of initial PCE after 1,000-h 60°C ATT. Using an undoped, morphologically stable inorganic HTM is an even better strategy. CuSCN, a cheap p-type semiconductor,

has a work function well-aligned with the perovskites', high hole mobility, and excellent thermal stability (Zhao et al., 2015). The problem of intermixing with hydrophilic perovskites when solution-processed had kept CuSCN from being effective HTM for n–i–p PSCs. Quickly coating CuSCN solution onto a spinning perovskite film enables the formed n–i–p PSC to have a conformal CuSCN HTM. After solving the issue of CuSCN HTM's reacting with Au cathode under photo-bias by inserting a reduced graphene oxide spacer between the HTM and the cathode, the unencapsulated device (D1) retained 95% of initial PCE after 1,000-h 60°C ATT in N_2. A similar n–i–p PSC applying CuSCN/cheap carbon paste as the HTM-cathode combination (Arora et al., 2019) further had extreme longevity (95%@2,000 h), though with a slightly lower PCE of 18% than the target ≥20% of this mini-review.

So far, the PSCs discussed in this section are n–i–p PSCs. n–i–p PSCs suffer from the problems above, and their most used anode-ETM combination, i.e., FTO/c-TiO_2/mp-TiO_2, involving high-temperature processes such as spray pyrolysis, is difficult to fabricate. The easy-to-fabricate p–i–n device structure of cathode/HTM/perovskite/C_{60}/BCP/anode was proven effective for PSCs (Liu et al., 2018). The ETM of 1 nm C_{60} with 7.5 nm BCP is thick enough to protect the device from a current leak, and the HTM can be so thin (∼10 nm) that dopants are no more needed. With the perovskite additives discussed before (D13 and D14), promising stability of p–i–n PSCs was achieved.

CONCLUSION

This mini-review summarized recent progress in stabilizing PSCs with PCE beyond 20%. An ideal long-lived PSC should have stable compositions of the perovskite and CTMs under moisture, thermal, or light stress. Doping a perovskite can manipulate its tolerance factor and elevate its structural and thermal stabilities to a preliminary level (e.g., D7 and D8). A perovskite's surface has a higher defect density than that of its bulk, which makes the surface more sensitive to the stresses. The surface area can be diminished by improving the perovskite's crystallinity employing crystallization-promoting additives (e.g., D0, D2, D10, and D14). Applying a surface-passivating additive reduces the surface defect density (e.g., D0, D2, D4, D6, D10, and D13); if the surface-passivating additive induces the formation of a hydrophobic moisture barrier, the perovskite can further resist the moisture stress (e.g., D4, D6, and D13). An ion-regenerating additive can resume perovskite ions consumed after PSC operation (e.g., D11). Regarding CTM stability, HTM's moisture stability can be improved by reducing HTM's hygroscopicity (e.g., D4 and D5). The thermal stability can be enhanced by applying HTMs with higher or without T_g (e.g., D1, D4, D9, and D12). Eliminating sensitive perovskite/HTM interface (e.g., D3) or adopting a stable p–i–n structure (e.g., D13 and D14) solves both moisture and thermal problems.

Promising dopants, additives, and CTMs of D0–D14, like their predecessors, will soon be used as standard components of a PSC. For example, the easy-to-fabricate p–i–n device structure may be applied with a perovskite precursor solution including ratio-optimized dopants and a crystallization-promoting additive like SN filmed to increase the crystallinity; an $OASO_4$ solution may be coated onto the pristine perovskite film to enhance its moisture resistivity. Although the results were encouraging, to more explicitly reveal a PSC's realistic performance, future researchers are suggested to use an AAT condition with unencapsulated PSC aged under appropriate, controlled humidity and temperature. For high-efficiency PSCs surviving high-temperature AATs have been getting more common, the next challenge will be large-area PSC mass production.

AUTHOR CONTRIBUTIONS

The author confirms being the sole contributor of this work and has approved it for publication.

ACKNOWLEDGMENTS

The author was grateful for the financial support of the Ministry of Science and Technology of Taiwan.

SUPPLEMENTARY MATERIAL

The Supplementary Material for this article can be found online at: https://www.frontiersin.org/articles/10.3389/fchem.2020.00592/full#supplementary-material

REFERENCES

Arora, N., Dar, M. I., Akin, S., Uchida, R., Baumeler, T., Liu, Y., et al. (2019). Low-cost and highly efficient carbon-based perovskite solar cells exhibiting excellent long-term operational and UV stability. *Small* 15:1904746. doi: 10.1002/smll.201904746

Arora, N., Dar, M. I., Hinderhofer, A., Pellet, N., Schreiber, F., Zakeeruddin, S. M., et al. (2017). Perovskite solar cells with CuSCN hole extraction layers yield stabilized efficiencies greater than 20%. *Science* 358, 768–771. doi: 10.1126/science.aam5655

Bi, D., Li, X., Milić, J. V., Kubicki, D. J., Pellet, N., Luo, J., et al. (2018). Multifunctional molecular modulators for perovskite solar cells with over 20% efficiency and high operational stability. *Nat. Commun.* 9, 4925–4931. doi: 10.1038/s41467-018-06709-w

Cappel, U. B., Daeneke, T., and Bach, U. (2012). Oxygen-induced doping of spiro-MeOTAD in solid-state dye-sensitized solar cells and its impact on device performance. *Nano Lett.* 12, 4925–4931. doi: 10.1021/nl302509q

Chen, L., Tan, Y. Y., Chen, Z. X., Wang, T., Hu, S., Nan, Z. A., et al. (2019). Toward long-term stability: single-crystal alloys of cesium-containing mixed cation and mixed halide perovskite. *J. Am. Chem. Soc.* 141, 1665–1671. doi: 10.1021/jacs.8b11610

Gao, X. X., Luo, W., Zhang, Y., Hu, R., Zhang, B., Züttel, A., et al. (2020a). Stable and high-efficiency methylammonium-free perovskite solar cells. *Adv. Mater.* 32:1905502. doi: 10.1002/adma.201905502

Gao, Y., Wu, Y., Liu, Y., Chen, C., Bai, X., Yang, L., et al. (2020b). Dual functions of crystallization control and defect passivation enabled by an ionic compensation strategy for stable and high-efficient perovskite solar cells. *ACS Appl. Mater. Inter.* 12, 3631–3641. doi: 10.1021/acsami.9b19538

Grancini, G., Roldán-Carmona, C., Zimmermann, I., Mosconi, E., Lee, X., Martineau, D., et al. (2017). One-year stable perovskite solar cells by 2D/3D interface engineering. *Nat. Commun.* 8:15684. doi: 10.1038/ncomms15684

Green, M. A., Dunlop, E. D., Levi, D. H., Hohl-Ebinger, J., Yoshita, M., and Ho-Baillie, A. W. (2019). Solar cell efficiency tables (version 55). *Prog. Photovoltaics* 28, 3–15. doi: 10.1002/pip.3102

Han, Y., Meyer, S., Dkhissi, Y., Weber, K., Pringle, J. M., Bach, U., et al. (2015). Degradation observations of encapsulated planar $CH_3NH_3PbI_3$ perovskite solar cells at high temperatures and humidity. *J. Mater. Chem. A* 3, 8139–8147. doi: 10.1039/C5TA00358J

Hoefler, S. F., Trimmel, G., and Rath, T. (2017). Progress on lead-free metal halide perovskites for photovoltaic applications: a review. *Monatsh. Chem.* 148, 795–826. doi: 10.1007/s00706-017-1933-9

Hou, Y., Du, X., Scheiner, S., McMeekin, D. P., Wang, Z., Li, N., et al. (2017). A generic interface to reduce the efficiency-stability-cost gap of perovskite solar cells. *Science* 358, 1192–1197. doi: 10.1126/science.aao5561

Jena, A. K., Kulkarni, A., and Miyasaka, T. (2019). Halide perovskite photovoltaics: background, status, and future prospects. *Chem. Rev.* 119, 3036–3103. doi: 10.1021/acs.chemrev.8b00539

Jeon, N. J., Na, H., Jung, E. H., Yang, T. Y., Lee, Y. G., Kim, G., et al. (2018). A fluorene-terminated hole-transporting material for highly efficient and stable perovskite solar cells. *Nat. Energy* 3, 682–689. doi: 10.1038/s41560-018-0200-6

Jung, E. H., Jeon, N. J., Park, E. Y., Moon, C. S., Shin, T. J., Yang, T. Y., et al. (2019). Efficient, stable and scalable perovskite solar cells using poly(3-hexylthiophene). *Nature* 567, 511–515. doi: 10.1038/s41586-019-1036-3

Kim, M., Kim, G. H., Lee, T. K., Choi, I. W., Choi, H. W., Jo, Y., et al. (2019). Methylammonium chloride induces intermediate phase stabilization for efficient perovskite solar cells. *Joule* 3, 2179–2192. doi: 10.1016/j.joule.2019.06.014

Kojima, A., Teshima, K., Shirai, Y., and Miyasaka, T. (2009). Organometal halide perovskites as visible-light sensitizers for photovoltaic cells. *J. Am. Chem. Soc.* 131, 6050–6051. doi: 10.1021/ja809598r

Lee, J. W., Dai, Z., Han, T. H., Choi, C., Chang, S. Y., Lee, S. J., et al. (2018). 2D perovskite stabilized phase-pure formamidinium perovskite solar cells. *Nat. Commun.* 9:3021. doi: 10.1038/s41467-018-05454-4

Li, Z., Yang, M., Park, J. S., Wei, S. H., Berry, J. J., and Zhu, K. (2016). Stabilizing perovskite structures by tuning tolerance factor: formation of formamidinium and cesium lead iodide solid-state alloys. *Chem. Mater.* 28, 284–292. doi: 10.1021/acs.chemmater.5b04107

Liu, D., Wang, Q., Traverse, C. J., Yang, C., Young, M., Kuttipillai, P. S., et al. (2018). Impact of ultrathin C_{60} on perovskite photovoltaic devices. *ACS Nano* 12, 876–883. doi: 10.1021/acsnano.7b08561

Liu, Y., Akin, S., Pan, L., Uchida, R., Arora, N., Milić, J. V., et al. (2019). Ultrahydrophobic 3D/2D fluoroarene bilayer-based water-resistant perovskite solar cells with efficiencies exceeding 22%. *Sci. Adv.* 5:eaaw2543. doi: 10.1126/sciadv.aaw2543

Ma, S., Bai, Y., Wang, H., Zai, H., Wu, J., Li, L., et al. (2020). 1000 h operational lifetime perovskite solar cells by ambient melting encapsulation. *Adv. Energy. Mater.* 10:1902472. doi: 10.1002/aenm.201902472

National Renewable Energy Laboratory (2020). *Best Research-Cell Efficiency Chart*. Available online at: https://www.nrel.gov/pv/cell-efficiency.html (accessed April 6, 2020).

Park, N. G., and Segawa, H. (2018). Research direction toward theoretical efficiency in perovskite solar cells. *ACS Photonics* 5, 2970–2977. doi: 10.1021/acsphotonics.8b00124

Seo, J. Y., Kim, H. S., Akin, S., Stojanovic, M., Simon, E., Fleischer, M., et al. (2018). Novel p-dopant toward highly efficient and stable perovskite solar cells. *Energy Environ. Sci.* 11, 2985–2992. doi: 10.1039/C8EE01500G

Song, Z., Abate, A., Watthage, S. C., Liyanage, G. K., Phillips, A. B., Steiner, U., et al. (2016). Perovskite solar cell stability in humid air: partially reversible phase transitions in the PbI_2-CH_3NH_3I-H_2O system. *Adv. Energy Mater.* 6:1600846. doi: 10.1002/aenm.201600846

Wang, L., Zhou, H., Hu, J., Huang, B., Sun, M., Dong, B., et al. (2019). A Eu^{3+}-Eu^{2+} ion redox shuttle imparts operational durability to Pb-I perovskite solar cells. *Science* 363, 265–270. doi: 10.1126/science.aau5701

Wang, Y., Wu, T., Barbaud, J., Kong, W., Cui, D., Chen, H., et al. (2019). Stabilizing heterostructures of soft perovskite semiconductors. *Science* 365, 687–691. doi: 10.1126/science.aax8018

Yang, S., Chen, S., Mosconi, E., Fang, Y., Xiao, X., Wang, C., et al. (2019). Stabilizing halide perovskite surfaces for solar cell operation with wide-bandgap lead oxysalts. *Science* 365, 473–478. doi: 10.1126/science.aax3294

Zhao, K., Munir, R., Yan, B., Yang, Y., Kim, T., and Amassian, A. (2015). Solution-processed inorganic copper(I) thiocyanate (CuSCN) hole transporting layers for efficient p–i–n perovskite solar cells. *J. Mater. Chem. A* 3, 20554–20559. doi: 10.1039/C5TA04028K

Zheng, X., Hou, Y., Bao, C., Yin, J., Yuan, F., Huang, Z., et al. (2020). Managing grains and interfaces via ligand anchoring enables 22.3%-efficiency inverted perovskite solar cells. *Nat. Energy* 5, 131–140. doi: 10.1038/s41560-019-0538-4

Zhou, T., Lai, H., Liu, T., Lu, D., Wan, X., Zhang, X., et al. (2019). Highly efficient and stable solar cells based on crystalline oriented 2D/3D hybrid perovskite. *Adv. Mater.* 31:1901242. doi: 10.1002/adma.201901242

Conflict of Interest: The author declares that the research was conducted in the absence of any commercial or financial relationships that could be construed as a potential conflict of interest.

frontiers in Chemistry

ORIGINAL RESEARCH
published: 04 September 2020
doi: 10.3389/fchem.2020.00752

Luminescence in Manganese (II)-Doped $SrZn_2S_2O$ Crystals From Multiple Energy Conversion

*Ronghua Ma[1], Shaohui Mao[1], Chunfeng Wang[1], Yonghong Shao[1], Zhihao Wang[2], Yu Wang[2], Sicen Qu[3] and Dengfeng Peng[1]**

[1] Key Laboratory of Optoelectronic Devices and Systems of Ministry of Education and Guangdong Province, College of Physics and Optoelectronic Engineering, Shenzhen University, Shenzhen, China, [2] International Collaborative Laboratory of 2D Materials for Optoelectronics Science and Technology of Ministry of Education, SZU–NUS Collaborative Innovation Center for Optoelectronic Science & Technology, Institute of Microscale Optoelectronics, Shenzhen University, Shenzhen, China, [3] Department of Physical Education, Shenzhen University, Shenzhen, China

Under the excitation of ultraviolet, X-ray, and mechanical stress, intense orange luminescence (Mn^{2+}, $^4T_1 \rightarrow {}^6A_1$) can be generated in Mn^{2+}-doped $SrZn_2S_2O$ crystal in orthorhombic space group of $Pmn2_1$. Herein, the multiple energy conversion in $SrZn_2S_2O:Mn^{2+}$, that is, photoluminescence (PL), X-ray-induced luminescence, and mechanoluminescence, is investigated. Insight in luminescence mechanisms is gained by evaluating the Mn^{2+} concentration effects. Under the excitation of metal-to-ligand charge-transfer transition, the most intense PL is obtained. X-ray-induced luminescence shows similar features with PL excited by band edge UV absorption due to the same valence band to conduction band transition nature. Benefiting much from trap levels introduced by Mn^{2+} impurities, the quenching behavior mechanoluminescence is more like the directly excited PL from Mn^{2+} d-d transitions. Interestingly, this concentration preference leads to varying degrees of spectral redshift in each mode luminescence. Further, $SrZn_2S_2O:Mn^{2+}$ exhibits a good linear response to the excitation power, which makes it potential candidates for applications in X-ray radiation detection and mechanical stress sensing.

Keywords: light emission, mechanoluminescence, multimode luminescence, X-ray, $SrZn_2S_2O$

OPEN ACCESS

Edited by:
Guohua Jia,
Curtin University, Australia

Reviewed by:
Zhiguo Xia,
University of Science and Technology Beijing, China
Hai Guo,
Zhejiang Normal University, China

****Correspondence:***
Dengfeng Peng
pengdengfeng@szu.edu.cn

Specialty section:
This article was submitted to Physical Chemistry and Chemical Physics, a section of the journal Frontiers in Chemistry

Received: *29 June 2020*
Accepted: *21 July 2020*
Published: *04 September 2020*

Citation:
Ma R, Mao S, Wang C, Shao Y, Wang Z, Wang Y, Qu S and Peng D (2020) Luminescence in Manganese (II)-Doped $SrZn_2S_2O$ Crystals From Multiple Energy Conversion. Front. Chem. 8:752. doi: 10.3389/fchem.2020.00752

INTRODUCTION

Luminescent materials could somehow absorb electrical, optical, chemical, thermal, or mechanical energy and turn it into light emission through a radiative transition. In the last centuries, researchers have been working persistently on optimizing of preparation technique, exploring new materials to meet the rising demand for high-performance luminescent materials in applications such as lighting (Meyer and Tappe, 2015; Xu et al., 2016; Zak et al., 2017), display (Withnall et al., 2011; Ballato et al., 2013), sensing (Eliseeva and Bunzli, 2010; Olawale et al., 2011; Wang et al., 2013; Hu et al., 2014), optoelectronics (Li et al., 2015, 2017), and anti-counterfeiting (Zhang et al., 2018a). While pursuing its state-of-the-art materials by realizing one mode of energy transformation, one single material that could efficiently transform multiple types of energy to light emission has entered people's vision. These materials may bring to life many new appealing applications in the interdisciplinary fields (Singh et al., 2011; Liu et al., 2018; Xu et al., 2018; Zhang et al., 2018b, 2020; Jiang et al., 2019; Sang et al., 2019).

During the past decades, mechanoluminescent materials with the capability of converting mechanical energy to light emission are attracting more and more attention for their potential applications in stress sensing, anti-counterfeiting, display, structure fatigue diagnosis, and flexible optoelectronics (Chandra and Chandra, 2011; Jeong et al., 2014; Liu et al., 2019; Wang C. et al., 2019; Wang X. et al., 2019; Zuo et al., 2019; Wang et al., 2020). On the other hand, almost immediately after the discovery of X-rays, people started eagerly to find efficient X-ray phosphors or scintillators that absorb X-ray and emit light (Blasse, 1994; Büchele et al., 2015; Chen et al., 2018; Lian et al., 2020). With a strong ability to absorb X-ray photons, impurity-doped ML materials may also be good scintillators with intense X-ray-induced emission and find their application in X-ray detection. Recently, much effort has been independently made to optimize the performance of ML and X-ray phosphors. Starting from the two classic ML materials, that is, Eu^{2+}-doped $SrAl_2O_4$ and Mn^{2+}/Cu^{2+}-doped ZnS, in the early stage, many impurity-doped systems have been discovered (Peng et al., 2015; Zhang et al., 2019). Among these, some typical oxysulfides notably enriched the color of ML emission due to its good acceptance for a large number of activators (Zhang et al., 2013, 2015). It is proved that some new oxysulfide semiconductors that doped with luminescent ions, for instance, transitional metals and lanthanide ions doped CaZnOS (Huang, 2016; Huang et al., 2017; Du et al., 2019), SrZnOS (Chen et al., 2020), and BaZnOS (Li et al., 2016) single compounds as well as CaZnOS-ZnS heterojunctions (Peng et al., 2020) show novel ML performances that result in diverse applications. Meanwhile, some oxysulfides, such as Gd_2O_2S-based luminescent material (Büchele et al., 2015), has been commercialized and confirmed to be good X-ray phosphors. As oxysulfides show a strong ability to absorb high-energy X-ray photons, they may be good scintillators to meet the rising demand for radiation detection materials as well.

$SrZn_2S_2O$, as a newly discovered oxysulfide semiconductor with close-packed corrugated double layers of ZnS_3O tetrahedron in its crystal structure, was first reported by Hans-Conrad zur Loye's group (Tsujimoto et al., 2018) and found to function as a high-stable photocatalyst capable of reducing and oxidizing water (Nishioka et al., 2019). Deducing from its non-central symmetry crystal structure and appropriate band structure, impurity-doped $SrZn_2S_2O$ could have good ML performance, which was already proved recently (Chen et al., 2020). Herein, we report Mn^{2+}-doped $SrZn_2S_2O$ material could simultaneously respond to UV light or X-ray exposure or mechanical actions with intense orange emission and realize multiple-energy conversions. Besides mechanical stimulation, $SrZn_2S_2O$:Mn^{2+} can also respond to X-ray exposure with strong visible emission. The ML performance is optimized by choosing the optimal preparation condition and tuning the doping concentration. Strong relevance between ML intensity and the applied mechanical force makes $SrZn_2S_2O$:Mn^{2+} a good candidate for dynamic stress visualization. Notably, the differences in quenching behavior provide us a better understanding of the ML process. This multimode energy conversion behavior might be used in manufacturing future sensing devices.

EXPERIMENTAL

Materials Preparation

The samples were prepared by using a high-temperature solid-state reaction. To obtain x mol% Mn^{2+}-doped $SrZn_2S_2O$, that is, $SrZn_{2(1-x\%)}S_2O$:2x% Mn^{2+} (x = 0, 0.25, 0.5, 0.75, 1, 2, 3, 4, 6, and 8), high purity of ZnS (99.99%, Aladdin), $SrCO_3$ (99.9%, Aldrich), and $MnCO_3$ (>99%, Sinopharm Group Co. Ltd.) with mole ratio of 2-2x%:1:2x%, were used as starting materials. A total of 20 g of raw materials was precisely weighed and then thoroughly mixed by wet grinding in absolute ethanol. After dried in an oven at 80°C, the raw materials were calcined at 1,000°C for 4 h in Ar atmosphere (purity, 99.99%). The sintered product was grounded into fine powders for subsequent characterization.

Mechanoluminescence Film Fabrication

A "suspension deposition" method is applied to fabricate the mechanoluminescence (ML) film for ML test and exhibition. In a typical case, 0.2 g $SrZn_2S_2O$:Mn^{2+} ML powder and 0.06 g UV curing adhesive (LEAFTOP 9307) were ultrasonically dispersed in ethanol, followed by a rapid transfer into a 3 × 3-cm square frame stainless mold placed on one piece of the ethylene-vinyl acetate-covered poly(ethylene terephthalate) film in a laminating film (Deli, no. 3817). The mold was removed after the volatilization of ethanol; then, the two pieces of ethylene-vinyl acetate-covered poly(ethylene terephthalate) films were folded together very carefully. Subsequently, the film was exposed in UV light to solidify the adhesive and then packaged by going through a thermal laminator.

Characterization

X-ray diffraction (XRD) patterns were recorded by a Bruker D2 phase X-ray diffraction analyzer. Scanning electron microscope images were obtained from a 3 Hitachi SU 8020 scanning electron microscope. Energy-dispersive X-ray element maps were obtained on a HOBIRA EMAX X-ray detector. Photoluminescence (PL) spectra were measured by Hitachi F-4600 spectrophotometer equipped with an R928 photomultiplier detector. The ML emission spectra were recorded by a home-built measuring apparatus with a linear motor, digital push–pull gauge, and QE65pro fiber optic spectrometer (Ocean Optics). The X-ray-induced emission spectra were obtained by Omni-λ 300i spectrograph (Zolix) equipped with an X-ray tube (Model RACA-3, Zolix Instruments Co., Ltd., Beijing, China).

To acquire the ML spectra, we stick the ML film on a quartz glass plate firmly fixed on the table. On the front side, the digital push–pull gauge with a metal attachment is fixed on a platform connected to a linear motor. On the backside, the fiber connected with the QE65pro fiber optic spectrometer is fixed on the same platform over against the metal attachment. The push–pull gauge tunes the acting force of the metal attachment on ML film, and the programmed linear motor controls the movement of the platform. During the test, the motion of metal attachment on ML film generates light emission, whereas the fiber collects the signal synchronously.

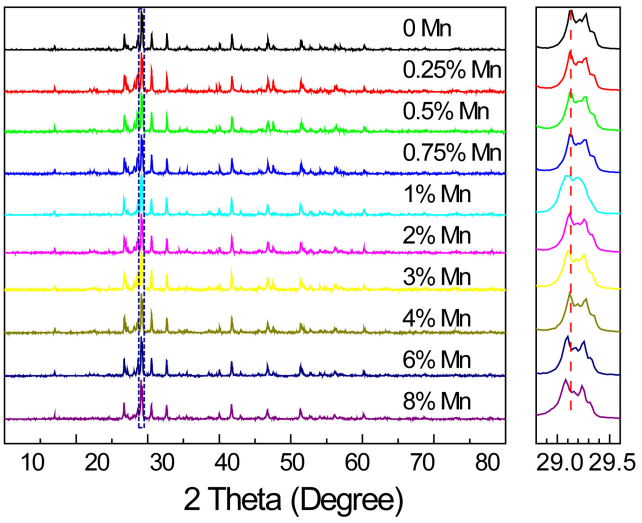

FIGURE 1 | X-ray diffraction patterns of $SrZn_{2(1-x\%)}S_2O$:2x% Mn^{2+} with a series of Mn^{2+} concentrations (x = 0, 0.25, 0.5, 0.75, 1, 2, 3, 4, 6, and 8), and an enlargement of the highest diffraction peak marked by a dotted rectangle is given in the right side.

RESULTS AND DISCUSSION

We found that 1,000°C was the most suitable temperature for the preparation of $SrZn_2S_2O$:Mn^{2+} to get a good crystallinity while avoiding any decomposition (**Supplementary Figure 1**). The experimental XRD pattern of the sample calcined at 1,000°C for 4 h matches well with the theoretical calculated powder X-ray diffraction result based on work of Hans-Conrad Tsujimoto et al. (2018), which indicates that the single phase of $SrZn_2S_2O$ in orthorhombic space group of $Pmn2_1$ (no. 31) was successfully synthesized (**Supplementary Figure 2**). In the $SrZn_2S_2O$ crystal structure, each Zn atom is coordinated with 1 O atom and 3 S atoms as ZnS_3O tetrahedron, whereas Sr^{2+} ions vertically separate close-packed corrugated double layers of ZnS_3O tetrahedron. Mn^{2+} will occupy the Zn^{2+} site due to their close radius (Mn^{2+} is slightly larger than Zn^{2+}) and similar chemical properties. As a result, the XRD peaks show a slight shift toward lower angle in $SrZn_2S_2O$:Mn^{2+} with increasing Mn^{2+}-doping concentration, and there is no second phase found even when Mn^{2+} concentration is rather high (**Figure 1**). The success in the synthesis of heavily doped $SrZn_2S_2O$:Mn^{2+} makes it easier for further performance tuning to get the desired material performances. After grinding and sifting, we got fine powder several micrometers in size with no regular shape for all the characterization and property tests. Energy-dispersive X-ray spectroscopy verifies the presence of the doped Mn element and its uniform distribution together with Zn, S, Sr, and O elements as a single phase $SrZn_2S_2O$:Mn^{2+} (**Supplementary Figure 3**).

PL properties of Mn^{2+}-doped $SrZn_2S_2O$ are investigated. Under ultraviolet excitation at 310 nm (**Figure 2A**), a broadband orange emission (~520–700 nm) centered at about 580 nm corresponding to $^4T_1 \rightarrow {}^6A_1$ transition of Mn^{2+} in $SrZn_2S_2O$ lattice. With increasing Mn^{2+}-doping amount, the emission band shows a slight redshift of about 5 nm and a slightly raising band tail at long wavelength due to reduced energy difference by an exchange interaction effect between two neighboring Mn^{2+} cations (Barthou, 1994; Vink et al., 2001). The emission intensity increases at lower Mn^{2+} concentrations, and then, a fast decrease is witnessed due to the comprehensive effects of excitation efficiency changes and concentration quenching. The corresponding excitation spectra (**Figure 2B**) comprise a broad UV band including band edge absorption of $SrZn_2S_2O$ host at ~270 nm and metal-to-ligand charge transfer ($ML_{CB}CT$) (Norberg et al., 2004; Badaeva et al., 2011) absorption of Mn^{2+} centered at ~320 nm and several smaller bands in the visible light region due to d-d transitions of Mn^{2+}. Among these, the UV band, or more precisely, the $ML_{CB}CT$ band of Mn^{2+} shows a distinct redshift. Correspondingly, three excitation routes are proposed in the luminescence mechanism depicted in **Figure 2C**. Namely, route 1 represents the excitonic transition ($SrZn_2S_2O$ VB→ CB transition), route 2 represents the charge-transfer states transition (Mn^{2+} 3d→ CB transition), and route 3 represents d-d transitions of Mn^{2+} (Mn^{2+}: $^6A_1(^6S) \rightarrow {}^4E(^4D)$, $^4T_2(^4D)$, $(^4A_1,{}^4E)(^4G)$,$^4T_2(^4G)$ or $^4T_1(^4G)$), whereas notably, each excitation routes performs inconsistently with increasing Mn^{2+}-doping concentration (**Supplementary Figure 4**). Because strong concentration quenching of the orange emission occurs when Mn^{2+} concentration is higher than 4% for Mn^{2+} direct excitation (route 3), the concentration effects of routes 1 and 2, with a much lower quenching concentration, should be dominated by the host lattice-related excitation process and the energy transfer process.

Whereas, the undoped $SrZn_2S_2O$ is white under daylight lamp lighting, with increasing Mn^{2+}-doping concentration, $SrZn_2S_2O$:Mn^{2+} gets darker and darker pink colors (**Figure 2D**) owing to the slight absorption of blue and green light by Mn^{2+} d-d transitions. Illuminated by a 254-nm UV lamp, the undoped $SrZn_2S_2O$ shows no luminescence, whereas varied orange emission is observed in these doped samples (**Figure 2E**). **Figure 2F** displays the chromaticity diagram with International Commission on Illumination (CIE) coordinate (x, y) values obtained from the PL spectra under excitation at 310 nm. All chromaticity points locate in the orange region between the yellow and red region, with increasing Mn^{2+} concentration; the CIE coordinate (x, y) varies systematically from (0.538, 0.460) to (0.559, 0.437) due to the redshift of PL. To summarize, $SrZn_2S_2O$:Mn^{2+} realizes light energy conversion, especially, UV to orange light conversion with Mn^{2+} concentration around 1%.

We also studied the potential of $SrZn_2S_2O$:Mn^{2+} in energy conversion from X-ray to visible light. When $SrZn_2S_2O$ is irradiated by X-ray, a large number of electron-hole pairs will be generated mainly via photoelectric effect when absorbing X-ray energy, and later, Mn^{2+} is excited by the energy transferred from the electron-hole pair, followed by an orange light emission process (**Figure 3A**) (Blasse, 1994; Cao et al., 2016; Teng et al., 2020; Zhang et al., 2020). Observed under X-ray irradiation (**Figure 3B**, **Supplementary Figure 4**,

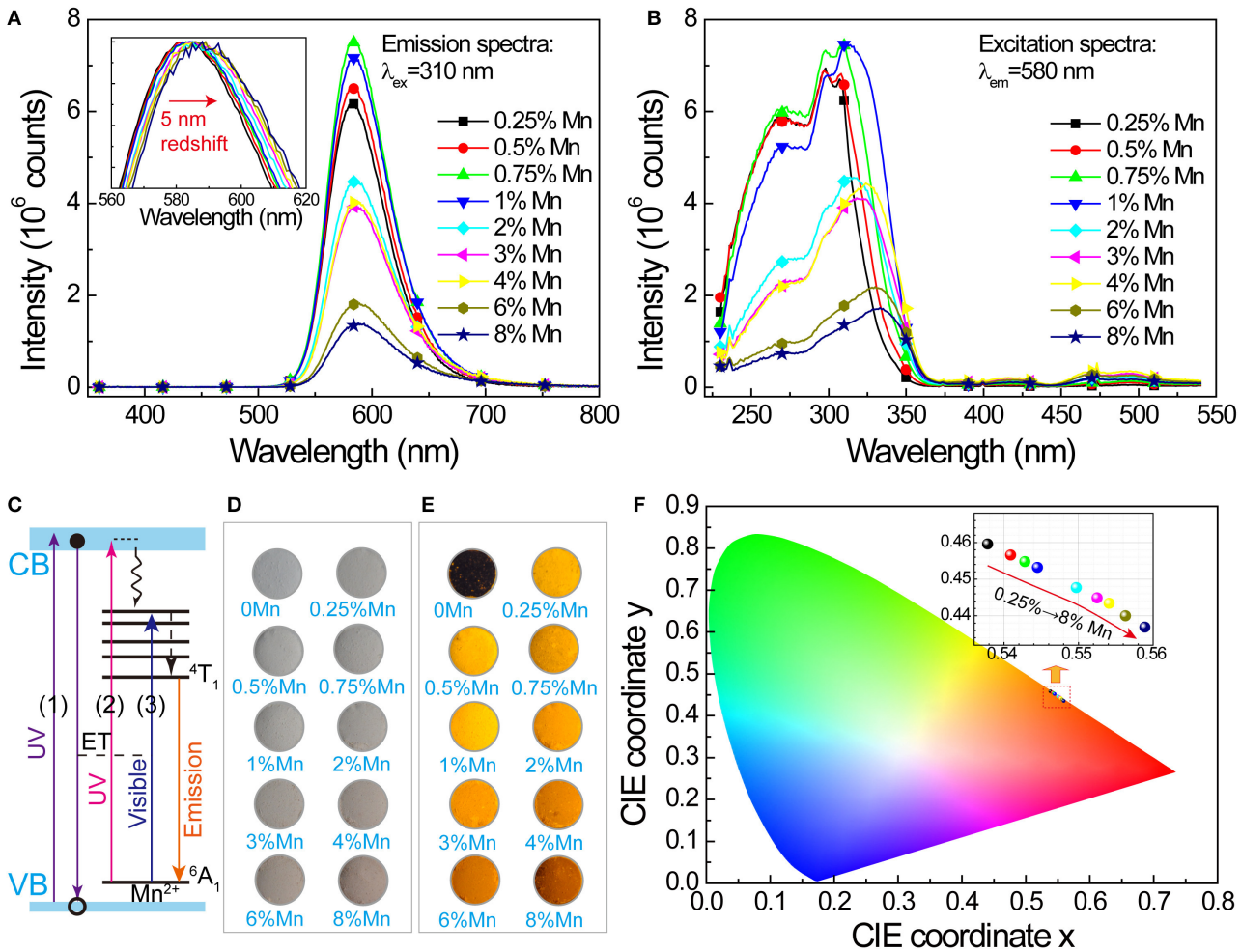

FIGURE 2 | Photoluminescence in $SrZn_{2(1-x\%)}S_2O$:2x% Mn^{2+}, with x = 0.25, 0.5, 0.75, 1, 2, 3, 4, 6, and 8. **(A)** PL spectra under 310 nm excitation. Inset shows a 5-nm redshift of the normalized PL band with increasing doping concentration. **(B)** Corresponding PLE spectra monitoring 580-nm emission. **(C)** Luminescence mechanism of $SrZn_2S_2O$:Mn expressed by energy level diagram. Optical images of the samples: **(D)** under daylight lamp lighting and **(E)** illuminated by 254-nm UV lamp. **(F)** CIE coordinate (x, y) values obtained from the PL spectra under 310-nm excitation; the inset shows the enlargement of the marked area.

and **Supplementary Video 1**), 0.25% Mn^{2+}-doped sample exhibits the most intense orange emission, and the X-ray-induced luminescence (XIL) decreases with increasing Mn^{2+} concentration. This trend is verified by the XIL spectra (**Figure 3C**) obtained under excitation of X-ray source operating at U = 50 kV and I = 40 μA, whereas a slight redshift by 3 nm of XIL band is observed. As X-ray irradiation produces electron-hole pairs, which is similar to UV band-edge excitation (PLE route 1), a similar concentration effect is predictable (**Supplementary Figure 5**). The severe concentration quenching most probably caused by band structure changes of $SrZn_2S_2O$ brought by Mn^{2+} doping through the so-called Auger de-excitation effect (White et al., 2011; Peng et al., 2012) resulting in remarkably increased non-radiative transition probability. Lightly Mn^{2+} impurity-doped is favored for $SrZn_2S_2O$:Mn^{2+} to fulfill the X-ray to visible light energy conversion. We further investigated XIL with varied X-ray source operating conditions (**Figure 4**). When the operating current is fixed at 40 μA (**Figure 4A**), the integral XIL intensity increased non-linearly with increasing operating voltage, as X-ray photon with higher energy can generate more electron-hole pairs (Scholze et al., 1996). While fixing operating voltage at 50 kV (**Figure 4B**), the integral XIL intensity is highly proportional to the operating current, which makes $SrZn_2S_2O$:Mn^{2+} material suite well for X-ray detection application.

Besides UV light and X-ray energy, the potential of $SrZn_2S_2O$:Mn^{2+} to convert mechanical energy to orange light emission was reported recently by Rong-Jun Xie's group (Chen et al., 2020). As an important aspect of this multiple-energy conversion materials, the mechanoluminscence (ML) in $SrZn_2S_2O$:Mn^{2+} was further investigated herein. We fabricated the ML films containing $SrZn_2S_2O$:Mn^{2+} ML powders for ML tests with a structure depicted in **Figure 5A** (the fabrication process and the test detail are described in the *Experimental*).

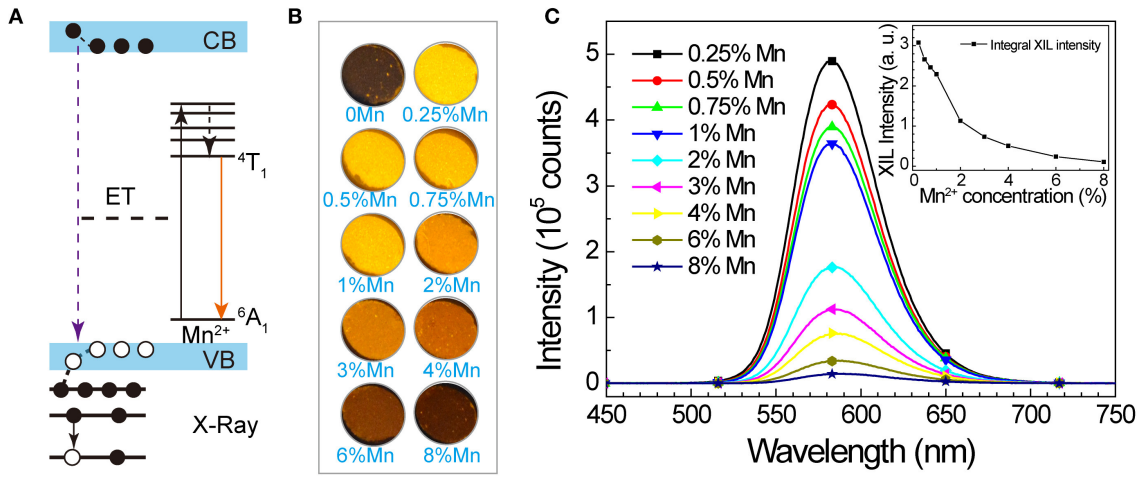

FIGURE 3 | X-ray-induced luminescence in $SrZn_{2(1-x\%)}S_2O$:2x% Mn^{2+}, with x = 0.25, 0.5, 0.75, 1, 2, 3, 4, 6, and 8. **(A)** Scheme of proposed XIL mechanism in $SrZn_2S_2O$:Mn^{2+}. **(B)** Optical images of the samples under X-ray irradiation. **(C)** X-ray-induced emission spectra under excitation of X-ray source operating at U = 50 kV and I = 40 μA. Inset shows the integral intensity in relation to Mn^{2+} concentration.

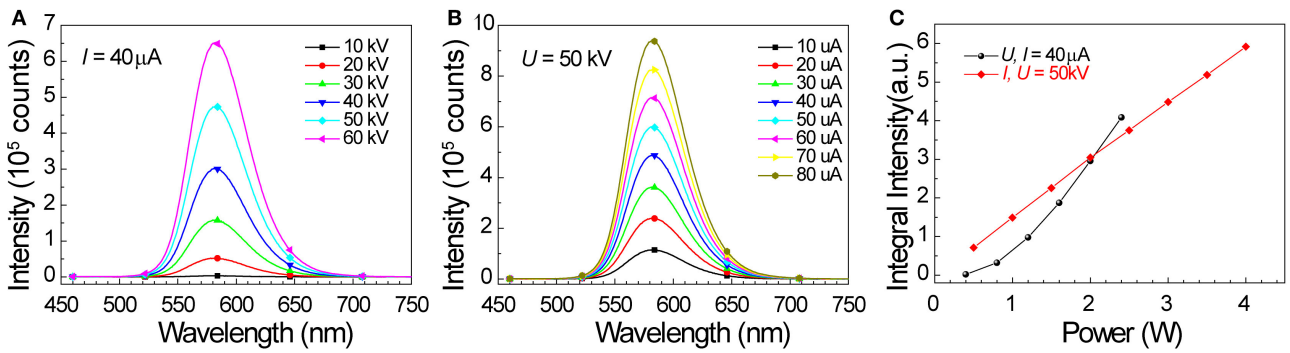

FIGURE 4 | X-ray-induced emission spectra of 0.25% Mn doped $SrZn_2S_2O$ under excitation of X-ray source operating at **(A)** I = 40 μA, U = 10, 20, 30, 40, 50, and 60 kV, and **(B)** U = 50 kV, I = 10, 20, 30, 40, 50, 60, 70, and 80 μA. **(C)** Integral XIL intensity obtained from XIL spectra in **(A,B)** in relation to operating power (P = UI).

Like ZnS:Mn^{2+} and CaZnOS:Mn^{2+} ML phosphors (Chandra et al., 2013; Tu et al., 2016), the ML of $SrZn_2S_2O$:Mn^{2+} is also reproducible with no need for extra energy supplement. Intrinsic vacancies and doped Mn^{2+} impurities bring in trap levels in the bandgap of $SrZn_2S_2O$. When mechanical strain is applied, the inner crystal piezopotential generated by a polarization of the non-central symmetry structure tilts the conduction and valence band. The trapped carriers might be released to the tilting energy band, followed by the recombination of electron-hole pairs and energy transfer to Mn^{2+}. ML is produced when the excited Mn^{2+} returns to ground state through radiative transition ($^4T_1 \rightarrow {}^6A_1$) (**Figure 5B**) (Du et al., 2019; Chen et al., 2020).

The Mn^{2+} concentration effects on ML properties were studied on homemade test equipment. **Figure 5C** shows the long exposure photos of ML when $SrZn_2S_2O$:Mn^{2+} samples were scraped with a force of 30 N (**Figure 5C**). Apparently, the ML brightness starts to decrease after increasing to a maximum when Mn^{2+} concentration is around 3%. The ML spectra were also obtained under 30 N. From the normalized ML spectra in **Figure 5D**, the redshift of the ML band moving from ∼590 nm in 0.25% Mn to ∼602 nm in 8% Mn is observed, which is larger than redshift in PL and XIL. Correspondingly, the CIE coordinate (x, y) moves from (0.557, 0.440) to (0.596, 0.401), as shown in **Figure 5F**. Noticed that severe quenching of ML happens only when the Mn^{2+}-doping concentration is higher than 3% (**Figure 5E**), which is quite different from the behavior in emissions excited by UV light and X-ray (**Supplementary Figure 5**) but very similar to emission under excitation of Mn^{2+} d-d transition (PLE route 3). ML spectra of 0 Mn-doped $SrZn_2S_2O$ were obtained under the same force of 30 N (**Supplementary Figure 6**). Pure $SrZn_2S_2O$ (0 Mn) does not exhibit any ML at all under the test conditions (<50 N). Three percent of Mn^{2+}-doped $SrZn_2S_2O$ is further investigated with changing forces (**Figure 5E**). The integral ML intensity shows a good linear relationship with the acting force at the beginning. With larger

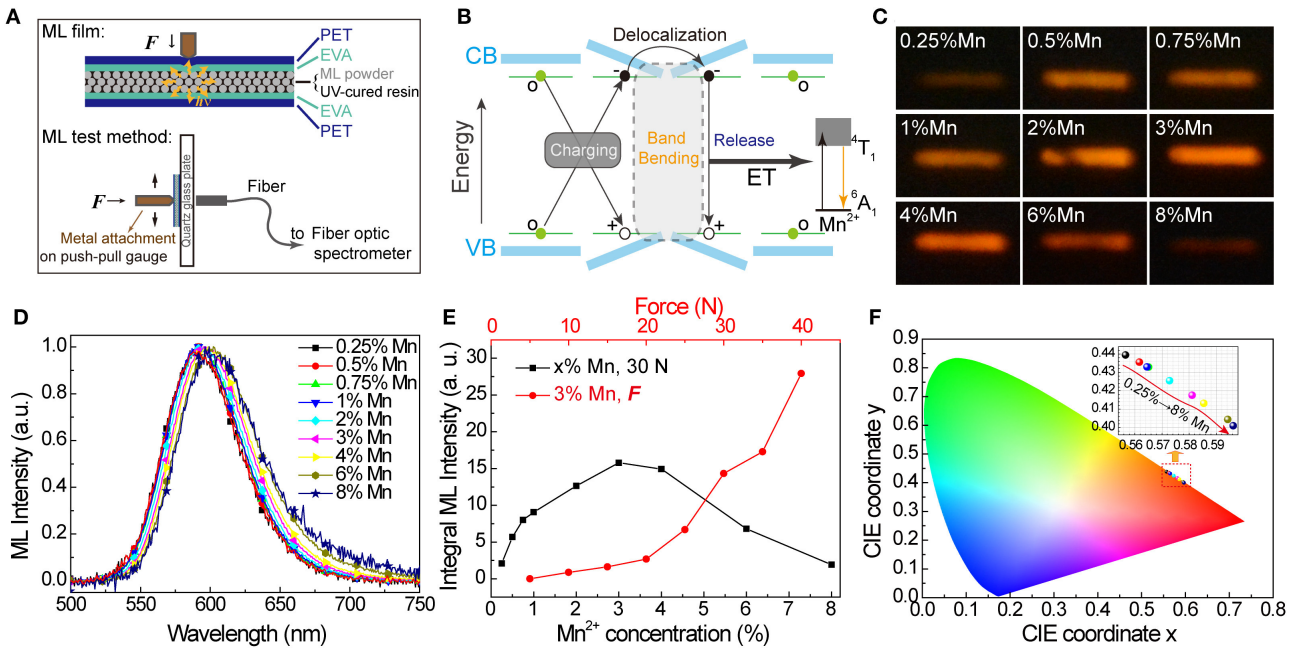

FIGURE 5 | Mechanoluminescence in $SrZn_{2(1-x\%)}S_2O$:2x% Mn^{2+}, with $x = 0.25, 0.5, 0.75, 1, 2, 3, 4, 6$, and 8. **(A)** Schematic diagram of the ML film structure and ML test method. **(B)** Scheme of proposed mechanism for mechanical-to-optical energy conversion. **(C)** Long exposure photos and **(D)** ML spectra (normalized) obtained under the same force of 30 N. **(E)** Integral ML intensity of ML spectra obtained under 30 N for all $SrZn_2S_2O$:Mn^{2+} samples and under varied forces for 3% Mn^{2+} doped $SrZn_2S_2O$. **(F)** CIE coordinate (x, y) values obtained from the ML spectra.

acting force, a bigger slope is observed due to the increased contact area resulting from the deformation of the testing ML film. This linear response to applied mechanical stress makes $SrZn_2S_2O$:Mn^{2+} a good candidate for stress sensing applications. We achieved visualization of dynamic pressure distribution during handwriting on ML film containing 3% Mn^{2+}-doped $SrZn_2S_2O$ phosphors by extracting the grayscale of the recorded long-exposure image (**Supplementary Figure 7** and **Supplementary Video 2**).

Previously, we, respectively, discussed the multiple energy conversion abilities in $SrZn_2S_2O$:Mn^{2+} to transform UV, X-ray, or mechanical energy into orange light emission. Noticeably different quenching behaviors have been observed for PL, XIL, and ML with increasing Mn^{2+}-doping concentration. XIL has the lowest quenching concentration, which has a similar trend with PL under host lattice excitation (PLE route 1). ML has the highest quenching concentration, which is more similar to PL under direct d-d excitation (PLE route 3). It is supposed that, to some extent, the ML performance of $SrZn_2S_2O$:Mn^{2+} benefits from trap levels introduced by Mn^{2+} doping, and this is quite different from the situation in CaZnOS:Mn^{2+} reported by Zhang et al. (2015). PL under metal-to-ligand charge transfer excitation (PLE route 2) has the mediate quenching concentration.

The average distance between two neighboring Mn^{2+} in $SrZn_2S_2O$ lattice decreases with increasing Mn^{2+}-doping concentration resulting in the formation of more and more Mn^{2+} pairs. Due to the exchange interaction effect, the energy difference between the ground state and the first excited state reduces when Mn^{2+} pairs are formed, leading to a redshift of emission band observed in all three energy conversion modes (Barthou, 1994; Vink et al., 2001; Zhang et al., 2015). Further, the differences in XIL, PL, and ML color with the same concentration as well as their color ranges manipulated by Mn^{2+} concentration effect (**Supplementary Figure 8**) could be explained by the preferences in Mn^{2+} doping concentration. Take the case of ML who prefers high Mn^{2+} concentration; paired Mn^{2+} will always emit a larger proportion of longer wavelength photons, which makes ML more reddish than PL and XIL. As Mn^{2+} concentration increases, more Mn^{2+} pairs will form in $SrZn_2S_2O$ lattice, and they emit an even larger proportion of longer wavelength photons leading to more redshift. The study of concentration quenching behaviors offers a better understanding of multiple energy conversion mechanisms in $SrZn_2S_2O$:Mn^{2+}.

CONCLUSION

In conclusion, we have presented Mn^{2+}-doped $SrZn_2S_2O$ crystals that display multimode energy conversion by turning X-ray, ultraviolet, and mechanical force energy into orange visible light energy via Mn^{2+} emission from $^4T_1 \rightarrow {}^6A_1$ transition. The varied excitation mode in XIL, PL, and ML

leads to performance sensitivity to doped Mn^{2+} impurities. By controlling Mn^{2+} concentration, we have obtained the most intense XIL with relatively low Mn^{2+} concentration and ML with much higher Mn^{2+} concentration, which both have a linear response to the corresponding excitation energy. The redshift of emission spectra is observed in luminescence from all three conversion modes, and the different preferences in Mn^{2+} impurities are believed to be responsible for the range of color change manipulated by Mn^{2+} doping concentration. This $SrZn_2S_2O:Mn^{2+}$ with the ability of multimode energy conversion may find its application in X-ray, UV, and mechanical stress sensing and detection and multiple energy driving light sources and displays.

DATA AVAILABILITY STATEMENT

All datasets presented in this study are included in the article/**Supplementary Material**.

AUTHOR CONTRIBUTIONS

RM and DP conceived the study, designed the experiments, and wrote the manuscript. RM, SM, CW, ZW, YW, SQ, and DP carried out the material synthesis, characterization, and measurements. RM, YS, and DP analyzed the data. All authors contributed to the article and approved the submitted version.

FUNDING

This work was supported by the National Natural Science Foundation of China (61875136), Shenzhen Fundamental Research Project (201708183000260, JCYJ20190808170601664), Guangdong Natural Science Foundation (No. 2020A1515011315), Shenzhen Peacock Plan (20171010874C), and Scientific Research Foundation as Phase II construction of high level University for the Youth Scholars of Shenzhen University (No. 000002110223).

ACKNOWLEDGMENTS

The authors would like to acknowledge Dr. Chen Xian for his help in PL tests, Mr. Jiang Fuchun for conducting the X-ray diffraction characterization, and the Electron Microscopy Center of Shenzhen University for the scanning electron microscope and energy-dispersive X-ray spectroscopy analysis.

SUPPLEMENTARY MATERIAL

The Supplementary Material for this article can be found online at: https://www.frontiersin.org/articles/10.3389/fchem.2020.00752/full#supplementary-material

Supplementary Video 1 | X-ray induced luminescence of 0.25% Mn^{2+} doped $SrZn_2S_2O$.

Supplementary Video 2 | Mechanoluminescence of the 3% Mn^{2+} doped $SrZn_2S_2O$.

REFERENCES

Badaeva, E., May, J. W., Ma, J., Gamelin, D. R., and Li, X. (2011). Characterization of excited-state magnetic exchange in Mn^{2+}-doped ZnO quantum dots using time-dependent density functional theory. *J. Phys. Chem. C* 115, 20986–20991. doi: 10.1021/jp206622e

Ballato, J., Lewis, J. S., and Holloway, P. (2013). Display applications of rare-earth-doped materials. *MRS Bull.* 24, 51–56. doi: 10.1557/S0883769400053070

Barthou, C. (1994). Mn^{2+} concentration effect on the optical properties of Zn_2SiO_4:Mn phosphors. *J. Electrochem. Soc.* 141:524. doi: 10.1149/1.2054759

Blasse, G. (1994). Scintillator materials. *Chem. Mater.* 6, 1465–1475. doi: 10.1021/cm00045a002

Büchele, P., Richter, M., Tedde, S. F., Matt, G. J., Ankah, G. N., Fischer, R., et al. (2015). X-ray imaging with scintillator-sensitized hybrid organic photodetectors. *Nat. Photonics* 9, 843–848. doi: 10.1038/nphoton.2015.216

Cao, J., Chen, W., Chen, L., Sun, X., and Guo, H. (2016). Synthesis and characterization of BaLuF5: Tb^{3+} oxyfluoride glass ceramics as nanocomposite scintillator for X-ray imaging. *Ceramics Int.* 42, 17834–17838. doi: 10.1016/j.ceramint.2016.08.114

Chandra, V. K., and Chandra, B. P. (2011). Suitable materials for elastico mechanoluminescence-based stress sensors. *Opt. Mater.* 34, 194–200. doi: 10.1016/j.optmat.2011.08.003

Chandra, V. K., Chandra, B. P., and Jha, P. (2013). Self-recovery of mechanoluminescence in ZnS:Cu and ZnS:Mn phosphors by trapping of drifting charge carriers. *Appl. Phys. Lett.* 103:161113. doi: 10.1063/1.4825360

Chen, C., Zhuang, Y., Tu, D., Wang, X., Pan, C., and Xie, R.-J. (2020). Creating visible-to-near-infrared mechanoluminescence in mixed-anion compounds $SrZn_2S_2O$ and SrZnSO. *Nano Energy* 68:104329. doi: 10.1016/j.nanoen.2019.104329

Chen, Q., Wu, J., Ou, X., Huang, B., Almutlaq, J., Zhumekenov, A. A., et al. (2018). All-inorganic perovskite nanocrystal scintillators. *Nature* 561, 88–93. doi: 10.1038/s41586-018-0451-1

Du, Y., Jiang, Y., Sun, T., Zhao, J., Huang, B., Peng, D., et al. (2019). Mechanically excited multicolor luminescence in lanthanide ions. *Adv. Mater.* 31:e1807062. doi: 10.1002/adma.201807062

Eliseeva, S. V., and Bunzli, J. C. (2010). Lanthanide luminescence for functional materials and bio-sciences. *Chem. Soc. Rev.* 39, 189–227. doi: 10.1039/B905604C

Hu, Z., Deibert, B. J., and Li, J. (2014). Luminescent metal-organic frameworks for chemical sensing and explosive detection. *Chem. Soc. Rev.* 43, 5815–5840. doi: 10.1039/C4CS00010B

Huang, B. (2016). Energy harvesting and conversion mechanisms for intrinsic upconverted mechano-persistent luminescence in CaZnOS. *Phys. Chem. Chem. Phys.* 18, 25946–25974. doi: 10.1039/C6CP04706H

Huang, B., Peng, D., and Pan, C. (2017). "Energy Relay Center" for doped mechanoluminescence materials: a case study on Cu-doped and Mn-doped CaZnOS. *Phys. Chem. Phys.* 19, 1190–1208. doi: 10.1039/C6CP07472C

Jeong, S. M., Song, S., Joo, K.-I., Kim, J., Hwang, S.-H., Jeong, J., et al. (2014). Bright, wind-driven white mechanoluminescence from zinc sulphide microparticles embedded in a polydimethylsiloxane elastomer. *Energy Environ. Sci.* 7, 3338–3346. doi: 10.1039/C4EE01776E

Jiang, T., Zhu, Y. F., Zhang, J. C., Zhu, J., Zhang, M., and Qiu, J. (2019). Multistimuli-responsive display materials to encrypt differentiated information in bright and dark fields. *Adv. Funct. Mater.* 29:1906068. doi: 10.1002/adfm.201906068

Li, L., Wong, K.-L., Li, P., and Peng, M. (2016). Mechanoluminescence properties of Mn^{2+}-doped BaZnOS phosphor. *J. Mater. Chem. C* 4, 8166–8170. doi: 10.1039/C6TC02760A

Li, X., Cao, F., Yu, D., Chen, J., Sun, Z., Shen, Y., et al. (2017). All inorganic halide perovskites nanosystem: synthesis, structural features, optical properties and optoelectronic applications. *Small* 13:1603996. doi: 10.1002/smll.201603996

Li, X., Rui, M., Song, J., Shen, Z., and Zeng, H. (2015). Carbon and graphene quantum dots for optoelectronic and energy devices: a review. *Adv. Funct. Mater.* 25, 4929–4947. doi: 10.1002/adfm.201501250

Lian, L., Zheng, M., Zhang, W., Yin, L., Du, X., Zhang, P., et al. (2020). Efficient and reabsorption-free radioluminescence in $Cs_3Cu_2I_5$ nanocrystals with self-trapped excitons. *Adv. Sci.* 7:2000195. doi: 10.1002/advs.202000195

Liu, J., Rijckaert, H., Zeng, M., Haustraete, K., Laforce, B., Vincze, L., et al. (2018). Simultaneously excited downshifting/upconversion luminescence from lanthanide-doped core/shell fluoride nanoparticles for multimode anticounterfeiting. *Adv. Funct. Mater.* 28:1707365. doi: 10.1002/adfm.201707365

Liu, L., Xu, C.-N., Yoshida, A., Tu, D., Ueno, N., and Kainuma, S. (2019). Scalable elasticoluminescent strain sensor for precise dynamic stress imaging and onsite infrastructure diagnosis. *Adv. Mater. Technol.* 4:1800336. doi: 10.1002/admt.201800336

Meyer, J., and Tappe, F. (2015). Photoluminescent materials for solid-state lighting: state of the art and future challenges. *Adv. Opt. Mater.* 3, 424–430. doi: 10.1002/adom.201400511

Nishioka, S., Kanazawa, T., Shibata, K., Tsujimoto, Y., Zur Loye, H. C., and Maeda, K. (2019). A zinc-based oxysulfide photocatalyst $SrZn_2S_2O$ capable of reducing and oxidizing water. *Dalton Trans* 48, 15778–15781. doi: 10.1039/C9DT03699G

Norberg, N. S., Kittilstved, K. R., Amonette, J. E., Kukkadapu, R. K., Schwartz, D. A., and Gamelin, D. R. (2004). Synthesis of colloidal Mn^{2+}:ZnO quantum dots and high-TC ferromagnetic nanocrystalline thin films. *J. Am. Chem. Soc.* 126, 9387–9398. doi: 10.1021/ja048427j

Olawale, D. O., Dickens, T., Sullivan, W. G., Okoli, O. I., Sobanjo, J. O., and Wang, B. (2011). Progress in triboluminescence-based smart optical sensor system. *J. Luminesci.* 131, 1407–1418. doi: 10.1016/j.jlumin.2011.03.015

Peng, B., Liang, W., White, M. A., Gamelin, D. R., and Li, X. (2012). Theoretical evaluation of spin-dependent auger de-excitation in Mn^{2+}-doped semiconductor nanocrystals. *J. Phys. Chem. C* 116, 11223–11231. doi: 10.1021/jp2118828

Peng, D., Chen, B., and Wang, F. (2015). Recent advances in doped mechanoluminescent phosphors. *ChemPlusChem* 80, 1209–1215. doi: 10.1002/cplu.201500185

Peng, D., Jiang, Y., Huang, B., Du, Y., Zhao, J., Zhang, X., et al. (2020). A ZnS/CaZnOS heterojunction for efficient mechanical-to-optical energy conversion by conduction band offset. *Adv. Mater.* 32:e1907747. doi: 10.1002/adma.201907747

Sang, J., Zhou, J., Zhang, J., Zhou, H., Li, H., Ci, Z., et al. (2019). Multilevel static-dynamic anticounterfeiting based on stimuli-responsive luminescence in a niobate structure. *ACS Appl. Mater. Interfaces* 11, 20150–20156. doi: 10.1021/acsami.9b03562

Scholze, F., Rabus, H., and Ulm, G. (1996). Measurement of the mean electron-hole pair creation energy in crystalline silicon for photons in the 50–1500 eV spectral range. *Appl. Phys. Lett.* 69, 2974–2976. doi: 10.1063/1.117748

Singh, S. K., Singh, A. K., and Rai, S. B. (2011). Efficient dual mode multicolor luminescence in a lanthanide doped hybrid nanostructure: a multifunctional material. *Nanotechnology* 22:275703. doi: 10.1088/0957-4484/22/27/275703

Teng, L., Zhang, W., Chen, W., Cao, J., Sun, X., and Guo, H. (2020). Highly efficient luminescence in bulk transparent Sr2GdF7:Tb^{3+} glass ceramic for potential X-ray detection. *Ceramics Int.* 46, 10718–10722. doi: 10.1016/j.ceramint.2020.01.079

Tsujimoto, Y., Juillerat, C. A., Zhang, W., Fujii, K., Yashima, M., Halasyamani, P. S., et al. (2018). Function of tetrahedral ZnS_3O building blocks in the formation of $SrZn_2S_2O$: a phase matchable polar oxysulfide with a large second harmonic generation response. *Chem. Mater.* 30, 6486–6493. doi: 10.1021/acs.chemmater.8b02967

Tu, D., Peng, D., Xu, C.-N., and Yoshida, A. (2016). Mechanoluminescence properties of red-emitting piezoelectric semiconductor MZnOS:Mn^{2+} (M = Ca, Ba) with layered structure. *J. Ceramic Soc. Japan* 124, 702–705. doi: 10.2109/jcersj2.15301

Vink, A. P., de Bruin, M. A., Roke, S., Peijzel, P. S., and Meijerink, A. (2001). Luminescence of exchange coupled pairs of transition metal ions. *J. Electrochem. Soc.* 148:E313. doi: 10.1149/1.1375169

Wang, C., Dong, L., Peng, D., and Pan, C. (2019). Tactile sensors for advanced intelligent systems. *Adv. Intell. Syst.* 2019:1900090. doi: 10.1002/aisy.201900090

Wang, C., Peng, D., and Pan, C. (2020). Mechanoluminescence materials for advanced artificial skin. *Sci. Bull.* 65,1147–1149. doi: 10.1016/j.scib.2020.03.034

Wang, X., Peng, D., Huang, B., Pan, C., and Wang, Z. L. (2019). Piezophotonic effect based on mechanoluminescent materials for advanced flexible optoelectronic applications. *Nano Energy* 55, 389–400. doi: 10.1016/j.nanoen.2018.11.014

Wang, X. D., Wolfbeis, O. S., and Meier, R. J. (2013). Luminescent probes and sensors for temperature. *Chem. Soc. Rev.* 42, 7834–7869. doi: 10.1039/c3cs60102a

White, M. A., Weaver, A. L., Beaulac, R., and Gamelin, D. R. (2011). Electrochemically controlled auger quenching of Mn^{2+} photoluminescence in doped semiconductor nanocrystals. *ACS Nano* 5, 4158–4168. doi: 10.1021/nn200889q

Withnall, R., Silver, J., Harris, P. G., Ireland, T. G., and Marsh, P. J. (2011). AC powder electroluminescent displays. *J. Soc. Information Display* 19:798. doi: 10.1889/JSID19.11.798

Xu, Z., Xia, Z., Lei, B., and Liu, Q. (2016). Full color control and white emission from CaZnOS:Ce^{3+},Na^{+},Mn^{2+} phosphors via energy transfer. *J. Mater. Chem. C* 4, 9711–9716. doi: 10.1039/C6TC03016E

Xu, Z., Xia, Z., and Liu, Q. (2018). Two-step synthesis and surface modification of CaZnOS:Mn^{2+} phosphors and the fabrication of a luminescent poly(dimethylsiloxane) film. *Inorg. Chem.* 57, 1670–1675. doi: 10.1021/acs.inorgchem.7b03060

Zak, P. P., Lapina, V. A., Pavich, T. A., Trofimov, A. V., Trofimova, N. N., and Tsaplev, Y. B. (2017). Luminescent materials for modern light sources. *Russian Chem. Rev.* 86, 831–844. doi: 10.1070/RCR4735

Zhang, J., Zhang, Y., Tao, J., and Zhu, Y. (2018a). Study on the light-color mixing of rare earth luminescent materials for anti-counterfeiting application. *Mater. Res. Express* 5:046201. doi: 10.1088/2053-1591/aab7da

Zhang, J.-C., Wang, X., Marriott, G., and Xu, C.-N. (2019). Trap-controlled mechanoluminescent materials. *Progress Mater. Sci.* 103, 678–742. doi: 10.1016/j.pmatsci.2019.02.001

Zhang, J.-C., Zhao, L.-Z., Long, Y.-Z., Zhang, H.-D., Sun, B., Han, W.-P., et al. (2015). Color manipulation of intense multiluminescence from CaZnOS:Mn^{2+} by Mn^{2+} concentration effect. *Chem. Mater.* 27, 7481–7489. doi: 10.1021/acs.chemmater.5b03570

Zhang, J. C., Pan, C., Zhu, Y. F., Zhao, L. Z., He, H. W., Liu, X., et al. (2018b). Achieving thermo-mechano-opto-responsive bitemporal colorful luminescence via multiplexing of dual lanthanides in piezoelectric particles and its multidimensional anticounterfeiting. *Adv. Mater.* 30:e1804644. doi: 10.1002/adma.201804644

Zhang, X., Zhao, J., Chen, B., Sun, T., Ma, R., Wang, Y., et al. (2020). Tuning multimode luminescence in Lanthanide(III) and Manganese(II) Co-Doped CaZnOS crystals. *Adv. Opt. Mater.* 8:2000274. doi: 10.1002/adom.202000274

Zhang, Z.-J., Feng, A., Chen, X.-Y., and Zhao, J.-T. (2013). Photoluminescence properties and energy levels of RE (RE = Pr, Sm, Er, Tm) in layered-CaZnOS oxysulfide. *J. Appl. Phys.* 114:213518. doi: 10.1063/1.4842815

Zuo, Y., Xu, X., Tao, X., Shi, X., Zhou, X., Gao, Z., et al. (2019). A novel information storage and visual expression device based on mechanoluminescence. *J. Mater. Chem. C* 7, 4020–4025. doi: 10.1039/C9TC00641A

Conflict of Interest: The authors declare that the research was conducted in the absence of any commercial or financial relationships that could be construed as a potential conflict of interest.

frontiers in Chemistry

CORRECTION
published: 05 January 2021
doi: 10.3389/fchem.2020.639045

Corrigendum: Luminescence in Manganese (II)-Doped $SrZn_2S_2O$ Crystals From Multiple Energy Conversion

*Ronghua Ma[1], Shaohui Mao[1], Chunfeng Wang[1], Yonghong Shao[1], Zhihao Wang[2], Yu Wang[2], Sicen Qu[3] and Dengfeng Peng[1]**

[1] Key Laboratory of Optoelectronic Devices and Systems of Ministry of Education and Guangdong Province, College of Physics and Optoelectronic Engineering, Shenzhen University, Shenzhen, China, [2] International Collaborative Laboratory of 2D Materials for Optoelectronics Science and Technology of Ministry of Education, SZU–NUS Collaborative Innovation Center for Optoelectronic Science & Technology, Institute of Microscale Optoelectronics, Shenzhen University, Shenzhen, China, [3] Department of Physical Education, Shenzhen University, Shenzhen, China

OPEN ACCESS

Approved by:
Frontiers Editorial Office,
Frontiers Media SA, Switzerland

***Correspondence:**
Dengfeng Peng
pengdengfeng@szu.edu.cn

Specialty section:
This article was submitted to Inorganic Chemistry, a section of the journal Frontiers in Chemistry

Received: 08 December 2020
Accepted: 09 December 2020
Published: 05 January 2021

Citation:
Ma R, Mao S, Wang C, Shao Y, Wang Z, Wang Y, Qu S and Peng D (2021) Corrigendum: Luminescence in Manganese (II)-Doped $SrZn_2S_2O$ Crystals From Multiple Energy Conversion. Front. Chem. 8:639045. doi: 10.3389/fchem.2020.639045

Keywords: light emission, mechanoluminescence, multimode luminescence, X-ray, $SrZn_2S_2O$

A Corrigendum on

Luminescence in Manganese (II)-Doped $SrZn_2S_2O$ Crystals From Multiple Energy Conversion
by Ma, R., Mao, S., Wang, C., Shao, Y., Wang, Z., Wang, Y., et al. (2020). Front. Chem. 8:752. doi: 10.3389/fchem.2020.00752

In the published article, there was an error in affiliation **1**. Instead of "***School of Physics and Optoelectronic Engineering, Shenzhen University, Shenzhen, China,***" it should be "***Key Laboratory of Optoelectronic Devices and Systems of Ministry of Education and Guangdong Province, College of Physics and Optoelectronic Engineering, Shenzhen University, Shenzhen, China.***"

The authors apologize for this error and state that this does not change the scientific conclusions of the article in any way. The original article has been updated.

frontiers in Chemistry

ORIGINAL RESEARCH
published: 28 October 2020
doi: 10.3389/fchem.2020.00796

The $Cs_2AgRhCl_6$ Halide Double Perovskite: A Dynamically Stable Lead-Free Transition-Metal Driven Semiconducting Material for Optoelectronics

Pradeep R. Varadwaj[1,2]* *and Helder M. Marques*[2]

[1] Department of Chemical System Engineering, School of Engineering, The University of Tokyo, Tokyo, Japan, [2] Molecular Sciences Institute, School of Chemistry, University of the Witwatersrand, Johannesburg, South Africa

OPEN ACCESS

Edited by:
Zongyou Yin,
Australian National University, Australia

Reviewed by:
Jizhong Song,
Nanjing University of Science and Technology, China
Zhiguo Xia,
University of Science and Technology Beijing, China

***Correspondence:**
Pradeep R. Varadwaj
pradeep@t.okayama-u.ac.jp;
prv.aist@gmail.com

Specialty section:
This article was submitted to Inorganic Chemistry, a section of the journal Frontiers in Chemistry

Received: *07 May 2020*
Accepted: *29 July 2020*
Published: *28 October 2020*

Citation:
Varadwaj PR and Marques HM (2020) The $Cs_2AgRhCl_6$ Halide Double Perovskite: A Dynamically Stable Lead-Free Transition-Metal Driven Semiconducting Material for Optoelectronics. Front. Chem. 8:796. doi: 10.3389/fchem.2020.00796

A-Site doping with alkali ions, and/or metal substitution at the B and B′-sites, are among the key strategies in the innovative development of $A_2BB'X_6$ halide double perovskite semiconducting materials for application in energy and device technologies. To this end, we have investigated an intriguing series of five halide-based non-toxic systems, $A_2AgRhCl_6$ (A = Li, Na, K, Rb, and Cs), using density functional theory at the SCAN-*rVV*10 level. The lattice stability and bonding properties emanating from this study of $A_2AgRhCl_6$ matched well with those that have already been synthesized, characterized and discussed [viz. Cs_2AgBiX_6 (X = Cl, Br)]. Exploration of traditional and recently proposed tolerance factors has enabled us to identify $A_2AgRhCl_6$ (A = K, Rb and Cs) as stable double perovskites. The band structure and density of states calculations suggested that the electronic transition from the top of the valence band [Cl(3p)+Rh(4d)] to the bottom of the conduction band [(Cl(3p)+Rh(4d)] is inherently direct at the X-point of the first Brillouin zone. The (non-spin polarized) bandgap of these materials was found in the range 0.57–0.65 eV with SCAN-*rVV*10, which were substantially smaller than those computed with hybrid HSE06 and PBE0, and quasi-particle GW methods. This, together with the appreciable refractive index and high absorption coefficient in the region covering the range 1.0–4.5 eV, enabled us to demonstrate that $A_2AgRhCl_6$ (A = K, Rb, and Cs) are likely candidate materials for photoelectric applications. The results of our phonon calculations at the harmonic level suggested that the $Cs_2AgRhCl_6$ is the only system that is dynamically stable (no imaginary frequencies found around the high symmetry lines of the reciprocal lattice), although the elastic moduli properties suggested all five systems examined are mechanically stable.

Keywords: $A_2AgRhCl_6$ halide double perovskites, first-principles studies, optoelectronic properties, geometrical, dynamical and mechanical stabilities, DOS and band structures

INTRODUCTION

Dynamically and Mechanically Stable Halide Double Perovskites are an important class of light harvesting materials for application in solar energy technology and optoelectronics (Greul et al., 2017; Matthews et al., 2017; Xiao et al., 2017; Zhao X.-G. et al., 2017; Chen et al., 2018; Lei et al., 2018; Li H. et al., 2018; Li T. et al., 2018; Luo et al., 2018; Tan et al., 2018; Xu et al., 2018; Chu et al., 2019; Zhao et al., 2019; Zhou Y. et al., 2019). They are characterized by the chemical formula $A_2BB'X_6$, where A is generally a monocationic organic or alkali metal species such as MA^+ (methyl ammonium), Cs^+, Rb^+; B is an alkali metal ion or a transition metal atom in its +1 oxidation state (for example, Cu^+, Ag^+, Na^+); B′ is a transition or main group metal ion in the +3 oxidation state (In^{3+}, Bi^{3+}, Sb^{3+}, Cr^{3+}); and the X sites are occupied by halide ions. Examples of widely examined halide double perovskites include $Cs_2AgSbBr_6$ (Wei et al., 2019), Cs_2AgBiX_6 (Greul et al., 2017; Chen et al., 2018; Lei et al., 2018), Cs_2CuInX_6 (Zhao X.-G. et al., 2017), and Cs_2AgInX_6 (Volonakis et al., 2017), where $A = Cs^+$, $B = Ag^+/Cu^+$, $B' = In^{3+}$, Bi^{3+}, and $X^- = Cl^-$, Br^-, I^-.

Many $A_2BB'X_6$ perovskites such as $Cs_2AgSbBr_6$ (Wei et al., 2019) and Cs_2AgBiX_6 (X = Cl, Br) (Mcclure et al., 2016) have been synthesized and their optoelectronic properties delineated. The great majority of them exhibited indirect bandgap transitions so they are not ideal for thin film photovoltaic applications (Mcclure et al., 2016; Volonakis et al., 2017; Zhao X.-G. et al., 2017; Wei et al., 2019). Many with direct bandgaps were also synthesized, but the first onset of optical absorption for several of them was beyond what might be expected from the Shockley–Queisser (S-Q) limit (Shockley and Queisser, 1961). For instance, $Cs_2InAgCl_6$ has a direct bandgap of 3.3 eV, in which the first onset of optical absorption was observed at 380 nm, with a second absorption at 585 nm (Volonakis et al., 2017); this is therefore not suitable for application in a solar cell because the S-Q limit suggests that the maximum theoretical efficiency of a solar cell can be achieved with materials that, among other properties, exhibit direct bandgaps between 1.1 and 1.4 eV (Rühle, 2016).

The search for ideal candidate materials for photovoltaics can be achieved through A, B, and B′-site doping (Yang et al., 2018) and this has already led to the discovery of many direct bandgap 2D and 3D semiconducting materials that are environmentally friendly and stable (Slavney et al., 2018; Jana et al., 2019; Yao et al., 2020; Belding et al.,). Doping assists in changing the characteristic properties of the resulting materials by modifying, *inter alia*, the lattice parameters, cell volume, lattice density and bonding environments that manipulate the bandgap and the character of the valence band maximum (VBM) and the conduction band minimum (CBM) (Zhao et al., 2018; Wang Z. et al., 2019). Examples of such doped materials include the sodium-based perovskites $Cs_2NaB'X_6$ (B′ = Sb, Bi; X = Cl, Br, I) that produced the iodide perovskites Cs_2NaSbI_6 and Cs_2NaBiI_6, with optimal bandgaps of 2.03 and 2.43 eV, respectively. Since Cs_2NaSbI_6, Cs_2NaBiI_6, and $Cs_2NaSbBr_6$ exhibited appreciable absorption coefficients in the visible range, accompanied by p-p valence to conduction band transitions, these have been suggested as materials for solar cell applications (Zhao et al., 2018). Similarly, others (Yang et al., 2018) have observed that the bandgap of $Cs_2AgIn_xBi_{1-x}Cl_6$ can be tuned from indirect (x = 0, 0.25, and 0.5) to direct (x = 0.75 and 0.9) by manipulating the percentage of doping, and that they exhibited 3 times greater absorption cross section, lower sub-bandgap trap states, and more than 5 times the photoluminescence quantum efficiency (PLQE) compared to those observed for indirect bandgap nanocrystals such as $Cs_2AgBiCl_6$. Bandgap tuning by alloying of $Cs_2AgBiCl_6$ nanocrystals resulted in a series of $Cs_2Na_xAg_{1-x}BiCl_6$ (x = 0, 0.25, 0.5, 0.75, and 1) double perovskite nanocrystals that showed an increase in optical bandgap from 3.39 eV (x = 0) to 3.82 eV (x = 1) and a 30-fold increment in weak photoluminescence (Lamba et al., 2019). Other materials generated by replacing the B′-site species in $A_2BB'X_6$ with transition metals such as Mn^{3+} (Locardi et al., 2018; Nandha and Nag, 2018; Zhou J. et al., 2019), Cr^{3+} (Zhao et al., 2019), etc., via partial or heavy doping play a significant role in the discovery of innovative halide double perovskite materials for optoelectronics (Jain et al., 2017; Bartel et al., 2019; Cai et al., 2019; Li and Yang, 2019).

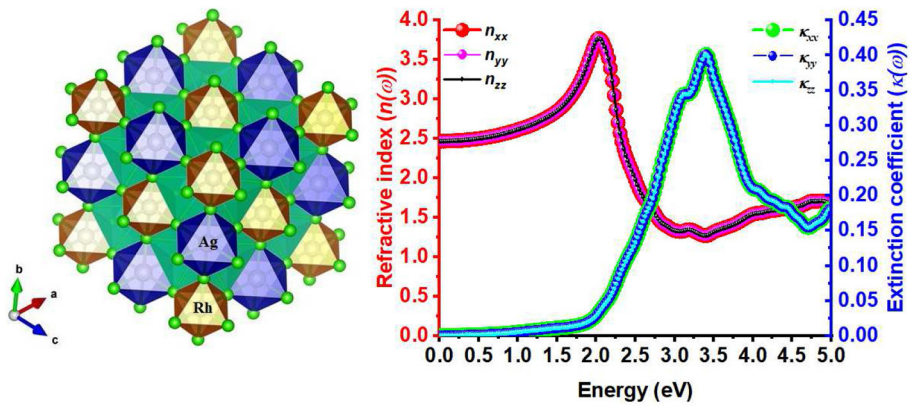

GRAPHICAL ABSTRACT | DFT modeling of the $Cs_2AgRhCl_6$ halide double perovskite (left) predicts a mechanically and dynamically stable material with reasonably high indices of refraction (right), suggesting possible application in optoelectronics.

In this study, the electronic structures of a series of five double-halide perovskites $A_2AgRhCl_6$ (A = Li, Na, K, Rb, and Cs) are theoretically investigated using density functional theory at the SCAN-*rVV*10, PBE and PBEsol levels. We analyze their structural stability by means of the widely used octahedral and Goldsmith tolerance factors. An attempt is made to explore the same property using the Global Instability Index, as well as using a newly proposed tolerance factor, to demonstrate whether the traditionally-used octahedral and Goldsmith tolerance factors are adequate for identifying stable perovskites. The lattice constants, cell volume, cell density, density of states, and electronic structure properties are examined and discussed in light of the role that the *A*-site substitution (by the lighter alkali cations) plays in modifying the properties of $Cs_2AgRhCl_6$. The optical properties are investigated by calculating linear response characteristics such as the real and imaginary parts of the dielectric function, absorption coefficient, reflectivity and energy loss spectra. The reliability of electronic bandgaps of SCAN-*rVV*10 and those calculated using other GGA methods (GGA = Generalized Gradient Approximation) is assessed by comparing them with those calculated using HSE06, PBE0 and GW methods. The phonon modes, as well as the elastic properties, are calculated using density functional perturbation theory (DFPT) and finite difference method (FD) to probe the dynamical and mechanical stabilities, and the putative suitability of these materials for photovoltaic applications.

COMPUTATIONAL DETAILS

The conventional unit-cell structures (lattice parameters, ionic positions and volumes, *etc.*) of $A_2AgRhCl_6$ (each comprises 40 atoms) were fully optimized using DFT. The same calculations were performed on their primitive unit cells (each comprises 10 atoms). The *k*-point mesh 8 × 8 × 8 centered at Γ was used for sampling the first Brillouin zone. The projector augmented wave (PAW) method (Blöchl, 1994), together with an energy cut-off of 520 eV for a plane wave basis set, was used. The equilibrium positions of the ions were calculated by structural optimization, where the internal degrees of freedom and lattice constants, along with the volume of the unit cell, were allowed to vary until the residual forces per atom were <0.006 eV/Å. The maximum and average forces acting on each ion were minimized to 0.006 and 0.004 eV/Å, respectively. Instead of a default value of 10^{-4}, the allowed error in the total energy for relaxation of the electronic degrees of freedom was set to 10^{-8} eV. Calculations involving both spin and non-spin polarizations were performed.

The three different DFT functionals employed for the relaxation of the geometry of $A_2AgRhCl_6$ were SCAN-*rVV*10 (Sun et al., 2015; Sun J. et al., 2016; Buda et al., 2017), PBE (Perdew et al., 1996) and PBEsol (Perdew et al., 2008). The reason for choosing three functionals is that we were interested in determining the extent to which the latter two functionals underestimate the bandgaps of the systems under investigation compared to SCAN-*rVV*10, since they generally underestimate the bandgap of halide single and double perovskites compared to both experiment and the computationally expensive GW and HSE06 (Volonakis et al., 2017; Lamba et al., 2019; Umadevi and Watson, 2019; Wang H.-C. et al., 2019). We note that the newly-proposed SCAN-*rVV*10 functional is one of the strongly constrained and appropriately normed meta-generalized gradient approximation (meta-GGA) functionals that is considered to model well metallic, insulating and semiconducting materials (Sun et al., 2015; Sun J. et al., 2016; Buda et al., 2017). The *rVV*10 part of the functional accounts for the non-local correlation part required to appropriately describe van der Waals (vdW) interaction (Peng et al., 2016; Chakraborty et al., 2018; Zhang et al., 2018; Anh et al., 2019). Bokdam et al. have demonstrated that the SCAN functional accounts for short range dispersion effects—which conventional hybrid functionals do not account for—and is the most suitable functional to study the atomic structure of hybrid perovskite materials (Bokdam et al., 2017). The Vienna *Ab initio* Simulation Package (VASP) was used for all calculations (Kresse and Furthmüller, 1996a,b).

The tetrahedron method with Blöchl corrections was used for the calculation of the density of states (DOS) of $A_2AgRhCl_6$. Their electronic band structures were calculated using a standard Self-Consistent (SC) procedure, followed by a subsequent non-SC calculation (VASP, 2020e). The 15 × 15 × 15 *k*-point mesh was used for sampling the Brillouin zone and the primitive cells were used. The DOS and band structures of $A_2AgRhCl_6$ were plotted using Pyband (Qijingzheng) and Sumo (Ganose et al., 2018).

The optical properties, such as the real and imaginary parts of the frequency dependent dielectric function, were computed on the SCAN-*rVV*10 geometries using the PBEsol functional (Perdew et al., 2008), a functional that has been extensively used to calculate the linear response properties of halide perovskites (Brivio et al., 2013; Frost et al., 2014; Savory et al., 2016b; Jong et al., 2018). In these calculations, the number of empty conduction band states were doubled, together with the number of frequency grid points, which was set to 2000. The Density Functional Perturbation Theory (DFPT) method was adopted (Gonze, 1997; Gonze and Lee, 1997; Baroni et al., 2001; VASP, 2020b). The Γ-centered *k*-point meshes 8 × 8 × 8, 10 × 10 × 10, and 18 × 18 × 18, blocked Davidson iteration scheme, energy cut-off of 520 eV, and a tightly converged electronic wavefunction (within 10^{-8} eV) were used.

Although the SCAN-*rVV*10 functional was used for the calculation of lattice properties, density of states, and electronic band structures, it cannot be combined with DFPT for the evaluation of linear response (optical) properties due to its lack of implementation in VASP 5.4. For this reason, and for comparison purpose with the DFPT/PBEsol results, a separate set of calculations was performed using the meta-GGA functional using a Γ-centered *k*-point mesh 12 × 12 × 12 that invoked an electronic minimization algorithm for an exact diagonalization of the matrix, in which the derivative of the cell-periodic part of the orbitals w.r.t. $\mathbf{k}$, $|\nabla_k u_{nk}\rangle$, was calculated using finite differences given by Equation (1) (VASP, 2020c),

$$| \nabla_k \bar{u}_{nk}\rangle = \sum_{n \neq n'} | \bar{u}_{n'k}\rangle \langle \bar{u}_{n'k} | \frac{\partial [H(k) - \varepsilon_{nk} S(k)}{\varepsilon_{nk} - \varepsilon_{n'k}} | \bar{u}_{nk}\rangle \qquad (1)$$

where $H(\boldsymbol{k})$ and $S(\boldsymbol{k})$ are the Hamiltonian and overlap operator for the cell-periodic part of the orbitals, and the sum over n' must include a sufficiently large number of unoccupied states.

The dynamical and mechanical stabilities of $A_2AgRhCl_6$ were examined using computed phonon band structures and elastic properties, respectively (Mouhat and Coudert, 2014; Togo and Tanaka, 2015; Kagdada et al., 2018). The former calculations were carried out using Phonopy (Togo and Tanaka, 2015). Both the DFPT/PBEsol and FD (Finite Difference) (Monserrat, 2018; VASP, 2020d) methods were used to calculate force constants in the reciprocal space. The 2 × 2 × 2 supercell structures (each 320 atoms) constructed using the conventional unit-cells of $A_2AgRhCl_6$ (A = Cs, Rb) (each 40 atoms) were supplied. The same practice was adopted to generate the supercell structures (each 80 atoms) using the primitive unit-cells of the system, and were used. Because the above calculations for systems with 320 atoms can be computationally very expensive, we used a 1 × 1 × 1 Γ-center scheme for k-point sampling integrations, together with an energy cut-off of 520 eV. For the latter supercells (80 atoms per supercell), a 4 × 4 × 4 k-mesh was used without changing other constraints.

The elastic coefficients (Mouhat and Coudert, 2014) of the stiffness matrix $\mathbf{C}_{ij}$ of $A_2AgRhCl_6$ (A = Cs, Rb, K, Li) were calculated within the harmonic approximation and finite differences to determine the second derivatives (Hessian matrix and phonon frequencies). A k-point mesh 6 × 6 × 6 was used. In all calculations referred to above, the SCAN-$rVV10$ optimized geometries of $A_2AgRhCl_6$ were used.

RESULTS AND DISCUSSION

Geometrical Properties and Stability

The spin-polarized and spin non-polarized calculations gave very similar values for the total energies of each $A_2AgRhCl_6$. The calculated energy difference of the latter from the former (*per formula unit*) is −6.6, −7.3, −6.5, −5.2, and −3.6 meV for $Cs_2AgRhCl_6$, $Rh_2AgRhCl_6$, $K_2AgRhCl_6$, $Na_2AgRhCl_6$, and $Li_2AgRhCl_6$, respectively. Hence the spin-polarized systems were relatively more stable than the non-spin polarized systems. Unless otherwise stated, we report below the results of the most stable spin-polarized systems. We also confirm that the Rh^{3+} ions in $A_2AgRhCl_6$ had no local magnetic moments. Therefore, the chemical systems with perovskite stoichiometry examined in this work, $A_2AgRhCl_6$, contain low spin Rh^{3+} and are non-magnetic.

The selected lattice properties of $A_2AgRhCl_6$ obtained with SCAN-$rVV10$ are given in **Table 1**; those calculated using PBE and PBEsol are given in **Table S1**. As expected, the lattice constants are equal, $a = b = c$, for each member of the series $A_2AgRhCl_6$. The largest value of the lattice constants found with SCAN-$rVV10$ was for $Cs_2AgRhCl_6$, 10.087 Å (**Table 1**); the decrease across the series studied correlates with the decrease in the ionic radius of the A-site cation. This is accompanied by a decrease in the metal–Cl and A–Cl bond distances and a contraction in cell volumes (**Table 2**). All the structures preserved a face-centered cubic symmetry (space group $Fm\bar{3}m$, **Figure 1**).

The PBE and PBEsol functionals predicted larger and smaller cell volumes and lattice constants compared to those of SCAN-$rVV10$, respectively (see **Table S1**). There is no experimental data available for these systems for comparison. To verify the reliability of SCAN-$rVV10$, we optimized the geometry of $Cs_2AgBiCl_6$ (and $Cs_2AgBiBr_6$) using the same theoretical method, in conjunction with the same k-point mesh and

TABLE 1 | Selected geometrical (lattice, volumetric, density, and stability) properties of $A_2AgRhCl_6$ (A = Cs, Rb, K, Na, Li) obtained with SCAN-$rVV10$.

Compound	$a = b = c$ /Å	$\alpha = \beta = \gamma$ /deg	Volume/Å^3	ρ /gcm^{-3}	*GII* /v.u.
$Cs_2AgRhCl_6$	10.087	90	1026.2	4.46	0.121
$Rb_2AgRhCl_6$	9.960	90	988.0	4.00	0.148
$K_2AgRhCl_6$	9.898	90	968.6	3.44	0.170
$Na_2AgRhCl_6$	9.305	90	805.2	3.87	0.595
$Li_2AgRhCl_6$	9.803	90	941.9	3.08	0.423

Conventional unit cells used.

TABLE 2 | Selected bond distances of $A_2AgRhCl_6$ (A = Li, Na, K, Rb, Cs).

Compound	r(Rh–Cl) /Å	r(Ag–Cl) /Å	r(A–Cl) /Å
$Cs_2AgRhCl_6$	2.374	2.669	3.569
$Rb_2AgRhCl_6$	2.359	2.622	3.524
$K_2AgRhCl_6$	2.349	2.598	3.500
$Na_2AgRhCl_6$	2.252	2.400	3.290
$Li_2AgRhCl_6$	2.335	2.567	3.468

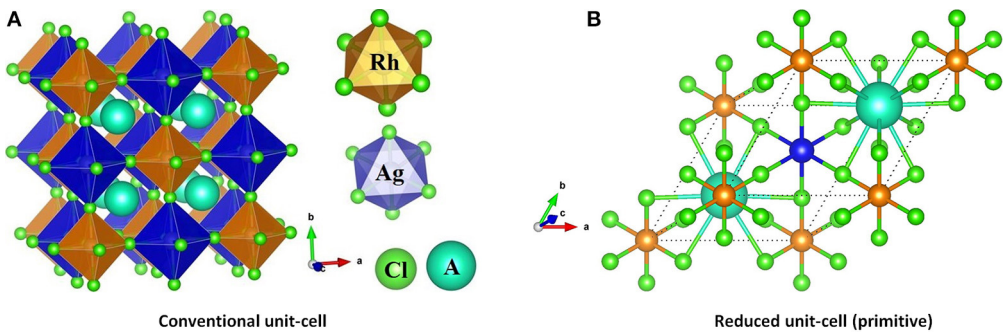

FIGURE 1 | (A) SCAN-$rVV10$ relaxed polyhedral model of the conventional unit-cell of $A_2AgRhCl_6$, showing the coordination between the alkali metal anion and the halide anions. **(B)** The (reduced) primitive cell contains one unit of each of $RhCl_6$ and $AgCl_6$ octahedra in a face-centered cubic structure (space group $Fm\bar{3}m$).

convergence criteria used for $A_2AgRhCl_6$ as detailed above. Our calculations gave a value of 10.667 Å (and 11.234 Å) for a (= $b = c$) for these two systems, which is in good agreement with the experimental value of 10.77687 Å (and 11.27123 Å) (Mcclure et al., 2016). The predicted (and experimental) cell volumes for $Cs_2AgBiCl_6$ and $Cs_2AgBiBr_6$ were 1210.33 Å^3 (1251.6356 Å^3) and 1417.87 Å^3 (1431.904 Å^3), respectively. We note that there is variability in the reported experimental cell volumes and lattice constants of these halide double perovskites, possibly due to variability in sample preparation and the experimental procedures adopted. For instance, Slavney et al. have reported experimental a and V values of 11.2499 and 1423.7901 Å^3 for $Cs_2AgBiBr_6$ (Slavney et al., 2016), somewhat different to those reported by others (Mcclure et al., 2016; Zhou et al., 2017); the values we obtained were similar to those reported by Mcclure et al. (2016). This demonstrates that the predictability SCAN-*rVV*10 is better than that of PBE and PBEsol, and that this method is useful for the prediction of 3D crystal structures of related compounds.

Whether compounds of the type ABO_3 (Li et al., 2004; Liu et al., 2008), ABX_3 and $ABB'X_6$ (Bartel et al., 2019) have a perovskite structure has often been judged based on the values of the octahedral factor μ and Goldschmidt tolerance factor, t, given by Equation (2):

$$\mu = (r_B/r_X); \quad t = {}^{r_A+r_X}\!/_{\sqrt{2}(r_B+r_X)} \tag{2}$$

For ABX_3 and $ABB'X_6$ perovskite crystals, $0.813 < t < 1.107$ and $0.415 < \mu < 0.895$. Structures with μ and t values outside these ranges (as generally found for non-perovskites) cannot be regarded as stable perovskites, and those close to 1.0 are cubic. We used Shannon's radii (Shannon, 1976) for the ions in $A_2AgRhCl_6$ and for calculated μ and t (**Table 3**). The value of $\mu = 0.50$ for $A_2AgRhCl_6$ is constant because $r_{X=Cl}$ and r_B [B=(r_{Ag}+r_{Rh})/2] are the same for all five members of the series. This, and the values calculated for t, suggest that the first four members of the series form stable perovskite structures. $Cs_2AgRhCl_6$ was recently recognized to form a double perovskite structure ($\mu = 0.50$ and $t = 0.96$) (Bartel et al., 2019); we found that three other members of the series studied ($Rb_2AgRhCl_6$, $K_2AgRhCl_6$ and $Na_2AgRhCl_6$) may also form stable perovskite structures. However, with $t = 0.71$, $Li_2AgRhCl_6$ is unlikely to have a perovskite structure. Such a low t value is generally observed for significantly distored perovskites (viz. orthorhombic).

Other approaches, such as energy phase diagrams (Filip et al., 2018) and the global instability index (*GII*) (Salinas-Sanchez et al., 1992; Yamada et al., 2018) have been used for examining the feasibility of a compound adopting a perovskite structure. We have also used *GII* to shed more light on the probable stability of $A_2AgRhCl_6$ as perovskites, as *GII* is a measure of geometrical stability.

GII = 0.0 valence units (v.u.) for geometrically stable perovskite structures without steric distortions, and for empirically unstable structures, GII > 0.2 v.u. (Yamada et al., 2018). By definition, *GII* is the root mean square of the bond discrepancy index in the unit cell given by Equation (3),

$$GII = \sqrt{\sum_{i=1}^{N} d_i^2/N} \tag{3}$$

where N is the number of ions, and d is the bond discrepancy factor. The latter is defined as the deviation of the bond valence sum (*BVS*) from the formal valence (Salinas-Sanchez et al., 1992; Yamada et al., 2018) which can be calculated using the sum of bond valences (s_{ij}) around any specific ion. It is given by: $BVS = \sum_{i=1}^{n} s_{ij}$, where $s_{ij} = \exp\left((l_0 - l_{ij})/b\right)$, l_{ij} is a bond length, l_0 is the bond valence parameter empirically determined using experimental room-temperature structural data, and b is the bond softness parameter. A detail of how this was done has been discussed in a number of previous studies (Brese and O'keeffe, 1991; Gagné and Hawthorne, 2015; Brown, 2017).

The *GII* values for $A_2AgRhCl_6$ (A = Cs, Rb, K, Na, Li) are given in **Table 1**. They are within the narrow range 0.12 v.u. < *GII* < 0.18 v.u. for A = Cs, Rb and K, but *GII* = 0.595 v.u. for A = Na and 0.423 v.u. for A = Li. This indicates that the first three are expected to form crystallographically stable perovskite structures, whereas the latter two are not. For comparison, $SrTiO_3$, $CaTiO_3$, $NaTaO_3$, $LaAlO_3$, and $BaZrO_3$, were reported to have *GII* values of 0.006, 0.273, 0.102, 0.027, and 0.003 v.u., respectively, and crystallized into cubic perovskite structures under ambient conditions (Yamada et al., 2018).

There is no mutual agreement on whether $A_2AgRhCl_6$ will form a stable perovskite when using *GII* or the μ and t combination. This is unsurprising since t is not always a good predictor as it gives a high false-positive rate (51%) in the region of t where a perovskite is expected ($0.825 < t < 1.059$). Bartel et al. have tested a set of 576 ABX_3 species and have found that t correctly predicted 94% of the known perovskites, but also 49% of the non-perovskites (Bartel et al., 2019). Because of this relatively poor predictability, these workers have proposed a new tolerance factor, τ, defined by Equation (4),

$$\tau = r_X/r_B - n_A\left(n_A - (r_A/r_B)/\ln(r_A/r_B)\right) \tag{4}$$

TABLE 3 | Shannon's ionic radii (r) of ions, octahedral factor (μ), Goldschmidt tolerance factor (t), and new tolerance factor (τ) for $A_2AgRhCl_6$ (A = Cs, Rb, K, Na, Li).

Compound	r_A/Å	r[Ag^+] /Å	r[Rh^{3+}] /Å	r_B = [[r(Ag^+)+r(Rh^{3+})]/2] /Å	Cl^-/Å	$\mu = r_B/r_X$	t	τ
$Cs_2AgRhCl_6$	1.88	1.15	0.67	0.91	1.81	0.50	0.96	3.84
$Rb_2AgRhCl_6$	1.72	1.15	0.67	0.91	1.81	0.50	0.92	3.96
$K_2AgRhCl_6$	1.64	1.15	0.67	0.91	1.81	0.50	0.90	4.05
$Na_2AgRhCl_6$	1.39	1.15	0.67	0.91	1.81	0.50	0.83	4.59
$Li_2AgRhCl_6$	0.92	1.15	0.67	0.91	1.81	0.50	0.71	75.10

where n_A is the oxidation state of A, r_i is the ionic radius of ion i, and $r_A > r_B$ by definition. Although the second term of τ is different to t, the first term incorporates the octahedral term μ that manifests itself in the probability maps, particularly in the lower bound on r_B where perovskites are expected as r_X is varied. As r_X increases, r_B must similarly increase to enable the formation of stable BX_6 octahedra. In particular, τ was shown to generalize outside the training set of 1034 experimentally observed single and double perovskites (91% accuracy) and was applied to identify 23,314 new double perovskites ($A_2BB'X_6$) ranked by their probability of being stable as perovskites based on the ranges of τ ($\tau < 4.18$) that defines the decision boundary between a perovskite and a non-perovskite. Our results for τ are listed in **Table 3**; they indicate that $A_2AgRhCl_6$ (A = Cs, Rb, K) are stable perovskites ($3.84 < \tau < 4.05$), but $Na_2AgRhCl_6$ ($\tau < 4.59$) is only partially stable while $Li_2AgRhCl_6$ ($\tau < 75.10$) is significantly unstable as a perovskite, and can be predicted to have a non-perovskite structure. These conclusions are in good agreement with the inferences drawn using *GII*.

It is worth mentioning that the coordination environment of Li^+ in $Li_2AgRhCl_6$ is not remarkably different from that of the other A-site ions in the series $A_2AgRhCl_6$. The results of our calculations show that the alkali cations lie near the center of each cube in **Figure 1** where they are involved in a dodecahedral arrangement with the coordinating Cl^- ions of $A_2AgRhCl_6$. This is evident in the data in **Table 3**; the Li–Cl bond distances are marginally smaller than those of the A–Cl (A = Cs, Rb, K) bond distances. The discrepancy in the trend in these distances between $Li_2AgRhCl_6$, $Na_2AgRhCl_6$ and $K_2AgRhCl_6$ is an artifact of the PAW potential in which the 3s and 2p semi-core states of Na were treated as valence states; consequently, the lattice constants and volume of $Na_2AgRhCl_6$ are predicted to be smaller than those of $Li_2AgRhCl_6$ (**Table 1**). It should also be noted that the indices μ, t, and τ were calculated using the ionic radii proposed by Shannon (1976), where the ionic radius of Li^+ is for an 8-coordinate ion, whereas the ionic radii for the other ions are in a dodecahedral environment. This probably accounts for the very large τ value of 75.10 calculated for $Li_2AgRhCl_6$.

Bandgap, Band Dispersion and Density of States Analyses

$Cs_2AgRhCl_6$ is a direct bandgap material, as are the other members of the series. The bandgap (E_g) of $Cs_2AgRhCl_6$ with SCAN-*rVV*10 is 0.57 eV, indicating the possibility of electronic transition between the VBM and CBM. The A-site substitution in $A_2AgRhCl_6$ by lighter alkali atoms has a very small effect on the magnitude of E_g, and were found to vary between 0.57 and 0.65 (**Table 4** and **Table S3**). On the other hand, the PBEsol and PBE functionals gave E_g of 0.42 and 0.55 eV for $Cs_2AgRhCl_6$ (**Table S1**), respectively. This shows how these two functionals slightly underestimate E_g compared to the SCAN-*rVV*10 functional, while retaining the direct nature of the bandgap transition between the VBM and CBM.

From the plot of the density states (DOS) and electronic band structure of $Cs_2AgRhCl_6$ (**Figures 2A,B**, respectively), it was found that the VBM is of Cl(3p)–Rh (4d) character. In particular, the non-bonding orbital states t_{2g} (d_{xy}, d_{yz}, d_{xz}) of Rh and the 3p orbital states of Cl cause the dispersion of the valence band just below the Fermi level. The calculated normalized contribution of Rh(4d) and Cl(3p) to the VBM are 68.4 and 28.5%, respectively. The contribution of the alkali and Ag atoms to the VBM of $Cs_2AgRhCl_6$ are negligibly small (1–2%).

By contrast, the edge associated with the CBM is largely derived from the Rh(4d) empty anti-bonding states e_g (d_z2, $d_x2_{-y}2$), but the entire band is formed using contributions from Ag, Rh and Cl states leading to its dispersion far above the Fermi level. For example, the normalized contribution of Rh(4d), Cl(3p), and Ag(5s) to the CBM of $Cs_2AgRhCl_6$ were 61.6, 23.3, and 6.3%, respectively. These vary marginally upon the replacement of the A-site cation by lighter elements of the alkali group. For instance, the contribution of Rh(4d), Cl(3p), and Ag(5s) to the CBM of $Rb_2AgRhCl_6$ was 61.0, 23.5, and 6.0%, respectively, whereas those of $Rb_2AgRhCl_6$ were 60.8, 23.6, and 6.0%, respectively. Since the CBM is far away, and at the same time, the VBM is just below the fermi level, one might conclude that $A_2AgRhCl_6$ are p-type conducting materials (Wang H.-C. et al., 2019). The spin-polarized DOS and band structures of the first three members of the series are shown in **Figures S1–S3**, revealing that spin-polarization does not have any marked impact on the orbital character of CBM and VBM.

We note that the qualitative nature of orbital character responsible for the HOMO and LUMO bands do not change when the conventional cells of the corresponding systems were used for the same analysis. This suggests that the 4d orbitals of Rh^{3+} do indeed play a predominant role in driving the HOMO and LUMO bands of the studied systems (**Figure S4A**). However, the nature of the dispersion associated with the valence and conduction bands is significantly affected (**Figure S4B**). As can be seen, the band structure resembles the presence of parabolic double bands along the line $L \rightarrow \Gamma \rightarrow W \rightarrow X$ evaluated using the same band labels defined for the $Fm\bar{3}m$ point group for a conventional cell (Bilbao Crystallographic Server). The bands are symmetric with respect to the mid-point of the Γ-X path, and are significantly flatter along Γ-X-W path that are associated with the valence band. These are clearly the effects of the double cell which can be thought as a supercell of the cubic halide perovskite. The flat bands indicate that there is no direct interaction between halide atoms along those directions, and the empty band dispersion shows that there is little interaction between Rh and the other atoms. It is therefore expected that the mobility of electrons associated with the conduction band edge should be faster than those of the holes at the valence band edge. Although this is reflected on the effective masses of the charge carriers discussed in the following section, it should be noted that the high-symmetry k-point paths are all defined for the primitive cell, but not for conventional cells. This explains why the origin of the bandgap transition is shifted from the X-point (**Figure 2**) to the center of the Brillioun zone Γ-point (**Figure S4B**). Accordingly, the band structure shown in **Figure S4A** could be misleading; band unfolding is likely to recover the actual nature of the HOMO and LUMO bands that are apparent in **Figure 2** and **Figures S1–S3**.

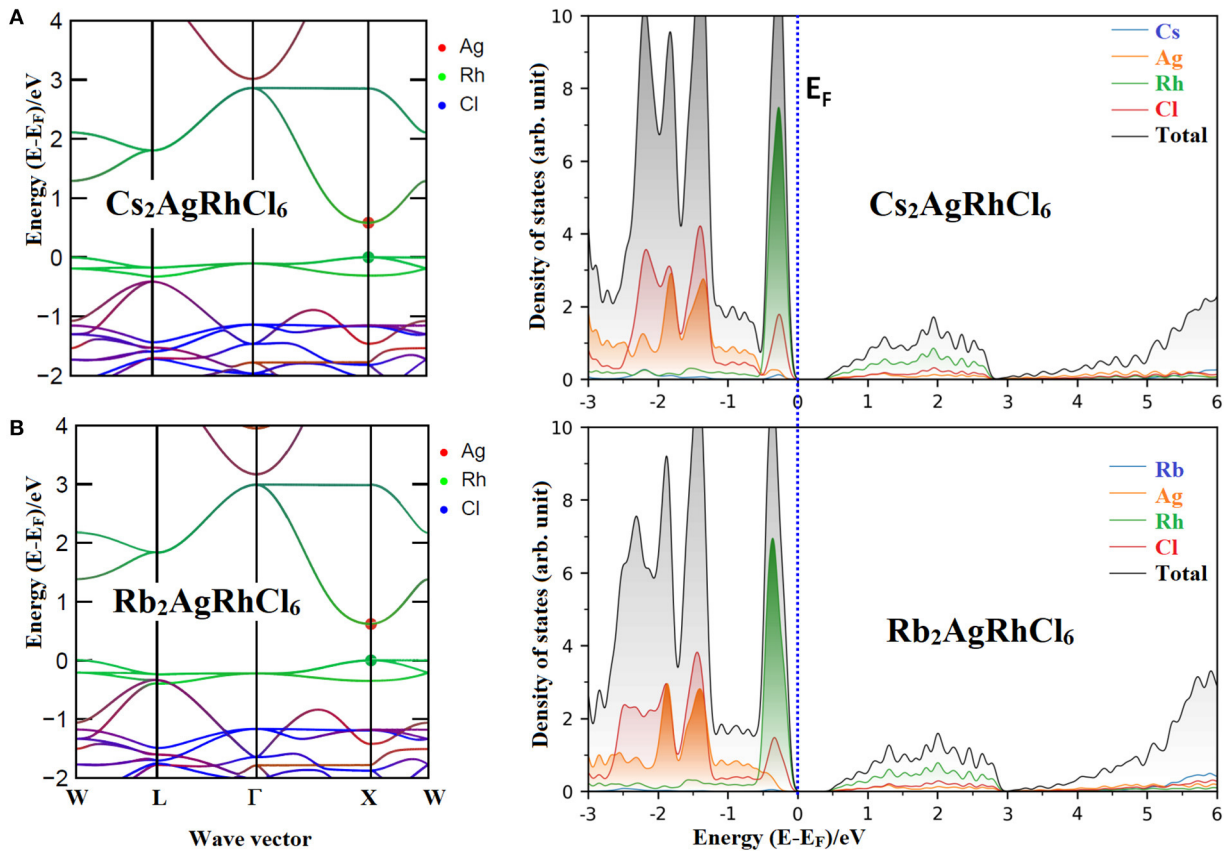

FIGURE 2 | Comparison of the non-spin polarized atom-projected electronic band structure and partial (and total) density of states of **(A)** $Cs_2AgRhCl_6$ with **(B)** $Rb_2AgRhCl_6$. Different color codes were used for each plot. The *k*-vector types of space group $Fm\bar{3}m$ were used for band structures.

Nature of Effective Masses and Their Mobility

We found that the top of the valence band is flatter than the bottom of the conduction band; the latter is appreciably parabolic. A similar flatter nature of the valence band was reported for bulk $Cs_2AgInCl_6$, which originated from Ag 4d and Cl 3p orbitals (Meng et al., 2017; Tran et al., 2017; Volonakis et al., 2017). In such a case, it is often observed that the hole effective mass (m_h^*) associated with the VBM is larger than the electron effective mass (m_e^*) of the CBM. Concomitantly, it is expected that the carrier mobility of the former is slower than that of the latter. The difference in the carrier masses arises from the nature of the curvature of the bottom of the conduction band (for electrons), or of the top of valence band (for holes); this is inversely proportional to the second derivative of the energy as a function of the wave vector **k**, and is described by the dispersion relationship shown in Equation (5),

$$m^* = \pm \frac{\hbar^2}{\partial^2 E(\mathrm{k}) / \partial \mathrm{k}^2} \tag{5}$$

where the + and – signs refers electrons and holes, respectively (Hartmann et al., 1982; Opoku et al., 2017). Using parabolic fitting of the band edges, it was found that the spin-up holes and electrons are the dominant charge carriers. The VBM comprises two degenerate bands. One of them is heavier than the other. This is arguably due to the fact that one of these bands is very flat along $X \rightarrow W$ and other is parabolic (see **Figures 2A,B**). For the lighter HOMO band, the hole masses are heavier along the $X \rightarrow \Gamma$ direction compared to the $X \rightarrow W$ direction, a feature that is consistent in all five $A_2AgRhCl_6$ systems examined (**Tables 4** and **S3**). The same behavior is associated with the effective masses of electrons that are virtually isotropic (values between 0.45 and 0.50 m_0), suggesting that the charge transport would be predominant along the $X \rightarrow W$ direction.

The effective masses and bandgaps of $A_2AgRhCl_6$ obtained using non-spin polarized calculations were very similar to those calculated using the spin-polarized setting (see **Table 4** and **Table S3**). **Figure 3** illustrates the functional dependence of effective mass on the bandgap for the series $A_2AgRhCl_6$, which is independent of the nature of the spin- and non-polarized calculations performed. Nevertheless, the average effective mass of electrons is approximately 0.45 m_0, whereas that of the hole is 1.94 m_0 for $Cs_2AgRhCl_6$, where m_0 is the free electron mass. These values are, respectively, 0.48 and 1.55 m_0 for $Rb_2AgRhCl_6$; 0.49 and 1.45 m_0 for $K_2AgRhCl_6$; 0.50 and 1.32 m_0 for $Na_2AgRhCl_6$; and 0.50 and 1.28 m_0 for $Li_2AgRhCl_6$.

TABLE 4 | Non-spin-polarized effective masses of electrons and holes obtained using the parabolic fitting of the lower conduction band and upper valence band for $A_2AgRhCl_6$ (A = Cs, Rb, K, Na, Li)[a]. Primitive cells used.

Compound	E_g/eV	Nature of E_g	Carrier type	Direction			
				X→Γ	X→W	Average	ratio ($\lvert m_e^*/m_h^* \rvert$)
$Cs_2AgRhCl_6$	0.58	Direct at X	m_h^*/m_0	−2.43	−1.44	−1.94	
			m_e^*/m_0	0.56	0.35	0.45	0.23
$Rb_2AgRhCl_6$	0.62	Direct at X	m_h^*/m_0	−1.73	−1.37	−1.55	
			m_e^*/m_0	0.61	0.34	0.48	0.31
$K_2AgRhCl_6$	0.64	Direct at X	m_h^*/m_0	−1.55	−1.35	−1.45	
			m_e^*/m_0	0.64	0.34	0.49	0.34
$Na_2AgRhCl_6$	0.65	Direct at X	m_h^*/m_0	−1.36	−1.28	−1.32	
			m_e^*/m_0	0.66	0.34	0.50	0.38
$Li_2AgRhCl_6$	0.66	Direct at X	m_h^*/m_0	−1.31	−1.25	−1.28	
			m_e^*/m_0	0.67	0.34	0.50	0.39

[a] m_0 *is the rest mass of the electron* (9.11×10^{-31} *kg*).

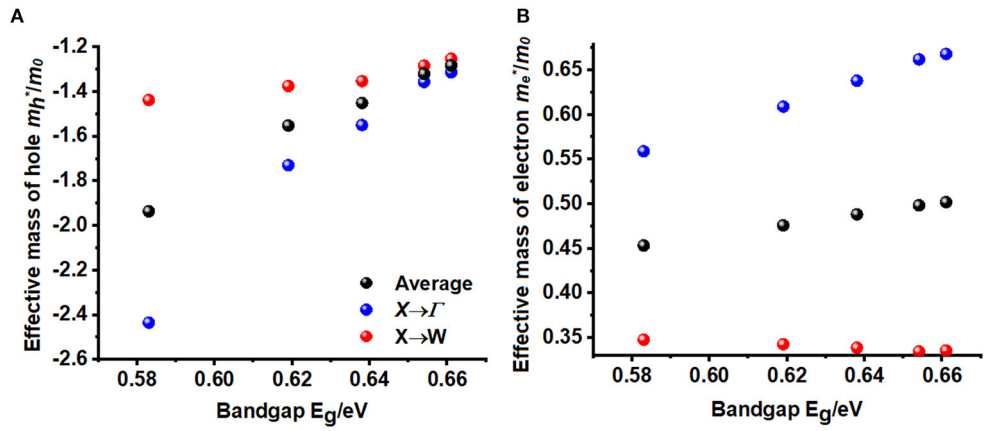

FIGURE 3 | Dependence of non-spin polarized effective mass of **(A)** holes and **(B)** electrons holes on the bandgap E_g for $A_2AgRhCl_6$ (A = Cs, Rb, K, Na, Li).

As mentioned above, the hole masses for one of the flatter valence bands should be heavier, reducing the average hole mobility. Indeed, this is what we have observed. It is smaller along the $X \rightarrow \Gamma$ direction than $X \rightarrow W$ direction (viz. 2.43 m_0 vs. 27.0 m_0); they are therefore are not incorporated in the average values shown in **Table 4** and **Table S3**. A similar result was reported elsewhere for the $Cs_2InCuCl_6$ double perovskite (Pham et al., 2019).

These results not only suggest that the average spin-up holes are heavier than that of the spin-up electrons for $A_2AgRhCl_6$, but the relatively low electron effective mass also signifies the presence of n-type conductivity, as observed for the CdSe semiconductor, for example (Hartmann et al., 1982). Our result is consistent with Si, for which the electron mobilities are higher than hole mobilities. Since the hole mass for $A_2AgRhCl_6$ is comparable to that of other systems (Wang Z. et al., 2019), the contribution of the holes to charge transfer is unlikely to be very large (Park, 2019) and the lifetime of the charge carriers for these semiconductors is likely to be determined by electron-electron collisions (Kao, 2004; Morkoc, 2009; Fu and Zhao, 2018). The ratio m_e^*/m_h^* provides the nature of electron-hole (e-h) pair stability in a recombination process (Zhang et al., 2012a,b; Dong et al., 2015; Faraji et al., 2015; De Lazaro et al., 2017; Opoku et al., 2017). In general, the larger the m_e^*/m_h^* ratio, the smaller the rate of recombination of the photoinduced charges. For instance, values of m_e^* and m_h^* were found to be 0.24 m_0 and 0.23 m_0, respectively, for $MAPbI_3$ (Filip et al., 2015). Similarly, they were 0.41 m_0 (0.34 m_0) and 0.35 m_0 (0.37 m_0) along the R to X direction for $CsPbCl_3$ ($CsPbBr_3$), respectively; 0.53 m_0 (0.37 m_0) along the L to W direction and 0.15 m_0 (0.14 m_0) along the X to Γ direction for $Cs_2AgBiCl_6$ ($Cs_2AgBiBr_6$), respectively (Mcclure et al., 2016). In all these cases, the ratio m_e^*/m_h^* is in the range 0.28 and 1.09, which is consistent with the majority of charge carriers in halide perovskites being large polarons; the slow recombination of these polarons underlies long carrier lifetime and diffusion length (Hoye et al., 2018; Zhang et al., 2019).

Our calculations gave m_h^*/m_e^* values in the range between 2.6 ($Li_2AgRhCl_6$) and 4.4 ($Cs_2AgRhCl_6$), suggesting that these may be possible candidate materials for light-based device applications.

Optical Properties

Insight into the optical properties of a solid state system can be obtained using the frequency dependent complex dielectric function $\varepsilon(\omega)$, a property that has been widely used to provide insight into, among other properties, the extent of charge screening, electron-hole coupling, and the electronic and ionic contributions to chemical bonding (Brivio et al., 2013; Walsh, 2015; Luo et al., 2017; Kirchartz et al., 2018; Wilson et al., 2019). The difference between the electronic and ionic dielectric constants ($\varepsilon_{\text{ionic}}$ and $\varepsilon_{\text{electronic}}$) assists to elucidate the polarity of the chemical bonds and the softness of the vibrations in a semiconducting material. The nature of the (picosecond) response of lattice vibrations (phonon modes) can be extracted, which can then be used to explain the extent of ionic and lattice polarizations required for a fundamental understanding of the photovoltaic performance of a material. If $\varepsilon_1(\omega) = \varepsilon^{(1)}_{\alpha\beta}(\omega)$ is the real part, and $\varepsilon_2(\omega) = \varepsilon^{(2)}_{\alpha\beta}(\omega)$ is the imaginary part of the frequency dependent $\varepsilon(\omega)$, then $\varepsilon(\omega)$ can be written as $\varepsilon(\omega) = \varepsilon_1(\omega) + i\varepsilon_2(\omega) = \varepsilon^{(1)}_{\alpha\beta}(\omega) + i\varepsilon^{(2)}_{\alpha\beta}(\omega)$. We used the Kubo-Greenwood relationship (Equation 6) for the calculation of the frequency dependent dielectric matrix associated with $\varepsilon^{(2)}_{\alpha\beta}(\omega)$. This was determined upon summing over the empty states.

$$\varepsilon^{(2)}_{\alpha\beta}(\omega) = \frac{4\pi^2 e^2}{\Omega} \lim_{q\to 0} \frac{1}{q^2} \sum_{c,\upsilon,k} 2w_k \delta(\varepsilon_{ck} - \varepsilon_{\upsilon k} - \omega) \times \langle u_{ck+e\alpha q} | u_{\upsilon k} \rangle \langle u_{\upsilon k+e\beta q} | u_{\upsilon k} \rangle \quad (6)$$

In Equation (6), the subscripts c and υ refer to conduction and valence band states, respectively, and u_{ck} is the cell periodic part of the orbitals at the k-point k. The real part $\varepsilon^{(1)}_{\alpha\beta}(\omega)$ of the dielectric function is related to $\varepsilon^{(2)}_{\alpha\beta}(\omega)$ via the Kramers-Kronig transformation given given by Equation (7), where P denotes the Cauchy principal value, and η is a small complex shift.

$$\varepsilon^{(1)}_{\alpha\beta}(\omega) = 1 + \frac{2}{\pi} P \int_0^{\infty} \frac{\varepsilon^{(2)}_{\alpha\beta}(\omega')\omega'}{\omega'^2 - \omega^2 + i\eta} d\omega' \quad (7)$$

The energy (or frequency) dependence of the dielectric function of $A_2AgRhCl_6$ in depicted in **Figure 4**. The curves of the real part of the dielectric function suggest that the electronic contribution to the static dielectric constant $\varepsilon(0)$ is appreciably

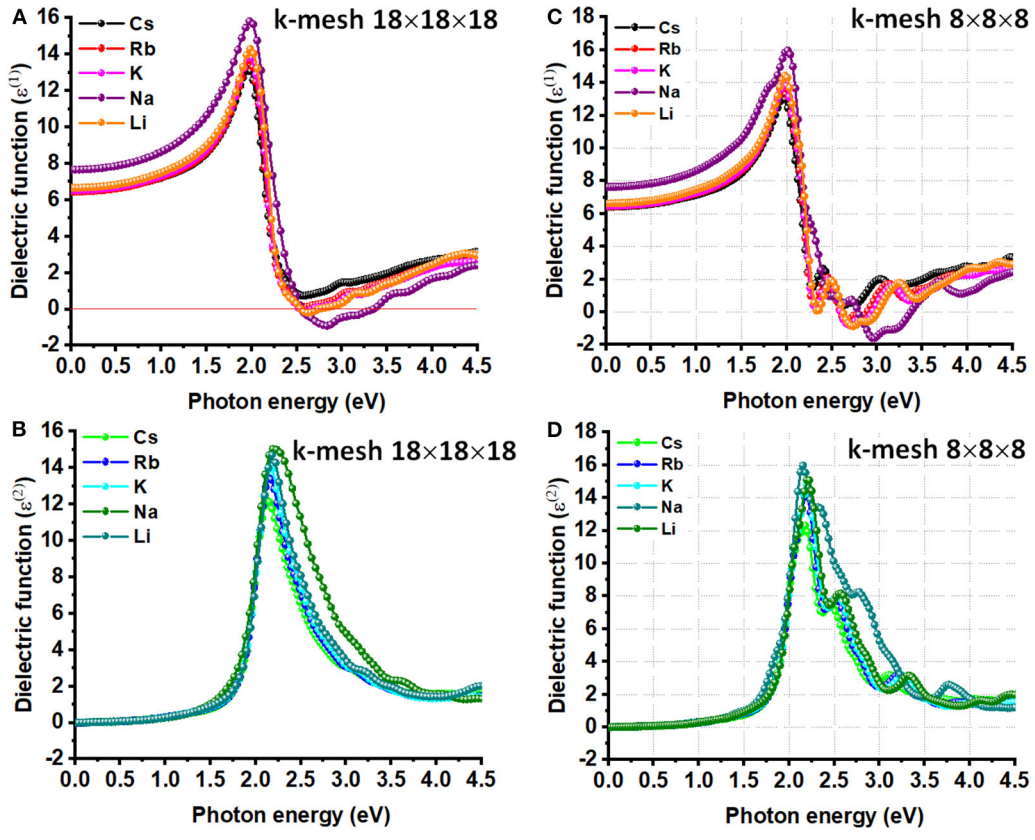

FIGURE 4 | The **(A)** real and **(B)** imaginary parts of dielectric function $\varepsilon(\omega)$ plotted against the photon energy for $A_2AgRhCl_6$ (A = Li, K, Na, Rb, Cs), obtained using DFPT/PBEsol. Shown in **(C)** and **(D)** are the corresponding plots obtained using *k*-mesh 8x8x8. The primitive cells used.

large, where $\varepsilon(0) = \varepsilon_\infty + \varepsilon_0$ (the first and last terms represent the electronic and ionic contributions, respectively). ε_∞ is related to the vibrational polar phonons of the lattice (Yu, 2019), and is due to the (femtosecond) response of the electron density (Zangwill, 2019).

The ionic contribution, ε_0, is due to the (picosecond) response of lattice vibrations (phonon modes); it is proportional to the polarity of the chemical bonds and the softness of the vibrations. The high frequency dielectric constant (ε_∞), which is also called the optical dielectric constant, is found to be isotropic because of the cubic nature of each of the five systems examined. Its value is around 6.5 for $Cs_2AgRhCl_6$, which is also the zero-frequency limit of $\varepsilon_1(\omega)$. This is the smallest across the series; of course, this is compared to the ε_∞ values of 6.5, 6.5, 7.7, and 6.7 calculated for $Rb_2AgRhCl_6$, $K_2AgRhCl_6$, $Na_2AgRhCl_6$ and $Li_2AgRhCl_6$, respectively. The size of the *k*-mesh has a very marginal effect on the zero-frequency limit of of $\varepsilon_1(\omega)$ (viz. **Figure 4A** vs. **Figure 4C**), regardless of the nature of the cell type used (**Figure 4** vs. **Figure S5**). As noted above, the unusual trend in value of ε_∞ for $Na_2AgRhCl_6$ may be a consequence of the plane wave basis set or the spin-polarized setting. The former could be corrected if the p-type semi-core states were to be treated as valence states, among other cut-off settings.

The ε_∞ value of 6.5 found for $Cs_2AgRhCl_6$ is comparable to that reported for other absorbing materials (Wilson et al., 2019), e.g., CdTe ($\varepsilon_\infty = 7.1$), $MAPbI_3$ ($\varepsilon_\infty = 6.0$), $MAPbBr_3$ ($\varepsilon_\infty = 5.2$), $MAPbCl_3$ ($\varepsilon_\infty = 4.2$) and $CsPbI_3$ ($\varepsilon_\infty = 5.3$). It is well-known that ε_∞ is computationally sensitivity to the choice of electronic structure Hamiltonian and the level of geometry optimization; ε_∞ values between 4.0 and 7.1 have been reported for the same material ($MAPbI_3$), and experimentally determined to lie between 4.0 and 6.5 (Wilson et al., 2019). The experimental variability in ε_∞ is either due to surface effects (Leguy et al., 2016a), or the assumptions taken in data processing (Hirasawa et al., 1994), or indeed other factors (Wilson et al., 2019). Using spectrospic ellipsometry methods, the optical dielectric constant was reported to be 4.8–5.1 near the absorption edge of $CH_3NH_3PbBr_3$ organic-inorganic hybrid perovskite thin films, correspinding to a bandgap of 2.3 eV (Alias et al., 2016).

The maximum of $\varepsilon_1(\omega)$ is approximately 13.0 for $Cs_2AgRhCl_6$. It shows up in the region between 0 and 4.5 eV. This becomes 13.7, 14.1, 15.5, and 14.3 for $Rb_2AgRhCl_6$, $K_2AgRhCl_6$, $Na_2AgRhCl_6$ and $Li_2AgRhCl_6$, respectively. The first corresponds to a photon energy of 2.0 eV, whereas those for others correspond to an energy around 2.0 eV. The use of smaller *k*-grid has some effect on the height of the peak, but not on the position of its occurrence (**Figure 4A** vs. **Figure 4C**). These results suggest that decreasing the size of the alkali metal ion in the lattice increases the high frequency response behavior, but the nature of the transitions involved between the VBM and CBM is of similar character.

On the other hand, the transition peaks in the curves of $\varepsilon_2(\omega)$, which are directly related to the optical absorption process, occur at energies between 2.10 and 2.20 eV. These are located at higher energies than those in the $\varepsilon_1(\omega)$ curves (see above). Whereas the $\varepsilon_2(\omega)$ curves are quasi-symmetric and resemble a Lorentz-like resonant behavior that corresponds to bound electrons, the $\varepsilon_1(\omega)$ curves are anti-symmetric and show dispersion-like behavior. The $\varepsilon_1(\omega)$ spectra for $K_2AgRhCl_6$, $Na_2AgRhCl_6$, and $Li_2AgRhCl_6$ are strongly positive at low energies. It reaches a maximum value around 2.0 and then decreases. It becomes negative at the crossover energy around 2.5 eV and then becomes positive. The negative feature is likely to be a Drude-tail (Khatri et al., 2011; Eaton et al., 2018), thus indicating the quasi-metallic behavior of these materials in a specific region (Xu et al., 2008; Murtaza et al., 2011). This is not the case for $Cs_2AgRhCl_6$ and $Rb_2AgRhCl_6$. We note that the Drude feature appears in the $\varepsilon_1(\omega)$ spectra using DFPT, which is persisent regardless of the size the *k*-mesh and cell-type used [**Figure 4** and **Figure S5** (Top)], is not evident in that calculated using SCAN-*rVV*10 (**Figure S6**), suggesting that it could be an artifact of DFPT.

The appreciable dielectric features delineated above are also evidence of the spectra of absorption coefficient $\alpha(\omega)$, reflectivity $R(\omega)$, and energy loss function $L(\omega)$, calculated using Equations (8), (9), and (10), respectively (Dresselhaus, 2001; Ma et al., 2014), where c and ω are the speed of light in vacuum and frequency of light wave, respectively. The calculated real and imaginary parts of the dielectric function of each system were used.

$$\alpha(\omega) = \frac{\sqrt{2}\omega}{c}\left\{\left[\varepsilon_1^2(\omega) + \varepsilon_2^2(\omega)\right]^{1/2} - \varepsilon_1(\omega)\right\}^{1/2} \quad (8)$$

$$R(\omega) = \left|\frac{\sqrt{\varepsilon_1(\omega) + i\varepsilon_2(\omega)} - 1}{\sqrt{\varepsilon_1(\omega) + i\varepsilon_2(\omega)} + 1}\right|^2, \quad (9)$$

$$L(\omega) = \mathrm{Im}(\tfrac{-1}{\varepsilon(\omega)}) = \frac{\varepsilon_2(\omega)}{\varepsilon_1^2(\omega) + i\varepsilon_2^2(\omega)} \quad (10)$$

As noted elsewhere (Meng et al., 2017), absorption coefficients below 10^4 cm^{-1} are regarded as a weak absorption; this may lead to a tail in the absorption coefficient curve of a UV-Vis spectrum. However, inspection of **Figure 5A** shows that the absorption starts around the VBM to the CBM transition region for all $A_2AgRhCl_6$. The absorption coefficient increases with an increase of photon energy, and reaches a maximum at 2.2 eV, which is in reasonable agreement with the maximum oscillator peak of ε_2 as α is dependent on it (Equation 8). Since this occurs in the visible region, these systems could be useful in photovoltaic and photodetector applications (Wang et al., 2020). Specifically, the value of α at the highest peak varies between 6.4×10^5 cm^{-1} ($Cs_2AgRhCl_6$) and 8.3×10^5 cm^{-1} ($Na_2AgRhCl_6$); there should therefore be an appreciable absorption of light by these systems.

The computed absorption coefficient curves of $A_2AgRhCl_6$ show an onset around 1.1 and 1.3 eV; these are consistent with the SCF bandgaps predicted with SCAN-*rVV*10 (**Table S2**). The Tauc plot, **Figure 5B**, provides similar insight, since it is often used to extract the bandgaps from experimental absorption spectra (Eom et al., 2017; Tang et al., 2017; Habibi and Eslamian, 2018; Ji et al., 2018). The peak feature in the visible region with an appreciable absorption coefficient is a strong indication that $A_2AgRhCl_6$ are potential candidates for possible optoelectronic applications.

Since the VBM and CBM are substantially of Rh(4d) character, it is likely that the ligand field electronic transitions involved between them have d-d type metallic character (Ford, 2016). The Tanabe-Sugano diagram (Tanabe and Sugano, 1954) for a low

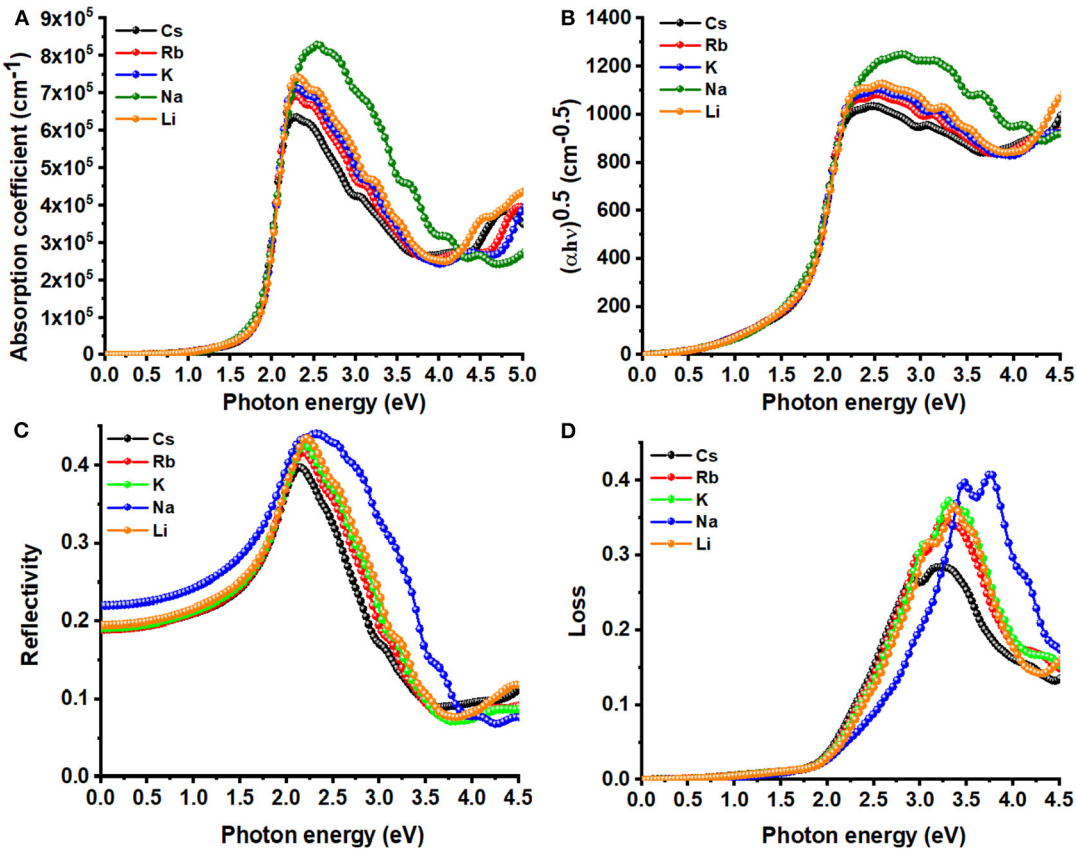

FIGURE 5 | Dependence of the **(A)** absorption coefficient, **(C)** reflectivity, **(D)** energy-loss function on the photon energy of $A_2AgRhCl_6$ (A = Li, K, Na, Rb, Cs). Displayed in **(B)** is the Tauc plot for the corresponding systems. Primitive cells and k-mesh 18 × 18 × 18 used.

spin d^6 ion in an O_h environment indicates that the two lowest energy spin-allowed transitions from the $^1A_{1g}$ state of the ion are, in order of increasing energy, $^1A_{1g} \rightarrow {}^1T_{1g}$ and $^1A_{1g} \rightarrow {}^1T_{2g}$. The spin-forbidden transitions $^1A_{1g} \rightarrow {}^3T_{1g}$ and $^1A_{1g} \rightarrow {}^3T_{2g}$ occur at longer wavelength. For instance, in some Rh^{3+}-doped sodium borosilicate glasses thee spin-allowed transitions occur at 449 and 297 nm (2.76 and 4.17 eV, respectively) and the spin-forbidden transitions occur in the 600–2000 nm (2.0–0.62 eV) range (Wen et al., 2017). The emission onset and peak positions for Cs_2NaMCl_6:M' (M = Y, In, Sc; M′ = Rh^{3+}) were reported between 1.3–1.4 and 1.04–1.07 eV, respectively, and ascribed to a $^1A_1 \rightarrow {}^3T_1$ transition (Campochiaro et al., 1992). The observation of a peak emission at ∼1,600 nm (0.77 eV) of the single luminescence band in the infrared spectral region in Rh^{3+}-doped AgBr crystals was also ascribed to this spin-forbidden transition (Spoonhower et al., 1986).

We observe an absorption envelope beginning around the fundamental bandgap and expending into the visible and UV regions for $A_2AgRhCl_6$ (see **Figures 5A**). The three principal peaks were found around 2.2, 2.5, and 3.2 eV for $Cs_2AgRhCl_6$. The dominant absorption, around 2.2 eV, is attributed to the lower energy, spin-allowed transition ($^1A_{1g} \rightarrow {}^1T_{1g}$); the higher energy spin-allowed transition ($^1A_{1g} \rightarrow {}^2T_{1g}$) occurs around 3.2 eV. The lower energy shoulder on the main transition, around 2.5 eV, is ascribed to the spin-forbidden $^1A_{1g} \rightarrow {}^3T_{1g}$ transition. These transitions are prominent in the dielectric spectra shown in **Figure 4D**.

The complex refractive index ($n + i\kappa$) is a fundamental property of a solid material that describes the propagation velocity of light in the medium, thus allowing one to recognize whether such a material is potentially useful for optoelectronics (Schubert et al., 2007). The real and imaginary parts of the complex refractive index, called the static refractive index ($n(\omega)$) and extinction coefficient ($\kappa(\omega)$), were calculated using Equations (11) and (12), respectively (Dresselhaus, 2001; Li et al., 2009; Jong et al., 2016; Dong et al., 2017). Depending on the nature of the bulk material, the value of $n(\omega)$ varies, but $\kappa(\omega)$ is generally small for semiconductors (Baranoski and Krishnaswamy, 2010).

$$n(\omega) = \left[\frac{\sqrt{\varepsilon_1^2 + \varepsilon_2^2} + \varepsilon_1}{2}\right]^{1/2} \tag{11}$$

$$\kappa(\omega) = \left[\frac{\sqrt{\varepsilon_1^2 + \varepsilon_2^2} - \varepsilon_1}{2}\right]^{1/2} \tag{12}$$

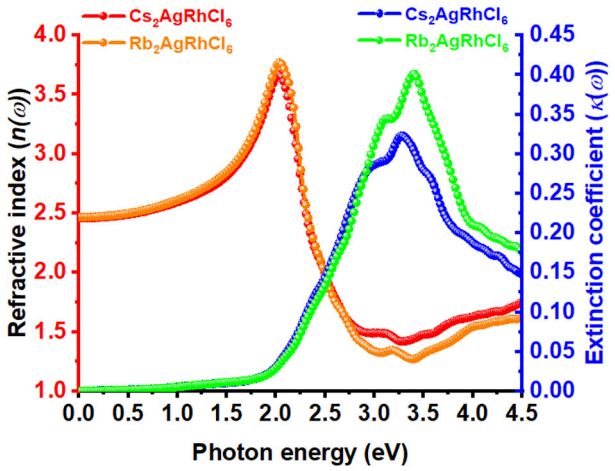

FIGURE 6 | The dependence of the real and imaginary parts of the complex refractive index for $Cs_2AgRhCl_6$ and $Rb_2AgRhCl_6$. Although the corresponding spectra of $A_2AgRhCl_6$ (A = K, Na, Li) were of similar nature, they are not shown to avoid the complexity of the plot.

The static refractive index at the zero frequency limit of bulk $Cs_2AgRhCl_6$ is calculated to be 2.46, whereas that of $Rb_2AgRhCl_6$ is 2.47. Alkali introduction at the *A*-site caused a small increase in *n*, with values ranging between 2.46 and 2.50; this is caused by the contraction of the crystal lattice. As shown in **Figure 6**, $n(\omega)$ increases to a maximum value of 3.67 and 3.78 at the highest peaks, positioned at an energy of 2.03 eV for $Cs_2AgRhCl_6$ and $Rb_2AgRhCl_6$, respectively. Such large values of $n(\omega)$ are expected of optical ambient materials, with a typical refractive index of 2.5–3.5 (Schubert et al., 2007). For instance, the refractive index at the absorption edge was 2.29 and 2.61 for $CH_3NH_3PbBr_3$ (Alias et al., 2016) and $CH_3NH_3PbI_3$ (Löper et al., 2015) perovskites, respectively. $CH_3NH_3PbI_3$ (Löper et al., 2015) as a single crystal and thin film, has a refractive index of 2.45 [at 800 nm (1.55 eV)] and 1.95, respectively (Löper et al., 2015).

The value of *n* for halide perovskites is significantly larger than that of SiO_2 (1.09; Popova et al., 1972; Kitamura et al., 2007−1.45; Malitson, 1965; Tan, 1998) or most polymers, making them a good material for resonant nanostructures due to their high optical contrast. Because *n* for $Cs_2AgRhCl_6$ is much lower than that of Si ($n = 3.673$; Refractiveindex.Info; Aspnes and Studna, 1983) or GaAs (3.4–3.7; Kachare et al., 1976; Aspnes et al., 1986; Jellison, 1992; Skauli et al., 2003), it provides high optical contrast with these materials in advanced hybrid structures (Makarov et al., 2019). By contrast, the extinction coefficient for $Cs_2AgRhCl_6$ is calculated to be very small and is close to 0.006 near the fundamental absorption edge of dispersion (**Figure 6**). This is comparable to the experimental κ values of 0.00014657, 0.08, and 0.005 reported for SiO_2 (Popova et al., 1972; Kitamura et al., 2007), GaAs (Aspnes et al., 1986), and Si (Aspnes and Studna, 1983), respectively.

As can be seen from **Figure 6**, the values of the real and imaginary parts of the refractive index for each $A_2AgRhCl_6$ are substantially different to each other. Since reflectivity *R* is related to the refractive indices via $R = \left((n^2 - \kappa^2)/(n^2 + \kappa^2)\right)^2$ and that *n* is several 100 orders of magnitude larger than κ at any specific critical point of the refractive index spectrum, it is clear that since $n \neq k$ the optical reflectivity will have a minimum value across the entire energy range investigated. This is seen in the reflectivity spectra calculated using the dielectric function (Equation 9), **Figure 5C**, in which a minimum reflection of $< 10\%$ occurs in the region above 3.5 eV. The maximum of 38–45% light is likely to be reflected at the peak positions around 2.1 eV, and it is 15–25% around the onset of absorption. The reflectivity spectra of other systems reported elsewhere have similar characteristics (Peng et al., 2013; Ma et al., 2014; Saini et al., 2017; Mohamed et al., 2018). The energy loss function is plotted in **Figure 5D**. It is a measure of the loss of the energy of the electrons passing between energy bands. The maximum energy loss is calculated to lie between 32% ($Cs_2AgRhCl_6$) and 45% ($Na_2AgRhCl_6$) at energies of 3.2 and 3.6 eV, respectively.

Although the DFPT/PBEsol based optical properties described above were obtained using the primitive cells of $A_2AgRhCl_6$, the conventional cell geometries of these systems utilized for the same purpose using the same method did not significantly affect the location and height of peak features in the dielectric spectrum (**Figure S5**). However, when the same characteristics were investigated using SCAN-*rVV*10, it was found that although the nature of the transition features associated with the optical absorptions did not change markedly, the peak positions were blue-shifted. These were as large as 0.7–0.9 eV and the peak heights were reduced appreciably (**Figure S6**). In addition, the zero-frequency limit of $\varepsilon^{(1)}$ of $A_2AgRhCl_6$, which were found between 6.5 and 8.0 (**Figure 4A**), is reduced, so they are predicted around 5.0 (**Figure S6**), yet confirming that the electronic contribution to the static dielectric constant is reasonably high.

Because of the appreciable inconsistency between the onsets of optical absorption in the dielectric spectra calculated using SCAN-*rVV*10 and DFPT/PBEsol, we extended our calculations to compute the bandgap of the studied systems using quasiparticle G_0W_0 and GW_0 methods (Hedin, 1965; Van schilfgaarde et al., 2006; VASP, 2020a), based on Many-Body Perturbation Theory (MBPT), where G_0 is one-particle Green's function, W_0 is the screened Coulomb interaction, and GW_0 is the most usual step beyond single-shot GW (G_0W_0) to iterate the quasi-particle energies in the Greens functions. The G_0W_0 approach calculated the Green's function G_0 from the SCAN-*rVV*10 wavefunction in a non-self-consistent manner, and a perturbative scheme was utilized for the calculation of screened exchange in W_0. In general, G_0W_0 calculates the quasi-particle energies from a single *GW* iteration by neglecting all off-diagonal matrix elements of the self-energy and employing a Taylor expansion of the self-energy around the DFT energies. The self-energy and one-shot calculations were performed using a $6 \times 6 \times 6$ *k*-mesh. Interestingly, the SCAN-*rVV*10 predicted optical absorption edges associated with the imaginary part of the dielectric spectra (**Figure S6**) are in good agreement with the nature of the G_0W_0 and GW_0 bandgaps of the corresponding systems. For instance, the G_0W_0 bandgaps were 2.43, 2.46 and 2.49 eV for $Cs_2AgRhCl_6$, $Rb_2AgRhCl_6$, and $K_2AgRhCl_6$ with the SCAN-*rVV*10 wavefunctions, respectively (**Table S2**).

Similar calculations with the popular Heyd–Scuseria–Ernzerhof functional (HSE06) (Krukau et al., 2006; Savory et al., 2016a) and a 4 × 4 × 4 *k*-mesh gave bandgaps between 2.3 and 2.0 eV, showing an underestimation compared to G_0W_0 and GW_0 (**Table S2**). **Table S7** compares the lattice and bandgap properties of $Cs_2AgRhCl_6$ obtained from various computational approaches with those experimentally reported and calculated in this work for $Cs_2AgB'Cl_6$ (B' = In, Bi, Sb, Tl) (Zhou et al., 2018; Zhou J. et al., 2019).

The large difference between the GGA/meta-GGA and GW/HSE06 bandgaps is not very surprising given that the former ones generally underestimate bandgaps for single and double perovskite semiconductors (Ganose et al., 2017; Umadevi and Watson, 2019). For example, the reported PBE bandgap for $Cs_2AgInCl_6$ is 0.95 eV (Kumar et al., 2020), compared to the experimental value of 3.3 eV (Volonakis et al., 2017). Similarly, the bandgaps of 0.89 eV (PBEsol) and 1.1.17–1.61 eV (PBE) (Lu et al., 2016; Sun P.-P. et al., 2016; Zhao Y.-Q. et al., 2017) were reported for $CH_3NH_3GeI_3$, and those of the hybrid functional range from 1.70 to 2.04 eV (Sun P.-P. et al., 2016; Zhao Y.-Q. et al., 2017), whereas the experimental value for which is 1.90 eV (Stoumpos et al., 2015). There is also precedence that the inclusion of dispersion correction further reduces the bandgaps, and this is likely the case with the GGA and HSE06 methods (Umadevi and Watson, 2019). The bandgaps found in the current study for $A_2AgRhCl_6$ are smaller/larger than, or comparable to, those of 2.19, 2.77, 2.33, and 3.00 eV reported for $Cs_2AgBiCl_6$, $Cs_2AgBiBr_6$, $MAPbBr_3$ and $MAPbCl_3$ (MA = methyl ammonium), respectively (Mcclure et al., 2016). There are other such double perovskite systems reported elsewhere (Jain et al., 2017; Zhao X.-G. et al., 2017; Locardi et al., 2018), which were stable and exhibited a direct bandgap in the spectral range relevant for solar energy conversion (1.5–2.5 eV), including Cs_2AgInX_6, Rb_2AgInX_6, and Rb_2CuInX_6 (X = Cl, Br). Clearly, the rhodium-based double perovskites examined in this study, which display excitonic features in the visible and UV regions, may be useful for applications in photoelectric detectors. $MAPbBr_3$ is an exemplar photovoltaic semiconductor, with an experimental bandgap of 2.33 eV (Niemann et al., 2016; Varadwaj et al., 2018), which has been recognized as a material for photovoltaics and photodetectors (Saraf and Maheshwari, 2018).

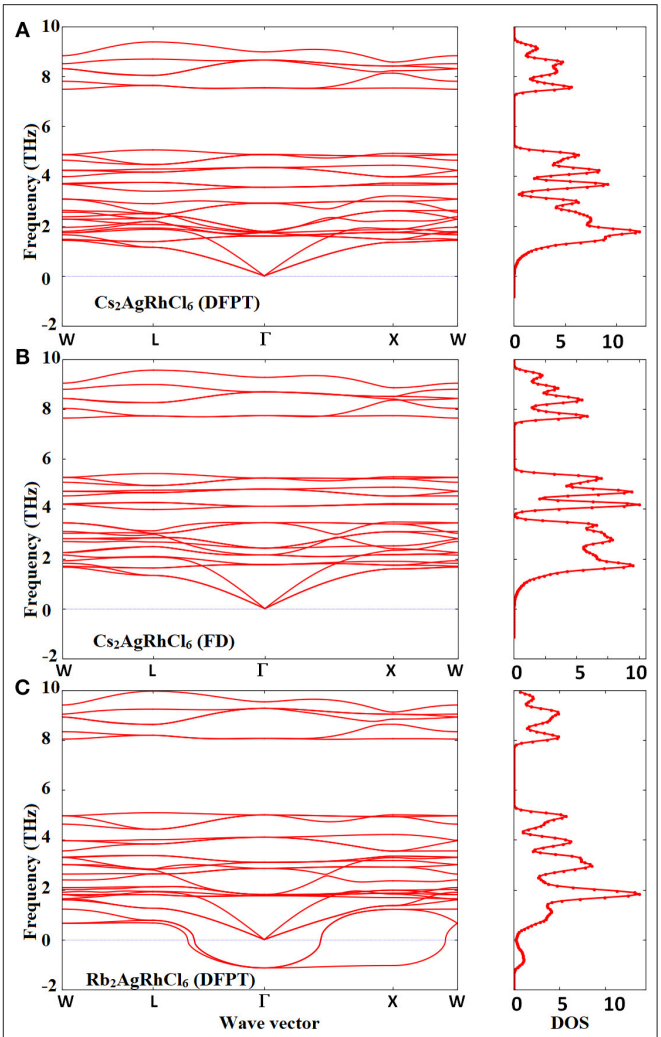

FIGURE 7 | Comparison of the phonon dispersion and total phonon density of states (a.u.) of $Cs_2AgRhCl_6$ calculated using the **(A)** DFPT/PBEsol and **(B)** FD (finite difference) methods. Shown in **(C)** are the corresponding features for $Rb_2AgRhCl_6$, calculated using DFPT/PBEsol method with the supercell approach. Phonon "soft" modes are present around the Brillouin-zone boundary points and $\Gamma \rightarrow X \rightarrow W$ for $Rb_2AgRhCl_6$.

Phonon Features and Lattice Stability

The phonon band structures of $Cs_2AgRhCl_6$ and $Rb_2AgRhCl_6$ are illustrated in **Figure 7** and **Figure S7**. The force constants defining the change in force on a reference atom in response to the displacement of another were used to construct a dynamics matrix. The matrix was then diagonalized. This gave the eigenvalues (normal mode phonon frequencies) and associated eigenvectors (phonon motion). As expected, there are three acoustic and several optical phonon modes. Although this is evidence of the dispersion curves shown in **Figure S8**, in which case, the conventional cells were used, two of these modes are found to be degenerate when the primitive cells used, showing the cell geometry plays an important role in unraveling the degeneracy involved. The acoustic modes are present below 1.5 THz and the optic modes are limited to the frequency interval 1.0–10.0 THz for $Cs_2AgRhCl_6$. These phonons are all stable across the Brillouin-zone boundary points, including the *W*, *L*, *Γ*, and *X*-points. This is true regardless of the nature of computational method employed (DFPT/PBEsol and FD, **Figures 7A,B**)—spin-polarized or non-spin polarized (see **Figure S7**). The only difference between the two theoretical approaches is that the phonon frequencies are somewhat different, with the FD method overestimating them compared to the DFPT/PBEsol method. However, all of them recognize the $Cs_2AgRhCl_6$ crystal lattice to be dynamically stable (Mouhat and Coudert, 2014).

For $Rb_2AgRhCl_6$ (**Figure 7C**), as well as the other three members of the $A_2AgRhCl_6$ series (not shown), the phonons

are unstable along the entire path, especially along the paths $L \rightarrow \Gamma$, $\Gamma \rightarrow X$ and $X \rightarrow W$. They are associated with negative vibrational frequencies, which are due to the metastable lattice of the double perovskite induced by the alkali substitution at the *A*-site. The negative phonon modes are the so-called soft modes and are prominent, especially at the center of the Brillouin zone (Γ–point). This is evidence of the phonon density of states shown in **Figure S9B** (bottom), when compared against that shown in **Figure S9A** for $Cs_2AgRhCl_6$. The origin of such an instability for $Rb_2AgRhCl_6$ is probably a consequence of lattice softening induced by the softening of the shear constants for long wave phonons (Böni et al., 1988), and may not be ascribed to phonon instability that is generally caused by the softening of the transverse acoustic phonons near zone boundaries (Nakanishi et al., 1982; Liu et al., 2016). This is because the instability is primary associated with optical phonons, as the acoustic modes are unaffected. A somehow similar result was obtained for the other two members of the series, $A_2AgRhCl_6$ (A = Na, Li), but this is due to significant phonon and lattice instabilities tailored both by the acoustic phonons of low frequency and the optical modes of high frequency (not shown). Halide perovskites such as $FAPbI_3$, $MAPbI_3$, $MAPbBr_3$, and $CsPbBr_3$ were shown to exhibit phonon instabilities around the Brillouin-zone boundary points, which was significant at the *R*- and *M*-points; the imaginary frequency associated with the R-point was as large as 1.5 THz (for $CsPbBr_3$; Yang et al., 2017). This was attributed to the disorder introduced in the material by the anisotropic nature of the organic ion and octahedral tilting (Leguy et al., 2016b).

Mechanical (Elastic) Properties

There are only three independent elastic constants (C_{11}, C_{12}, and C_{44}) associated with the stiffness matrix C_{ij} of cubic crystals that represent the directional mechanical responses of the crystals for different directions of applied forces (Mouhat and Coudert, 2014). The longitudinal distortion, C_{11}, is based on the longitudinal compression, and describes the hardness. The transverse distortion, C_{12}, is based on the transverse expansion, which is related to Poisson's ratio. The shear elastic parameter, C_{44}, is based on the shear modulus that represent the stiffness of the crystal. Our caclualtions gave all eigenvalues λ_i of the $C_{ij} = C_{ji}$ matrix to be real and positive for all $A_2AgRhCl_6$ systems (**Table S4**). The Born criteria (Mouhat and Coudert, 2014) of the cubic system (i) $C_{11} - C_{12} > 0$; (ii) $C_{11} + 2C_{12} > 0$; (iii) $C_{44} > 0$ are also satisfied (see **Table S5** for values of the elastic constants). This, along with the real and positive character of all the six eigenvalues of the stiffness matrix, points to the mechanical stability of all the five $A_2AgRhCl_6$ systems (Mouhat and Coudert, 2014).

The three stiffness constants are found in the order $C_{11} > C_{12} > C_{44}$ (**Table S5**). The effect of the *A*-site cation on these constants is to increase C_{11} along the series ($Cs_2AgRhCl_6 > Rb_2AgRhCl_6 > K_2AgRhCl_6 > Li_2AgRhCl_6$), consistent with the decreasing ionic radii of the alkali ions. There was a concomitant decrease of C_{12} and C_{44} along the same line. This shows that alkali substitution at the *A*-site has a marked effect on C_{11} compared to C_{12} and C_{44}; hence the longitudinal compression is increasingly larger compared to the transverse and shear distortions when passing from Cs^+ through Rb^+ to K^+ to Li^+. Because $C_{11} \neq C_{12} + 2C_{44}$, which is undoubtedly the result of significant longitudinal distortion, especially for systems containing Rb^+, K^+ and Li^+, we conclude that $A_2AgRhCl_6$ (A = Rb, K, Li) are not strictly isotropic.

The shear constant C_{44}, which measures plastic deformation, is less than $(C_{11} - C_{12})/2$ for each $A_2AgRhCl_6$. That is, the difference between them ($[C_{44} - ((C_{11} - C_{12})/2)]$) is negative (see **Table S5**). It increases from $Cs_2AgRhCl_6$ to $Rb_2AgRhCl_6$ to $K_2AgRhCl_6$ to $Li_2AgRhCl_6$, and hence the shear softening increases in the order $Cs_2AgRhCl_6 < Rb_2AgRhCl_6 < K_2AgRhCl_6 < Li_2AgRhCl_6$. This trend is roughly preserved for the shear modulus (see K values in **Table S6**), although the value of K for $Cs_2AgRhCl_6$ is slightly smaller than that for $Rb_2AgRhCl_6$ (15.47 GPa vs. 15.50 GPa). Clearly, the softening in the shear constant that results in very large negative values of $[C_{44} - ((C_{11} - C_{12})/2)]$ (**Table S4**), except for $Cs_2AgRhCl_6$, probably explains the presence of the observed degenerate transverse branches shown in **Figures 7A,B**, and the lattice instability observed for $Rb_2AgRhCl_6$ and other members of the series (see **Figure 7C** and **Figure S8**).

There is no obvious trend observed between the mean values of Young's modulus (Y), Bulk modulus (B), and shear modulus (K) for any given $A_2AgRhCl_6$ (**Table S6**). For instance, the arithmetic mean values of these moduli were 40.91 (41.28), 38.39 (40.88), and 15.47 (15.50) GPa for $Cs_2AgRhCl_6$ ($Rb_2AgRhCl_6$), respectively, whereas such a trend is altered for the remaining two systems, with the corresponding values of 41.9 (42.01), 38.6 (29.23), and 14.3 (10.62), respectively. The Young's modulus, which is the ratio of stress to strain, and a measure of stiffness, is found to be largest, 41.28 (40.91) GPa, for $Cs_2AgRhCl_6$ ($Rb_2AgRhCl_6$), showing that they are relatively stiffer than $K_2AgRhCl_6$ and $Li_2AgRhCl_6$. This ultimately suggests that the contribution of covalence in chemical bonds is larger in the former two than in the latter two systems since stiffer solids usually feature significant covalent bond character. The bulk modulus B, which quantifies the resistance to fracture and was calculated using the expression $B = (C_{11} + 2C_{12})/3$, shows a clear increasing trend in the series: $Cs_2AgRhCl_6$ (38.39 GPa) > $Rb_2AgRhCl_6$ (40.88 GPa) > $K_2AgRhCl_6$ (41.92 GPa) > $Li_2AgRhCl_6$ (42.01 GPa). This may lead to the interpretation that $Cs_2AgRhCl_6$ is relatively strengthened compared to other systems across the series and could be more resistant to external forces such as pressure and temperature.

From the values of the elastic properties listed in **Table 5**, it is quite clear that the anisotropy in Young's modulus, linear compressibility, Bulk modulus and Poisson's ratio is very marginal for $Cs_2AgRhCl_6$. This becomes very marked for $Li_2AgRhCl_6$, and the anisotropy increases in the series from Cs^+ through Rb^+ to K^+ to Li^+.

The empirical measures of brittle/ductile response of mechanical solids are Pugh's criterion (K/B ratio) (Pugh, 1954) and the Cauchy pressure C_P ($C_P = C_{12} - C_{44}$ for cubic crystals). (Johnson, 1988; Kamran et al., 2009). Materials with K/B > 1.75 are ductile while those with K/B < 1.75 are brittle (Pan and Guan, 2017; Singh et al., 2018). Our calculation gave a K/B value of 2.48 and 2.64 for $Rb_2AgRhCl_6$ and $Rb_2AgRhCl_6$, respectively, and a C_P value of 12.6 and 14.3 GPa, respectively.

TABLE 5 | Some selected elastic constants of $A_2AgRhCl_6$ (A = Cs, Rb, K, Li) [a,b].

System	Young's modulus		Linear compressibility		Shear modulus		Poisson's ratio	
	Y_{min}/GPa	Y_{max}/GPa	β_{min}/TPa^{-1}	β_{max}/ TPa^{-1}	K_{min}/GPa	K_{max}/GPa	σ_{min}	σ_{max}
$Cs_2AgRhCl_6$	40.73	41.17	8.68	8.68	15.39	15.58	0.32	0.33
	1.01		1.00		1.01		1.03	
$Rb_2AgRhCl_6$	34.54	53.37	8.15	8.15	12.71	20.81	0.20	0.49
	1.55		1.00		1.64		2.45	
$K_2AgRhCl_6$	28.40	59.07	7.95	7.95	10.24	23.35	0.15	0.59
	2.08		1.0		2.28		4.05	
$Li_2AgRhCl_6$	15.07	64.73	7.93	7.93	5.23	26.04	0.07	0.78
	4.30		1.0		4.98		11.17	

[a] *Each second line entry represents the extent of anisotropy.*
[b] *Subscripts min and max in Y, β, K, and σ represent minimum and maximum values, respectively.*

The former property unequivocally suggests the ductile nature of these materials, and the positive nature of C_P is expected of any ductile metals, such as Ni or Al, for example (Kamran et al., 2009; Ivanovskii, 2012). This may be consistent with the observation that materials that feature metallic bonding exhibit a positive Cauchy pressure (Thompson and Clegg, 2018). From the mean values of Poisson's ratio σ (values between 0.32 and 0.38 in **Table S6**), it is obvious that the chemical bonding between metal ions and Cl is increasingly ionic across the series from $Cs_2AgRhCl_6$ to $Rb_2AgRhCl_6$ to $K_2AgRhCl_6$ to $Li_2AgRhCl_6$, given that σ is close to 0.1 – 0.28 for covalent materials (Haines et al., 2001).

CONCLUSION

This study used density functional theory to describe the nature of the geometric stability, electronic, transport, optical, and dynamic lattice properties of the series $A_2AgRhCl_6$ (A = Li, Na, K, Rb, Cs). Although the bandgap of these systems was close to 0.57–0.65 eV with SCAN-*rVV*10, this was, as expected, appreciably underestimated with the traditionally recommended functionals PBE and PBEsol. All these GGA and meta-GGA methods have shown here to be consistently underestimated the bandgaps compared to the quasi-particle GW and hybrid functional HSE06/PBE0 methods, which predict the bandgaps in the visible region, revealing possible application of the studied systems in optoelectronics.

The use of the Global Instability Index suggested that $Cs_2AgRhCl_6$, $Rb_2AgRhCl_6$, and $K_2AgRhCl_6$ might possess perovskite-quality face-centered cubic structures. This was consistent with what emerged from the recommended combination of Goldsmith's tolerance and octahedral factors. However, with the application of the newly-proposed tolerance factor, the first three heavier members of the series were identified as perovskites and the remaining two lighter members as significantly unstable structures. Nevertheless, all showed nearly similar band structure, DOS, and bandgap features. It was shown that the CBM and VBM of $A_2AgRhCl_6$ originated mainly from the 4d states of the octahedron Rh^{3+} ion, with a non-negligible contribution from the 3p states of the 6-coordinate Cl^- ions.

The reasonably small effective masses of the charge carriers gave evidence of the presence of (quasi) bipolar conductivity and high mobility. These properties, together with the impressive electronic transition features in the dielectric function spectra, high refractive indices, and high absorption coefficients have enabled to us to conclude that the materials studied may be suitable for application in optoelectronics. However, the phonon and elastic properties examined in this study showed that $A_2AgRhCl_6$ (A = Li, Na, K, Rb) were dynamically unstable and mechanically stable. This was not the case for $Cs_2AgRhCl_6$, which was predicted to be both dynamically and mechanically stable; this suggests its experimental synthesis and an exploration of its properties appears to be justified.

DATA AVAILABILITY STATEMENT

The raw data supporting the conclusions of this article will be made available by the authors, without undue reservation.

AUTHOR CONTRIBUTIONS

PV: conceptualization, problem design, investigation, literature survey, supervision, and writing—original draft. PV and HM writing—review and editing. All authors contributed to the article and approved the submitted version.

FUNDING

A part of this research was financially supported by the University of the Witwatersrand, RSA.

ACKNOWLEDGMENTS

PV thanks Prof. K. Yamashita for support. This work was conducted using the various facilities provided by the University of Tokyo.

SUPPLEMENTARY MATERIAL

The Supplementary Material for this article can be found online at: https://www.frontiersin.org/articles/10.3389/fchem.2020.00796/full#supplementary-material

REFERENCES

Alias, M. S., Dursun, I., Saidaminov, M. I., Diallo, E. M., Mishra, P., Ng, T. K., et al. (2016). Optical constants of $CH_3NH_3PbBr_3$ perovskite thin films measured by spectroscopic ellipsometry. *Opt. Express* 24, 16586–16594. doi: 10.1364/OE.24.016586

Anh, L. T., Wada, M., Fukui, H., Kawatsu, T., and Iitaka, T. (2019). First-principles calculations of the epsilon phase of solid oxygen. *Sci. Rep.* 9:8731. doi: 10.1038/s41598-019-45314-9

Aspnes, D. E., Kelso, S. M., Logan, R. A., and Bhat, R. (1986). Optical properties of AlxGa1–x As. *J. Appl. Phys.* 60, 754–767. doi: 10.1063/1.337426

Aspnes, D. E., and Studna, A. A. (1983). Dielectric functions and optical parameters of Si, Ge, GaP, GaAs, GaSb, InP, InAs, and InSb from 1.5 to 6.0 eV. *Phys. Rev. B* 27, 985–1009. doi: 10.1103/PhysRevB.27.985

Baranoski, G. V. G., and Krishnaswamy, A. (2010). *Light and Skin Interactions, Simulations for Computer Graphics Applications*. Amsterdam: Elsevier Inc.

Baroni, S., De Gironcoli, S., Dal Corso, A., and Giannozzi, P. (2001). Phonons and related crystal properties from density-functional perturbation theory. *Rev. Mod. Phys.* 73, 515–562. doi: 10.1103/RevModPhys.73.515

Bartel, C. J., Sutton, C., Goldsmith, B. R., Ouyang, R., Musgrave, C. B., Ghiringhelli, L. M., et al. (2019). New tolerance factor to predict the stability of perovskite oxides and halides. *Sci. Adv.* 5:eaav0693. doi: 10.1126/sciadv.aav0693

Belding, J., Gupta, S., and Kramer, R. *Investigation of Direct Band Gap Solar Cells Through the Use of Cs-Sb-Halide Double Perovskites*. Available online at: https://cpb-us-w2.wpmucdn.com/u.osu.edu/dist/e/45951/files/2018/04/hc3FinalReportPdf-v4s6d8.pdf (accessed April 19, 2020).

Bilbao Crystallographic Server. Available online at: https://www.cryst.ehu.es/ (accessed July 24, 2020).

Blöchl, P. E. (1994). Projector augmented-wave method. *Phys. Rev. B.* 50, 17953–17978. doi: 10.1103/PhysRevB.50.17953

Bokdam, M., Lahnsteiner, J., Ramberger, B., Schäfer, T., and Kresse, G. (2017). Assessing density functionals using many body theory for hybrid perovskites. *Phys. Rev. Lett.* 119:145501. doi: 10.1103/PhysRevLett.119.145501

Böni, P., Axe, J. D., Shirane, G., Birgeneau, R. J., Gabbe, D. R., Jenssen, H. P., et al. (1988). Lattice instability and soft phonons in single-crystal $La_{2-x}Sr_xCuO_4$. *Phys. Rev. B* 38, 185–194. doi: 10.1103/PhysRevB.38.185

Brese, N. E., and O'keeffe, M. (1991). Bond-valence parameters for solids. *Acta Cryst. B* 47, 192–197. doi: 10.1107/S0108768190011041

Brivio, F., Walker, A. B., and Walsh, A. (2013). Structural and electronic properties of hybrid perovskites for high-efficiency thin-film photovoltaics from first-principles. *APL Mater.* 1:042111. doi: 10.1063/1.4824147

Brown, I. D. (2017). What is the best way to determine bond-valence parameters? *IUCrJ* 4, 514–515. doi: 10.1107/S2052252517011782

Buda, I. G., Lane, C., Barbiellini, B., Ruzsinszky, A., Sun, J., and Bansil, A. (2017). Characterization of thin film materials using SCAN meta-GGA, an accurate nonempirical density functional. *Sci. Rep.* 7:44766. doi: 10.1038/srep44766

Cai, Y., Xie, W., Teng, Y. T., Harikesh, P. C., Ghosh, B., Huck, P., et al. (2019). High-throughput computational study of halide double perovskite inorganic compounds. *Chem. Mater.* 31, 5392–5401. doi: 10.1021/acs.chemmater.9b00116

Campochiaro, C., Mcclure, D. S., and Patterson, H. H. (1992). One- and two-photon spectroscopy of the hexafluoroplatinate(IV) ion. *Inorg. Chem.* 31, 2809–2813. doi: 10.1021/ic00039a027

Chakraborty, A., Dixit, M., Aurbach, D., and Major, D. T. (2018). Predicting accurate cathode properties of layered oxide materials using the SCAN meta-GGA density functional. *NPJ Comput. Mater.* 4:60. doi: 10.1038/s41524-018-0117-4

Chen, M., Ju, M.-G., Carl, A. D., Zong, Y., Grimm, R. L., Gu, J., et al. (2018). Cesium titanium(IV) bromide thin films based stable lead-free perovskite solar cells. *Joule* 2, 558–570. doi: 10.1016/j.joule.2018.01.009

Chu, L., Ahmad, W., Liu, W., Yang, J., Zhang, R., Sun, Y., et al. (2019). Lead-free halide double perovskite materials: a new superstar toward green and stable optoelectronic applications. *Nano-Micro Lett.* 11:16. doi: 10.1007/s40820-019-0244-6

De Lazaro, S. R., Ribeiro, R. A. P., and Lacerda, L. H. D. S. (2017). "Quantum chemistry applied to photocatalysis with TiO_2, titanium dioxide," ed M. Janus (IntechOpen). Available online at: https://www.intechopen.com/books/titanium-dioxide/quantum-chemistry-applied-to-photocatalysis-with-tio2

Dong, L., Jia, R., Xin, B., Peng, B., and Zhang, Y. (2017). Effects of oxygen vacancies on the structural and optical properties of β-Ga2O3. *Sci. Rep.* 7:40160. doi: 10.1038/srep40160

Dong, M., Zhang, J., and Yu, J. (2015). Effect of effective mass and spontaneous polarization on photocatalytic activity of wurtzite and zinc-blende ZnS. *APL Materials* 3:104404. doi: 10.1063/1.4922860

Dresselhaus, M. S. (2001). *Solid State Physics. Part II. Optical Properties of Solids*, Vol. 6. Lecture Notes, Massachusetts Institute of Technology, Cambridge, MA, USA.

Eaton, M., Catellani, A., and Calzolari, A. (2018). VO_2 as a natural optical metamaterial. *Opt. Express* 26, 5342–5357. doi: 10.1364/OE.26.005342

Eom, K., Kwon, U., Kalanur, S. S., Park, H. J., and Seo, H. (2017). Depth-resolved band alignments of perovskite solar cells with significant interfacial effects. *J. Mat. Chem. A* 5, 2563–2571. doi: 10.1039/C6TA09493G

Faraji, M., Sabzali, M., Yousefzadeh, S., Sarikhani, N., Ziashahabi, A., Zirak, M., et al. (2015). Band engineering and charge separation in the Mo1–xWxS2/TiO2 heterostructure by alloying: first principle prediction. *RSC Adv.* 5, 28460–28466. doi: 10.1039/C5RA00330J

Filip, M. R., Liu, X., Miglio, A., Hautier, G., and Giustino, F. (2018). Phase diagrams and stability of lead-free halide double perovskites Cs2BB′X6: B = Sb and Bi, B′ = Cu, Ag, and Au, and X = Cl, Br, and I. *J. Phys. Chem. C* 122, 158–170. doi: 10.1021/acs.jpcc.7b10370

Filip, M. R., Verdi, C., and Giustino, F. (2015). GW band structures and carrier effective masses of CH3NH3PbI3 and hypothetical perovskites of the type APbI3: A = NH4, PH4, AsH4, and SbH4. *J. Phys. Chem. C* 119, 25209–25219. doi: 10.1021/acs.jpcc.5b07891

Ford, P. C. (2016). From curiosity to applications. A personal perspective on inorganic photochemistry. *Chem. Sci.* 7, 2964–2986. doi: 10.1039/C6SC00188B

Frost, J. M., Butler, K. T., Brivio, F., Hendon, C. H., Van Schilfgaarde, M., and Walsh, A. (2014). Atomistic origins of high-performance in hybrid halide perovskite solar cells. *Nano Lett.* 14, 2584–2590. doi: 10.1021/nl500390f

Fu, H., and Zhao, Y. (2018). "9 - Efficiency droop in GaInN/GaN LEDs," in *Nitride Semiconductor Light-Emitting Diodes (LEDs)*, 2nd Edn, eds J. Huang, H.-C. Kuo, and S.-C. Shen (Cambridge: Woodhead Publishing), 299–325.

Gagné, O. C., and Hawthorne, F. C. (2015). Comprehensive derivation of bond-valence parameters for ion pairs involving oxygen. *Acta Cryst. B* 71, 562–578. doi: 10.1107/S2052520615016297

Ganose, A. M., Jackson, A. J., and Scanlon, D. O. (2018). Sumo: command-line tools for plotting and analysis of periodic *ab initio* calculations. *J. Open Source Software* 3:717. doi: 10.21105/joss.00717

Ganose, A. M., Savory, C. N., and Scanlon, D. O. (2017). Electronic and defect properties of (CH3NH3)2Pb(SCN)2I2 analogues for photovoltaic applications. *J. Mat. Chem. A* 5, 7845–7853. doi: 10.1039/C7TA01688C

Gonze, X. (1997). First-principles responses of solids to atomic displacements and homogeneous electric fields: Implementation of a conjugate-gradient algorithm. *Phys. Rev. B* 55, 10337–10354. doi: 10.1103/PhysRevB.55.10337

Gonze, X., and Lee, C. (1997). Dynamical matrices, born effective charges, dielectric permittivity tensors, and interatomic force constants from density-functional perturbation theory. *Phys. Rev. B* 55, 10355–10368. doi: 10.1103/PhysRevB.55.10355

Greul, E., Petrus, M. L., Binek, A., Docampo, P., and Bein, T. (2017). Highly stable, phase pure Cs2AgBiBr6 double perovskite thin films for optoelectronic applications. *J. Mater. Chem. A* 5, 19972–19981. doi: 10.1039/C7TA06816F

Habibi, M., and Eslamian, M. (2018). Facile and low-cost mechanical techniques for the fabrication of solution-processed polymer and perovskite thin film transistors. *J. Phys. Commun.* 2:075018. doi: 10.1088/2399-6528/aad3a6

Haines, J., Léger, J. M., and Bocquillon, G. (2001). Synthesis and design of superhard materials. *Ann. Rev. Mat. Res.* 31, 1–23. doi: 10.1146/annurev.matsci.31.1.1

Hartmann, H., Mach, R., and Selle, B. (1982). "Wide Gap II-VI compounds as electronic materials," in *Current Topics in Material Science,* ed E. Kaldis (Amsterdam: Oxford: North-Holland), 18.

Hedin, L. (1965). New method for calculating the one-particle green's function with application to the electron-gas problem. *Phys. Rev.* 139, A796–A823. doi: 10.1103/PhysRev.139.A796

Hirasawa, M., Ishihara, T., Goto, T., Uchida, K., and Miura, N. (1994). Magnetoabsorption of the lowest exciton in perovskite-type

compound (CH3NH3)PbI3. *Phys. B Cond. Matter* 201, 427–430. doi: 10.1016/0921-4526(94)91130-4

Hoye, R. L. Z., Eyre, L., Wei, F., Brivio, F., Sadhanala, A., Sun, S., et al. (2018). Fundamental carrier lifetime exceeding 1 μs in Cs2AgBiBr6 double perovskite. *Adv. Mater. Interfaces* 5:1800464. doi: 10.1002/admi.201800464

Ivanovskii, A. L. (2012). Mechanical and electronic properties of diborides of transition 3d−5d metals from first principles: Toward search of novel ultra-incompressible and superhard materials. *Prog. Mat. Sci.* 57, 184–228. doi: 10.1016/j.pmatsci.2011.05.004

Jain, A., Voznyy, O., and Sargent, E. H. (2017). High-throughput screening of lead-free perovskite-like materials for optoelectronic applications. *J. Phys. Chem. C* 121, 7183–7187. doi: 10.1021/acs.jpcc.7b02221

Jana, M. K., Janke, S. M., Dirkes, D. J., Dovletgeldi, S., Liu, C., Qin, X., et al. (2019). Direct-bandgap 2D silver–bismuth iodide double perovskite: the structure-directing influence of an oligothiophene spacer cation. *J. Am. Chem. Soc.* 141, 7955–7964. doi: 10.1021/jacs.9b02909

Jellison, G. E. (1992). Optical functions of GaAs, GaP, and Ge determined by two-channel polarization modulation ellipsometry. *Opt. Mater.* 1, 151–160. doi: 10.1016/0925-3467(92)90022-F

Ji, C., Wu, Z., Lu, L., Wu, X., Wang, J., Liu, X., et al. (2018). High thermochromic performance of Fe/Mg co-doped VO2 thin films for smart window applications. *J. Mat. Chem. C* 6, 6502–6509. doi: 10.1039/C8TC01111G

Johnson, R. A. (1988). Analytic nearest-neighbor model for fcc metals. *Phys. Rev. B* 37, 3924–3931. doi: 10.1103/PhysRevB.37.3924

Jong, U.-G., Yu, C.-J., Kim, Y.-S., Kye, Y.-H., and Kim, C.-H. (2018). First-principles study on the material properties of the inorganic perovskite $Rb_{1-x}Cs_xPbI_3$ for solar cell applications. *Phys. Rev. B* 98:125116. doi: 10.1103/PhysRevB.98.125116

Jong, U.-G., Yu, C.-J., Ri, J.-S., Kim, N.-H., and Ri, G.-C. (2016). Influence of halide composition on the structural, electronic, and optical properties of mixed $CH_3NH_3Pb(I_{1-x}Br_x)3$ perovskites calculated using the virtual crystal approximation method. *Phys. Rev. B* 94:125139. doi: 10.1103/PhysRevB.94.125139

Kachare, A. H., Spitzer, W. G., and Fredrickson, J. E. (1976). Refractive index of ion-implanted GaAs. *J. Appl. Phys.* 47, 4209–4212. doi: 10.1063/1.323292

Kagdada, H. L., Jha, P. K., Spiewak, P., and Kurzydłowski, K.J. (2018). Structural stability, dynamical stability, thermoelectric properties, and elastic properties of GeTe at high pressure. *Phys. Rev. B* 97:134105. doi: 10.1103/PhysRevB.97.134105

Kamran, S., Chen, K., and Chen, L. (2009). *Ab initio* examination of ductility features of fcc metals. *Phys. Rev. B* 79:024106. doi: 10.1103/PhysRevB.79.024106

Kao, K. C. (2004). "3 - Optical and electro-optic processes," in *Dielectric Phenomena in Solids,* ed K.C. Kao (San Diego, CA: Academic Press), 115–212.

Khatri, H., Aryae, K., Collins, R. W., and Marsillac, S. (2011). *Electronic and Structural Properties of Copper Selenide (Cu2_xSe) Thin Films as Determined by in-situ Real-Time and ex-situ Characterization*. IEEE. Available online at: https://www.researchgate.net/publication/261086174_Electronic_and_structural_properties_of_copper_selenide_Cu2-xSe_thin_films_as_determined_by_in-situ_real-time_and_ex-situ_characterization (accessed April 26, 2020).

Kirchartz, T., Markvart, T., Rau, U., and Egger, D. A. (2018). Impact of small phonon energies on the charge-carrier lifetimes in metal-halide perovskites. *J. Phys. Chem. Lett.* 9, 939–946. doi: 10.1021/acs.jpclett.7b03414

Kitamura, R., Pilon, L., and Jonasz, M. (2007). Optical constants of silica glass from extreme ultraviolet to far infrared at near room temperature. *Appl. Opt.* 46, 8118–8133. doi: 10.1364/AO.46.008118

Kresse, G., and Furthmüller, J. (1996a). Efficiency of *ab-initio* total energy calculations for metals and semiconductors using a plane-wave basis set. *Comput. Mat. Sci.* 6, 15–50. doi: 10.1016/0927-0256(96)00008-0

Kresse, G., and Furthmüller, J. (1996b). Efficient iterative schemes for *ab initio* total-energy calculations using a plane-wave basis set. *Phys. Rev. B* 54:11169. doi: 10.1103/PhysRevB.54.11169

Krukau, A. V., Vydrov, O. A., Izmaylov, A. F., and Scuseria, G. E. (2006). Influence of the exchange screening parameter on the performance of screened hybrid functionals. *J. Chem. Phys.* 125:224106. doi: 10.1063/1.2404663

Kumar, M., Jain, M., Singh, A., and Bhattacharya, S. (2020). *Bandgap Engineering by Sublattice Mixing in Cs2AgInCl6: High-throughput Screening from First-principles*. Available online at: https://arxiv.org/abs/2004.07991

Lamba, R. S., Basera, P., Bhattacharya, S., and Sapra, S. (2019). Band gap engineering in Cs2(NaxAg1–x)BiCl6 double perovskite nanocrystals. *J. Phys. Chem. Lett.* 10, 5173–5181. doi: 10.1021/acs.jpclett.9b02168

Leguy, A. M. A., Azarhoosh, P., Alonso, M. I., Campoy-Quiles, M., Weber, O. J., Yao, J., et al. (2016a). Experimental and theoretical optical properties of methylammonium lead halide perovskites. *Nanoscale* 8, 6317–6327. doi: 10.1039/C5NR05435D

Leguy, A. M. A., Goñi, A. R., Frost, J. M., Skelton, J., Brivio, F., Rodríguez-Martínez, X., et al. (2016b). Dynamic disorder, phonon lifetimes, and the assignment of modes to the vibrational spectra of methylammonium lead halide perovskites. *Phys. Chem. Chem. Phys.* 18, 27051–27066. doi: 10.1039/C6CP03474H

Lei, L.-Z., Shi, Z.-F., Li, Y., Ma, Z.-Z., Zhang, F., Xu, T.-T., et al. (2018). High-efficiency and air-stable photodetectors based on lead-free double perovskite Cs2AgBiBr6 thin films. *J. Mater. Chem. C* 6, 7982–7988. doi: 10.1039/C8TC02305K

Li, C., Soh, K. C. K., and Wu, P. (2004). Formability of ABO3 perovskites. *J. Alloys Cmpds* 372, 40–48. doi: 10.1016/j.jallcom.2003.10.017

Li, H., Shan, X., Neu, J. N., Geske, T., Davis, M., Mao, P., et al. (2018). Lead-free halide double perovskite-polymer composites for flexible X-ray imaging. *J. Mater. Chem. C* 6, 11961–11967. doi: 10.1039/C8TC01564C

Li, L., Wang, W., Liu, H., Liu, X., Song, Q., and Ren, S. (2009). First principles calculations of electronic band structure and optical properties of Cr-doped ZnO. *J. Phys. Chem. C* 113, 8460–8464. doi: 10.1021/jp811507r

Li, T., Zhao, X., Yang, D., Du, M.-H., and Zhang, L. (2018). Intrinsic defect properties in halide double perovskites for optoelectronic applications. *Phys. Rev. Appl.* 10:041001. doi: 10.1103/PhysRevApplied.10.041001

Li, Y., and Yang, K. (2019). High-throughput computational design of organic–inorganic hybrid halide semiconductors beyond perovskites for optoelectronics. *Energy Environ. Sci.* 12, 2233–2243. doi: 10.1039/C9EE01371G

Liu, X., Gu, J., Shen, Y., and Li, J. (2016). Crystal metamorphosis at stress extremes: how soft phonons turn into lattice defects. *NPG Asia Mater.* 8:e320. doi: 10.1038/am.2016.154

Liu, X., Hong, R., and Tian, C. (2008). Tolerance factor and the stability discussion of ABO3-type ilmenite. *J. Mater. Sci. Mater. Electron.* 20:323. doi: 10.1007/s10854-008-9728-8

Locardi, F., Cirignano, M., Baranov, D., Dang, Z., Prato, M., Drago, F., et al. (2018). Colloidal synthesis of double perovskite Cs2AgInCl6 and Mn-doped Cs2AgInCl6 nanocrystals. *J. Am. Chem. Soc.* 140, 12989–12995. doi: 10.1021/jacs.8b07983

Löper, P., Stuckelberger, M., Niesen, B., Werner, J., Filipič, M., Moon, S.-J., et al. (2015). Complex refractive index spectra of CH3NH3PbI3 perovskite thin films determined by spectroscopic ellipsometry and spectrophotometry. *J. Phys. Chem. Lett.* 6, 66–71. doi: 10.1021/jz502471h

Lu, X., Zhao, Z., Li, K., Han, Z., Wei, S., Guo, C., et al. (2016). First-principles insight into the photoelectronic properties of Ge-based perovskites. *RSC Adv.* 6, 86976–86981. doi: 10.1039/C6RA18534G

Luo, J., Wang, X., Li, S., Liu, J., Guo, Y., Niu, G., et al. (2018). Efficient and stable emission of warm-white light from lead-free halide double perovskites. *Nature* 563, 541–545. doi: 10.1038/s41586-018-0691-0

Luo, L., Men, L., Liu, Z., Mudryk, Y., Zhao, X., Yao, Y., et al. (2017). Ultrafast terahertz snapshots of excitonic Rydberg states and electronic coherence in an organometal halide perovskite. *Nature Commun.* 8:15565. doi: 10.1038/ncomms15565

Ma, X., Li, D., Zhao, S., Li, G., and Yang, K. (2014). The electronic and optical properties of quaternary GaAs1-x-yNxBiyalloy lattice-matched to GaAs: a first-principles study. *Nanoscale Res. Lett.* 9:580. doi: 10.1186/1556-276X-9-580

Makarov, S., Furasova, A., Tiguntseva, E., Hemmetter, A., Berestennikov, A., Pushkarev, A., et al. (2019). Halide-perovskite nanophotonics: halide-perovskite resonant nanophotonics. *Adv. Opt. Mat.* 7:1970002. doi: 10.1002/adom.201970002

Malitson, I. H. (1965). Interspecimen comparison of the refractive index of fused silica*,†. *J. Opt. Soc. Am.* 55, 1205–1209. doi: 10.1364/JOSA.55.001205

Matthews, P. D., Lewis, D. J., and O'brien, P. (2017). Updating the road map to metal-halide perovskites for photovoltaics. *J. Mater. Chem. A* 5, 17135–17150. doi: 10.1039/C7TA04544A

Mcclure, E. T., Ball, M. R., Windl, W., and Woodward, P. M. (2016). Cs2AgBiX6 (X = Br, Cl): new visible light absorbing, lead-free

halide perovskite semiconductors. *Chem. Mater.* 28, 1348–1354. doi: 10.1021/acs.chemmater.5b04231

Meng, W., Wang, X., Xiao, Z., Wang, J., Mitzi, D. B., and Yan, Y. (2017). Parity-forbidden transitions and their impact on the optical absorption properties of lead-free metal halide perovskites and double perovskites. *J. Phys. Chem. Lett.* 8, 2999–3007. doi: 10.1021/acs.jpclett.7b01042

Mohamed, B., Allel, M., Bendouma, D., Miloud, B., and Baghdad, M. (2018). Improved electronic structure and optical performance of Bi2Te3-xSex from first-principle calculations within TB-mBJ exchange potential. *Mater. Res.* 21:e20170553. doi: 10.1590/1980-5373-mr-2017-0553

Monserrat, B. (2018). Electron–phonon coupling from finite differences. *J. Phys Condens. Matter* 30:083001. doi: 10.1088/1361-648X/aaa737

Morkoc, H. (2009). *Handbook of Nitride Semiconductors and Devices*. Weinheim: Wiley-VCH GmbH and Co.

Mouhat, F., and Coudert, F.-X. (2014). Necessary and sufficient elastic stability conditions in various crystal systems. *Phys. Rev. B* 90:224104. doi: 10.1103/PhysRevB.90.224104

Murtaza, G., Ahmad, I., Amin, B., Afaq, A., Maqbool, M., Maqssod, J., et al. (2011). Investigation of structural and optoelectronic properties of BaThO3. *Opt. Mater.* 33, 553–557. doi: 10.1016/j.optmat.2010.10.052

Nakanishi, N., Nagasawa, A., and Murakami, Y. (1982). Lattice stability and soft modes. *J. Phys. Colloques* 43, C4-35–C34-55. doi: 10.1051/jphyscol:1982403

Nandha, K. N., and Nag, A. (2018). Synthesis and luminescence of Mn-doped Cs2AgInCl6 double perovskites. *Chem. Commun.* 54, 5205–5208. doi: 10.1039/C8CC01982G

Niemann, R. G., Kontos, A. G., Palles, D., Kamitsos, E. I., Kaltzoglou, A., Brivio, F., et al. (2016). Halogen effects on ordering and bonding of $CH_3NH_3^+$ in $CH_3NH_3PbX_3$ (X = Cl, Br, I) hybrid perovskites: a vibrational spectroscopic study. *J. Phys. Chem. C* 120, 2509–2519. doi: 10.1021/acs.jpcc.5b11256

Opoku, F., Govender, K. K., Van Sittert, C. G. C. E., and Govender, P. P. (2017). Understanding the mechanism of enhanced charge separation and visible light photocatalytic activity of modified wurtzite ZnO with nanoclusters of ZnS and graphene oxide: from a hybrid density functional study. *New J. Chem.* 41, 8140–8155. doi: 10.1039/C7NJ01942D

Pan, Y., and Guan, W. M. (2017). Probing the balance between ductility and strength: transition metal silicides. *Phys. Chem. Chem. Phys.* 19, 19427–19433. doi: 10.1039/C7CP03182C

Park, C. R. (2019). *Advanced Thermoelectric Materials*. Beverly, MA: Scrivener Publishing (Wiley).

Peng, H., Yang, Z.-H., Perdew, J. P., and Sun, J. (2016). Versatile van der waals density functional based on a meta-generalized gradient approximation. *Phys. Rev. X* 6:041005. doi: 10.1103/PhysRevX.6.041005

Peng, W., Li, X., and Du, J. (2013). First Principles investigations on structural, elastic, electronic, and optical properties of Li_2CdGeS_4. *Mater. Trans.* 54, 2167–2172. doi: 10.2320/matertrans.M2013186

Perdew, J. P., Burke, K., and Ernzerhof, M. (1996). Generalized gradient approximation made simple. *Phys. Rev. Lett.* 77, 3865–3868. doi: 10.1103/PhysRevLett.77.3865

Perdew, J. P., Ruzsinszky, A., Csonka, G. I., Vydrov, O. A., Scuseria, G. E., Constantin, L. A., et al. (2008). Restoring the density-gradient expansion for exchange in solids and surfaces. *Phys. Rev. Lett.* 100:136406. doi: 10.1103/PhysRevLett.100.136406

Pham, H. Q., Holmes, R. J., Aydil, E. S., and Gagliardi, L. (2019). Lead-free double perovskites Cs2InCuCl6 and (CH3NH3)2InCuCl6: electronic, optical, and electrical properties. *Nanoscale* 11, 11173–11182. doi: 10.1039/C9NR01645G

Popova, S., Tolstykh, T., and Vorobev, V. (1972). Optical characteristics of amorphous quartz in the 1400–200 cm^{-1} region. *Opt. Spectrosc.* 33, 444–445.

Pugh, S. F. (1954). XCII. Relations between the elastic moduli and the plastic properties of polycrystalline pure metals. London, Edinburgh, and Dublin. *Phil. Mag. J. Sci.* 45, 823–843. doi: 10.1080/14786440808520496

Qijingzheng pyband. Available online at: https://github.com/QijingZheng/pyband (accessed April 20, 2020)

Refractiveindex.Info. *Refractive Index Database*. Available online at: https://refractiveindex.info/?shelf=mainandbook=Siandpage=Aspnes (accessed April 27, 2020).

Rühle, S. (2016). Tabulated values of the Shockley–Queisser limit for single junction solar cells. *Solar Energy* 130, 139–147. doi: 10.1016/j.solener.2016.02.015

Saini, P. K., Ahlawat, D., and Singh, D. (2017). Study of electronic structure and optical properties of zinc-blende and rocksalt structures of HgSe : A DFT study. *J. Metal. Mat. Sci.* 59, 29–37.

Salinas-Sanchez, A., Garcia-Muñoz, J. L., Rodriguez-Carvajal, J., Saez-Puche, R., and Martinez, J. L. (1992). Structural characterization of R2BaCuO5 (R = Y, Lu, Yb, Tm, Er, Ho, Dy, Gd, Eu and Sm) oxides by X-ray and neutron diffraction. *J. Solid State Chem.* 100, 201–211. doi: 10.1016/0022-4596(92)90094-C

Saraf, R., and Maheshwari, V. (2018). Self-powered photodetector based on electric-field-induced effects in MAPbI3 perovskite with improved stability. *ACS App. Mater. Interfaces* 10, 21066–21072. doi: 10.1021/acsami.8b05860

Savory, C. N., Ganose, A. M., Travis, W., Atri, R. S., Palgrave, R. G., and Scanlon, D. O. (2016a). An assessment of silver copper sulfides for photovoltaic applications: theoretical and experimental insights. *J. Mat. Chem. A* 4, 12648–12657. doi: 10.1039/C6TA03376H

Savory, C. N., Walsh, A., and Scanlon, D. O. (2016b). Can Pb-free halide double perovskites support high-efficiency solar cells? *ACS Energy Lett.* 1, 949–955. doi: 10.1021/acsenergylett.6b00471

Schubert, E. F., Kim, J. K., and Xi, J.-Q. (2007). Low-refractive-index materials: a new class of optical thin-film materials. *Phys. Stat. Sol.* 244, 3002–3008. doi: 10.1002/pssb.200675603

Shannon, R. D. (1976). Revised effective ionic radii and systematic studies of interatomic distances in halides and chalcogenides. *Acta Cryst. A*32, 751–767. doi: 10.1107/S0567739476001551

Shockley, W., and Queisser, H. J. (1961). Detailed balance limit of efficiency of p-n junction solar cells. *J. Appl. Phys.* 32, 510–519. doi: 10.1063/1.1736034

Singh, S., Valencia-Jaime, I., and Romero, A. H. (2018). Effect of spin-orbit coupling on the elastic, mechanical, and thermodynamic properties of Bi-Sb binaries. *Phys. Rev. B* 97:054108. doi: 10.1103/PhysRevB.97.054108

Skauli, T., Kuo, P. S., Vodopyanov, K. L., Pinguet, T. J., Levi, O., Eyres, L. A., et al. (2003). Improved dispersion relations for GaAs and applications to nonlinear optics. *J. Appl. Phys.* 94, 6447–6455. doi: 10.1063/1.1621740

Slavney, A. H., Hu, T., Lindenberg, A. M., and Karunadasa, H. I. (2016). A Bismuth-Halide double perovskite with long carrier recombination lifetime for photovoltaic applications. *J. Am. Chem. Soc.* 138, 2138–2141. doi: 10.1021/jacs.5b13294

Slavney, A. H., Leppert, L., Saldivar Valdes, A., Bartesaghi, D., Savenije, T. J., Neaton, J. B., et al. (2018). Small-band-gap halide double perovskites. *Angew Chem. Int. Edn.* 57, 12765–12770. doi: 10.1002/anie.201807421

Spoonhower, J. P., Burberry, M. S., and Baxter, S. M. (1986). Infrared radiative recombination in Rh3+?doped AgBr. *Solid State Commun.* 59, 843–849. doi: 10.1016/0038-1098(86)90641-1

Stoumpos, C. C., Frazer, L., Clark, D. J., Kim, Y. S., Rhim, S. H., Freeman, A. J., et al. (2015). Hybrid germanium iodide perovskite semiconductors: active lone pairs, structural distortions, direct and indirect energy gaps, and strong nonlinear optical properties. *J. Am. Chem. Soc.* 137, 6804–6819. doi: 10.1021/jacs.5b01025

Sun, J., Remsing, R. C., Zhang, Y., Sun, Z., Ruzsinszky, A., Peng, H., et al. (2016). Accurate first-principles structures and energies of diversely bonded systems from an efficient density functional. *Nat. Chem.* 8, 831–836. doi: 10.1038/nchem.2535

Sun, J., Ruzsinszky, A., and Perdew, J. P. (2015). Strongly constrained and appropriately normed semilocal density functional. *Phys. Rev. Lett.* 115:036402. doi: 10.1103/PhysRevLett.115.036402

Sun, P.-P., Li, Q.-S., Yang, L.-N., and Li, Z.-S. (2016). Theoretical insights into a potential lead-free hybrid perovskite: substituting Pb2+ with Ge2+. *Nanoscale* 8, 1503–1512. doi: 10.1039/C5NR05337D

Tan, C. Z. (1998). Determination of refractive index of silica glass for infrared wavelengths by IR spectroscopy. *J. Non-Cryst. Solids* 223, 158–163. doi: 10.1016/S0022-3093(97)00438-9

Tan, Z., Li, J., Zhang, C., Li, Z., Hu, Q., Xiao, Z., et al. (2018). Highly efficient blue-emitting bi-doped Cs2SnCl6 perovskite variant: photoluminescence induced by impurity doping. *Adv. Funct. Mater.* 28:1801131. doi: 10.1002/adfm.201801131

Tanabe, Y., and Sugano, S. (1954). On the absorption spectra of complex ions. *I. J. Phys. Soc. Jpn.* 9, 753–766. doi: 10.1143/JPSJ.9.753

Tang, Z., Bessho, T., Awai, F., Kinoshita, T., Maitani, M. M., Jono, R., et al. (2017). Hysteresis-free perovskite solar cells made of potassium-doped organometal halide perovskite. *Sci. Rep.* 7:12183. doi: 10.1038/s41598-017-12436-x

Thompson, R. P., and Clegg, W. J. (2018). Predicting whether a material is ductile or brittle. *Curr. Opinion Solid State Mat. Sci.* 22, 100–108. doi: 10.1016/j.cossms.2018.04.001

Togo, A., and Tanaka, I. (2015). First principles phonon calculations in materials science. *Scripta Mater.* 108, 1–5. doi: 10.1016/j.scriptamat.2015.07.021

Tran, T. T., Panella, J. R., Chamorro, J. R., Morey, J. R., and Mcqueen, T. M. (2017). Designing indirect–direct bandgap transitions in double perovskites. *Mater. Horizons* 4, 688–693. doi: 10.1039/C7MH00239D

Umadevi, D., and Watson, G. W. (2019). Quasiparticle GW Calculations on lead-free hybrid germanium iodide perovskite CH3NH3GeI3 for photovoltaic applications. *ACS Omega* 4, 5661–5669. doi: 10.1021/acsomega.8b03291

Van schilfgaarde, M., Kotani, T., and Faleev, S. (2006). Quasiparticle self-consistent GW theory. *Phys. Rev. Lett.* 96:226402. doi: 10.1103/PhysRevLett.96.226402

Varadwaj, A., Varadwaj, P. R., and Yamashita, K. (2018). Revealing the chemistry between band gap and binding energy for lead-/tin-based trihalide perovskite solar cell semiconductors. *ChemSusChem* 11, 449–463. doi: 10.1002/cssc.201701653

VASP (2020a). *Bandgap of Si in GW*. Available online at: https://www.vasp.at/wiki/index.php/Bandgap_of_Si_in_GW (accessed July 25, 2020).

VASP (2020b). *Ionic Contributions to the Frequency Dependent Dielectric Function of NaCl*. Available online at: https://www.vasp.at/wiki/index.php/Ionic_contributions_to_the_frequency_dependent_dielectric_function_of_NaCl#cite_note-gajdos:prb:2006-1 (accessed April 20, 2020).

VASP (2020c). *LPEAD*. Available online at: https://www.vasp.at/wiki/index.php/LPEAD (accessed July 26, 2020).

VASP (2020d). *Phonons From Finite Differences*. Available online at: https://www.vasp.at/wiki/index.php/Phonons_from_finite_differences (accessed July 28, 2020).

VASP (2020e). *Si_Bandstructure*. Available online at: https://www.vasp.at/wiki/index.php/Si_bandstructure (accessed April 20, 2020).

Volonakis, G., Haghighirad, A. A., Milot, R. L., Sio, W. H., Filip, M. R., Wenger, B., et al. (2017). $Cs_2InAgCl_6$: a new lead-free halide double perovskite with direct band gap. *J. Phys. Chem. Lett.* 8, 772–778. doi: 10.1021/acs.jpclett.6b02682

Walsh, A. (2015). Principles of chemical bonding and band gap engineering in hybrid organic–inorganic halide perovskites. *J. Phys Chem. C* 119, 5755–5760. doi: 10.1021/jp512420b

Wang, H.-C., Pistor, P., Marques, M.,a,.L., and Botti, S. (2019). Double perovskites as p-type conducting transparent semiconductors: a high-throughput search. *J. Mat. Chem. A* 7, 14705–14711. doi: 10.1039/C9TA01456J

Wang, Q., Hu, Z., and Shao, X. (2020). Exploring electronic, optoelectronic, and thermoelectric properties of ternary compound MgSrSe2 from first-principles study. *AIP Adv.* 10:045010. doi: 10.1063/5.0002946

Wang, Z., Ganose, A. M., Niu, C., and Scanlon, D. O. (2019). Two-dimensional eclipsed arrangement hybrid perovskites for tunable energy level alignments and photovoltaics. *J. Mat. Chem. C* 7, 5139–5147. doi: 10.1039/C9TC01325C

Wei, F., Deng, Z., Sun, S., Hartono, N. T. P., Seng, H. L., Buonassisi, T., et al. (2019). Enhanced visible light absorption for lead-free double perovskite Cs2AgSbBr6. *Chem. Commun.* 55, 3721–3724. doi: 10.1039/C9CC01134J

Wen, H., Cheng, B.-M., and Tanner, P. A. (2017). Optical properties of selected 4d and 5d transition metal ion-doped glasses. *RSC Adv.* 7, 26411–26419. doi: 10.1039/C7RA04062H

Wilson, J. N., Frost, J. M., Wallace, S. K., and Walsh, A. (2019). Dielectric and ferroic properties of metal halide perovskites. *APL Mater.* 7:010901. doi: 10.1063/1.5079633

Xiao, Z., Du, K.-Z., Meng, W., Wang, J., Mitzi, D. B., and Yan, Y. (2017). Intrinsic instability of Cs2In(I)M(III)X6 (M = Bi, Sb; X = Halogen) double perovskites: a combined density functional theory and experimental study. *J. Am. Chem. Soc.* 139, 6054–6057. doi: 10.1021/jacs.7b02227

Xu, B., Li, X., Sun, J., and Yi, L. (2008). Electronic structure, ferroelectricity and optical properties of CaBi2Ta2O9. *Eur. Phys. J. B* 66, 483–487. doi: 10.1140/epjb/e2008-00461-9

Xu, Q., Yang, D., Lv, J., Sun, Y.-Y., and Zhang, L. (2018). Perovskite solar absorbers: materials by design. *Small Methods* 2:1700316. doi: 10.1002/smtd.201700316

Yamada, I., Takamatsu, A., and Ikeno, H. (2018). Complementary evaluation of structure stability of perovskite oxides using bond-valence and density-functional-theory calculations. *Sci. Tech. Adv. Mater.* 19, 101–107. doi: 10.1080/14686996.2018.1430449

Yang, B., Mao, X., Hong, F., Meng, W., Tang, Y., Xia, X., et al. (2018). Lead-free direct band gap double-perovskite nanocrystals with bright dual-color emission. *J. Am. Chem. Soc.* 140, 17001–17006. doi: 10.1021/jacs.8b07424

Yang, J., Wen, X., Xia, H., Sheng, R., Ma, Q., Kim, J., et al. (2017). Acoustic-optical phonon up-conversion and hot-phonon bottleneck in lead-halide perovskites. *Nat. Commun.* 8:14120. doi: 10.1038/ncomms14120

Yao, Y., Kou, B., Peng, Y., Wu, Z., Li, L., Wang, S., et al. (2020). (C3H9NI)4AgBiI8: a direct-bandgap layered double perovskite based on a short-chain spacer cation for light absorption. *Chem. Commun.* 56, 3206–3209. doi: 10.1039/C9CC07796K

Yu, C.-J. (2019). Advances in modelling and simulation of halide perovskites for solar cell applications. *J. Phys. Energ* 1:022001. doi: 10.1088/2515-7655/aaf143

Zangwill, A. (2019). *Modern Electrodynamics*. Cambridge: Cambridge University Press.

Zhang, H., Liu, L., and Zhou, Z. (2012a). First-principles studies on facet-dependent photocatalytic properties of bismuth oxyhalides (BiOXs). *RSC Adv.* 2, 9224–9229. doi: 10.1039/c2ra20881d

Zhang, H., Liu, L., and Zhou, Z. (2012b). Towards better photocatalysts: first-principles studies of the alloying effects on the photocatalytic activities of bismuth oxyhalides under visible light. *Phys. Chem. Chem. Phys.* 14, 1286–1292. doi: 10.1039/C1CP23516H

Zhang, M., Zhang, X., Lin, H.-Q., and Lu, G. (2019). Radiative recombination of large polarons in halide perovskites. *J. Phys. Condens. Matter* 31:165701. doi: 10.1088/1361-648X/ab0158

Zhang, Y., Kitchaev, D. A., Yang, J., Chen, T., Dacek, S. T., Sarmiento-Pérez, R. A., et al. (2018). Efficient first-principles prediction of solid stability: towards chemical accuracy. *NPJ Comput. Mater.* 4:9. doi: 10.1038/s41524-018-0065-z

Zhao, F., Song, Z., Zhao, J., and Liu, Q. (2019). Double perovskite Cs2AgInCl6:Cr3+: broadband and near-infrared luminescent materials. *Inorg. Chem. Front.* 6, 3621–3628. doi: 10.1039/C9QI00905A

Zhao, S., Yamamoto, K., Iikubo, S., Hayase, S., and Ma, T. (2018). First-principles study of electronic and optical properties of lead-free double perovskites Cs2NaBX6 (B = Sb, Bi; X = Cl, Br, I). *J. Phys. Chem. Solids* 117, 117–121. doi: 10.1016/j.jpcs.2018.02.032

Zhao, X.-G., Yang, D., Sun, Y., Li, T., Zhang, L., Yu, L., et al. (2017). Cu–In Halide perovskite solar absorbers. *J. Am. Chem. Soc.* 139, 6718–6725. doi: 10.1021/jacs.7b02120

Zhao, Y.-Q., Liu, B., Yu, Z.-L., Ma, J., Qiang, W., He, P.-B., et al. (2017). Strong ferroelectric polarization of CH3NH3GeI3 with high-absorption and mobility transport anisotropy: theoretical study. *J. Mat. Chem. C* 5, 5356–5364. doi: 10.1039/C7TC01166K

Zhou, J., Rong, X., Molokeev, M. S., Zhang, X., and Xia, Z. (2018). Exploring the transposition effects on the electronic and optical properties of Cs2AgSbCl6via a combined computational-experimental approach. *J. Mat. Chem. A* 6, 2346–2352. doi: 10.1039/C7TA10062K

Zhou, J., Rong, X., Zhang, P., Molokeev, M. S., Wei, P., Liu, Q., et al. (2019). Manipulation of Bi3+/In3+ transmutation and Mn2+-doping effect on the structure and optical properties of double perovskite Cs2NaBi1-xInxCl6. *Adv. Opt. Mat.* 7:1801435. doi: 10.1002/adom.201801435

Zhou, J., Xia, Z., Molokeev, M. S., Zhang, X., Peng, D., and Liu, Q. (2017). Composition design, optical gap and stability investigations of lead-free halide double perovskite Cs2AgInCl6. *J. Mater. Chem. A* 5, 15031–15037. doi: 10.1039/C7TA04690A

Zhou, Y., Askar, A. M., Pöhls, J.-H., Iyer, A. K., Oliynyk, A. O., Shankar, K., et al. (2019). Hexagonal double perovskite Cs2AgCrCl6. *Z. Anorg. Allg. Chem.* 645, 323–328. doi: 10.1002/zaac.201800351

Conflict of Interest: The authors declare that the research was conducted in the absence of any commercial or financial relationships that could be construed as a potential conflict of interest.

frontiers in Chemistry

ORIGINAL RESEARCH
published: 09 November 2020
doi: 10.3389/fchem.2020.575288

Preparation of Ni_3Fe_2@NC/CC Integrated Electrode and Its Application in Zinc-Air Battery

Hui Hu[1,2], *Xiaofei Ling*[2], *Chaogui Tan*[1], *Jianguo Lin*[1], *Xiaopeng Han*[2*] *and Wenbin Hu*[2*]

[1] School of Materials Science and Engineering, Xiangtan University, Xiangtan, China, [2] Tianjin Key Laboratory of Composite and Functional Materials, School of Materials Science and Engineering, Tianjin University, Tianjin, China

Reasonable design and development of a low-cost and high-efficiency bifunctional electrocatalyst for oxygen evolution reaction (OER) and oxygen reduction reaction (ORR) is essential for promoting the development of Zinc-air battery technology. Herein, we obtained an integrated catalytic electrode, NiFe nanoparticles supported on nitrogen-doped carbon (NC) directly grown on the carbon cloth (designated as Ni_3Fe_2@NC/CC), by pyrolysis of bimetallic NiFe metal-organic framework (MOF) precursor. There is a synergistic effect between nickel and iron component, which enhances the bifunctional catalytic activity. In addition, the underlying carbon cloth is conducive to the efficient electron transfer and also benefits the uniform loading of catalytically active materials. Thus, the integrated electrode shows good OER/ORR dual-functional catalytic performance, and the OER overpotential is much lower than that of the traditional drop-coating electrode and precious metal catalyst (IrO_2). Moreover, the Ni_3Fe_2@NC/CC integrated electrode used in zinc-air batteries shows good flexibility and cycle stability. Our findings provide a new avenue for the development of efficient and stable bifunctional oxygen electrocatalysts.

Keywords: zinc-air battery, integrated electrode, NiFe nanoparticle, nitrogen-doped carbon, OER/ORR

OPEN ACCESS

Edited by:
Hongbo Li,
Beijing Institute of Technology, China

Reviewed by:
Khaled Mohammad Saoud,
Virginia Commonwealth University School of the Arts, Qatar
Bao Yu Xia,
Huazhong University of Science and Technology, China

***Correspondence:**
Xiaopeng Han
xphan@tju.edu.cn
Wenbin Hu
wbhu@tju.edu.cn

Specialty section:
This article was submitted to Nanoscience, a section of the journal Frontiers in Chemistry

Received: *23 June 2020*
Accepted: *12 October 2020*
Published: *09 November 2020*

Citation:
Hu H, Ling X, Tan C, Lin J, Han X and Hu W (2020) Preparation of Ni_3Fe_2@NC/CC Integrated Electrode and Its Application in Zinc-Air Battery. Front. Chem. 8:575288. doi: 10.3389/fchem.2020.575288

INTRODUCTION

The crisis from environmental and energy issues have driven the research and development of new energy technologies on a global scale (Poizot and Dolhem, 2011; Larcher and Tarascon, 2015; Chu et al., 2016; Stamenkovic et al., 2016; Li and Wang, 2019; Chen et al., 2020). Among new energy technologies, sustainable energy conversion and storage technologies such as fuel cells, electrolyzed water devices, and metal-air batteries are developing rapidly (Anantharaj et al., 2016; Lee et al., 2016a; Zhang et al., 2016; Li and Lu, 2017; Yu et al., 2019; Wang et al., 2020). The metal-air battery has received increasing attention attribute to the advantages of low cost, high specific energy density, remarkable long-term stability, and environmental benignity (Fu et al., 2017b; Pan et al., 2018; Xiong and Ivey, 2018). Moreover, the theoretical energy density of metal-air battery is 5∼10 times than that of lithium-ion batteries (Gu et al., 2017). Metal-air batteries include a metal anode (metal=lithium, zinc, magnesium, aluminum, etc.) and an air cathode. On the one hand, the metal-air battery is suitable for practical applications due to its abundant resources, low price, and environmental friendliness (Chen et al., 2018; Wang et al., 2019). On the other hand, the battery performance can be further improved by optimizing the electrode reaction kinetic of the air cathode (Cheng and Chen, 2012; Lee et al., 2016a). During the charge-discharge process, the electrode reactions on the air cathode are oxygen evolution reaction (OER) and oxygen

reduction reaction (ORR) (Jiang et al., 2016; Han et al., 2017; Suen et al., 2017). Rational design and synthesis of catalytic materials to promote the process of OER/ORR have attracted the interest of many researchers.

So far, precious metals and their alloys are still considered to be state-of-the-art electrocatalysts for OER/ORR, such as Pt-based material catalysts with high ORR activity, Ir-based or Ru-based material catalysts with high OER activity (Lee et al., 2012; Liu et al., 2019a). However, the prohibitive cost, low reserves, and poor stability severely restrict the large-scale production and commercial application. Since transition metals (such as iron, cobalt, and nickel) based catalysts have the characteristics of low cost, earth-abundance, and good chemical stability, they are recognized as ideal materials to replace noble metals (Han et al., 2019a; Shi et al., 2019). In recent years, there has been a lot of research results on transition metal catalysts (Aijaz et al., 2016; Han et al., 2016). Transition metal, transition metal alloys and their derivatives (such as oxides, hydroxides and carbides) are developed as low-cost oxygen electrocatalysts, which have become a kind of substitute for precious metals and have attracted widespread attention (Gong et al., 2013; Cai et al., 2016; Fu et al., 2017a; Liu et al., 2019b; Xie et al., 2019). However, a large number of experimental studies have shown that it is difficult for a single metal catalyst to meet the bifunctional catalytic requirements (Liang et al., 2013; Park et al., 2017; Li et al., 2018). Therefore, the development of OER/ORR bifunctional catalysts based on earth-abundant elements with satisfied electrochemical activity and excellent stability still remains a great challenge.

The synergistic effect between different metals in bimetallic materials can effectively change the electronic structure of materials and reduce the free energy of reaction, leading to the effective bifunctional capability (Su et al., 2017). Besides, rational design of catalytic electrode structure is an important approach to improve the electrochemical performance. The traditional electrode preparation process is to disperse the powdered catalyst in a solvent and prepare an electrode slurry, which is then coated on carbon cloth or carbon paper to prepare the final air cathode. The preparation method not only makes the catalyst loaded on the support non-uniform, but also causes the weak interaction between the functional phase and the support, resulting in poor electrode stability. Moreover, the binder added in the preparation of electrode slurry will cover the catalytic active site and increase the interfacial resistance, unfavorable for the activity enhancement.

In this work, a novel NiFe nanoparticles supported on nitrogen-doped carbon (NC) hybrid material, directly grown on the carbon cloth (designated as Ni_3Fe_2@NC/CC), was proposed and synthesized as an integrated electrode for promoting OER/ORR electrocatalysis and zinc-air batteries. The designed synthetic strategy includes a chemical precipitation method and then a one-step pyrolysis procedure. Compared with the traditional electrode in which Ni_3Fe_2@NC is prepared as an electrode slurry drop-coated on carbon cloth, the Ni_3Fe_2@NC/CC integrated electrode exhibits greatly improved catalytic activity. When the anodic current density reaches 10 mA cm^{-2}, the OER overpotential is 238 mV, which is lower than the Ni_3Fe_2@NC drop coating electrode (340 mV) and the precious metal oxide IrO_2 (400 mV). The Ni_3Fe_2@NC/CC also exhibits remarkable long-term catalytic durability. It can be directly used as the positive electrode for practical aqueous and flexible semi-solid zinc-air batteries, which deliver large discharging capacity, more than 80 discharging-charging cycles and good flexibility.

EXPERIMENTAL SECTION

Materials Synthesis

In a typical synthetic procedure, potassium hexamethylene ferrite (1.33 g) was put in a 200 mL beaker, and then added in 100 mL deionized water and pre-treated carbon cloths to form settled solution A. In the meantime, nickel nitrate hexahydrate (1.74 g) and trisodium citrate (2.36 g) were dissolved into 200 mL water to form clear solution B. Solution A and solution B were mixed under strong magnetic stirring to form a homogeneous solution. After 24 h standing and ripening, NiFe-MOFs coated carbon cloths were taken out to dry at room temperature. At the same time, the solution was centrifuged to obtain the solid, washed with water and ethanol for three times, and then dried at room temperature to achieve the NiFe-MOFs powder. The NiFe-MOFs carbon cloths and powders were transferred into the porcelain boat. And then, the boat was placed in a tube furnace, heated to 500°C with a slow heating rate of 2°C min^{-1} under Ar atmosphere and kept for 1 h. After the temperature was naturally down to room temperature, the obtained integrated electrode and powder sample were collected and signed as Ni_3Fe_2@NC/CC and Ni_3Fe_2@NC, respectively.

Materials Characterization

The phase and crystal structure were characterized by an X-ray diffraction analyzer (XRD, Bruker D8 Advanced, CuKα radiation). Scanning electron microscope (SEM, s4800 Hitachi, 30 kV) with energy dispersive spectrometer (EDS), transmission electron microscope (TEM, JEOL JEM-2100F, 200 kV) and high-angle annular dark-field scanning transmission electron microscope (HAADF-STEM, JEM-ARM200F, 200 kV) were used to observe the microstructure and nanostructure of samples. The chemical valence and surface composition were detected by Thermo Scientific X-ray photoelectron spectroscopy (XPS, Escalab 250Xi).

Electrocatalytic Measurements

The electrochemical performance was tested at the IviumStat workstation. The electrochemical test is carried out in a three-electrode system, including a working electrode, a reference electrode, and a counter electrode. The integrated Ni_3Fe_2@NC/CC electrode prepared in this work can be directly used as the working electrode. The saturated calomel electrode is the reference electrode, and the carbon rod or platinum is the counter electrode. The obtained Ni_3Fe_2@NC powder samples were made into working electrodes according to traditional electrode preparation methods for comparison. Electrode slurry was prepared by suspending 10 mg Ni_3Fe_2@NC in a mixed solvent of deionized water 0.68 mL, isopropanol 0.23 mL, and Nafion 0.09 mL (v/v/v = 15/5/2). For noble metal catalysts, 8 mg IrO_2 was mixed with 2 mg carbon powder. The OER

working electrode was prepared by the drop-casting method, and the slurry was deposited on 1.0 × 1.0 cm^2 carbon cloth (loading mass is about 1.0 mg cm^{-2}) and dried at 60°C. The OER performance was tested in 1M KOH saturated with high purity N_2. IrO_2 electrode is also prepared by the same process. The ink of the catalyst was deposited on the glass carbon of the rotating disk electrode (RDE) with a diameter of 5 mm to prepare an ORR working electrode. Then, 10 μL of the resulting ink was coated on the electrode and dried in the air environment. The ORR performance of the catalyst was measured in 0.1 M KOH solution saturated with oxygen. First, several cyclic voltammetry (CV) curves were performing until the signal was stable. Linear sweep voltammetry of ORR and OER was performed at a scan rate of 10 mV s^{-1}. The electrochemical impedance spectroscopy is performed in the frequency range of 100 kHz to 100 mHz. The electric double-layer capacitance (C_{dl}) was measured by CV. For data analysis, convert the potential to a reversible hydrogen electrode (RHE) according to the following formula: E (vs. RHE) = E (vs. SCE) + 0.059 × pH + 0.241 V. The OER polarization measurements were iR-corrected. The Koutecky-Levich (K-L) curve is obtained by the following formula:

$$\frac{1}{I} = \frac{1}{I_k} + \frac{1}{I_d} = \frac{1}{nFAkC^0} - \frac{1}{0.62nFAD_{O_2}^{2/3}\nu^{-1/6}C^0\omega^{1/2}}$$

Among them, I, I_k and I_d represent measurement, kinetics and limit diffusion current density, n is the number of electrons transferred by oxygen reduction, F is the Faraday constant, A (cm^2) is the geometric area of the electrode, k is the rate constant of the reaction, and C^0 is the oxygen constant in a saturated 0.1 M KOH solution, D is the oxygen diffusion coefficient, ν is the solvent dynamic viscosity, and ω is the speed in rad s^{-1}.

Assembly of Aqueous Zn-Air Batteries

The aqueous zinc-air battery was constructed by the anode, the cathode, and the electrolyte. The anode of the battery was a zinc plate, the electrolyte was 6.0 M KOH and 0.2 M $ZnCl_2$ solution, and the air cathode was a catalyst coated on a 1 × 1 cm^2 carbon cloth. The integrated electrode obtained in this work was directly used as an air cathode. Before testing, high-purity oxygen must be allowed to enter the electrolyte for about 20 min to reach the oxygen saturation state. During the test, oxygen should be continuously introduced at a small flow rate to ensure oxygen saturation of the electrolyte. The open-circuit voltage and reversible cycle of the zinc-air battery were tested by the LAND-CT2001A testing device.

Assembly of Flexible Semi-Solid Zn-Air Batteries

The flexible semi-solid zinc-air battery was composed of a zinc anode, a Polyvinyl alcohol (PVA) KOH solid electrolyte, and Ni_3Fe_2@NC/CC air cathode. The preparation method of the PVA-KOH electrolyte was shown below. Dissolve 3 g of PVA powder in 25 mL of deionized water and stir thoroughly at 90 °C to form a clear solution. Then add 6 mL 9 M KOH solution to

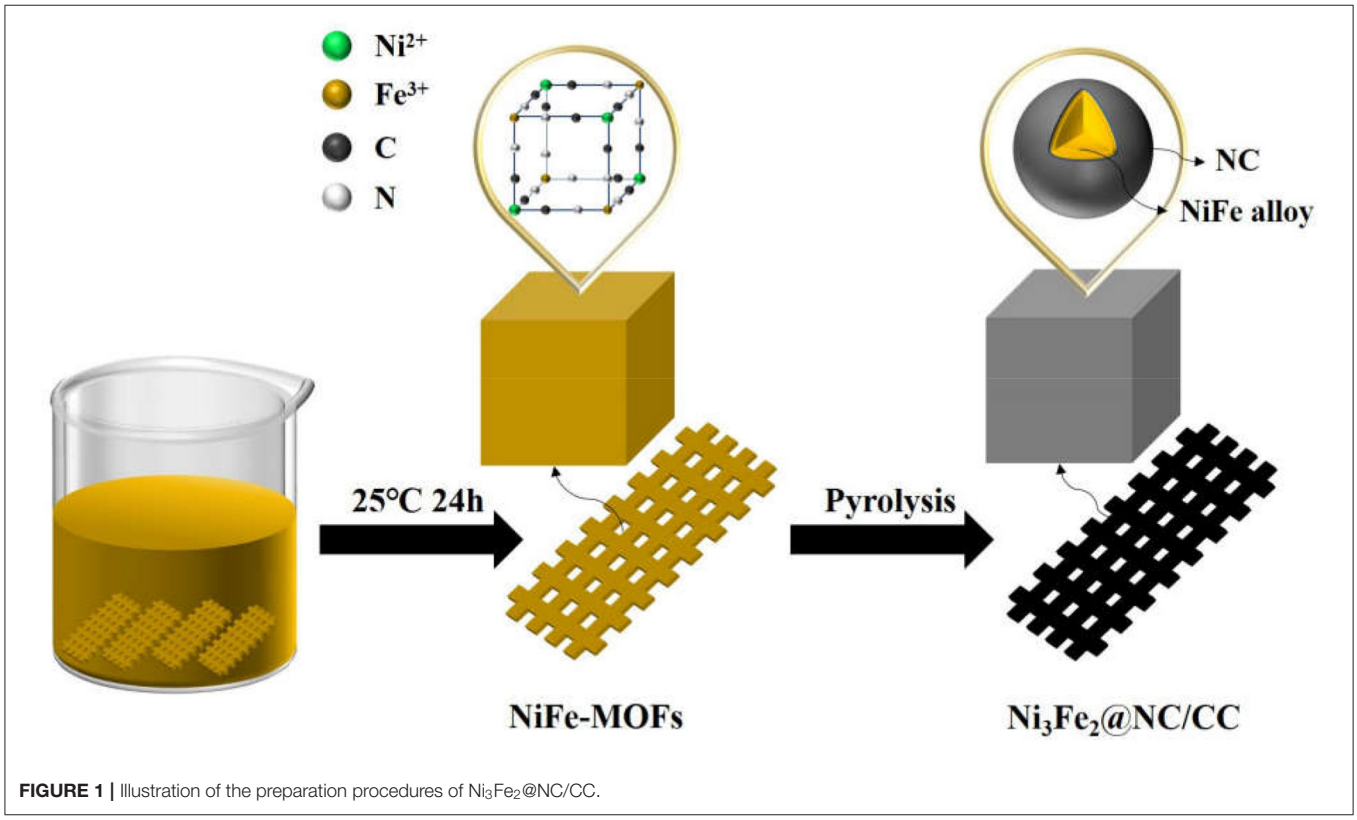

FIGURE 1 | Illustration of the preparation procedures of Ni_3Fe_2@NC/CC.

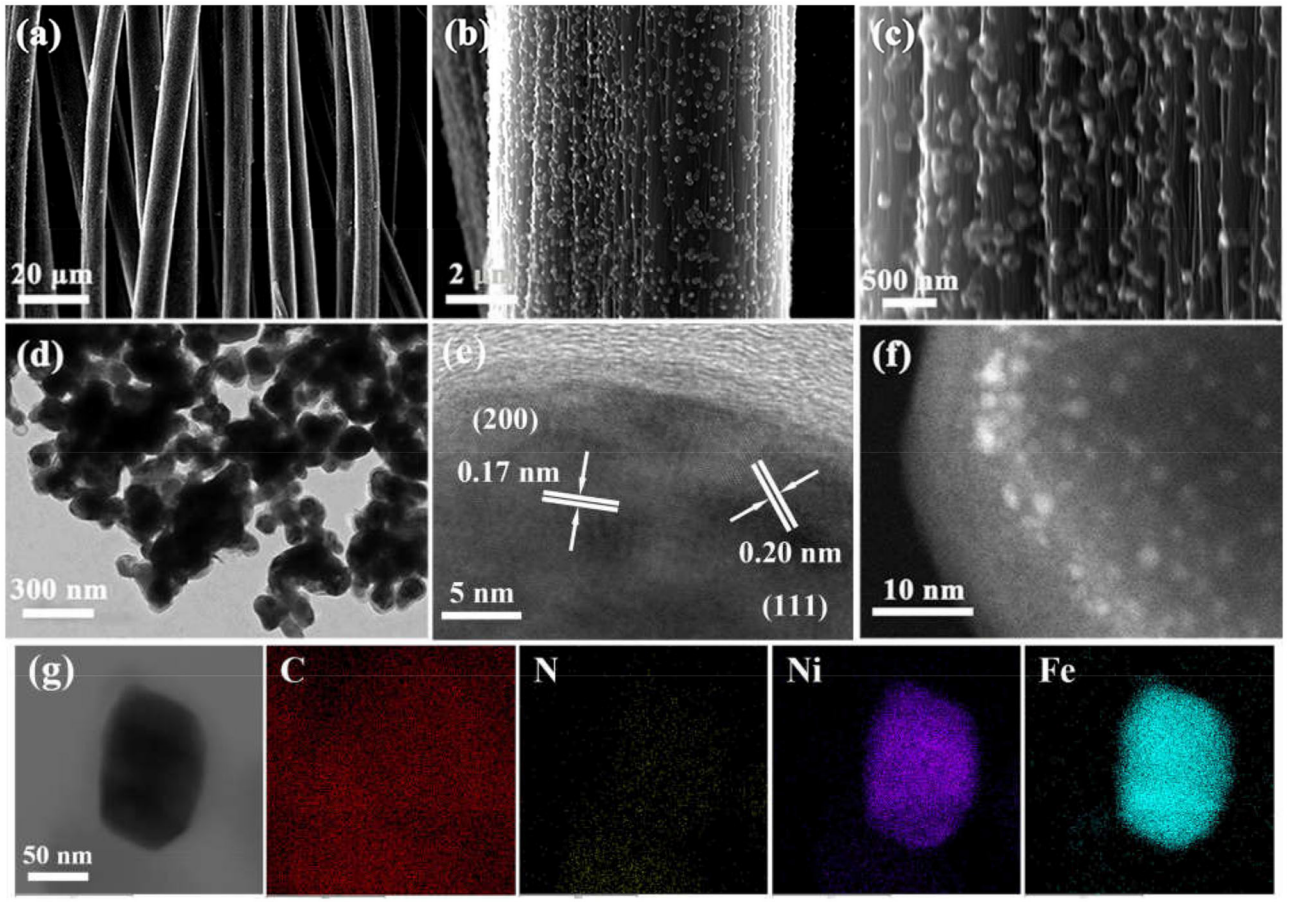

FIGURE 2 | (a–c) SEM images from low to high magnification of Ni_3Fe_2@NC/CC. **(d)** TEM, **(e)** HRTEM, **(f)** HAADH-STEM, and **(g)** elemental mapping images of Ni_3Fe_2@NC.

mix, continue to stir at 90°C for 4 h, then put in the refrigerator to freeze for at least 3 h.

RESULTS AND DISCUSSION

Figure 1 schematically elucidates the preparation process of the Ni_3Fe_2@NC/CC. In brief, nickel (II) nitrate hexahydrate, sodium citrate, and potassium ferricyanide are co-precipitated in deionized water to form NiFe-MOFs precursor. Carbon cloths are added during the precipitation formation. Ni_3Fe_2@NC and Ni_3Fe_2@NC/CC are finally achieved by calcining the precursor and the carbon cloth under the argon atmosphere at 773 K, respectively. The NiFe-MOFs nanoparticles with particle size about 100 nm uniformly loaded on the carbon fiber (**Supplementary Figures 1A–C**, Supporting Information). The XRD pattern of the precursor that had been sonicated from the carbon cloth was consistent with the theoretically fitted $Ni_3[Fe(CN)_6]_2{\cdot}H_2O$, (Zhang et al., 2017), which means the successful formation of the NiFe-MOFs precursor (**Supplementary Figure 2**). After calcination at 773 K under an argon atmosphere, the organic precursors were carbonized into NC and the nanoparticles were anchored on the NC matrix. XRD analysis of the resultant composites elucidated that the dominant phase was bimetal NiFe with three obvious diffraction peaks at 44, 51, and 75°, which can be assigned, respectively, to the (111), (200), and (220) planes of NiFe alloy (**Supplementary Figure 3A**). Energy dispersive spectrum (EDS) showed that the atomic ratio of Ni and Fe in the calcined sample was 3:2 (**Supplementary Figure 3B** and **Supplementary Table 1**). Comprehensive analysis of XRD and EDS data demonstrates the successful synthesis of nickel-iron nanoparticles on the N-doped carbon nanocube structure. Furthermore, as shown in **Figures 2a–c**, Ni_3Fe_2@NC nanoparticles evenly loaded on the carbon cloth with the average particle size of ∼100 nm. For further structural analysis of nanoparticles on carbon cloth, put the calcined integrated electrode in absolute ethanol and sonicate, and the dissolving sample was taken to perform TEM test. TEM further confirms the nanoparticles with the size of about 100 nm (**Figure 2d**). The high-resolution TEM (HRTEM) image proved distinct domains of NiFe alloy with the interplanar spacing of 0.20

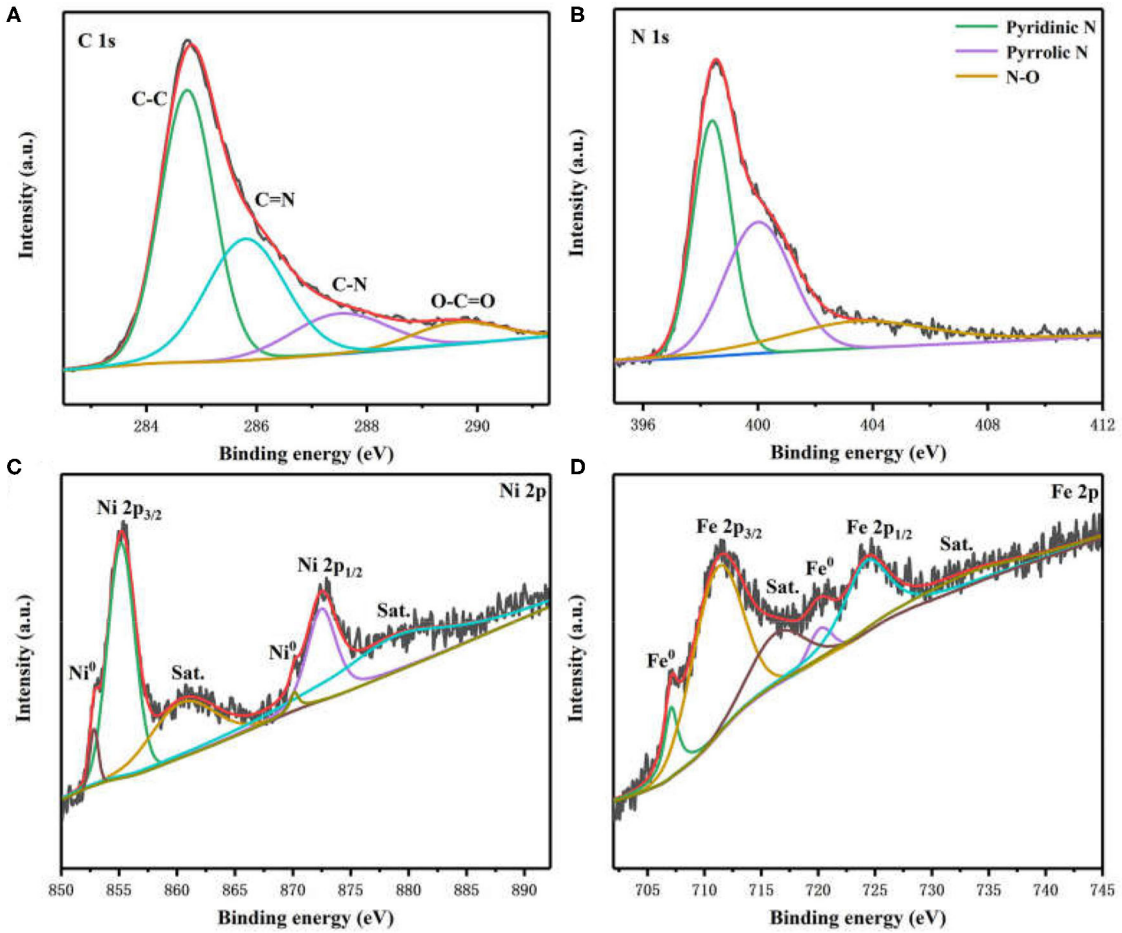

FIGURE 3 | High-resolution XPS spectra of **(A)** C 1 s, **(B)** N 1 s, **(C)** Ni 2p, and **(D)** Fe 2p in Ni_3Fe_2@NC.

and 0.17 nm, corresponding to the (111) and (200) facets of NiFe alloy, respectively (**Figure 2e**). To further characterize the NiFe alloy, an aberration-corrected high-angle annular dark-field scanning transmission electron microscope (HAADF-STEM) test was performed on it. The HAADF-STEM image showed NiFe alloy with a heavier element mass on an NC substrate exists in the form of bright spots, and the particle size of the NiFe alloys is about 2 ∼ 3 nm (**Figure 2f**). Also, elemental mapping of Ni_3Fe_2@NC revealed the homogeneous dispersion of C, N, Ni, and Fe species throughout the entire nanoarchitecture (**Figure 2g**), suggesting the uniform loading of NiFe nanoparticles on N-doped carbon structure.

X-ray photoelectron spectroscopy (XPS) was employed to characterize the chemical states and surface structure of Ni_3Fe_2@NC materials. The photoelectron peaks in XPS survey spectra confirm the existence of C, N, O, Fe, and Ni species (**Supplementary Figure 4**). The high-resolution C 1s spectrum revealed the presence of C-C (284.7 eV), C=N (285.8 eV), C-N (287.5 eV), and O-C=O (289.6 eV) bonds in Ni_3Fe_2@NC (**Figure 3A**) (Sheng et al., 2011; Gao et al., 2014). The N 1s spectrum was deconvoluted into three peaks, which can be assigned to pyridinic N (398.5 eV), pyrrolic N (400.2 eV), and N-O (403.5 eV) (**Figure 3B**) (Niu et al., 2015; Han et al., 2019b). However, it is worth noting that pyridinic N can bond with metal atoms. The existence of C=N and C-N bond indicated the successful doping of N into the carbon skeleton. The two peaks at 852.8 and 855.2 eV in Ni 2p spectrum were ascribed to Ni $2p_{3/2}$ of Ni^0 and Ni^{2+} (**Figure 3C**), respectively. The other two fitting peaks at 870.1 and 872.5 eV were attributed to Ni $2p_{1/2}$ of Ni^0 and Ni^{2+} (Lee et al., 2016b; Yang et al., 2016; Huang et al., 2017; Wan et al., 2017). The two shakeup satellites of ionic state nickel located at 860.4 and 878.9 eV. The peaks in the Fe 2p spectrum included two peaks of zero-valence state (707.1 and 720.2 eV) and two peaks of high valence state (711.1 and 724.2 eV) with two peaks of shakeup satellites (716.3 and 733.2 eV), which were derived from NiFe nanoparticle and Fe-N species (**Figure 3D**) (Cui et al., 2013; Jiang et al., 2015; Dai et al., 2016). In general, these aforementioned results demonstrated the presence of NiFe alloy and the metal-N coordination in prepared Ni_3Fe_2@NC/CC electrode.

The electrocatalytic activities of Ni_3Fe_2@NC/CC were evaluated by comparing with noble metal IrO_2 catalyst and Ni_3Fe_2@NC in a typical three-electrode configuration using 1.0 M KOH solution as the electrolyte. As displayed in the OER

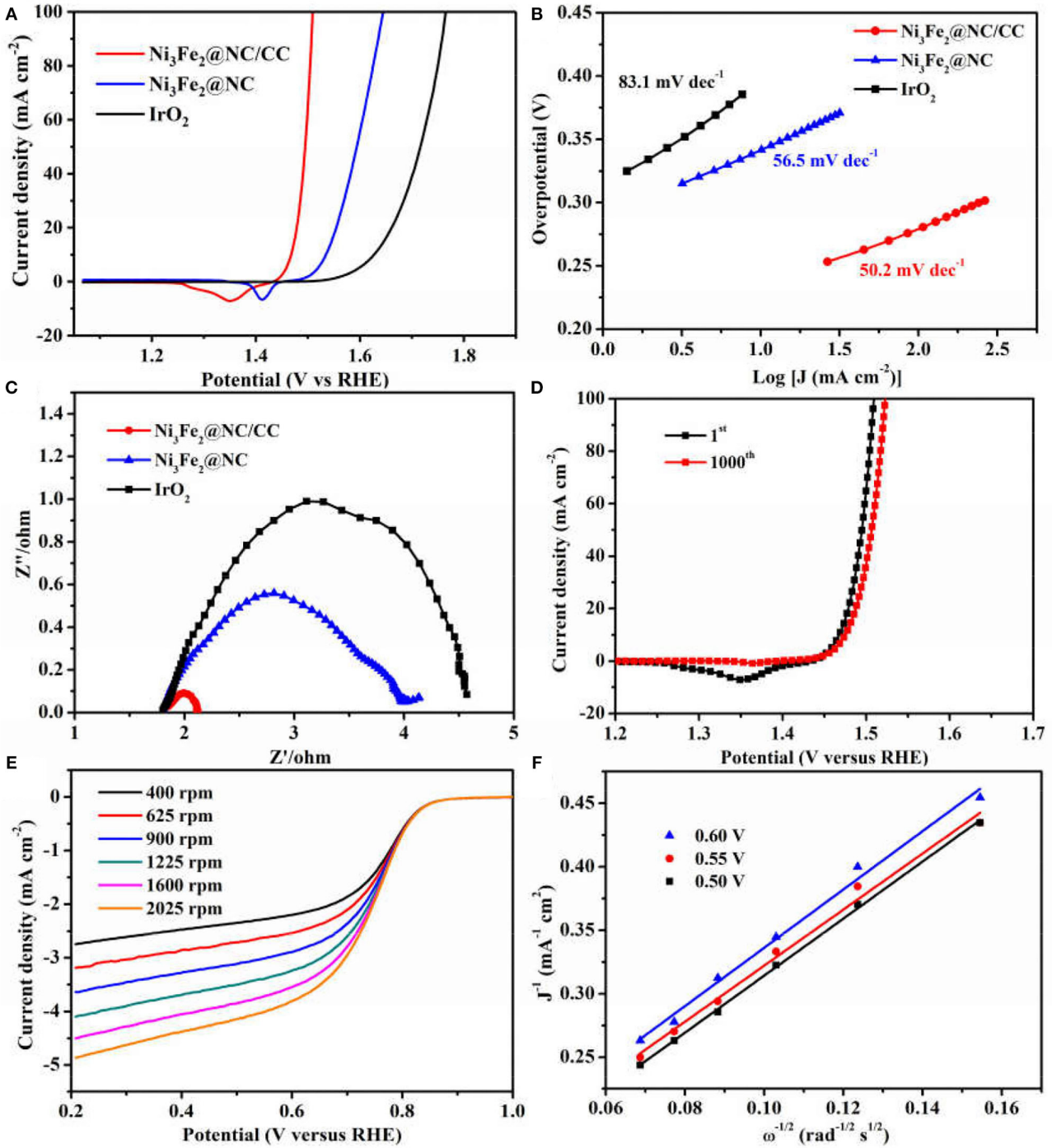

FIGURE 4 | (A) OER polarization curves of Ni_3Fe_2@NC/CC, Ni_3Fe_2@NC, and IrO_2. **(B)** Corresponding Tafel plots. **(C)** Corresponding EIS spectra. **(D)** OER LSV plots of Ni_3Fe_2@NC/CC before and after 1,000 cycles. **(E)** ORR polarization curves of Ni_3Fe_2@NC at different rotation rates. **(F)** The K-L plots for Ni_3Fe_2@NC at different potentials.

linear sweep voltammograms (LSV), Ni_3Fe_2@NC/CC possessed superior OER activity (**Figure 4A**). Ni_3Fe_2@NC/CC required an overpotential of 238 mV to reach a 10 mA cm^{-2} current density, which was much lower than those of Ni_3Fe_2@NC (340 mV) and IrO_2 (400 mV). The OER activity of Ni_3Fe_2@NC/CC actually surpasses most previously reported electrocatalysts (**Table 1**). The fitted Tafel plots revealed that Ni_3Fe_2@NC/CC equipped a Tafel slope of 50.2 mV dec^{-1}, lower than that of Ni_3Fe_2@NC

TABLE 1 | The OER performance of the recently reported highly active catalysts.

Catalyst	Substrate	Electrolyte	Current density (mA cm^{-2})	Overpotential (mV)	References
Ni_3Fe_2@NC/CC	Carbon cloth	1.0 M KOH	10	238	This work
NiFe LDH	Ni foam	1.0 M KOH	10	490	Chen et al., 2019
$NiCo_2O_4$	Ni foam	1.0 M KOH	10	270	Fang et al., 2018
Fe-doped NiO_x	GCE	1.0 M KOH	10	310	Wu et al., 2017
$NiFe_2O_4$	GCE	0.1 M KOH	10	440	Li et al., 2015
$NiCo_2S_4$ NW	Ni foam	1.0 M KOH	10	400	Sivanantham et al., 2016
Ni_3FeN-NPs	GCE	1.0 M KOH	10	280	Jia et al., 2016
Ni-Co-Fe NNCs	Copper	1.0 M KOH	10	316	Barati Darband et al., 2019
a-Co_2Fe	GCE	1.0 M KOH	10	290	Zhu et al., 2020
$Co_3FeS_{1.5}(OH)_6$	GCE	0.1 M KOH	10	358	Wang et al., 2017
NiCoP/C nanoboxes	GCE	1.0 M KOH	10	330	He et al., 2017

(56.5 mV dec^{-1}) and IrO_2 (83.1 mV dec^{-1}), which indicated its favorable reaction kinetic (**Figure 4B**). Electrochemical impedance spectroscopy (EIS) analysis suggested that the charge-transfer resistance (R_{ct}) values were around 0.3, 2.2, and 3.4 Ω for Ni_3Fe_2@NC/CC, Ni_3Fe_2@NC and IrO_2, respectively (**Figure 4C**), which was an indication that a rapid charge transfer rate in Ni_3Fe_2@NC/CC. This trend was in accordance with the polarization results and Tafel data. The above results show that, compared with the traditional drop-coated electrode, the integrated electrode gives excellent catalytic activity, which fully confirmed the structural advantages of the integrated electrode in improving the overall electrochemical activity. In addition to its high catalytic activity, the long-term stability of Ni_3Fe_2@NC/CC is also an important parameter for practical performance. As shown in **Supplementary Figure 5**, the catalyst Ni_3Fe_2@NC/CC exhibited remarkable OER stability at a constant current of 10 mA cm^{-2} after continuous operation for 200 min. The LSV curve of Ni_3Fe_2@NC/CC nearly overlapped the initial one after continuous 1,000 cyclic voltammetry (CV) cycles (**Figure 4D**). This result manifested that the Ni_3Fe_2@NC/CC hybrid can still maintain its activity after a large number of cycles and has fairly good stability. It can be seen from the **Supplementary Figure 6** that the morphology of the Ni_3Fe_2@NC/CC has not changed significantly after the stability test, which further proves the strong interaction. Since bifunctional oxygen catalytic performance is required in rechargeable Zinc-air battery, the ORR activity of synthesized composites was assessed by coating on rotating disk electrodes (RDEs). As displayed in **Figure 4E**, Ni_3Fe_2@NC exhibited an onset potential of 0.87 V, a half-wave potential of 0.73 V, and a limiting diffusion current density of 4.5 mA cm^{-2} at a rotating speed of 1,600 round per minute (rpm), which is comparable to many reported bifunctional oxygen electrocatalysts (**Supplementary Table 2**). The fitted Koutechy-Levich plot of Ni_3Fe_2@NC disclosed an apparent 4-electron reaction pathway, which is deemed to a highly efficient mechanism dominating the ORR process (**Figure 4F**). The electrochemically active surface area (EASC) was measured by the double-layer capacitance (C_{dl}) to be 2.5 mF cm^{-2} for Ni_3Fe_2@NC, indicating the benefits of NiFe nanoparticles and NC substrate in exposing more electrochemical active sites (**Supplementary Figures 7A,B**). Apart from the catalytic activity, Ni_3Fe_2@NC also showed remarkable ORR catalytic stability. After 9 h continuous chronoamperometric treatment, the active current retention of Ni_3Fe_2@NC was 80% (**Supplementary Figure 8**). The long-term stability was further demonstrated by the almost overlapping CV curves after 1,000 cycles (**Supplementary Figure 8** inset). The aforementioned experimental results jointly confirm that the Ni_3Fe_2@NC/CC hybrid electrode has efficient bifunctional OER/ORR performance and long-term durability, indicating that it has promising application prospects in reversible oxygen electrocatalysis for rechargeable metal-air batteries and regenerative fuel cells.

A home-made liquid zinc-air battery was constructed to evaluate the practical electrochemical performance of Ni_3Fe_2@NC/CC, in which a zinc plate was served as the anode, the Ni_3Fe_2@NC/CC integrated electrode as the air cathode, and 6.0 M KOH and 0.2 M $ZnCl_2$ as the electrolyte (**Figure 5A**). The alkaline zinc-air batteries based on Ni_3Fe_2@NC/CC materials exhibit a steady open-circuit voltage of 1.45 V (**Figure 5B**). In addition, with the current density of 5 mA cm^{-2} and the duration of each cycle of 20 min, the cycle chargeability of the secondary battery was further studied (**Figure 5C**). It is worth noting that under the catalysis of Ni_3Fe_2@NC/CC electrode, the discharge voltage of the battery is 1.11 V, the charging voltage is 1.95 V, the voltage gap is 0.84 V, and the energy efficiency is 56.9%. Small voltage decay is observed after 80 cycles for Ni_3Fe_2@NC/CC cathode, which reflects the excellent rechargeability and is much better than the precious metal Pt/C-IrO_2 catalyst (< 50 cycles). The discharge specific capacity of a primary Zinc-air battery with Ni_3Fe_2@NC/CC cathode is 655 mA h g^{-1} at 20 mA cm^{-2} based on the mass of consumed zinc (**Supplementary Figure 9**). Encouraged by the potential application for portable and wearable devices, a flexible solid-state zinc-air battery was assembled with zinc plate anode, PVA-KOH electrolyte and Ni_3Fe_2@NC/CC integrated cathode. The open circuit voltage of solid zinc-air battery promoted by Ni_3Fe_2@NC/CC can reach 1.37 V, again indicating the efficient ORR activity of the integrated cathode (**Supplementary Figure 10**). As shown in **Figure 5D** inset, a light emitting diode (LED) screen was powered

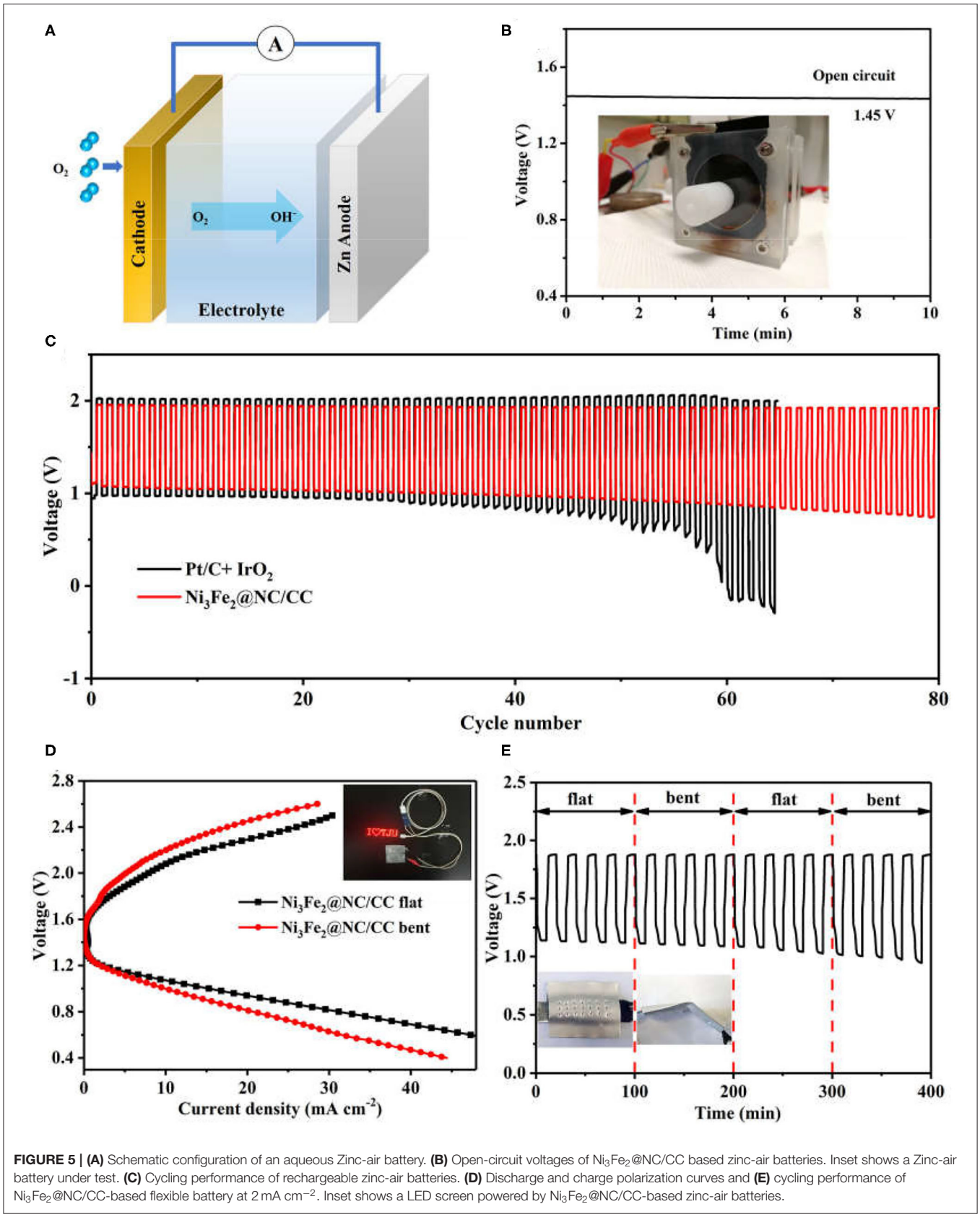

FIGURE 5 | (A) Schematic configuration of an aqueous Zinc-air battery. **(B)** Open-circuit voltages of Ni_3Fe_2@NC/CC based zinc-air batteries. Inset shows a Zinc-air battery under test. **(C)** Cycling performance of rechargeable zinc-air batteries. **(D)** Discharge and charge polarization curves and **(E)** cycling performance of Ni_3Fe_2@NC/CC-based flexible battery at 2 mA cm^{-2}. Inset shows a LED screen powered by Ni_3Fe_2@NC/CC-based zinc-air batteries.

by two Ni_3Fe_2@NC/CC-based solid flexible Zinc-air batteries in series. The voltage-current polarization curves revealed that the Ni_3Fe_2@NC/CC cathode possessed a good charge-discharge performance (**Figure 5D**). The discharge voltage at 10 mA cm^{-2} is 1.09 V and the charge voltage is 2.08 V when the battery is flat. Moreover, the battery exhibits considerable flexibility. When the assembled battery is bent about 30°, the polarization curve shows that the discharge voltage is 1.07 V at a current density of 10 mA cm^{-2}, which is only 1.8% lower than the discharge voltage in the flat state of the battery, and the charging voltage is 2.20 V, which is 5.7% higher. As shown in **Figure 5E**, the assembled battery can be alternately flat and bent (once every 5 charge-discharge cycles). Under a large mechanical strain, the battery can maintain a good charge and discharge cycle under continuous charging and discharging conditions. These results fully prove the good flexibility and cycle stability of Ni_3Fe_2@NC/CC-based rechargeable zinc-air batteries.

CONCLUSION

In conclusion, Ni_3Fe_2@NC/CC integrated electrode was prepared by uniformly loading nickel-iron bimetallic nanoparticles on nitrogen-doped carbon nanostructures grown on carbon cloth support by chemical precipitation and then high-temperature calcination. The preparation technology of the integrated electrode with the catalyst uniformly supported on the conductive carrier is simple, and the electrode presents high catalytic activity and good stability. The prepared Ni_3Fe_2@NC/CC shows enhanced OER/ORR activity and durability either in electrochemical half-reaction tests or reversible zinc-air batteries, which is superior to noble metals and many previously developed electrocatalysts. Further experimental analysis demonstrates the advantages of *in-situ* integrated electrode in facilitating the electrode transfer and strong interaction between the active materials and the current collector, thereby promoting the electrocatalytic performance. Our findings provide a simple strategy for the preparation of bimetallic nanocomposites and open up a new way for the development of promising hybrid catalysts for electrochemical and energy-related applications.

DATA AVAILABILITY STATEMENT

The original contributions presented in the study are included in the article/**Supplementary Material**, further inquiries can be directed to the corresponding author/s.

AUTHOR CONTRIBUTIONS

HH and XL conducted the experiments and write the manuscript. CT helped with operating the experiments and data analysis. JL and XH interpreted the results. XH and WH supervised the research. All authors approved the submission of final manuscript.

FUNDING

This work was supported by the National Natural Science Foundation of China (51972224 and U1601216), Young Elite Scientists Sponsorship Program by CAST (2018QNRC001).

SUPPORTING INFORMATION

SEM images and XRD pattern of precursors, XRD pattern, EDS, survey XPS, CVs, C_{dl} and chronoamperometric curves of Ni_3Fe_2@NC/CC. Primary discharge curve of zinc-air battery, Table of comparison of OER/ORR electrocatalytic performance.

SUPPLEMENTARY MATERIAL

The Supplementary Material for this article can be found online at: https://www.frontiersin.org/articles/10.3389/fchem.2020.575288/full#supplementary-material

REFERENCES

Aijaz, A., Masa, J., Rosler, C., Xia, W., Weide, P., Botz, A. J., et al. (2016). Co@Co_3O_4 encapsulated in carbon nanotube-grafted nitrogen-doped carbon polyhedra as an advanced bifunctional oxygen electrode. *Angew. Chem. Int. Ed.* 55, 4087–4091. doi: 10.1002/anie.201509382

Anantharaj, S., Ede, S. R., Sakthikumar, K., Karthick, K., Mishra, S., and Kundu, S. (2016). Recent trends and perspectives in electrochemical water splitting with an emphasis on sulfide, selenide, and phosphide catalysts of Fe, Co, and Ni: a review. *ACS Catal.* 6, 8069–8097. doi: 10.1021/acscatal.6b02479

Barati Darband, G., Aliofkhazraei, M., and Rouhaghdam, A. S. (2019). Facile electrodeposition of ternary Ni-Fe-Co alloy nanostructure as a binder free, cost-effective and durable electrocatalyst for high-performance overall water splitting. *J. Colloid Interface Sci.* 547, 407–420. doi: 10.1016/j.jcis.2019.03.098

Cai, P., Ci, S., Zhang, E., Shao, P., Cao, C., and Wen, Z. (2016). FeCo alloy nanoparticles confined in carbon layers as high-activity and robust cathode catalyst for Zn-air battery. *Electrochim. Acta* 220, 354–362. doi: 10.1016/j.electacta.2016.10.070

Chen, A., Zhang, X., and Zhou, Z. (2020). Machine learning: accelerating materials development for energy storage and conversion. *InfoMat.* 2, 553–576. doi: 10.1002/inf2.12094

Chen, R., Hung, S. F., Zhou, D., Gao, J., Yang, C., Tao, H., et al. (2019). Layered structure causes bulk NiFe layered double hydroxide unstable in alkaline oxygen evolution reaction. *Adv. Mater.* 31:1903909. doi: 10.1002/adma.201903909

Chen, X., Zhong, C., Liu, B., Liu, Z., Bi, X., Zhao, N., et al. (2018). Atomic layer Co_3O_4 nanosheets: the key to knittable Zn-air batteries. *Small* 14:1702987. doi: 10.1002/smll.201702987

Cheng, F., and Chen, J. (2012). Metal-air batteries: from oxygen reduction electrochemistry to cathode catalysts. *Chem. Soc. Rev.* 41, 2172–2192. doi: 10.1039/c1cs15228a

Chu, S., Cui, Y., and Liu, N. (2016). The path towards sustainable energy. *Nat. Mater.* 16, 16–22. doi: 10.1038/nmat4834

Cui, H.-J., Shi, J.-W., Yuan, B., and Fu, M.-L. (2013). Synthesis of porous magnetic ferrite nanowires containing Mn and their application in water treatment. *J. Mater. Chem. A* 1, 5902–5907. doi: 10.1039/c3ta01692g

Dai, Y., Chan, Y., Jiang, B., Wang, L., Zou, J., Pan, K., et al. (2016). Bifunctional Ag/Fe/N/C catalysts for enhancing oxygen

reduction via cathodic biofilm inhibition in microbial fuel cells. *ACS Appl. Mater. Interfaces* 8, 6992–7002. doi: 10.1021/acsami.5b11561

Fang, L., Jiang, Z., Xu, H., Liu, L., Guan, Y., Gu, X., et al. (2018). Crystal-plane engineering of $NiCo_2O_4$ electrocatalysts towards efficient overall water splitting. *J. Catal.* 357, 238–246. doi: 10.1016/j.jcat.2017.11.017

Fu, G., Cui, Z., Chen, Y., Xu, L., Tang, Y., and Goodenough, J. B. (2017a). Hierarchically mesoporous nickel-iron nitride as a cost-efficient and highly durable electrocatalyst for Zn-air battery. *Nano Energy* 39, 77–85. doi: 10.1016/j.nanoen.2017.06.029

Fu, J., Cano, Z. P., Park, M. G., Yu, A., Fowler, M., and Chen, Z. (2017b). Electrically rechargeable zinc-air batteries: progress, challenges, and perspectives. *Adv. Mater.* 29:1604685. doi: 10.1002/adma.201604685

Gao, M. R., Cao, X., Gao, Q., Xu, Y. F., Zheng, Y. R., Jiang, J., et al. (2014). Nitrogen-doped graphene supported $CoSe_2$ nanobelt composite catalyst for efficient water oxidation. *ACS Nano* 8, 3970–3978. doi: 10.1021/nn500880v

Gong, M., Li, Y., Wang, H., Liang, Y., Wu, J. Z., Zhou, J., et al. (2013). An advanced Ni-Fe layered double hydroxide electrocatalyst for water oxidation. *J. Am. Chem. Soc.* 135, 8452–8455. doi: 10.1021/ja4027715

Gu, P., Zheng, M., Zhao, Q., Xiao, X., Xue, H., and Pang, H. (2017). Rechargeable zinc–air batteries: a promising way to green energy. *J. Mater. Chem. A* 5, 7651–7666. doi: 10.1039/C7TA01693J

Han, L., Dong, S., and Wang, E. (2016). Transition-metal (Co, Ni, and Fe)-based electrocatalysts for the water oxidation reaction. *Adv. Mater.* 28, 9266–9291. doi: 10.1002/adma.201602270

Han, X., Ling, X., Wang, Y., Ma, T., Zhong, C., Hu, W., et al. (2019a). Generation of nanoparticle, atomic-cluster, and single-atom cobalt catalysts from zeolitic imidazole frameworks by spatial isolation and their use in zinc-air batteries. *Angew. Chem. Int. Ed.* 58, 5359–5364. doi: 10.1002/anie.201901109

Han, X., Ling, X., Yu, D., Xie, D., Li, L., Peng, S., et al. (2019b). Atomically dispersed binary Co-Ni sites in nitrogen-doped hollow carbon nanocubes for reversible oxygen reduction and evolution. *Adv. Mater.* 31:e1905622. doi: 10.1002/adma.201905622

Han, X., Wu, X., Zhong, C., Deng, Y., Zhao, N., and Hu, W. (2017). $NiCo_2S_4$ nanocrystals anchored on nitrogen-doped carbon nanotubes as a highly efficient bifunctional electrocatalyst for rechargeable zinc-air batteries. *Nano Energy* 31, 541–550. doi: 10.1016/j.nanoen.2016.12.008

He, P., Yu, X. Y., and Lou, X. W. (2017). Carbon-incorporated nickel-cobalt mixed metal phosphide nanoboxes with enhanced electrocatalytic activity for oxygen evolution. *Angew. Chem. Int. Ed.* 56, 3897–3900. doi: 10.1002/anie.201612635

Huang, L., Ge, X., and Dong, S. (2017). A facile conversion of a Ni/Fe coordination polymer to a robust electrocatalyst for the oxygen evolution reaction. *RSC Adv.* 7, 32819–32825. doi: 10.1039/C7RA04280A

Jia, X., Zhao, Y., Chen, G., Shang, L., Shi, R., Kang, X., et al. (2016). Ni_3FeN nanoparticles derived from ultrathin nife-layered double hydroxide nanosheets: an efficient overall water splitting electrocatalyst. *Adv. Energy Mater.* 6:1502585. doi: 10.1002/aenm.201502585

Jiang, H., Yao, Y., Zhu, Y., Liu, Y., Su, Y., Yang, X., et al. (2015). Iron carbide nanoparticles encapsulated in mesoporous Fe-N-doped graphene-like carbon hybrids as efficient bifunctional oxygen electrocatalysts. *ACS Appl. Mater. Interfaces* 7, 21511–21520. doi: 10.1021/acsami.5b06708

Jiang, W. J., Gu, L., Li, L., Zhang, Y., Zhang, X., Zhang, L. J., et al. (2016). Understanding the high activity of Fe-N-C electrocatalysts in oxygen reduction: Fe/Fe_3C nanoparticles boost the activity of $Fe\text{-}N_{(x)}$. *J. Am. Chem. Soc.* 138, 3570–3578. doi: 10.1021/jacs.6b00757

Larcher, D., and Tarascon, J. M. (2015). Towards greener and more sustainable batteries for electrical energy storage. *Nat Chem* 7, 19–29. doi: 10.1038/nchem.2085

Lee, D. U., Xu, P., Cano, Z. P., Kashkooli, A. G., Park, M. G., and Chen, Z. (2016a). Recent progress and perspectives on bi-functional oxygen electrocatalysts for advanced rechargeable metal–air batteries. *J. Mater. Chem. A* 4, 7107–7134. doi: 10.1039/C6TA00173D

Lee, S. M., Cho, A., and Cho, Y. S. (2016b). Enhanced optical and piezoelectric characteristics of transparent Ni-doped $BiFeO_3$ thin films on a glass substrate. *RSC Adv.* 6, 16602–16607. doi: 10.1039/C5RA27674H

Lee, Y., Suntivich, J., May, K. J., Perry, E. E., and Shao-Horn, Y. (2012). Synthesis and activities of rutile IrO_2 and RuO_2 nanoparticles for oxygen evolution in acid and alkaline solutions. *J. Phys. Chem. Lett.* 3, 399–404. doi: 10.1021/jz2016507

Li, C., Tan, H., Lin, J., Luo, X., Wang, S., You, J., et al. (2018). Emerging Pt-based electrocatalysts with highly open nanoarchitectures for boosting oxygen reduction reaction. *Nano Today* 21, 91–105. doi: 10.1016/j.nantod.2018.06.005

Li, M., Xiong, Y., Liu, X., Bo, X., Zhang, Y., Han, C., et al. (2015). Facile synthesis of electrospun MFe_2O_4 (M = Co, Ni, Cu, Mn) spinel nanofibers with excellent electrocatalytic properties for oxygen evolution and hydrogen peroxide reduction. *Nanoscale* 7, 8920–8930. doi: 10.1039/C4NR07243J

Li, X., and Wang, J. (2019). One-dimensional and two-dimensional synergized nanostructures for high-performing energy storage and conversion. *InfoMat* 2, 3–32. doi: 10.1002/inf2.12040

Li, Y., and Lu, J. (2017). Metal–air batteries: will they be the future electrochemical energy storage device of choice? *ACS Energy Lett.* 2, 1370–1377. doi: 10.1021/acsenergylett.7b00119

Liang, H.-W., Wei, W., Wu, Z.-S., Feng, X., and Müllen, K. (2013). Mesoporous metal–nitrogen-doped carbon electrocatalysts for highly efficient oxygen reduction reaction. *J. Am. Chem. Soc.* 135, 16002–16005. doi: 10.1021/ja407552k

Liu, M., Zhao, Z., Duan, X., and Huang, Y. (2019a). Nanoscale structure design for high-performance Pt-based ORR catalysts. *Adv. Mater.* 31:1802234. doi: 10.1002/adma.201802234

Liu, Y., Dong, P., Li, M., Wu, H., Zhang, C., Han, L., et al. (2019b). Cobalt nanoparticles encapsulated in nitrogen-doped carbon nanotube as bifunctional-catalyst for rechargeable Zn-air batteries. *Front. Mater.* 6:85. doi: 10.3389/fmats.2019.00085

Niu, W., Li, L., Liu, X., Wang, N., Liu, J., Zhou, W., et al. (2015). Mesoporous N-doped carbons prepared with thermally removable nanoparticle templates: an efficient electrocatalyst for oxygen reduction reaction. *J. Am. Chem. Soc.* 137, 5555–5562. doi: 10.1021/jacs.5b02027

Pan, J., Tian, X. L., Zaman, S., Dong, Z., Liu, H., Park, H. S., et al. (2018). Recent progress on transition metal oxides as bifunctional catalysts for lithium-air and zinc-air batteries. *Batter. Supercaps* 2, 336–347. doi: 10.1002/batt.201800082

Park, J., Sa, Y. J., Baik, H., Kwon, T., Joo, S. H., and Lee, K. (2017). Iridium-based multimetallic nanoframe@nanoframe structure: an efficient and robust electrocatalyst toward oxygen evolution reaction. *ACS Nano* 11, 5500–5509. doi: 10.1021/acsnano.7b00233

Poizot, P., and Dolhem, F. (2011). Clean energy new deal for a sustainable world: from non-CO_2 generating energy sources to greener electrochemical storage devices. *Energy Environ. Sci.* 4, 2003–2019. doi: 10.1039/c0ee00731e

Sheng, Z. H., Shao, L., Chen, J. J., Bao, W. J., Wang, F. B., and Xia, X. H. (2011). Catalyst-free synthesis of nitrogen-doped graphene via thermal annealing graphite oxide with melamine and its excellent electrocatalysis. *ACS Nano* 5, 4350–4358. doi: 10.1021/nn103584t

Shi, X., Ling, X., Li, L., Zhong, C., Deng, Y., Han, X., et al. (2019). Nanosheets assembled into nickel sulfide nanospheres with enriched Ni^{3+} active sites for efficient water-splitting and zinc–air batteries. *J. Mater. Chem. A.* 7, 23787–23793. doi: 10.1039/C9TA03819A

Sivanantham, A., Ganesan, P., and Shanmugam, S. (2016). Hierarchical $NiCo_2S_4$ nanowire arrays supported on Ni Foam: an efficient and durable bifunctional electrocatalyst for oxygen and hydrogen evolution reactions. *Adv. Funct. Mater.* 26, 4661–4672. doi: 10.1002/adfm.201600566

Stamenkovic, V. R., Strmcnik, D., Lopes, P. P., and Markovic, N. M. (2016). Energy and fuels from electrochemical interfaces. *Nat. Mater.* 16, 57–69. doi: 10.1038/nmat4738

Su, C.-Y., Cheng, H., Li, W., Liu, Z.-Q., Li, N., Hou, Z., et al. (2017). Atomic modulation of FeCo-nitrogen-carbon bifunctional oxygen electrodes for rechargeable and flexible all-solid-state zinc-air battery. *Adv. Energy Mater.* 7:1602420. doi: 10.1002/aenm.201602420

Suen, N. T., Hung, S. F., Quan, Q., Zhang, N., Xu, Y. J., and Chen, H. M. (2017). Electrocatalysis for the oxygen evolution reaction: recent development and future perspectives. *Chem. Soc. Rev.* 46, 337–365. doi: 10.1039/C6CS00328A

Wan, H., Li, L., Zhang, J., Liu, X., Wang, H., and Wang, H. (2017). Nickel nanowire@porous $NiCo_2O_4$ nanorods arrays grown on nickel foam as efficient pseudocapacitor electrode. *Front. Energy Res.* 5:33. doi: 10.3389/fenrg.2017.00033

Wang, C., Yu, Y., Niu, J., Liu, Y., Bridges, D., Liu, X., et al. (2019). Recent progress of metal–air batteries—a mini review. *Appl. Sci.* 9:2787. doi: 10.3390/app9142787

Wang, H. F., Tang, C., Wang, B., Li, B. Q., and Zhang, Q. (2017). Bifunctional transition metal hydroxysulfides: room-temperature sulfurization and their applications in Zn-air batteries. *Adv. Mater.* 29:1702327. doi: 10.1002/adma.201702327

Wang, Y., Zhang, G., Ma, M., Ma, Y., Huang, J., Chen, C., et al. (2020). Ultrasmall NiFe layered double hydroxide strongly coupled on atomically dispersed FeCo-NC nanoflowers as efficient bifunctional catalyst for rechargeable Zn-air battery. *Sci. China Mater.* 63, 1182–1195. doi: 10.1007/s40843-020-1276-8

Wu, G., Chen, W., Zheng, X., He, D., Luo, Y., Wang, X., et al. (2017). Hierarchical Fe-doped NiO_x nanotubes assembled from ultrathin nanosheets containing trivalent nickel for oxygen evolution reaction. *Nano Energy* 38, 167–174. doi: 10.1016/j.nanoen.2017.05.044

Xie, Z., Zhang, C., He, X., Liang, Y., Meng, D., Wang, J., et al. (2019). Iron and nickel mixed oxides derived from Ni(II)Fe(II)-PBA for oxygen evolution electrocatalysis. *Front. Chem.* 7:539. doi: 10.3389/fchem.2019.00539

Xiong, M., and Ivey, D. G. (2018). Synthesis of bifunctional catalysts for metal-air batteries through direct deposition methods. *Batter. Supercaps* 2, 326–335. doi: 10.1002/batt.201800069

Yang, Y., Lin, Z., Gao, S., Su, J., Lun, Z., Xia, G., et al. (2016). Tuning electronic structures of nonprecious ternary alloys encapsulated in graphene layers for optimizing overall water splitting activity. *ACS Catal.* 7, 469–479. doi: 10.1021/acscatal.6b02573

Yu, L., Yi, Q., Yang, X., and Chen, Y. (2019). An easy synthesis of Ni-Co doped hollow C-N tubular nanocomposites as excellent cathodic catalysts of alkaline and neutral zinc-air batteries. *Sci. China Mater.* 62, 1251–1264. doi: 10.1007/s40843-019-9439-9

Zhang, J., Wang, T., Pohl, D., Rellinghaus, B., Dong, R., Liu, S., et al. (2016). Interface engineering of MoS_2/Ni_3S_2 heterostructures for highly enhanced electrochemical overall-water-splitting activity. *Angew. Chem. Int. Ed.* 55, 6702–6707. doi: 10.1002/anie.201602237

Zhang, L., Chang, C., Hsu, C.-W., Chang, C.-W., and Lu, S.-Y. (2017). Hollow nanocubes composed of well-dispersed mixed metal-rich phosphides in N-doped carbon as highly efficient and durable electrocatalysts for the oxygen evolution reaction at high current densities. *J. Mater. Chem. A.* 5, 19656–19663. doi: 10.1039/C7TA04905F

Zhu, W., Zhu, G., Yao, C., Chen, H., Hu, J., Zhu, Y., et al. (2020). Porous amorphous FeCo alloys as pre-catalysts for promoting the oxygen evolution reaction. *J. Alloys Compd.* 828:154465. doi: 10.1016/j.jallcom.2020.154465

Conflict of Interest: The authors declare that the research was conducted in the absence of any commercial or financial relationships that could be construed as a potential conflict of interest.

frontiers in Chemistry

MINI REVIEW
published: 09 December 2020
doi: 10.3389/fchem.2020.582146

A Mini Review of the Preparation and Photocatalytic Properties of Two-Dimensional Materials

Shuhua Hao[1†], Xinpei Zhao[2†], Qiyang Cheng[1†], Yupeng Xing[1], Wenxuan Ma[1], Xiaoke Wang[1], Gang Zhao[1] and Xijin Xu[1*]*

[1] Laboratory of Functional Micro and Nano Materials and Devices, School of Physics and Technology, University of Jinan, Jinan, China, [2] Department of Chemical Engineering and Safety, Binzhou University, Binzhou, China

The successful preparation and application of graphene shows that it is feasible for the materials with a thickness of a single atom or few atomic layers to exist stably in nature. These materials can exhibit unusual physical and chemical properties due to their special dimension effects. At present, researchers have made great achievements in the preparation, characterization, modification, and theoretical research of 2D materials. Because the structure of 2D materials is often similar, it has a certain degree of qualitative versatility. Besides, 2D materials often carry good catalytic performance on account of their more active sites and adjustable harmonic electronic structure. In this review, taking 2D materials as examples [graphene, boron nitride (h-BN), transition metal sulfide and so on], we review the crystal structure and preparation methods of these materials in recent years, focus on their photocatalyst properties (carbon dioxide reduction and hydrogen production), and discuss their applications and development prospects in the future.

Keywords: two-dimensional materials, preparation method, photocatalytic properties, catalytic effect, hydrogen production

OPEN ACCESS

Edited by:
Guohua Jia,
Curtin University, Australia

Reviewed by:
Huayang Zhang,
University of Adelaide, Australia
Da Chen,
China Jiliang University, China
Yazi Liu,
Nanjing Normal University, China

***Correspondence:**
Gang Zhao
sps_zhaog@ujn.edu.cn
Xijin Xu
sps_xuxj@ujn.edu.cn

† These authors have contributed equally to this work

Specialty section:
This article was submitted to Nanoscience, a section of the journal Frontiers in Chemistry

Received: *10 July 2020*
Accepted: *18 November 2020*
Published: *09 December 2020*

Citation:
Hao S, Zhao X, Cheng Q, Xing Y, Ma W, Wang X, Zhao G and Xu X (2020) A Mini Review of the Preparation and Photocatalytic Properties of Two-Dimensional Materials. Front. Chem. 8:582146. doi: 10.3389/fchem.2020.582146

INTRODUCTION

By physically or chemically weakening the intermolecular forces, many layered materials can be prepared as monolayer or less layered materials, which tend to take on a nanoscale appearance in one direction and are called 2D materials. As the dimension changes, the properties of these 2D materials are often changed. A typical example is graphene, which has been widely reported due to its unique properties, including spectral absorption, high specific surface area, high young's modulus, high carrier mobility, and molecular barrier.

After the discovery of the excellent properties of graphene, more researchers focused their research on 2D materials, and subsequently discovered more 2D materials (Novoselov et al., 2004). Jacoby made a series of summaries of 2D materials: according to the periodic table, 2D materials can be divided into five categories, including transition metal carbide and nitride (MXenes), single element alkene, organic materials, nitride and transition metal dihalides (Kang et al., 2016). Many studies have shown that the above mentioned 2D materials have a broad application prospect. In all the researches on the properties and applications of 2D materials, catalytic performance is always a particularly important core direction. Under the mediation of its structure and electron specificity, 2D materials have good activities in photocatalytic carbon dioxide reduction and hydrogen production, and the properties of 2D materials are related to their preparation method, crystal structure, and doping type (Guardia et al., 2014; Cai and Feng, 2016; Sun et al., 2018).

In this review, we will briefly describe the crystal structure and preparation methods of 2D materials [graphene, hexagonal boron nitride (h-BN), transition metal disulfide and so on], and their applications in the photocatalytic field, such as hydrogen production and carbon dioxide reduction. Then, we focus on the photocatalytic properties and performance regulation of the above-mentioned materials, and summarize all aspects of the 2D materials, and discuss the potential of 2D materials in future scientific development.

SEVERAL METHODS OF EXFOLIATING 2D MATERIALS

Since Novoselov et al. successfully exfoliated graphene in 2004, 2D materials have attracted wide attention due to their unique physical and chemical properties, and there is an increasing demand for them year by year (Novoselov et al., 2004). However, 2D material is still a new material, and the preparation method needs to be further improved. The common preparation process is often accompanied by some shortcomings, such as too low efficiency, product impurity, and even some risks, limiting the research and application of 2D material properties. At present, the more mature method is mainly mechanical exfoliation. That is, a variety of mechanical forces are used to resist the van der Waals force between layered materials, which generally can obtain the required form of materials, but the waste of raw materials is also a serious issue. In addition, in many studies, the redox method is often discussed concerning the preparation of 2D materials, because of the low energy consumption and high yield of reaction products in the reaction process. Although the method has a wide range of applications, it still has some shortcomings that are difficult to solve. For example, the spatial structure of 2D materials will be damaged in the process of redox reaction, which will affect the physical and chemical properties of 2D materials. At present, although the preparation of 2D materials by chemical vapor deposition method is a very common and mature technology, this method has certain risks, and it is accompanied by high cost, and low yield and doping amount (Novoselov et al., 2012). In addition to the methods mentioned above, there are many other methods for preparing 2D materials, most of which can only be used to prepare and exfoliate one or two 2D materials, and are often not universal. Cai et al. illustrated the process of various 2D material preparation methodologies with graphic pictures, including intercalation-assisted expansion and exfoliation, Mechanical force-assisted exfoliation and Exfoliation of layer materials with ions or molecules between layers (Cai et al., 2018), as shown in **Figures 1a-c**. In the following, we will summarize the research progress of these aspects and comment on the influence of these methods on the catalytic effect of 2D materials.

Mechanical Exfoliation Method

Compared with other 2D material preparation methods, mechanical force-assisted exfoliation has such advantages as wide application, high yield, and high purity. Because this method usually does not require the addition of other substances other than auxiliary substances to increase mechanical force, impurities are rarely introduced into the process. The principle of the mechanical stripping method is to make use of various mechanical forces to offset the van der Waals forces between layers. The most typical examples of the preparation of graphene by mechanical stripping are Novoselov et al. (2004), two Nobel Prize winners in physics, who successfully used the adhesive force of tape to offset the van der Waals force between the layers of the material.

In some graphene grinding processes, special properties of auxillaries are often used to process 2D materials in order to improve the exfoliation speed and prevent the structure of 2D materials from being damaged. For example, Zhao et al. used the auxiliary effect of dimethylformamide dispersion medium to grind and centrifuge the original material with a ball mill (Zhao et al., 2010). It is worth mentioning that, compared with the original materials with a thickness of 30 $\sim$ 80 nm, suspension of graphene was prepared by ultrasonic expansion of the original material in organic solvent, and the graphene prepared after centrifugation has a very small thickness of 0.8 $\sim$ 1.8 nm. The thickness, which proved that the above method is simple to operate and has high yield, which can be used as a method for large-scale preparation of graphene, before and after the experiment indicated that the graphene obtained was one or more layers. Thus, this method is simple to operate and has high yield, which can be used as a method for large-scale preparation of graphene. Wu et al. propose a novel method to exfoliate hexagonal boron nitride (h-BN) powders to produce boron nitride nanosheets by applying pure shear ball milling (Wu et al., 2019). Applying a vertical load to the milling balls could alter their pattern of motion, which also increased their average tangential force and number of contacts, resulting in higher exfoliation and less impact action on the bulk h-BN powders.

Simple mechanical ultrasound can no longer efficiently exfoliate layered materials to meet the requirements of preparing 2D materials, which leads to the exploration of new mechanical ultrasonic methods. Zhao et al. search for all kinds of ultrasound machines and ultimately design an ultrasonic instrument with magnetic stirring, which is a high-efficiency exfoliation method to obtain abundant and superior graphene, h-BN, MoS_2, and WS_2 nanosheets in aqueous solution (Zhao et al., 2016). In addition, Aparna et al. used the auxiliary effect of methanol solution of 1-pyridine formic acid, and this auxiliary effect can be applied to other 2D materials besides graphene (Aparna et al., 2013). Ji et al. select eight representative 2D materials (graphite, h-BN, MoS_2, WS_2, black phosphorus, metalorganic framework $Mn(C_6H_8O_4)$ (H_2O) and two kinds of layered coordination polymer) with diverse inter- and intra-layer bonding interactions for the study, proposing to use the ratio between the in-plane and out-of-plane elastic modulus (E) as a universal index, $A_{In/Out}$ $(= E_{In-plane}/E_{Out-of-plane})$, to quantify the ease level of a 2D material's mechanical exfoliation (Ji et al., 2018).

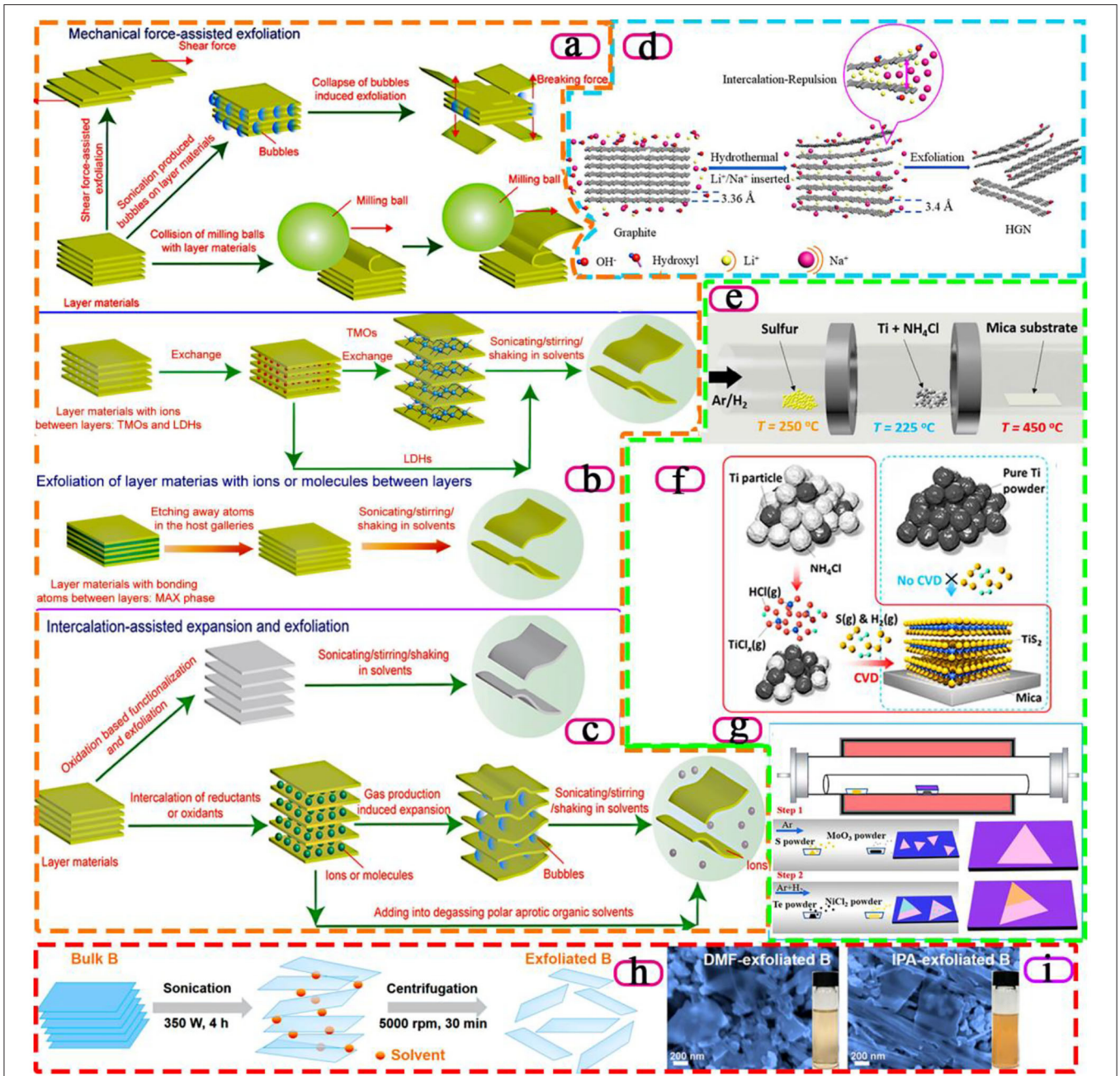

FIGURE 1 | Schematics of different methods to prepare 2D materials by exfoliating layer materials. **(a)** Mechanical force-assisted exfoliation. **(b)** Exfoliation of layer materials with ions or molecules between layers. **(c)** Intercalation-assisted expansion and exfoliation, (Cai et al., 2018). Copyright 2018, Royal Society of Chemistry. **(d)** Schematic illustration of exfoliating graphite by intercalating graphite with alkali-metal ions (Cheng et al., 2019). Copyright 2019, American Chemical Society. **(e)** Experimental setup for the CVD growth of TiS_2 nanosheets on mica substrates. **(f)** Schematic illustration of the CVD growth mechanism with NH_4Cl promoters (Gao et al., 2018). Copyright 2018, American Chemical Society. **(g)** Schematic illustrating the two-step CVD growth of $NiTe_2/MoS_2$ heterostructure (Zhai et al., 2020). Copyright 2020, American Chemical Society. **(h)** Schematic illustration of the sonication-assisted liquid-phase exfoliation process. **(i)** B sheets obtained by tip-sonication in DMF and IPA, respectively (Li et al., 2018). Copyright 2018, American Chemical Society.

Intercalation-Assisted Expansion and Exfoliation

There are also some unusual ways to prepare 2D materials, such as intercalation-assisted expansion and exfoliation, in which small molecules, non-covalently bonded molecules or polymers are inserted into a layered material and the material is stripped by reducing the van der Waals force of the layered layer. Since the invention of graphene in 2004, researchers have also tried the method of an ionic interlayer to prepare 2D materials. A "Chemical Weathering" exfoliation of atom-thick transition

metal dichalcogenides is proposed by Zhao et al. to efficiently exfoliate MoS_2 and WS_2 nanosheets (Zhao et al., 2015) As a result of the high chemical potentials of Na^+ and OH^- in the solution, the infiltration of Na^+ and OH^- into the interlayer space of MoS_2 or WS_2 crystal continuously occurs and leads to the accumulation of NaOH in the raw materials. When the concentration of NaOH in MoS_2 or WS_2 crystal exceeds the critical value (≈7.6%), the raw materials are eventually exfoliated into ultrathin pieces. As shown in **Figure 1d**, Cheng et al. develop Li^+/Na^+ co-intercalated exfoliation for graphene nanosheets by a hydrothermal method without the participation of any organic solvents (Cheng et al., 2019). The graphite is exfoliated into graphene nanosheets by intercalating graphite with different ratios of alkali-metal ions (Li^+, Na^+). The insertion of Li^+ and Na^+ expands the distance between graphene layers, which weakens the van der Waals force and effectively exfoliates graphene. Moreover, the thickness of the as-prepared graphene nanosheets was 2.65–2.78 nm.

The remarkable advantages of the Redox method are high production efficiency and low resource consumption. However, due to the large number of oxidant reducing agents used in the Redox process, environmental pollution is often caused in the preparation process, and defects may occur in the Redox process of 2D materials, resulting in performance differences of 2D materials. In addition, some 2D materials are difficult to prepare using the Redox method due to their inherent chemical properties.

The Hummers method is also a commonly used method for preparing 2D materials (Hummers and Offeman, 1958). After the reaction of graphite powder with potassium permanganate in concentrated sulfuric acid, graphene oxide flakes are obtained after stripping. The success of exfoliation is usually achieved by the action of functional groups such as C=O double bond and hydroxyl group produced by chemical reactions between layered structures (Georgakilas et al., 2012). Hou et al. studied the influence of the dosage of concentrated sulfuric acid (H_2SO_4) and potassium permanganate ($KMnO_4$) as well as the particle size of graphite raw material on the preparation process and performance of graphene sheet (Hou et al., 2020). The increase of oxidation degree of graphite material is beneficial to the escape of graphite oxide (GO) and the increase of concentration of concentrated sulfuric acid and potassium permanganate can improve the oxidation degree. Notably, sodium nitrate and sulfuric acid will have a synergistic effect on the preparation of 2D materials.

In the study of preparation of MXene, Cheng et al. found that MXene containing precious metal nanoparticles can undergo redox reaction (Cheng et al., 2020). In the reaction, the rare metal cation can absorb the electrons provided by MXene, so that MXene can be used as the reaction reducing agent without adding exogenous reducing agent, which reduces the pollution caused by introducing an exogenous reducing agent during the experiment. Although the above experiments did not solve the relationship between the preparation process of 2D materials and their physical/chemical properties, this study provided us with a new research idea.

Chemical Vapor Deposition

A common bottom-up method for preparing 2D films of materials is chemical vapor deposition (CVD), in which solid sediments are formed by chemical reactions to form films on the substrate surface, especially in the preparation of transition metal disulfide films. However, the preparation of 2D materials by vapor deposition method has certain risks, and it is accompanied by some disadvantages, such as the preparation process is not economical, and the products are not pure.

Li et al. prepared large area graphene films by combining copper foil with graphene films in this way (Li et al., 2009). Remarkably, they found that the resulting graphene films have different effects on different thicknesses of copper foil, showing different graphene thicknesses, but no monolayers. In addition, Eda et al. successfully prepared molybdenum disulphide with good photoluminescence by means of hexane solution of butyl lithium (Eda et al., 2011). Due to the difference between 2D material structure and block structure, the band gap structure of MoS_2 changed from indirect band gap to direct band gap after stripping from block material into layered material, resulting in the sudden increase of photoluminescence. This result provides a new direction for the structure research of nanoscale electronic materials. It is worth pointing out that Gao et al. report an ambient pressure CVD method to grow large-size, highly crystalline 2D TiS_2 nanosheets through *in-situ* generating titanium chloride as the gaseous precursor, solving the high oxophilicity of active Ti precursors (**Figures 1e,f**). The addition of the NH_4Cl promoter can react with Ti powders and switch the solid-phase sulfurization reaction into a CVD process, thus enabling the controllability over the size, shape, and thickness of the TiS_2 nanosheets via tuning the synthesis conditions (Gao et al., 2018). In **Figure 1g**, high quality 2D metal-semiconductor $NiTe_2/MoS_2$ heterostructure is prepared by two-step CVD growth. Moreover, Zhai et al. enhance electronic behavior and optoelectronic response by the epitaxial growth of metallic vdW layered materials that can bring a new method to improve the performance of optoelectronic devices (Zhai et al., 2020).

Liquid-Phase Exfoliation and Others

Liquid-phase exfoliation is also a common method. 2D materials that have been dispersed in the liquid phase are often expanded between their bulk layers, resulting in the reduction of intermolecular forces to the point where the ultrasonic wave produces enough energy to disperse the layers. As early as 2008, Coleman dispersed graphene in n-methyl pyrrolidone (NMP) solvent, used ultrasonic treatment for separation and centrifugation to remove impurities, and successfully prepared monolayer and less layer graphene without added oxides and structural defects through experimental tests (Coleman, 2009). Afterwards, to address the disadvantages of the above method, which requires a high boiling point and a large number of toxic basic solvents, they proposed another method: using surfactants to prepare graphene whose thickness is about 3 to 100 nm. Phosphorus can also be prepared in this way with the aid of the n-methyl-pyrrolidone (NMP) solvent (Brent et al., 2014). This method is also successful in the extraction of other 2D

materials, with Smith et al. successfully preparing a variety of inorganic layered materials such as h-BN, dispersion forms of transition metal disulfides and transition metal oxides (Smith et al., 2011). For the summary study, Coleman summarized the methods of a large number of 2D materials in the liquid phase stripping technology, and discussed the spatial structure, application direction and mass production of various 2D materials (Coleman, 2009). In addition to the above-mentioned aspects, ion embedding and ion exchange methods in the liquid phase have also been studied in detail, providing a more intuitive direction for the future 2D material research.

Compared with the methods of Redox and CVD, the liquid-phase exfoliation method is relatively simple and can be applied to the industrial preparation of some 2D materials. However, the thickness of the material obtained by ultrasonic stripping is often uneven and the impurities are difficult to remove, which is also an important problem for ultrasonic stripping of 2D materials. Li et al. demonstrate that high-quality few-layer B sheets can be prepared in large quantities by sonication-assisted liquid-phase exfoliation, as shown in **Figure 1h**. By simply varying the exfoliating solvent types and centrifugation speeds, the lateral size and thickness of the exfoliated B sheets (**Figure 1i**) can be controllably tuned (Li et al., 2018).

Because some 2D materials, such as graphene, TMD and h-BN, are more hydrophobic than bulk materials, in most cases, the addition of biomolecules as a stabilizer is conducive to the successful stripping and can improve the preparation efficiency. For example, Laaksonen et al. make use of the hydrophilicity of bovine serum protein and obtain better results in the traditional liquid-phase exfoliation experiment for 2D material (Laaksonen et al., 2010). Taking graphene, the most typical 2D material, as an example, Raccichini et al. comprehensively evaluated several aspects of the production methods of several 2D materials that are often considered by researchers (Raccichini et al., 2014).

PHOTOCATALYTIC PROPERTIES OF 2D MATERIALS

For years, people have realized the seriousness of the energy crisis and environmental pollution problem, and the solar energy induced the decomposition of water molecules to produce hydrogen and the degradation of pollutants is one of the typical solutions to these problems. The application of traditional materials in the catalytic reaction is accompanied by some difficulties, such as difficulty in controlling the reaction efficiency and high price (Xie et al., 2013; Benck et al., 2014; Zhao et al., 2020). 2D layered materials have only a single or a few nanometer layers and large specific surface area which exposed more atomic and functional surface structures, providing a large number of active sites and more intense reactions. The introduction of vacancy, dislocation, impurity, and functional group in 2D materials will change the catalytic properties of materials and make 2D materials become new catalysts. Photocatalysis of 2D materials can convert light energy into chemical energy (carbon-based fuel), effectively alleviate the greenhouse effect and improve the utilization efficiency of solar energy. In the current research background, although the reaction efficiency and reaction speed of 2D materials for catalysis are still not widely used, the application and research progress of new materials are still of great significance.

As early as 1972, researchers pointed out that based on the transparency of water, the light wavelength reflected by photocatalytic water splitting should be $<$190 nm (Fujishima and Honda, 1972). Subsequently, more semiconductor materials that can be used as catalysts were reported, such as TiO_2, ZnO, CdS, Fe_2O_3, SnO_2, WO_3 etc. However, traditional photocatalytic materials have some problems in the catalytic process, such as being uneconomic and having a large fluctuation of service life and low efficiency. Although conventional photocatalytic water splitting semiconductor materials have been developed for many years, their efficiency is still not up to the needs of industrialization. In the experiment of photoelectrode prepared by Liu et al. using heterogeneous WO_3 and Mn group hydrogen evolution catalyst, they believed that the photoelectrode should meet some requirements such as wide range absorption, high carrier mobility, long carrier life, high stability, and environmental friendliness (Liu et al., 2010). In order to satisfy the above conditions, the preparation of effective photocatalytic water splitting catalysts by reducing the dimension of materials has attracted much attention from the research field. In the study of 2D semiconductor materials, these three directions are all conducive to improving the efficiency of semiconductor induced light reaction of 2D materials, extending the wavelength of the excitation reaction, reducing the recombination between carriers and increasing the active sites around the surface (Dong et al., 2019; Sun et al., 2019; Yuan et al., 2019), as shown in **Figures 2a–f**.

In the application of traditional catalysts, there is a method to control the catalyst activity by treating the induced material itself. A quintessential method is the manufacture of TiO_2 (Chen J. et al., 2020) doped composite semiconductor with good catalytic effect, including but not limited to SnO_2/TiO_2 (Kusior et al., 2018), WO_3/TiO_2 (Wang et al., 2019), MoO_3/TiO_2 (Liu et al., 2016), SiO_2/TiO_2 (Cui et al., 2019), and ZrO_2/TiO_2. The development of 2D material catalysts is similar to that of traditional materials. Some people have found that the strong catalytic activity of 2D materials on composite nanocomposites based on density functional theory is due to the narrowing of band gaps. It is also demonstrated that 2D materials can be combined with effective photocatalysts to improve efficiency (Yang, 2017). The structures and properties of various nanocomposites are also studied comprehensively by density functional theory, and the theoretical results are verified by experiments (Zhao et al., 2021). **Figure 2g** shows that the change of reaction temperature and time used to prepare the material will affect the morphology of the material, different reaction conditions also have a certain degree of influence on the catalytic performance (Chen et al., 2017). Meanwhile, the above study laid a foundation for the photocatalytic application of 2D composites.

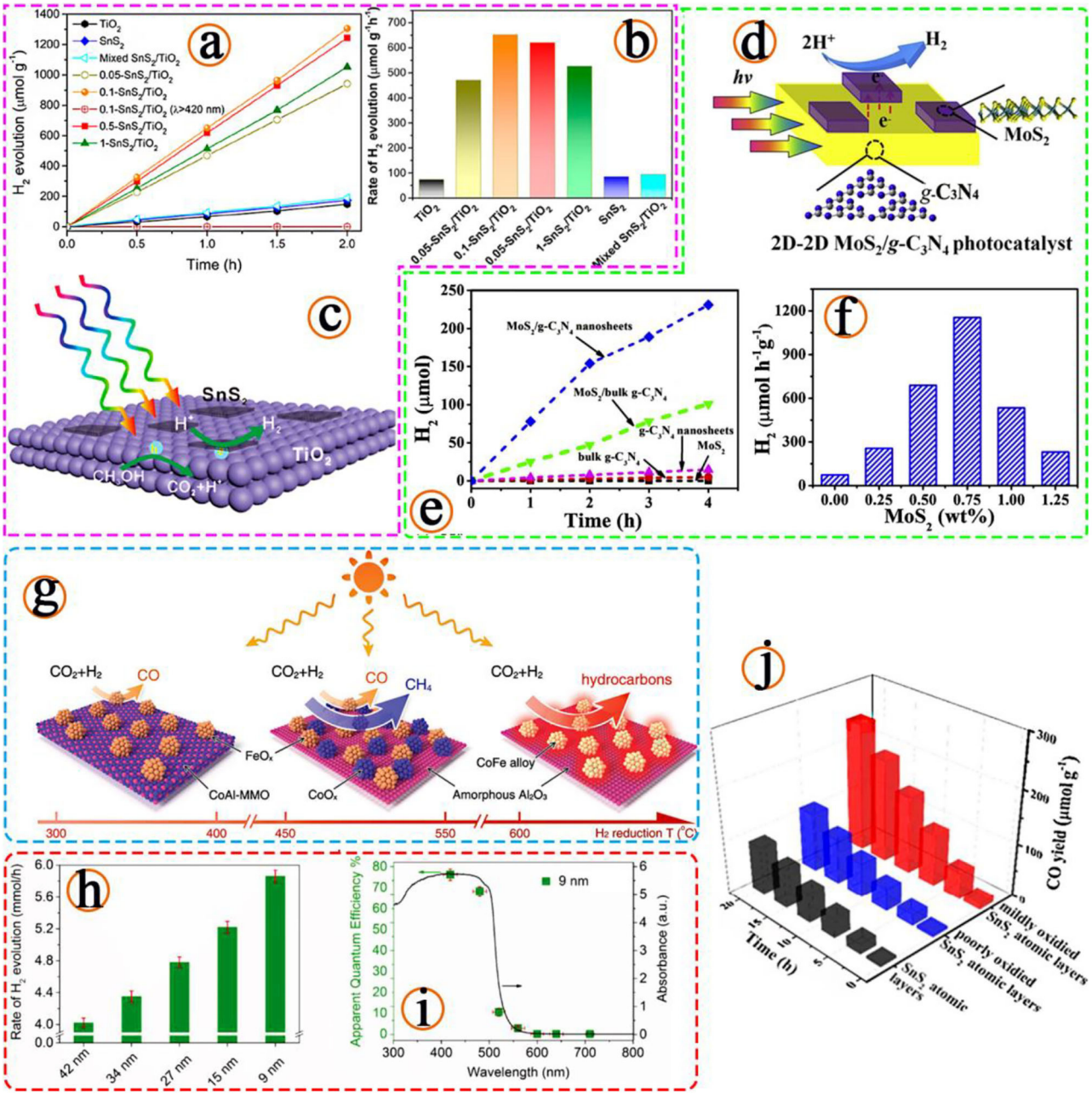

FIGURE 2 | (a) Photocatalytic H_2 evolution curves with different catalysts and **(b)** corresponding H_2 evolution rates. **(c)** Schematic illustration of the photoinduced electron transfer process at the interface of the 2D-2D SnS_2/TiO_2 photocatalyst for hydrogen production, (Sun et al., 2019). Copyright 2019, American Chemical Society. **(d)** Schematic diagrams of 2D-2D $MoS_2/g\text{-}C_3N_4$ nanosheets photocatalysts. **(e)** Time course of H_2 evolution over different g-C_3N_4-based photocatalysts. **(f)** The effect of MoS_2 amount on the photocatalytic H_2 evolution performance, (Yuan et al., 2019). Copyright 2019, Elsevier. **(g)** Illustration of the different CoFe-x catalysts formed by hydrogen reduction of a CoFeAl-LDH nanosheet precursor at different temperatures and the CO_2 hydrogenation selectivity of each CoFe-x catalyst is indicated, (Chen et al., 2017). Copyright 2017, Wiley. **(h)** The H_2 evolution rates of MoS_2/CdS composites with different lateral sizes of MoS_2. **(i)** Wavelength-dependent apparent quantum efficiency of H_2 evolution from the MoS_2 (≈9 nm) loaded CdS composite, (Yin et al., 2018). Copyright 2018, Wiley. **(j)** Stability photoreduction test for 1, 4, 8, 12, 16, and 20 h of CO_2 into CO under visible light irradiation for different samples, (Jiao et al., 2017). Copyright 2017, American Chemical Society.

Photocatalytic Activity of Graphene

Graphene, one of the most commonly used 2D materials, is also used in catalyst applications. As summarized by Deng et al. although the effect of the original graphene in catalytic reactions is often inert, the change in the electronic structure of graphene controlled by the crystal mechanism leads to the increase of

the catalytic activity of graphene (Deng et al., 2016). They classified these methods into five types: size effect, layer effect, edge and defect effect, curvature effect, dopant, and functional group effect.

Firstly, from the point of view of the photocatalytic water splitting of 2D materials to produce hydrogen, Xiang studied the composite photocatalyst (graphene/g-C_3N_4), which was prepared by calcining and impregnation reduction after the reduction of flowing nitrogen and hydrazine hydrate at 550°C (Xiang et al., 2011). It has been found that when graphene is used as the basis, the structure of graphene will affect the structure and optical properties of g-C_3N_4 catalyst, because graphene can effectively separate photogenerated charges as a conductive channel, thus improving the photocatalytic activity of g-C_3N_4. After a large number of experiments, the researchers compared the data and found that the best catalytic effect was when the mass content of graphene was 1.0%, the corresponding hydrogen production was 451μmol·h^{-1}·g^{-1}, 3.07 times higher than that of pure g-C_3N_4. What is more, Xiang et al. concluded that graphene is a promising dopant material in the visible light wavelength range and can be used to develop high-performance optical catalysts, which can also be used in sewage treatment and dye-sensitized solar cells. Similarly, Reduced GO (RGO) is seen as a carrier, a semiconductor, and a metal nanoparticle. Photoelectrons from the semiconductor can be transferred via RGO after exposure to ultraviolet light. This ability allows it to be used as a nano-catalyst material, since electrons can be transferred to the adsorbed material. Along with the investigation, the study of these composites can promote the industrialization of photoinduced hydrogen evolution reaction (Lightcap et al., 2010).

Photocatalytic degradation refers to the process of degradation of pollutants into innocuous outcome through the reaction process between free radicals and organic pollutants by using the highly active free radicals and photocatalysts produced by radiation in the reaction system. Wang et al. synthesized a new composite material, a graphene-based ultrathin barium titanate nanosheet with exposed {001} flat surface, with good photocatalytic activity (Wang et al., 2012). Through the success of the development of the new material, they summarized several key factors affecting the catalytic performance through spectral analysis, and gave several examples, including the formation of Ti-O-C bonds leading to a wider light absorption range, better charge separation rate, and a larger catalytic surface.

Graphene has the ability to adsorb pollutants and act as a semiconductor photocatalyst to degrade dye wastewater. The photocatalytic materials after 2D composites can not only rapidly transfer photogenerated electrons and rapidly separate electron holes, but also improve the adsorption performance of dyes. This kind of recombination 2D material has a broad application prospect and research value in the field of environment, because of its adsorption and catalytic degradation of environmental pollutants, such as heavy metals, dyes and persistent organic compounds, as well as environmental detection (Shen et al., 2014). Fan et al. compared the photocatalytic degradation performance of ZnO/GR composite nanosheets with that of ZnO and other materials by hydrothermal reaction and found that the catalytic performance of the composites was better (Fan et al., 2012). They believe that the photolithography of ZnO is inhibited by the composite material and ZnO/GR will be one of the key candidate materials for new catalysts. Doping of 2D composites is also a common method to improve their properties. One example is that Farhangi et al. doped titanium dioxide composite graphene sheets with iron and passed the sol-gel method (Farhangi et al., 2014). Compared with pure materials, the new Fe-TiO_2 with functionalized graphene flakes has better visible light absorption and conversion efficiency and higher photocatalytic activity. This experiment brings us to the conclusion that the photocatalytic intensity can be changed by improving the absorbability of dyes, expanding the optical response range, and improving the charge separation and differential transport performance. In addition, they carried out density functional calculations and found that the doping of atomic points works best when they are in the middle, which experimental results proved. This study of degradation provides a new way of thinking and direction for the study of 2D composites, which combines theory with practice.

Photocatalytic Activity of Transitional Metal Sulfides (TMDs)

In addition to widely studied Graphene, MoS_2 is also a common semiconductor catalytic material and is often used in 2D material induced photocatalytic experiments. In 2016, in the experiment of the photocatalytic performance of monolayer molybdenum disulfide on nanocomposites studied by Ding et al. the reasons for improving its photocatalytic activity and stability were explored, and the role of monolayer molybdenum disulfide as sensitizer and auxiliary catalyst (Ding et al., 2016). Compared with pure SnO_2, the bandgap of composite materials is smaller (0.49 eV), and the optical absorption spectrum can completely cover the visible region, even in the infrared region. They suggest that this dual effect may also be present in other MoS_2 semiconductor nanocomposites, paving the way for researchers to develop highly effective MoS_2 hybrid photocatalysts.

In the study of visible light catalytic carbon dioxide reduction reaction, 2D SnS_2 with partial oxidation state has good catalytic activity, because the material structure promotes the separation of electron holes, changes the adsorption energy of molecules, and improves the photocatalytic efficiency (Jiao et al., 2017; **Figure 2j**). In the experimental results, surface photovoltage and photoluminescence spectroscopy confirmed that the presence of hybrid oxides is conducive to the separation of charge and carrier. *In situ* Fourier transform infrared spectroscopy fully indicated that the main intermediate product of CO_2 photocatalytic reduction is COOH*. In addition, the researchers calculated by density functional theory that with the help of stable COOH* intermediates, the electron positions on Sn atoms generated by local oxidation can reduce the activation energy barrier of CO_2. Due to the above characteristics, the oxidized SnS_2 atomic layer showed a carbon monoxide production rate of 12.28 in the molg^{-1}h^{-1}, which was higher than the slightly oxidized and unoxidized SnS_2 by 2.3 and 2.6 times. In conclusion, it can be proved experimentally and theoretically that locally oxidized regions can improve the efficiency of charge separation and

promote the activation of carbon dioxide and open up new ways to reduce the greenhouse effect.

Similarly, by contacting the edges to create more active catalytic sites, monolayer molybdenum disulphide is synthesized with rich active sites by gradient liquid-phase exfoliation (Yin et al., 2018), as shown in **Figures 2h,i**. The prepared molybdenum disulphide shows excellent performance in the generation of H_2 by photocatalysis. The optimized monolayer MoS_2 nanometer sheet with an average transverse size of 9 nm can significantly improve the photocatalytic performance of MoS_2 nanometer sheet through synergistic action and lateral size change due to the increase of the active site density and the shortening of the charge diffusion distance.

Photocatalytic Activity of Graphitic Carbon Nitride

Graphitic carbon nitride (g-C_3N_4) with high physicochemical stability, a narrow band gap (2.7 eV), tunable electronic structure, low cost, non-toxicity, and most importantly, appropriate band edge, as a typical two-dimensional (2D) metal-free conjugated polymer semiconductor material, has been broadly applied in photocatalysis for H_2 production and CO_2 photoreduction. However, the limitations of g-C_3N_4, such as poor electric conductivity, trivial charge flexibility and disadvantaged visible light utilization, have been found in the study, which greatly limited its performance in photocatalysis. In that case, a variety of methods have been proposed to improve catalytic performance, including textural property design and constructing semiconductor heterojunctions, etc. Metal sulfides have attracted wide attention in photocatalytic hydrogen production because of their suitable band gap and catalytic function. SnS_2 was supported on 2D g-C_3N_4 for excellent and stable visible light photocatalytic hydrogen generation (Jing et al., 2018). The SnS_2 nanoparticles/g-C_3N_4 composites improving the rate of electron-hole pair separation exhibit the highest visible-light-driven H_2-generation rate of 6305.18 μmol h^{-1} g^{-1} without any noble metal as cocatalyst. And a mesoporous 3D/2D NiCoP/g-C_3N_4 heterostructure was synthesized (Li et al., 2020). This work has indicated that multidimensional heterojunctions of transition metal phosphides supported on g-C_3N_4 can dramatically increase the photocatalytic activity and stability by fabricating surface metal-N bonding states. These findings regarding the design, fabrication and photophysical properties of heterostructure systems may find use in other photocatalytic applications including CO_2 reduction and water purification. g-C_3N_4/NiAl-LDH 2D/2D hybrid heterojunction is used for high-performance photocatalytic reduction of CO_2 into renewable fuels (Tonda et al., 2018). In the process of photocatalysis, the construction of heterojunctions by combining two different semiconductors, especially the two-dimensional (2D) layered structure with appropriate conductive potential and valence band potential, is one of the most effective ways to improve the separation efficiency of photogenerated carriers. In addition, two-dimensional (2D) g-C_3N_4/BiOCl heterostructures demonstrate a facile strategy of interfacial oxygen vacancies (IOVs) with enhanced interfacial interaction to promote the photocatalytic conversion of CO_2 (Chen Y. et al., 2020). Z-Scheme assembly of 2D ZnV_2O_6/RGO/g-C_3N_4 nanosheets with RGO/pCN as solid-state electron mediators enables efficient CO_2 conversion under visible-light irradiation (Bafaqeer et al., 2019).

As mentioned above, in the study of catalytic performance of a variety of 2D materials, the introduction of functional 2D materials into a variety of semiconductor photocatalysts, or other methods such as adding semiconductor photocatalysts with 2D materials as the matrix can enhance the photocatalytic reactivity by virtue of the unique properties of 2D materials. These physical or chemical bonds made of 2D materials enable the composite to possess unique properties, such as multiple active sites, increased optical response range, and enhanced charge separation and transport performance, thus enhancing the photocatalytic performance of 2D materials. This has a good effect on our understanding of the photocatalytic reaction mechanism and the creation of industrializable catalysts.

2D materials have great structural advantages in the field of photocatalysis because of their high electrochemical nature on both basal planes and edges of 2D materials in energy conversion (e.g., TMDs), well-balanced hydrogen binding Gibbs free energy on the basal sites (e.g., 1T′ MoS_2), high specific surface area and abundant surface active sites, and the external performance is that 2D materials have outstanding catalytic performance. Not only the excellent performance, but also the unique 2D structure, is fairly attractive to researchers, providing advantages such as such as high cooperation. On this basis, the synthesized heterostructure and regular composite structure have better performance and work efficiency in the process of research.

CONCLUSION AND OUTLOOK

Regarding the preparation of 2D materials, we mainly talked about several preparation processes, such as the mechanical exfoliation method, Redox method, chemical vapor deposition method and ultrasonic liquid exfoliation method. In the preparation of materials, we pay special attention to the structure of the materials, because the catalytic effect of 2D materials is often related to morphology, phase structure, and porosity. For instance, pure graphene is inert, but after doping, it has a good catalytic performance. MoS_2 and WS_2 nanosheets not only have the effect of photolysis themselves, but also can replace precious metals as composite catalysts.

Generally, there are pure 2D catalysts which will utilize the unique characteristics of 2D materials in the catalytic reaction to improve the catalytic efficiency, 2D materials as doping or as carriers and other methods to prepare catalysts. Representative is the combination of 2D materials with traditional precious metal catalyst of Pt. At the same time, many processes to enhance the catalytic effect are introduced, including enhancing the transmission of charge, increasing the surface active sites, and lengthening the absorption spectrum. Obviously, part of the above preparation methods are first calculated by density functional principle and then verified by experiments and that also explains the importance of studying the catalytic

performance mechanism of 2D materials. In the reports of these catalysts, a slice of them have their own styles and unique preparation methods, which have opened up new ways for researchers to improve performance, enhance stability and improve yield.

It is widely believed that 2D materials have good catalytic potential. Although many good 2D materials or 2D materials based catalysts have been introduced above, the application of 2D materials in catalyst research is not limited to that and the research and development of new hybrid 2D material components still have great prospects. We believe that under more research background, under more scientific and theoretical analysis of 2D material structure, 2D catalysts will be more satisfactory in terms of preparation, efficiency, and stability. Even applying it to the process of industrialization does not take much time. In the future, the structure and morphology of 2D materials will be more diversified.

In addition, 2D structures are used as the foundation to participate in the design of more superstructures, including heterostructures, metal and non-metal doping, and coating. Even more prominent properties of 2D structures, such as magic horn graphene, will be discovered. And the realization of these prospects may require the efforts of researchers and the study of the problem from a different perspective.

AUTHOR CONTRIBUTIONS

All the authors contributed in preparation, characterization and analysis structure, performance of materials, discussed the results, and commented on the manuscript.

FUNDING

This work was supported by the National Natural Science Foundation of China (Grant Nos. 51802177 and 51672109), the Major Basic Program of the Natural Science Foundation of Shandong Province (Contract ZR2018ZC0842), Independent Cultivation Program of Innovation Team of Ji'nan City (Grant No. 2019GXRC011), and Natural Science Foundation of Shandong Province (Grant No. ZR2018BEM019).

REFERENCES

Aparna, R., Sivakumar, N., Balakrishnan, A., Sreekumar Nair, A., Nair, S. V., and Subramanian, K. R. V. (2013). An effective route to produce few-layer graphene using combinatorial ball milling and strong aqueous exfoliants. *J. Renew. Sustain. Ener.* 5:033123. doi: 10.1063/1.4809794

Bafaqeer, A., Khan, A. A., Amin, N. A. S., and Tahir, M. (2019). Indirect Z-scheme assembly of 2D ZnV_2O_6/RGO/g-C_3N_4 nanosheets with RGO/pCN as solid-state electron mediators toward visiblelight-enhanced CO_2 reduction. *Ind. Eng. Chem. Res.* 58, 8612–8624. doi: 10.1021/acs.iecr.8b06053

Benck, J. D., Hellstern, T. R., Kibsgaard, J., Chakthranont, P., and Jaramillo, T. F. (2014). Catalyzing the hydrogen evolution reaction (HER) with molybdenum sulfide nanomaterials, *ACS Catal.* 4, 3957–3971. doi: 10.1021/cs500923c

Brent, J. R., Savjani, N., Lewis, E. A., Haigh, S. J., Lewis, D. J., and O'Brien, P. (2014). Production of few-layer phosphorene by liquid exfoliation of black phosphorus. *Chem. Commun.* 50, 13338–13341. doi: 10.1039/C4CC05752J

Cai, X. K., Luo, Y. T., Liu, B. L., and Cheng, H. M. (2018). Preparation of 2D material dispersions and their applications. *Chem. Soc. Rev.* 47, 6224–6266. doi: 10.1039/C8CS00254A

Cai, Y. Q., and Feng, Y. P. (2016). Review on charge transfer and chemical activity of TiO_2: mechanism and applications. *Prog. Surf. Sci.* 91, 183–202. doi: 10.1016/j.progsurf.2016.11.001

Chen, G. B., Gao, R., Zhao, Y. F., Li, Z. H., Waterhouse, G. I. N., Shi, R., et al. (2017). Alumina-supported CoFe alloy catalysts derived from layered-double-hydroxide nanosheets for efficient photothermal CO_2 hydrogenation to hydrocarbons. *Adv. Mater.* 30:1704663. doi: 10.1002/adma.201704663

Chen, J., Zheng, H. Q., Zhao, Y., Que, M. D., Lei, X. P., Zhang, K., et al. (2020). Preparation of facet exposed $TiO_2/Ti_3C_2T_x$ composites with enhanced photocatalytic activity. *J. Phys. Chem. Solids.* 145:109565. doi: 10.1016/j.jpcs.2020.109565

Chen, Y., Cao, Y. H., Zhang, F. Y., Zou, Y. Z., Huang, Z. A., Ye, L. Q., et al. (2020). Interfacial oxygen vacancy engineered two-dimensional g-c_3n_4/biocl heterostructures with boosted photocatalytic conversion of CO_2. *ACS Appl. Energy Mater.* 3, 4610–4618. doi: 10.1021/acsaem.0c00273

Cheng, R. F., Hu, T., Hu, M. M., Li, C. J., Liang, Y., Wang, Z. H., et al. (2020). MXenes induce epitaxial growth of size-controlled noble nanometals: a case study for surface enhanced Raman scattering (SERS). *J. Mater. Sci. Technol.* 40, 119–127. doi: 10.1016/j.jmst.2019.09.013

Cheng, Z. L., Kong, Y. C., and Liu, Z. (2019). Li^+/Na^+ co-assisted hydrothermal exfoliation for graphite into few-layer graphene nanosheets and their excellent friction reducing performance. *ACS Sustain. Chem. Eng.* 7, 19770–19778. doi: 10.1021/acssuschemeng.9b05060

Coleman, J. N. (2009). Liquid-phase exfoliation of nanotubes and graphene. *Adv. Funct. Mater.* 19, 3680–3695. doi: 10.1002/adfm.200901640

Cui, L., Song, Y. H., Wang, F. K., Sheng, Y., and Zou, H. F. (2019). Electrospinning synthesis of SiO_2-TiO_2 hybrid nanofibers with large surface area and excellent photocatalytic activity. *Appl. Surf. Sci.* 488, 284–292. doi: 10.1016/j.apsusc.2019.05.151

Deng, D. H., Novoselov, K. S., Fu, Q., Zheng, N. F., Tian, Z. Q., and Bao, X. H. (2016). Catalysis with two-dimensional materials and their heterostructures. *Nat. Nanotechnol.* 11, 218–230. doi: 10.1038/nnano.2015.340

Ding, S.-S., Huang, W.-Q., Yang, Y.-C., Zhou, B.-X., Hu, W.-Y., Long, M.-Q., et al. (2016). Dual role of monolayer MoS_2 in enhanced photocatalytic performance of hybrid MoS_2/SnO_2 nanocomposite. *J. Appl. Phys.* 119:205704. doi: 10.1063/1.4952377

Dong, H. J., Zhang, X. X., Zuo, Y., Song, N., Xin, X., Zheng, B. H., et al. (2019). 2D Ti_3C_2 as electron harvester anchors on 2D g-C_3N_4 to create boundary edge active sites for boosting photocatalytic performance. *Appl. Catal. A-Gen.* 590:117367. doi: 10.1016/j.apcata.2019.117367

Eda, G., Yamaguchi, H., Voiry, D., Fujita, T., Chen, M., and Chhowalla, M. (2011). Photoluminescence from chemically exfoliated MoS_2. *Nano Lett.* 11, 5111–5116. doi: 10.1021/nl201874w

Fan, H. G., Zhao, X. T., Yang, J. H., Shan, X. N., Yang, L. L., Zhang, Y. J., et al. (2012). ZnO–graphene composite for photocatalytic degradation of methylene blue dye. *Catal. Commun.* 29, 29–34. doi: 10.1016/j.catcom.2012.09.013

Farhangi, N., Ayissi, S., and Charpentier, P. A. (2014). Fe doped TiO_2-graphene nanostructures: synthesis, DFT modeling and photocatalysis. *Nanotechnology* 25:305601. doi: 10.1088/0957-4484/25/30/305601

Fujishima, A., and Honda, K. (1972). Electrochemical photolysis of water at a semiconductor electrode. *Nature* 238, 37–38. doi: 10.1038/238037a0

Gao, Z. F., Ji, Q. Q., Shen, P. C., Han, Y., Leong, W. S., Mao, N. N., et al. (2018). *In-situ* generated volatile precursor for CVD growth of a semimetallic 2D dichalcogenide. *ACS Appl. Mater. Inter.* 10, 34401–34408. doi: 10.1021/acsami.8b13428

Georgakilas, V., Otyepka, M., Bourlinos, A. B., Chandra, V., Kim, N., Kemp, K. C., et al. (2012). Functionalization of graphene: covalent and non-covalent approaches, derivatives and applications. *Chem. Rev.* 112, 6156–6214. doi: 10.1021/cr3000412

Guardia, L., Paredes, J. I., Munuera, J. M., Villar-Rodil, S., Ayán-Varela, M., Martinez-Alonso, A., et al. (2014). Chemically exfoliated MoS_2 nanosheets as an efficient catalyst for reduction reactions in the aqueous phase. *ACS Appl. Mater. Inter.* 6, 21702–21710. doi: 10.1021/am506922q

Hou, Y., Lv, S., Liu, L., and Liu, X. (2020). High-quality preparation of graphene oxide via the Hummers' method: understanding the roles of the intercalator, oxidant, and graphite particle size. *Ceram. Int.* 46, 2392–2402. doi: 10.1016/j.ceramint.2019.09.231

Hummers, W. S., and Offeman, R. E. (1958). Preparation of graphitic oxide. *J. Am. Chem. Soc.* 80:1339. doi: 10.1021/ja01539a017

Ji, L. J., Qin, Y., Gui, D., Li, W., Li, Y. C., Li, X. D., et al. (2018). Quantifying the exfoliation ease level of 2D materials via mechanical anisotropy. *Chem. Mater.* 30, 8732–8738. doi: 10.1021/acs.chemmater.8b01082

Jiao, X. C., Li, X. D., Jin, X. Y., Sun, Y. F., Xu, J. Q., Liang, L., et al. (2017). Partially oxidized SnS_2 atomic layers achieving efficient visible-light-driven CO_2 reduction. *J. Am. Chem. Soc.* 139, 18044–18051. doi: 10.1021/jacs.7b10287

Jing, L. Q., Chen, Z. G., He, M. Q., Xie, M., Liu, J., Xu, H., et al. (2018). Different morphologies of SnS_2 supported on 2D g-C_3N_4 for excellent and stable visible light photocatalytic hydrogen generation. *ACS Sustain. Chem. Eng.* 6, 5132–5141. doi: 10.1021/acssuschemeng.7b04792

Kang, J., Sangwan, V. K., Wood, J. D., Liu, X. L., Balla, I., Lam, D., et al. (2016). Layer-by-layer sorting of rhenium disulfide via high-density isopycnic density gradient ultracentrifugation. *Nano Lett*. 16, 7216–7223. doi: 10.1021/acs.nanolett.6b03584

Kusior, A., Zych, L., Zakrzewska, K., and Radecka, M. (2018). Photocatalytic activity of TiO_2/SnO_2 nanostructures with controlled dimensionality/complexity. *Appl. Surf. Sci.* 471, 973–985. doi: 10.1016/j.apsusc.2018.11.226

Laaksonen, P., Kainlauri, M., Laaksonen, T., Shchepetov, A., Jiang, H., Ahopelto, J., et al. (2010). Interfacial engineering by proteins: exfoliation and functionalization of graphene by hydrophobins. *Angew. Chem. Int. Edit.* 49, 4946–4949. doi: 10.1002/anie.201001806

Li, C. M., Wu, H. H., Du, Y. H., Xi, S. B., Dong, H. J., Wang, S. H., et al. (2020). Mesoporous 3D/2D NiCoP/g-C_3N_4 heterostructure with Dual Co-N and Ni-N bonding states for boosting photocatalytic H_2 production activity and stability. *ACS Sustain. Chem. Eng.* 8, 12934–12943. doi: 10.1021/acssuschemeng.0c03496

Li, H. L., Jing, L., Liu, W. W., Lin, J. J., Tay, R. Y., Tsang, S. H., et al. (2018). Scalable production of few-layer boron sheets by liquid-phase exfoliation and their superior supercapacitive performance. *ACS Nano* 12, 1262–1272. doi: 10.1021/acsnano.7b07444

Li, X. S., Cai, W. W., An, J., Kim, S., Nah, J., Yang, D. X., et al. (2009). Large-area synthesis of high-quality and uniform graphene films on copper foils. *Science* 324, 1312–1314. doi: 10.1126/science.1171245

Lightcap, I. V., Kosel, T. H., and Kamat, P. V. (2010). Anchoring semiconductor and metal nanoparticles on a two-dimensional catalyst mat. Storing and shuttling electrons with reduced graphene oxide. *Nano Lett.* 10, 577–583. doi: 10.1021/nl9035109

Liu, H., Lv, T., Zhu, C. K., and Zhu, Z. F. (2016). Direct bandgap narrowing of TiO_2 /MoO_3 heterostructure composites for enhanced solar-driven photocatalytic activity. *Sol. Energ. Mat. Sol. C* 153, 1–8. doi: 10.1016/j.solmat.2016.04.013

Liu, R., Lin, Y. J., Chou, L.-Y., Sheehan, S. W., He, W. S., Zhang, F., et al. (2010). Water splitting by tungsten oxide prepared by atomic layer deposition and decorated with an oxygen-evolving catalyst. *Angew. Chem.* 123, 519–522. doi: 10.1002/ange.201004801

Novoselov, K. S., Fal'ko, V. I., Colombo, L., Gellert, P. R., Schwab, M. G., and Kim, K. (2012). A roadmap for graphene. *Nature* 490, 192–200. doi: 10.1038/nature11458

Novoselov, K. S., Geim, A. K., Morozov, S. V., Jiang, D., Zhang, Y., Dubonos, S. V., et al. (2004). Electric field effect in atomically thin carbon films. *Science* 306, 666–669. doi: 10.1126/science.1102896

Raccichini, R., Varzi, A., Passerini, S., and Scrosati, B. (2014). The role of graphene for electrochemical energy storage. *Nat. Mater.* 14, 271–279. doi: 10.1038/nmat4170

Shen, Y., Fang, Q., and Chen, B. L. (2014). Environmental applications of three-dimensional graphene-based macrostructures: adsorption, transformation, and detection. *Environ. Sci. Technol.* 49, 67–84. doi: 10.1021/es504421y

Smith, R. J., King, P. J., Lotya, M., Wirtz, C., Khan, U., De, S., et al. (2011). Large-scale exfoliation of inorganic layered compounds in aqueous surfactant solutions. *Adv. Mater.* 23, 3944–3948. doi: 10.1002/adma.201102584

Sun, L. Q., Zhao, Z. C., Li, S., Su, Y. P., Huang, L., Shao, N. N., et al. (2019). Role of SnS_2 in 2D−2D SnS_2/TiO_2 nanosheet heterojunctions for photocatalytic hydrogen evolution. *ACS Appl. Nano Mater.* 2, 2144–2151. doi: 10.1021/acsanm.9b00122

Sun, M. M., Dong, J. C., Lv, Y., Zhao, S. Q., Meng, C. X., Song, Y. J., et al. (2018). Pt@h-BN core–shell fuel cell electrocatalysts with electrocatalysis confined under outer shells. *Nano Res.* 11, 3490–3498. doi: 10.1007/s12274-018-2029-5

Tonda, S., Kumar, S., Bhardwaj, M., Yadav, P., and Ogale, S. (2018). g-C_3N_4/NiAl-LDH 2D/2D hybrid heterojunction for high-performance photocatalytic reduction of CO_2 into renewable fuels. *ACS Appl. Mater. Interfaces* 10, 2667–2678. doi: 10.1021/acsami.7b18835

Wang, W.-S., Wang, D.-H., Qu, W.-G., Lu, L.-Q., and Xu, A.-W. (2012). Large ultrathin anatase tio$_2$ nanosheets with exposed {001} facets on graphene for enhanced visible light photocatalytic activity. *J. Phys. Chem. C,* 116, 19893–19901. doi: 10.1021/jp306498b

Wang, X. G., Sun, M. H., Murugananthan, M., Zhang, Y. R., and Zhang, L. Z. (2019). Electrochemically self-doped WO_3/TiO_2 nanotubes for photocatalytic degradation of volatile organic compounds. *Appl. Catal. B-Environ.* 260:118205. doi: 10.1016/j.apcatb.2019.118205

Wu, G. Y., Yi, M. D., Xiao, G. C., Chen, Z. Q., Zhang, J. J., and Xu, C. H. (2019). A novel method for producing boron nitride nanosheets via synergistic exfoliation with pure shear ball milling and ultrasonication. *Ceram. Int.* 45, 23841–2384845. doi: 10.1016/j.ceramint.2019.08.058

Xiang, Q. J., Yu, J. G., and Jaroniec, M. (2011). Preparation and enhanced visible-light photocatalytic H_2-production activity of graphene/C_3N_4 composites. *J. Phys. Chem. C*, 115, 7355–7363. doi: 10.1021/jp200953k

Xie, J. F., Zhang, J. J., Li, S., Grote, F., Zhang, X. D., Zhang, H., et al. (2013). Controllable disorder engineering in oxygen-incorporated mos$_2$ ultrathin nanosheets for efficient hydrogen evolution, *J. Am. Chem. Soc.* 135, 17881–17888. doi: 10.1021/ja408329q

Yang, N. L. (2017). The preparation of nano composites and their applications in solar energy conversion || photocatalytic properties of graphdiyne and graphene modified TiO_2: from theory to experiment. Springer Theses, 4(Chapter 5), 93–110. doi: 10.1007/978-3-662-53485-4_5

Yin, L. S., Hai, X., Chang, K., Ichihara, F., and Ye, J. H. (2018). Synergetic exfoliation and lateral size engineering of MoS_2 for enhanced photocatalytic hydrogen generation. *Small* 14:1704153. doi: 10.1002/smll.201704153

Yuan, Y.-J., Shen, Z. K., Wu, S. T., Su, Y. B., Pei, L., Ji, Z. G., et al. (2019). Liquid exfoliation of g-C_3N_4 nanosheets to construct 2D-2D MoS_2/g-C_3N_4 photocatalyst for enhanced photocatalytic H_2 production activity. *Appl. Catal. B Environ.* 246, 120–128. doi: 10.1016/j.apcatb.2019.01.043

Zhai, X. K., Xu, X., Peng, J. B., Jing, F. L., Zhang, Q. L., Liu, H. J., et al. (2020). Enhanced optoelectronic performance from CVD-grown metal-semiconductor $NiTe_2/MoS_2$ heterostructures. *ACS Appl. Mater. Inter.* 12, 24093–24101. doi: 10.1021/acsami.0c02166

Zhao, G., Cheng, Y. L., Sun, P. X., Ma, W. X., Hao, S. H., Wang, X. K., et al. (2020). Biocarbon based template synthesis of uniform lamellar MoS_2 nanoflowers with excellent energy storage performance in lithium-ion battery and supercapacitors, *Electrochim. Acta*. 331:135262. doi: 10.1016/j.electacta.2019.135262

Zhao, G., Han, S., Wang, A. Z., Wu, Y. Z., Zhao, M. W., Wang, Z. P., et al. (2015). "Chemical weathering" exfoliation of atom-thick transition metal dichalcogenides and their ultrafast saturable absorption properties. *Adv. Funct. Mater.* 25, 5292–5299. doi: 10.1002/adfm.201501972

Zhao, G., Hao, S. H., Guo, J. H., Xing, Y. P., Zhang, L., and Xu, X. J. (2021). Design of p-n homojunctions in metal-free carbon nitride photocatalyst for overall water splitting. *Chinese J. Catal.* 42, 501–509. doi: 10.1016/S1872-2067(20)63670-1

Zhao, G., Wu, Y. Z., Shao, Y. L., and Hao, X. P. (2016). Large-quantity and continuous preparation of two-dimensional nanosheets. *Nanoscale* 8, 5407–5411. doi: 10.1039/C5NR07950K

Zhao, W. F., Wu, F. R., Wu, H., and Chen, G. H. (2010). Preparation of colloidal dispersions of graphene sheets in organic solvents by using ball milling. *J. Nanomater.* 2010, 1–5. doi: 10.1155/2010/528235

Conflict of Interest: The authors declare that the research was conducted in the absence of any commercial or financial relationships that could be construed as a potential conflict of interest.

Advantages of publishing in Frontiers

OPEN ACCESS
Articles are free to read for greatest visibility and readership

FAST PUBLICATION
Around 90 days from submission to decision

HIGH QUALITY PEER-REVIEW
Rigorous, collaborative, and constructive peer-review

TRANSPARENT PEER-REVIEW
Editors and reviewers acknowledged by name on published articles

Frontiers
Avenue du Tribunal-Fédéral 34
1005 Lausanne | Switzerland

Visit us: www.frontiersin.org
Contact us: frontiersin.org/about/contact

REPRODUCIBILITY OF RESEARCH
Support open data and methods to enhance research reproducibility

DIGITAL PUBLISHING
Articles designed for optimal readership across devices

FOLLOW US
@frontiersin

IMPACT METRICS
Advanced article metrics track visibility across digital media

EXTENSIVE PROMOTION
Marketing and promotion of impactful research

LOOP RESEARCH NETWORK
Our network increases your article's readership